

MECHANICAL AND THERMAL STUDY
OF HYDRATE BEARING SEDIMENTS

A Thesis
Presented to
The Academic Faculty

by

Tae Sup Yun

In Partial Fulfillment
of the Requirements of the Degree
Doctor of Philosophy in Civil and Environmental Engineering

Georgia Institute of Technology
August 2005

Copyright © by Tae Sup Yun

MECHANICAL AND THERMAL STUDY
OF HYDRATE BEARING SEDIMENTS

Approved by

J. Carlos Santamarina, Chairman
School of Civil and Environmental Engineering
Georgia Institute of Technology

J. David Frost
School of Civil and Environmental Engineering
Georgia Institute of Technology

Paul W. Mayne
School of Civil and Environmental Engineering
Georgia Institute of Technology

Glenn J. Rix
School of Civil and Environmental Engineering
Georgia Institute of Technology

Carolyn D. Ruppel
School of Earth and Atmospheric Science
Georgia Institute of Technology

Date Approved: May 24, 2005

ACKNOWLEDGEMENT

I would like to first thank to my advisor Dr. Carlos Santamarina for his guidance, support, generosity. It was a great fortune to meet him and to work with him making my Ph.D. experience at Georgia Tech. I have learned more by his research and life than I could express.

I would like to express my appreciation to my committee members for their insightful and helpful comments and suggestion: Dr. Carolyn Ruppel, Dr. David Frost, Dr. Glenn Rix and Dr. Paul Mayne. A special thanks goes to Dr. Carolyn Ruppel for her endless support, enthusiasm and many valuable opportunities she has given me.

I also want to thank my parent and sister for always believing I could accomplish anything. Most importantly, I would like to thank my dear wife – Deok Hyun for her unconditional love and continuous support for me.

I would like to thank past and current members of the Particulate Media Laboratory for their assistance, encouragement and discussion: Jong-Sub Lee, Angelica Palomino, Franco Francisca, Jose Alvarelllos, Julio Valdes, Guillermo Narsilio, Hyunki Kim, Joo-Yong Lee, Veronica R. Landa, Ahmed M. Bayoumi and Maria Cristina. I would also like to thank the Korean geotechnical society and friends in Korea. Many thanks go to Young-Jong Sim, Jong-Won Choi, Sungsoo Yoon and Duhwan Kim.

I wish to acknowledge the Georgia Institute of Technology, JIP and the American Chemical Society Petroleum Research Fund for providing funding for this research.

TABLE OF CONTENTS

ACKNOWLEDGEMENT.....	iii
LIST OF TABLES.....	viii
LIST OF FIGURES.....	ix
LIST OF MATHGRAMS.....	xiv
SUMMARY.....	xv
CHAPTER I INTRODUCTION.....	1
1.1 BACKGROUND.....	1
1.2 MOTIVATION AND IMPORTANCE.....	2
1.3 SCOPE – ORGANIZATION.....	3
CHAPTER II DECEMENTATION, SOFTENING AND COLLAPSE: CHANGES IN SMALL STRAIN STIFFNESS UNDER K_0 -LOADING.....	5
2.1 INTRODUCTION.....	5
2.2 BRIEF REVIEW OF PRIOR STUDIES.....	6
2.3 EXPERIMENTAL DESIGN.....	10
2.3.1 Sample Preparation.....	10
2.3.2 Test Devices.....	11
2.3.3 Test Procedure.....	13
2.4 EXPERIMENTAL RESULTS.....	14
2.4.1 Velocity-Stress Behavior.....	14
2.4.2 Volume Change – Threshold Vertical Strain.....	20
2.4.3 Optical Observations.....	22
2.5 ADDITIONAL OBSERVATIONS.....	22
2.6 CONCLUSIONS.....	26

CHAPTER III	MECHANICAL PROPERTIES OF TETRAHYDROFURAN HYDRATE BEARING SEDIMENTS.....	28
3.1	INTRODUCTION.....	28
3.2	LITERATURE REVIEW.....	29
3.3	EXPERIMENTAL STUDY.....	31
3.3.1	Tested Materials.....	31
3.3.2	Devices.....	37
3.3.3	Specimen Preparation and Test Procedure.....	38
3.3.4	Precautions Taking During the Experiments.....	41
3.4	EXPERIMENTAL RESULTS.....	44
3.4.1	Stress-Strain Response.....	44
3.4.2	Post-Failure Visual Inspection.....	46
3.5	ANALYSIS.....	46
3.5.1	Stiffness.....	46
3.5.2	Undrained Strength.....	49
3.5.3	Strength as a Function of Hydrate Concentration and Confinement.....	51
3.5.4	Poisson's Ratio.....	54
3.5.5	Micro-Mechanism of Shear Strength and Failure.....	56
3.6	DISCUSSION.....	58
3.7	CONCLUSIONS.....	61
CHAPTER IV	MICRO-SCALE STUDY OF HEAT TRANSFER IN PARTICULATE MATERIALS.....	62
4.1	INTRODUCTION.....	62
4.2	LITERATURE REVIEW.....	64
4.3	HEAT TRANSFER BETWEEN TWO PARTICLES-CONTACT LEVEL..	71
4.3.1	Numerical Simulation.....	71
4.3.2	Experimental Study: Infrared Imaging.....	75
4.3.3	Observations.....	75

4.4	THERMAL CONDUCTION IN A 1-D GRANULAR CHAIN-CHAIN LEVEL.....	76
4.4.1	Experimental Design.....	76
4.4.2	Equivalent 1-D Continuum Numerical Analysis.....	85
4.5	THERMAL CONDUCTION IN SOILS – MACRO-SCALE.....	91
4.5.1	Test Method.....	93
4.5.2	Experimental Study.....	95
4.5.3	Test Results.....	95
4.6	DISCUSSION.....	99
4.7	CONCLUSIONS.....	101
CHAPTER V MECHANISTIC STUDIES LENSING RELATED TO GAS HYDRATE FORMATION.....		103
5.1	INTRODUCTION.....	103
5.2	LITERATURE REVIEW.....	105
5.2.1	Ice Lens Formation in Soils.....	105
5.2.2	Thermodynamics.....	106
5.2.3	Governing Factors.....	108
5.2.4	Ice Lensing Models.....	112
5.3	EXPERIMENTAL STUDY AND ANALYSIS.....	113
5.3.1	Ice Lens Formation.....	113
5.3.2	Lens Growth - Micro-Scale Study.....	114
5.3.3	Lens Formation Controlled by Stress Boundary Condition.....	117
5.3.4	Finite Element Model.....	123
5.3.5	Unfrozen Water Content.....	125
5.3.6	Particle Size and Freezing Rate.....	126
5.4	DISCUSSION – GAS HYDRATE FORMATION.....	128
5.5	CONCLUSIONS.....	130
CHAPTER VI INSTRUMENTED HIGH-PRESSURE CHAMBER.....		134

6.1	INTRODUCTION.....	134
6.2	DESIGN AND CONSTRUCTION.....	137
6.2.1	Design Evolution.....	138
6.2.2	Pressure Chamber.....	138
6.2.3	Instrumented Rods.....	142
6.2.4	Rod Guide and Position Control System.....	147
6.3	MEASUREMENT PROCEDURE – DATA REDUCTION.....	150
6.4	FIELD TEST.....	156
6.5	CONCLUSIONS.....	157
CHAPTER VII CONCLUSIONS AND RECOMMENDATIONS.....		161
7.1	CONCLUSIONS.....	161
7.2	RECOMMENDATIONS AND FUTURE RESEARCH.....	164
REFERENCES.....		165
VITA.....		179

LIST OF TABLES

Table	Page
2.1 Specimen and test characteristics.....	11
3.1 The physical properties of ice, methane and THF hydrates.....	30
3.2 Features of frozen soil and hydrate bearing sediments.....	32
3.3 Test variables.....	34
3.4 Properties of tetrahydrofuran (THF).....	36
3.5 Specimen preparation procedures.....	40
3.6 Computed fitting parameters.....	51
4.1 Thermal properties of materials.....	66
4.2 Governing factors controlling thermal conductivity of soils.....	67
4.3 Empirical method to measure the thermal conductivity in soils.....	69
4.4 Theoretical thermal conductivity mixture models.....	70
4.5 Thermal diffusivity D and loss coefficient λ	91
4.6 Thermal diffusivity D and loss coefficient λ for individual particles with log scaled temperature calculation.....	92
4.7 Tested soil properties.....	96
5.1 Test conditions and observed features.....	115
5.2 Ice lenses formation under different stress boundary conditions.....	122
6.1 Features of ODP (Ocean Drilling Program) coring techniques.....	135
6.2 HYACE and HYACINTH systems.....	136
6.3 Design evolution of instrumentation.....	139
6.4 Design considerations and solutions.....	140
6.5 Drill bit - Tested and selected bits.....	145
6.6 Experimental difficulties and possible improvements for the IHPC system.....	158

LIST OF FIGURES

Figure	Page
1.1 Global occurrence of gas hydrates (Kvenvolden and Lorenson, 2001).....	2
2.1 Oedometer cell. (a) The top cap and the bottom plate of the oedometer cell where bender elements are housed. (b) Peripheral electronics.....	12
2.2 Evolution of shear wave time series during loading and unloading a dense uncemented soil specimen (initial void ratio $e_o = 0.78$).....	15
2.3 Evolution of shear wave time series during loading and unloading a dense, cemented soil specimen (initial void ratio $e_o = 0.71$, cement content: 4%, vertical seating pressure during hardening $\sigma'_{\text{seat}} = 18.7$ kPa).....	16
2.4 Evolution of shear wave time series during loading and unloading a loose, cemented soil specimen (initial void ratio $e_o = 1.14$, cement content: 2%, vertical seating pressure during hardening $\sigma'_{\text{seat}} = 18.7$ kPa).....	17
2.5 Shear wave velocity versus vertical effective stress - Summary. Note: The log-log plot highlights global trends but diminishes the effect of collapse on stiffness. (L: Solid line-loading. U: Dotted line-unloading. Initial vertical seating pressures during hardening $\sigma'_{\text{seat}} = 18.7$ kPa and $\sigma'_{\text{seat}} = 122.8$ kPa).....	18
2.6 Changes in void ratio with vertical effective stress in oedometric cell (L: Solid line-loading. U: Dotted line-unloading. C: Collapse. Vertical seating pressures during hardening $\sigma'_{\text{seat}} = 18.7$ kPa, $\sigma'_{\text{seat}} = 122.8$ kPa).....	21
2.7 Decementation softening and collapse: void ratio vs. shear wave velocity (L: Solid line-loading. U: Dotted line-unloading. H: Hardening. C: Collapse. Vertical seating pressures during hardening $\sigma'_{\text{seat}} = 18.7$ kPa and $\sigma'_{\text{seat}} = 122.8$ kPa).....	23
2.8 Schematic trends - Summary. Before cement hydration: fresh mixtures exhibit shear wave velocity higher than saturated uncemented soils due to capillarity. After cementation: the low-cementation loose soil collapses at lower stress than the high-cementation loose soil (solid lines correspond to loose specimens; "C" denotes collapse); the dense cemented soil specimens do not collapse (dotted lines correspond to dense specimens). At very high confinement: the shear wave velocity of cemented soils appears to asymptotically approach the shear wave velocity of uncemented soils (dashed lines).....	25
3.1 Characteristics of tested soils and SEM pictures (SEM pictures: courtesy of Angelica Palomino, 2003. Data: Santamarina and Cho 2001, Klein 1999, Parks 1990 and Guimaraes 2001) *: Specific surface is measured with the methylene blue method (wet method).....	35

3.2	Triaxial cell and peripheral electronics. Two thermocouples are embedded on the top and bottom plates. A strain gauged arch is mounted at the middle height of the specimen.....	37
3.3	Hydrate fraction by volume filling the pore space.....	39
3.4	Evaporation: evolution of n -value in THF· n H ₂ O solution with time for fluids with and without stirring (Assumption: all mass loss is due to THF evaporation).....	42
3.5	Effective number of available water molecules, starting from the stoichiometric mix ($n=17$) as a function of the water content and the specific surface of the soil. The assumed thickness of the double layer is $d = 5 \cdot 10^{-10}$ m.....	43
3.6	Phase transformation cycles. The freezing time decreases with increasing number of cycles.....	43
3.7	Stress versus axial strain. Thin lines are the post-peak response where localization is expected. Letters a, b and c denote 0.03, 0.5 and 1 MPa confining pressure. Note that kaolinite is plotted in a larger stress scale.....	45
3.8	Sand specimens after failure.....	47
3.9	Longitudinal stiffness at $(\sigma_1 - \sigma_3)/2$ versus effective confining pressure. The parameter β is computed for 0% hydrate bearing sediments. The exponent of the power relation $E = \alpha \cdot \sigma'^{\beta}$	48
3.10	Longitudinal stiffness at $(\sigma_1 - \sigma_3)/2$ versus undrained shear strength for all tested soils, with and without hydrates, and at all confining pressures.....	49
3.11	Undrained peak strength versus effective confining pressure and hydrate-filled porosity.....	50
3.12	Model coefficients estimated by Equation 3.4 (o indicates the precipitated silt specimens).....	52
3.13	Measured (symbol: o) and predicted (symbol: x) undrained shear strength.....	53
3.14	Lateral strain versus axial strain for tested specimens with different hydrate concentration, and subjected to various confining stresses. The thick solid line is 0% hydrate-bearing sediment, thin solid line denotes 50% hydrate-bearing sediments, and dotted line presents 100% hydrate-bearing sediments.....	55
3.15	Tangential stiffness normalized by the confining pressure σ'_o versus axial strain. The number 0, 50 and 100 represents the hydrate fraction in pore space. The arrow in each plot indicates the noticeable stiffness loss.....	57
3.16	Hydrate concentration versus normalized shear wave velocity (trend from Yun et al., 2005) and shear strength.....	59
3.17	Possible particle-level mechanisms involved in the shear strength of hydrate bearing sediments.....	60
4.1	FDM modeling condition. The shadowed and white region stand for the solid particle and pore space.....	72

4.2	Numerical study: heat evolution for different particle contact conditions. Case I: air in void space. Case II: air in void space and water meniscus at contact. Case III: water in void space.....	73
4.3	Temperature evolution with particle geometry. The continuous lines correspond to the granular case simulated in Figure 4.2. The dotted line is for an infinite solid medium (1: $t=6\text{sec}$, 2: $t=150\text{sec}$, 3: $t=3000\text{sec}$).....	74
4.4	Internal temperature evolution at the center of the three particles measured with thermocouples. The series of particles are heated at the bottom.....	76
4.5	Heat transfer in a granular chain - Test design. The core temperature in each particle is monitored while the heat is applied from the bottom.....	77
4.6	Particle column - Test conditions. The test name indicates: O-reference, R: retardation, L: load, M: meniscus, I: insulation.....	79
4.7	Temperature evolution for particle #2~9 with time.....	80
4.8	Time history comparison – Heat transfer under different contact and boundary conditions.....	83
4.9	The effects of heat loss and contact resistance on measured time histories.....	84
4.10	Measured and fitted thermal histories - Shown for selected particles (dotted line: experiment, solid line: numerical analysis).....	88
4.11	Contours of L_2 error surfaces for the joint inversion of D and λ . The value of λ increases linearly with D . Note that this trade off hinders inversion uniqueness.....	90
4.12	Profile of evaluated thermal diffusivity and loss coefficient. ‘ A ’ stands for the overall estimated value obtained by simultaneously taking into consideration all time series. Numbers 3 and 5 denote values computed for individual time series, in this case for the 3 rd and 5 th particles. In all cases, the logarithmic error definition and the L_2 norm are used to guide the inversion.....	92
4.13	Thermal conductivity measurement circuit - Thermal needle probe method.....	93
4.14	Temperature-time series. Identification of the steady state region.....	94
4.15	Microscopic images of tested sands.....	97
4.16	Changes in thermal conductivity with porosity. Maximum and minimum porosities are calculated from maximum and minimum void ratios $n=e/(1+e)$. Refer to Table 4.7.....	98
4.17	Effective thermal conductivity versus porosity. Experimental results shown as black dots (total of 39 measurements-6 sands). Model predictions are shown with lines. Series: Reuss (1929), Parallel: Voigt (1910), HS: Hashin-Shtrikman (U: upper bound and L: lower bound), GM: Geometric mean (Kumlutas, 2003), SC: Self consistent (Tarnawski and Leong, 2000), VF: Volume fraction (Roth et al., 1990)	100
4.19	Summary: possible heat transfer paths through particulate materials.....	102

5.1	Evidence of hydrate segregation in natural systems. (a) Hydrate lenses parallel to the strata. Hydrate vein normal to bedding from ODP Leg 204, (b) lens shape gas hydrate in the marine sediments at Gulf of Mexico (2002), (c) Hydrate vein (GeoTek, Inc.)	104
5.2	Particle size effect. The bold line constrains the range where ice lens is experimentally observed.....	109
5.3	Overburden pressure effect. The bold line constrains the range where ice lens is experimentally observed.....	110
5.4	Hydraulic conductivity effect. The bold line constrains the range where ice lens is experimentally observed.....	111
5.5	Experimental device designed to study ice lens formation – 1D heat front.....	115
5.6	Ice lens formation within different soils at various water content and salt concentration. Heat is removed from the top; the other specimen walls are thermally insulated.....	116
5.7	Ice lens growth with time. A thin opening at the lens tip is observed prior to lens growth.....	118
5.8	Displacement vectors in the sediment near the ice lens tip denoted. The red dots show the final point of each displacement. The bottom figure is an enlarged display of the region ahead of lens tip (unit: mm).....	119
5.9	Experimental configuration to study the effect of stress on lens formation.....	120
5.10	Lens formed in tension.....	121
5.11	Strain evolution within the cylindrical specimen subjected to loading on the groove faces (plain strain – elastic FEM).....	124
5.12	Unfrozen water content below 0°C temperature. Source: #7-Penner (1963), #9-Anderson and Morgenstern (1973), #20-Akimov et al.(1983), #28-Smith (1985), #42-Konrad and Duquennoi (1993).....	125
5.13	Critical velocity (V_c) versus particle radius (R). As the particle radius increases, a low critical velocity is needed to form ice lens.....	127
5.14	Calculated ice pressure in a frozen fringe in permafrost region. Dotted lines indicate the critical pressures (overburden pressure P_o + separation pressure P_{sep}). Ice lenses initiate when $P_i \geq P_o + P_{sep}$. The maximum depth where lenses can form is 492m.....	130
5.15	Gas hydrate stability zone and the possible lensing region in permafrost.....	131
5.16	Calculated ice pressure in a frozen fringe in seafloor condition. Dotted lines indicate the critical pressure (overburden pressure P_o + separation pressure P_{sep}). Ice lenses initiate when $P_i \geq P_o + P_{sep}$. The maximum depth where lenses can form is 804m from the seafloor.....	132
5.17	Gas hydrate stability zone and the possible lensing region in seafloor.....	133
6.1	Pressure core transfer mechanism. The manipulator slides the pressure core	

	from the storage chamber into the instrumented high-pressure chamber.....	140
6.2	The high pressure chamber (without instrumentation ports). End flanges are designed to attach to storage and extension chambers with quick clamps (all dimensions in mm)	143
6.3	Auxiliary tube to align smaller diameter core (HRC). 4 bolts tighten the tube...	144
6.4	Instrumented rods - Details (all dimensions in mm).....	146
6.5	Rod guide and position control system.....	148
6.6	Rod guide and position control system assembled in pressure chamber.....	151
6.7	Prototype of the IHPC. Instrumentations and parts are tested before building the entire IHPC system.....	152
6.8	Elastic wave signals measured in IHPC ($\sigma_c = 17$ MPa).....	152
6.9	Needle probe – Spectral response.....	153
6.10	Needle probe calibration.....	154
6.11	Load cell calibration	154
6.12	Peripheral electronics (Note that s is source, r is receiver).....	155
6.13	Test sites during the research cruise (map from Milkov and Sassen, 2001).....	157
6.14	Elastic wave velocities for recovered pressure core.....	159
6.15	Penetration force versus time at different penetration depths.....	160

LIST OF MATHGRAMS

Mathgram	Page
6.1 Pressure chamber mechanical design.....	141
6.2 Buckling load for instrumented rods	144
6.3 Screw equation: required torque.....	149

SUMMARY

Gas hydrate is a naturally occurring crystalline compound formed by water molecules and encapsulated gas molecules. The interest in gas hydrate reflects scientific, energy and safety concerns - climate change, future energy resources and seafloor stability. Gas hydrates form in the pore space of sediments, under high pressure and low temperature conditions. This research focuses on the fundamental understanding of hydrate bearing sediments, with emphasis on mechanical behavior, thermal properties and lens formation.

Load-induced cementation and decementation effects are explored with lightly cemented loose and dense soil specimens subjected to k_0 -loading; the small-strain stiffness evolution inferred from shear wave velocity measurement denounces stiffness loss prior to structural collapse upon loading. Systematic triaxial tests address the intermediate and large strain response of hydrate bearing sediments for different mean particle size, applied pressure and hydrate concentration in the pore space; hydrate concentration determines elastic stiffness and undrained strength when $S_{hyd} > 45\%$. A unique sequence of particle-level and macro-scale experiments provide new insight into the role of interparticle contact area, coordination number and pore fluid on heat transfer in particulate materials. Micro-mechanisms and necessary boundary conditions are experimentally analyzed to gain an enhanced understanding of hydrate lens formation in sediments; high specific surface soils and tensile stress fields facilitate lens formation. Finally, a new instrumented high-pressure chamber is designed, constructed and field tested. It permits measuring the mechanical and electrical properties of methane hydrate bearing sediments recovered from pressure cores without losing in situ pressure ($\sim 20\text{MPa}$).

CHAPTER I

INTRODUCTION

1.1 BACKGROUND

Gas hydrate is a naturally occurring crystalline compound formed by water molecules and encapsulated gas molecules. The general appearance resembles ice. Methane hydrates form at high pressure and low temperature, and are found in seafloor sediments and in permafrost regions. The known global occurrence of methane hydrates is shown in Figure 1.1.

Gas hydrate was first discovered in 1911 by Humphrey Davy and Michael Faraday; while experimenting with chlorine and water mixtures, they observed the formation of crystalline solid above the freezing temperature of water. Later research was dedicated to identifying the various kinds of gas molecules that can form hydrate under different conditions. E. G. Hammerschmidt found hydrate blocking oil and gas pipelines in the 1930's. Research followed on chemical additives that could inhibit hydrate formation. Natural gas hydrate was first recovered from sediments in the Black sea in 1974. Since then, hydrate fields have been identified worldwide through geophysical and deep sea drilling methods. Active Research & Development programs are currently undertaken in Canada, India, Japan, South Korea and U.S.A. among other countries.

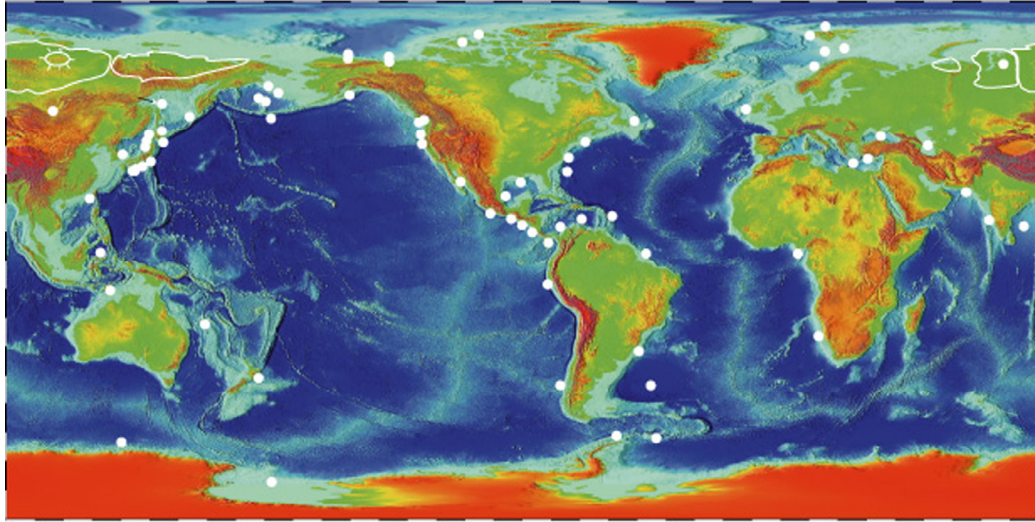


Figure 1.1 Global occurrence of gas hydrates (Kvenvolden and Lorenson, 2001)

1.2 MOTIVATION AND IMPORTANCE

The interest in gas hydrates reflects scientific, energy and safety concerns. Details follow.

Climate changes. Methane is a very effective greenhouse gas. Its potential impact on warming is much greater than that of carbon dioxide (Kvenvolden, 1999). Therefore, should methane be released into the atmosphere by gas hydrate dissociation, significant long term global warming effects would follow (Kvenvolden, 1999; Hornbach et al., 2004; Maslin et al., 2004).

Energy resources. Gas hydrate formation within sediments traps gas and reduces reservoir permeability. The amount of entrapped gas within the hydrate cage has been estimated to be more than twice the known carbon resources (20,000 trillion m³ in Collett, 2002; see also Dickens, 2001 and 2003). Hence, methane hydrate would be a magnificent

resource if economically viable recovery techniques are developed (Max and Lowrie, 1996; Collett and Kuuskraa, 1998; Parker, 2001).

Seafloor stability and safety. Gas hydrate formation within sediments stiffens seafloor sediments, and further sedimentation does not consolidate the hydrate bearing sediments. Therefore, hydrate decomposition would cause shear strength loss and massive failure of the seafloor in continental margins (Kayen and Lee, 1991; Cochonat et al., 2002; Sloan, 2003; Sultan et al., 2004-a, b; Maslin et al., 2004).

Gas hydrates can fill the pore space in sediments, form nodules, veins or lenses or develop into massive hydrate zones. Thus, the characterization of natural gas hydrate should take into consideration a fundamental understanding of hydrate bearing sediments rather than pure hydrate alone. Relatively low percentages of gas hydrates in sediments are typically reported (5-10% Guerin et al., 1999; 13-18% Ecker et al., 2000; 5-7% Holbrook, 2001).

Hydrate bearing sediments retrieved by coring experience dissociation due to the limited hydrate temperature and pressure stability conditions. Geophysical methods and in situ testing face equally challenging difficulties. In all cases, an in-depth understanding of the physical properties of hydrate bearing sediments is required to improve characterization and to address both scientific and engineering needs.

1.3 SCOPE - ORGANIZATION

The goal of this research is to attain a fundamental understanding of the behavior of hydrate bearing sediments with emphasis on mechanical and thermal properties and lens

formation. Measurements are analyzed at the particle-level to identify underlying microscale process. Finally, an instrumented high-pressure chamber is designed to measure the mechanical and electrical properties of methane bearing sediments from pressure cores. This information is organized into five chapters as follows.

Chapter 2 explores the evolution of small-strain stiffness in lightly cemented loose and dense soil specimens subjected to K_0 -loading. Emphasis is placed on stiffness loss and the associated structural collapse upon loading.

Chapter 3 documents a study of intermediate and large strain response of hydrate bearing sediments taking into consideration the mean particle size, the applied pressure and hydrate concentration in the pore space.

Chapter 4 describes a fundamental study of thermal conductivity in particulate materials involving both unique micro and macroscale experiments. Numerical modeling complements the experimental study.

Chapter 5 centers on the formation of hydrate lenses. Microscale mechanisms and necessary boundary conditions are experimentally analyzed, varying the thermal gradient, water content, soil type and applied pressure.

Chapter 6 documents the design, construction and calibration of a newly instrumented high-pressure chamber built to measure the mechanical and electrical properties of gas hydrate bearing sediments recovered by pressure coring.

Salient conclusions and recommendations for further studies are summarized in Chapter 7.

CHAPTER II

DECEMENTATION, SOFTENING AND COLLAPSE: CHANGES IN SMALL STRAIN STIFFNESS UNDER K_0 -LOADING

2.1 INTRODUCTION

Cementation increases the contact area between particles and bonds neighboring particles together. Light cementation is often sufficient to significantly increase the small-strain stiffness of soils, their dilative tendency, and the resistance to liquefaction. As the degree of cementation increases, the drained strength is impacted as well. Therefore, cementation can have a profound effect in the analysis of hydrate bearing sediments. These observations highlight the need for proper site characterization, improved laboratory test procedures that take into consideration sampling effects, and adequate material models.

Particle debonding and skeletal softening are readily observed under triaxial loading conditions (e.g., Airey and Fahey, 1991). Debonding and softening can also take place during unloading, even under isotropic conditions: soils cemented under confinement expand during unloading and the cement at interparticle contacts fails in tension (numerical observations in Zang and Wong, 1995; experimental observations in Fernandez and Santamarina, 2001); this is an inherent mechanism in sampling (data in Tatsuoka and Shibuya, 1991). In the case of hydrate bearing sediments, the depressurization of the granular skeleton can unload hydrates at contacts and produce their

de-stabilization (loss of cementation) even if global pore-fluid pressure conditions would indicate stable conditions.

Available cemented soil response data under K_0 -loading (e.g., Shibuya et al., 2001, and Leroueil and Hight, 2003) do not permit analyzing the development of debonding, softening and collapse. The purpose of this study is to explore the evolution of small-strain stiffness in lightly cemented loose and dense soil specimens subjected to K_0 -loading. Special emphasis is placed on identifying the association between stiffness loss and structural collapse upon loading. This study centers on cemented soils (rather than hydrate bearing sediments). It starts with a brief review of prior studies on cemented soils. Then the experimental methodology designed to study K_0 -loading effects is presented followed by results and discussion.

2.2 BRIEF REVIEW OF PRIOR STUDIES

Previous studies show that the effect of cementation on soil behavior depends on the amount and type of cementing agent, the grain size distribution of the soil (the higher the specific surface, the thinner the layer of cement around grains), density (interparticle coordination increases with density), and the degree of confinement at the time of cementation i.e., the stress-cementation history (Clough et al., 1981; Winkler, 1983; Acar and El-Tahir, 1986; Feda, 1995; Baig et al., 1997; Jarrad et al., 2000).

Cementing agents can deposit evenly around particles. However, cementation has maximum influence on the granular skeleton when cementing processes develop at contacts. This is the case when drying triggers cementation (a retracting capillary

meniscus causes fines migration and aggregation and salt precipitation at the contact), or when it is associated with phenomena such as contact yield, sintering and solution-precipitation (Bernabe et al., 1992). When a cementing agent precipitates around interparticle contacts, the load-induced stress distribution at the composite contact depends on the stiffness of the minerals that make the grains (E_{min}) and the cementing material (E_{cem}). Disregarding geometric effects: when $E_{min}/E_{cem} = 1$, the stress changes at the contact follows Hertzian behavior; when $E_{min}/E_{cem} \gg 1$, the mineral contact picks up the new load; and when $E_{min}/E_{cem} \ll 1$, stress concentration develops within the cementing material (Dvorkin and Yin, 1995; Zang and Wong, 1995; Sienkiewicz et al., 1996). In all cases, the cement is load-bearing; hence, it reduces the stress concentration within particles, and increases the crushing strength of the soil (Yin and Dvorkin, 1994; Dvorkin and Yin, 1995).

Two stress regimes can be identified. Under low-confinement, the behavior of the cemented soil is cementation-controlled, and the soil exhibits the following characteristics:

- The drained load deformation behavior is brittle (Lade and Overton, 1989; Airey and Fahey, 1991).
- Cementation controls the drained peak strength, and the shear strength intercept increases with cement content (Dupas and Pecker, 1979; Clough et al., 1981; Acar and El-Tahir, 1986; Dass et al., 1994).
- Post-peak, strain-softening is often accompanied by strain localization (Schanz, 1998).

- Interparticle bonds begin breaking prior to the peak strength of the soil (Feda, 1995). Debonding forms an interlocked blocky structure and the soil is more prone to dilate (Wissa and Ladd, 1965; Saxena and Lastrico, 1978; Saxena et al., 1988; Lade and Overton, 1989).
- Stiffness is cementation-controlled and quasi stress-independent, as in a linear solid (Baig et al., 1997).

Under high-confinement, the soil response is stress-controlled:

- The small-strain stiffness increases as confinement increases (even in the absence of debonding), approaching the power relation that characterizes freshly remolded granular materials (e.g., Hardin and Richart, 1963),

$$G_{\max} = A \left(\frac{\sigma'_m}{1\text{kPa}} \right)^\zeta \quad (2.1)$$

- where σ'_m is the mean effective stress on the shear plane, “ A ” is the stiffness at $\sigma'_m = 1\text{kPa}$, and “ ζ ” is the exponent (both “ A ” and “ ζ ” are experimentally determined).
- The large-strain load-deformation behavior changes towards a ductile, strain hardening response.
- The effective peak angle of shear strength ϕ'_{peak} is not significantly changed by the degree of initial cementation (Wissa and Ladd 1965; Acar and El-Tahir, 1986; Saxena et al., 1988; Reddy and Saxena, 1993).

In both confining stress regimes, the shear resistance gradually changes from cohesive to frictional as the imposed strain progresses and debonding takes place. Acoustic emission

counts associated with particle debonding decisively increase beyond 75-85% of the peak load (Landis and Shah, 1995). Therefore, the large-strain strength is characterized by $c = 0$ and residual friction angle ϕ_{res} , and it is independent of the degree of initial cementation in both low and high-confinement regimes (Clough et al., 1981). The transition stress between these two regimes increases as the cement content increases (Saxena et al., 1988; Dass et al., 1994; Baig et al., 1997).

The small strain stiffness of particulate materials is determined by the deformability of interparticle contacts due to stress concentration. From Hertzian contact theory, the small-strain stiffness of the granular skeleton (E_{skel}) is (e.g., Richart et al., 1970)

$$E_{skel} = \frac{r_c}{R} \cdot \frac{G_g}{(1-\nu_g)} \quad (2.2)$$

where r_c is the radius of the contact area (a measure of contact flatness), R is the particle radius, and G_g and ν_g are the shear modulus and Poisson's ratio of the mineral that makes the particles. Equation 2.2 highlights the importance of contact flatness (captured in r_c), regardless of the mechanism that causes it. In fact, applied confinement, cementation or even the viscous creep of the grain renders higher skeletal stiffness. Furthermore, Equation 2.2 explains the high sensitivity of small-strain soil stiffness E_{skel} to cementation, and the particularly beneficial effect of cement localization at interparticle contacts thus effectively increasing r_c (See Fernandez and Santamarina, 2001 for a detailed application of Equation 2.2 to cemented soils taking into consideration the cementation-stress history). In this study, the small-strain shear stiffness G_{max} is estimated from shear wave velocity V_s measurements,

$$G_{\max} = \rho \cdot V_s^2 \quad (2.3)$$

where ρ is the mass density of the medium.

2.3 EXPERIMENTAL DESIGN

Artificially cemented sands are used for this study, and subjected to K_0 -loading in a zero-lateral strain oedometric cell. Material, devices and procedures are described next.

2.3.1 *Sample Preparation*

Uniform, fine, angular sand is used to evaluate the behavior of cemented soils (Nevada sand, $e_{\min} = 0.533$, $e_{\max} = 0.888$, mean grain size $D_{50} = 0.14$ -to- 0.17 mm, uniformity coefficient $C_u = 1.67$). The cementing agent is Portland cement Type I (specific gravity $G_s = 3.15$). Eight samples are prepared with different initial void ratio, cement content and initial vertical stress at the time of cementation herein called the vertical seating pressure, σ'_{seat} . The initial void ratio, the vertical seating pressure, the maximum load and the number of loading and unloading steps for each test are summarized in Table 2.1. All tests are successfully duplicated to verify repeatability.

The sand is oven-dried for 24 hrs before testing. Uncemented soil specimens are prepared in the oedometric cell by funneling and tamping methods to attain either loose or dense conditions. When tamping is used, the same weight of soil is added to form each layer.

Artificially cemented soils are prepared by thoroughly mixing the cement and the sand; afterwards, a predetermined amount of water is added to the mixture. The wet

Table 2.1 Specimen and test characteristics.

Test No.	e_o	σ'_{sit} [kPa] during cementation	σ'_{max} [kPa]	Cement [%]	Number of loading / unloading steps
1	0.782	-	1062.5	0	10 / 9
2	1.139	18.7	1071.1	2	8 / 8
3	1.154	18.7	1071.1	4	8 / 8
4	0.953	122.8	1053.8	2	5 / 8
5	0.575	-	1062.5	0	10 / 9
6	0.695	18.7	1071.1	2	8 / 8
7	0.714	18.7	1071.1	4	8 / 8
8	0.636	122.8	1053.8	2	5 / 8

mixture is homogenized for 5 minutes and gradually scooped into the cell or tamped to produce loose and dense specimens. These specimens have higher void ratios than the corresponding uncemented, dry specimens due to interparticle capillary forces that prevent compaction. Capillary stabilization is most pronounced in the loose specimens, which are placed without tamping (Rao et al., 1995).

Once the cell is filled, the upper plate is placed on top of the specimen and the initial void ratio is determined.

2.3.2 Test Devices

The bottom plate and the top cap of the oedometric cell house the bender element pair. Each bender element is electrically shielded and grounded to prevent electrical cross-talk. Cell details are shown in Figure 2.1 (design documented in Fam and Santamarina, 1995 and see Shirley and Hampton, 1978; Dyvik and Madshus, 1985; Thomann and Hryciw,

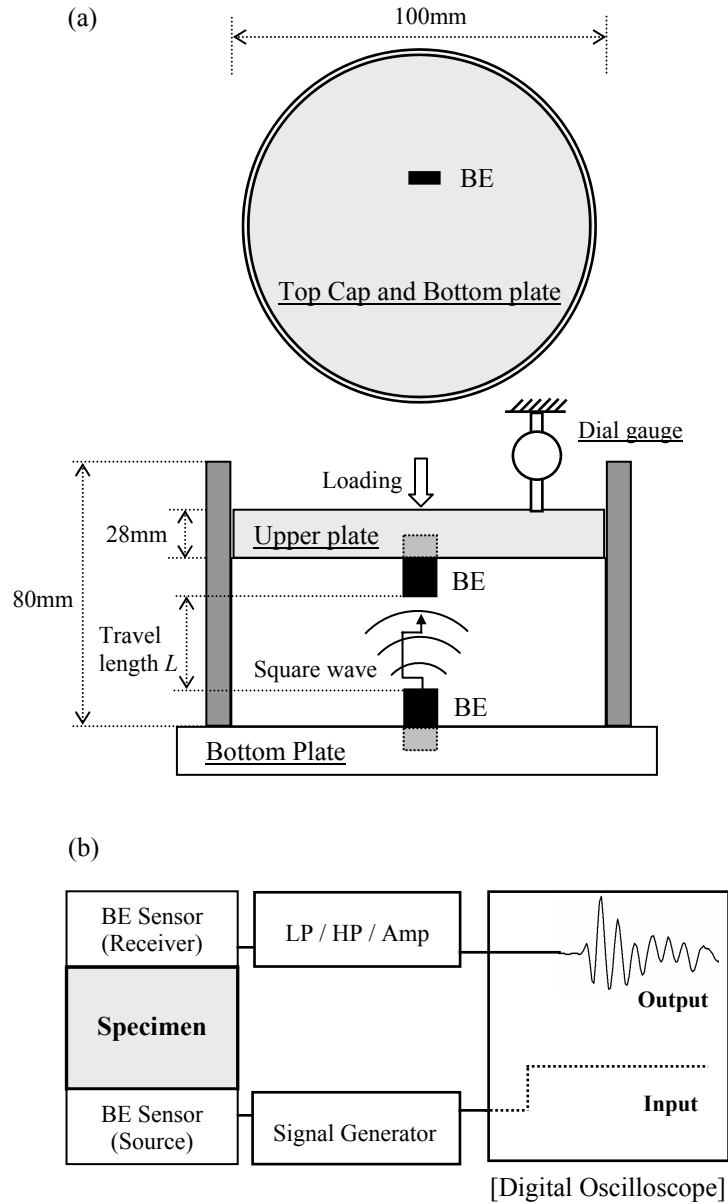


Figure 2.1 Oedometer cell. (a) The top cap and the bottom plate of the oedometer cell where bender elements are housed. (b) Peripheral electronics.

1990 and Kuwano and Jardine, 2002 for a discussion on bender element configuration and performance).

A signal generator (Krohn-Hite 1400A) delivers a 20Hz square wave. The signal captured with the receiver bender element is fed through a filter-amplifier (Krohn-Hite 3364, low-pass filter at $f = 50\text{kHz}$ and high-pass filter at $f = 100\text{Hz}$) into the digital storage oscilloscope (Rapid Systems R1016), where signals are digitized at 200kHz sampling frequency. The stacking of 256 signals permits reducing the non-coherent noise.

2.3.3 Test Procedure

The applied load is incrementally doubled at each loading stage reaching a maximum vertical effective stress of $\sigma'_{max} \cong 1\text{MPa}$. Each loading stage lasts 10-to-15 minutes. Shear wave velocity is measured at the end of this period before increasing the load. The same procedure is implemented during unloading.

The vertical seating pressure σ'_{seat} is reached before cement hardens (within 40 minutes after mixing), and it is maintained constant during the 24hr hardening period; either $\sigma'_{seat} = 18.7$ or $\sigma'_{seat} = 122.8\text{kPa}$ is used (Table 2.1).

The time at "first arrival" t_{first} is picked from the stored time series, taking into consideration near field effects (Sánchez-Salinero et al., 1986). The travel length L is taken as the tip-to-tip distance between bender elements (Figure 2.1). Finally, the shear wave velocity is computed as $V_s = L/t_{first}$.

After testing, specimens are observed with an optical microscope (Qimaging micropublisher 32-0028A-211) to identify the effects of loading or load-induced decementation.

2.4 EXPERIMENTAL RESULTS

Time series are presented for three characteristic cases. Figure 2.2 shows the variation in travel time during loading and unloading in uncemented specimens. In contrast, Figure 2.3 shows almost constant signatures for all load levels in the 4% cement specimen. Finally, Figure 2.4 presents the time series for the 2% loose specimen cemented at low vertical seating pressure. The sudden increase in travel time during loading in this specimen denotes the breakage of cementing bonds; there is also a marked increase in travel time during unloading, resembling the trend for the uncemented specimen in Figure 2.2. To facilitate the interpretation of results, velocity-stress and volume change trends are presented next.

2.4.1 Velocity-Stress Behavior

Uncemented Soils. The shear wave velocity of uncemented soils increases as the vertical effective stress increases. Velocity-stress data during loading and unloading are shown in Figure 2.5-a for loose and dense sands. Combining Equations 2.1 and 2.3, the velocity-stress relation for uncemented soils becomes $V_s = \alpha \cdot \sigma'_m{}^\beta$ where σ'_m is the mean stress in the polarization plane, that is the vertical applied stress times $(1+K_0)/2$. Data points are least squared fitted to determined α and β parameters: for loose sands $\alpha = 48\text{m/s}$ and $\beta = 0.248$; for dense sands, the corresponding parameters are $\alpha = 68\text{m/s}$ and $\beta = 0.192$. These values agree with published results for similar sands (compilation in Santamarina et al. 2001). The unloading trends plot above the loading trends because horizontal stresses are locked in the sand.

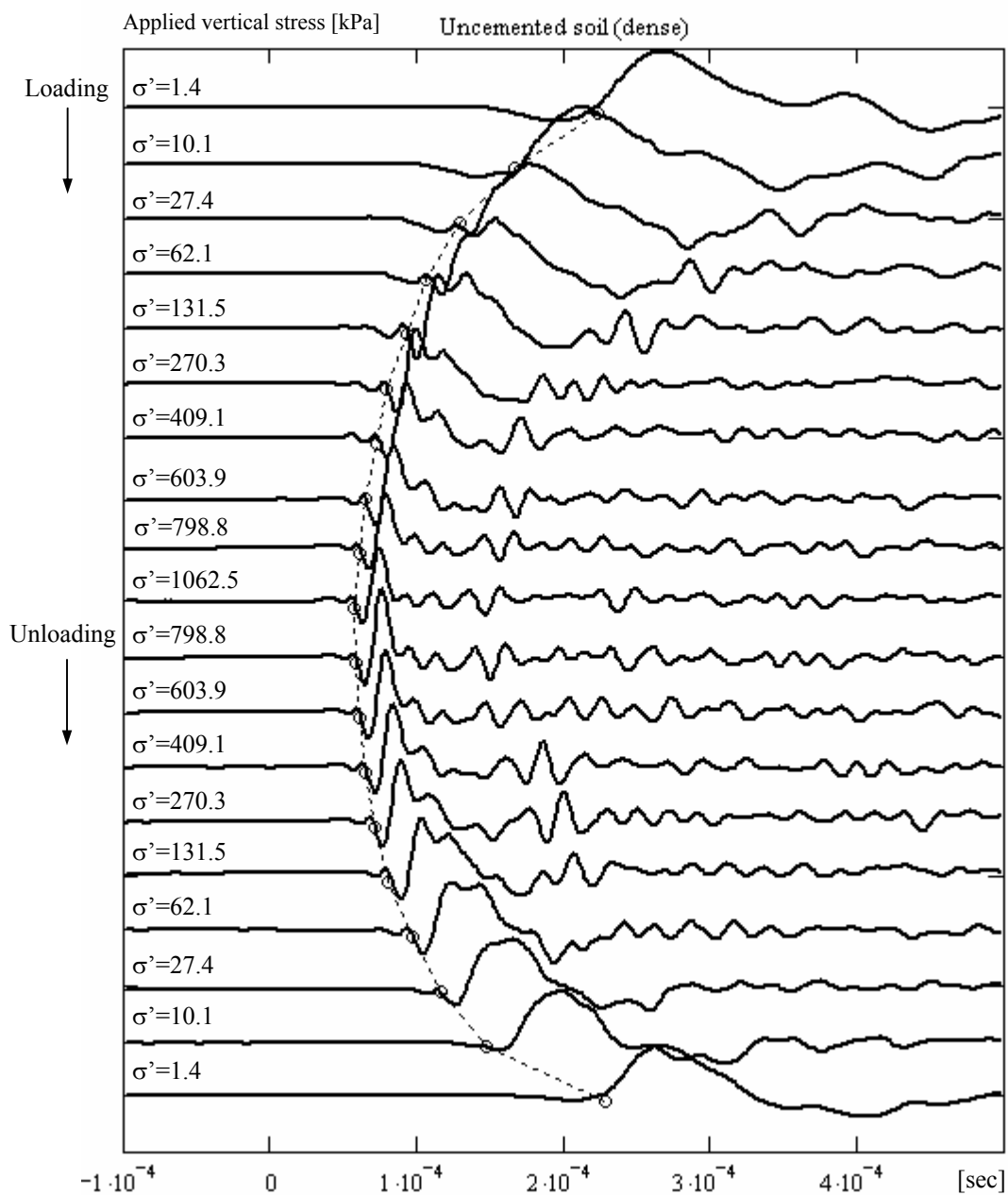


Figure 2.2 Evolution of shear wave time series during loading and unloading a dense uncemented soil specimen (initial void ratio $e_o = 0.78$).

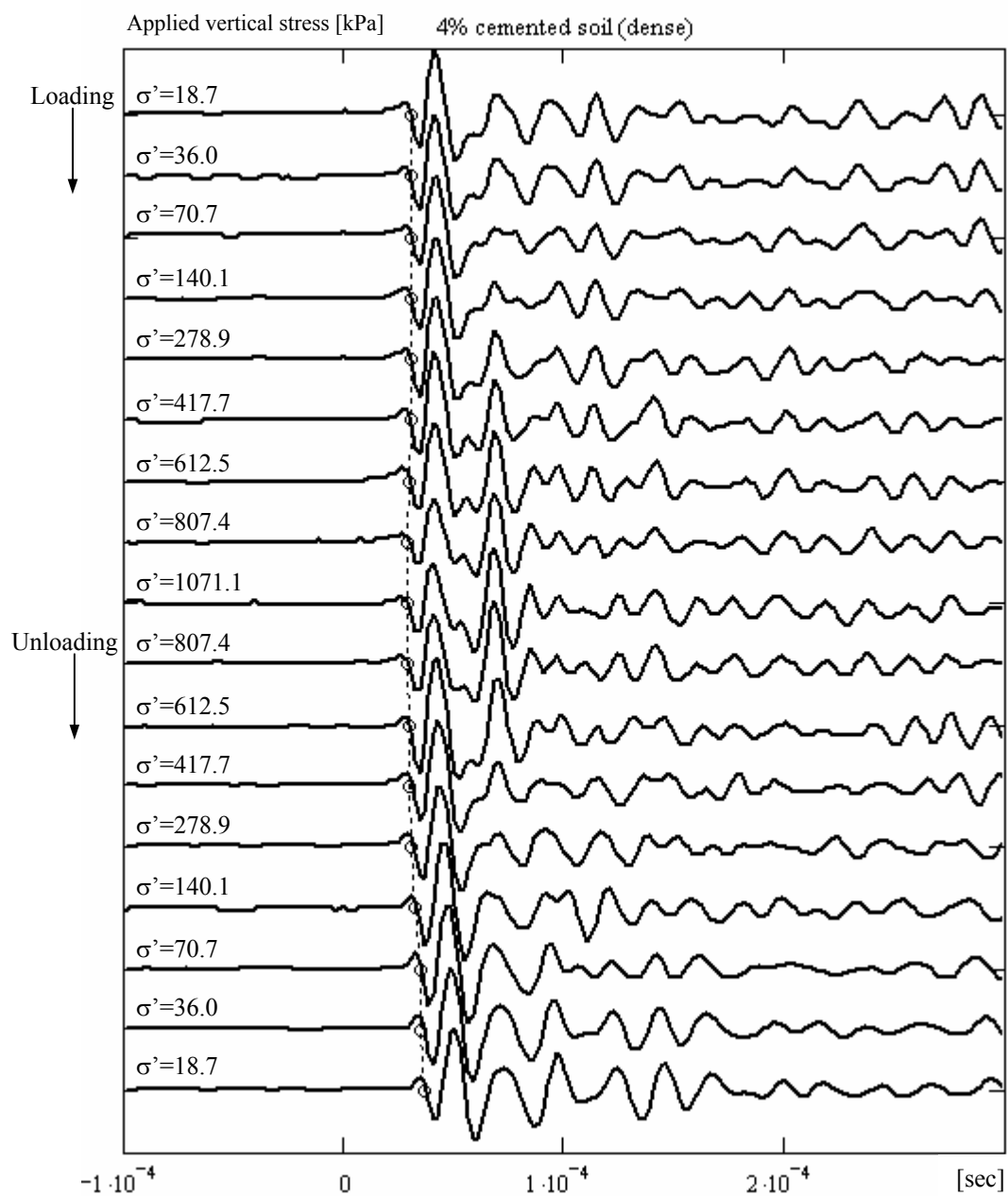


Figure 2.3 Evolution of shear wave time series during loading and unloading a dense, cemented soil specimen (initial void ratio $e_o = 0.71$, cement content: 4%, vertical seating pressure during hardening $\sigma'_{seat} = 18.7$ kPa).

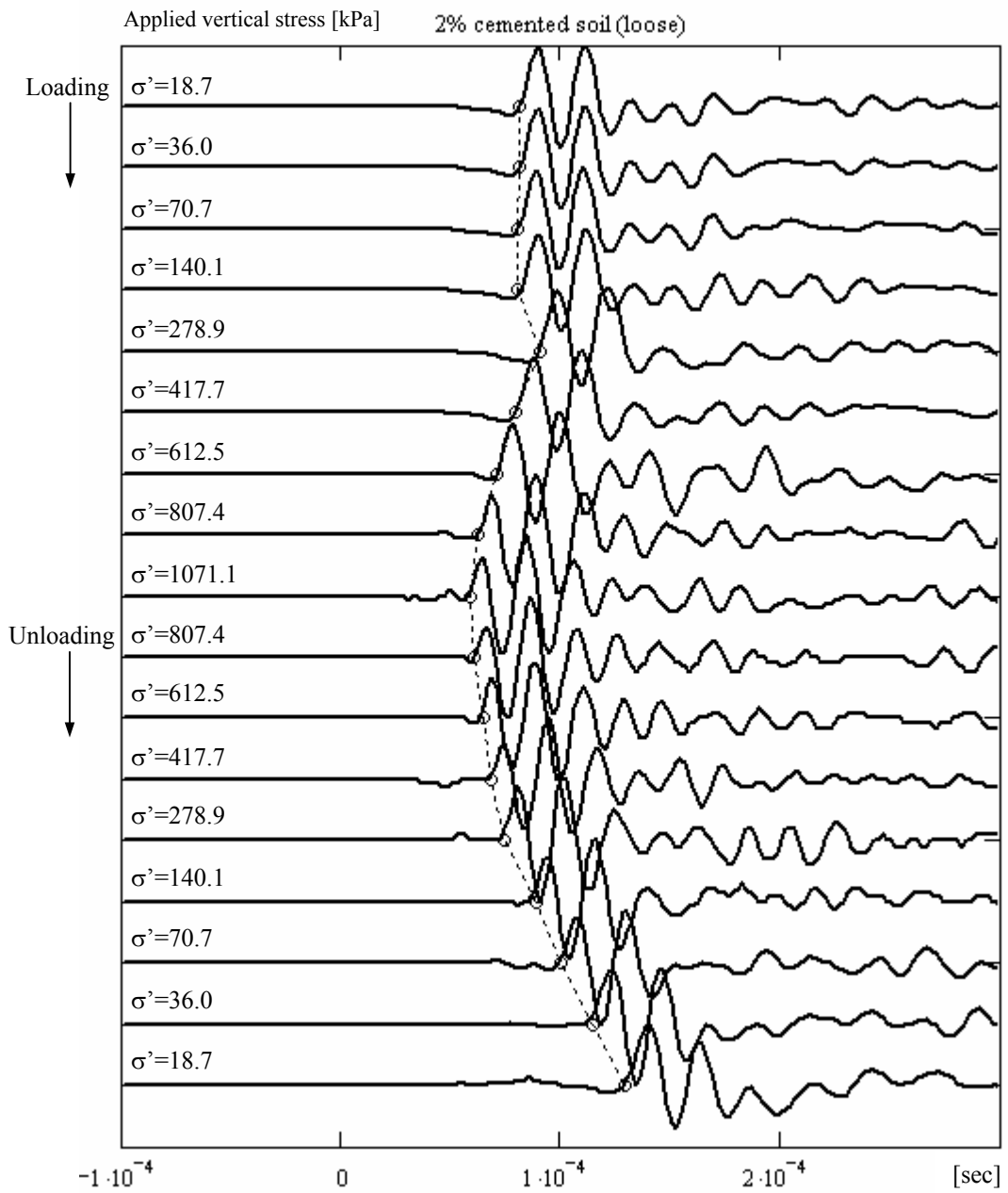


Figure 2.4 Evolution of shear wave time series during loading and unloading a loose, cemented soil specimen (initial void ratio $e_o = 1.14$, cement content: 2%, vertical seating pressure during hardening $\sigma'_{seat} = 18.7$ kPa).

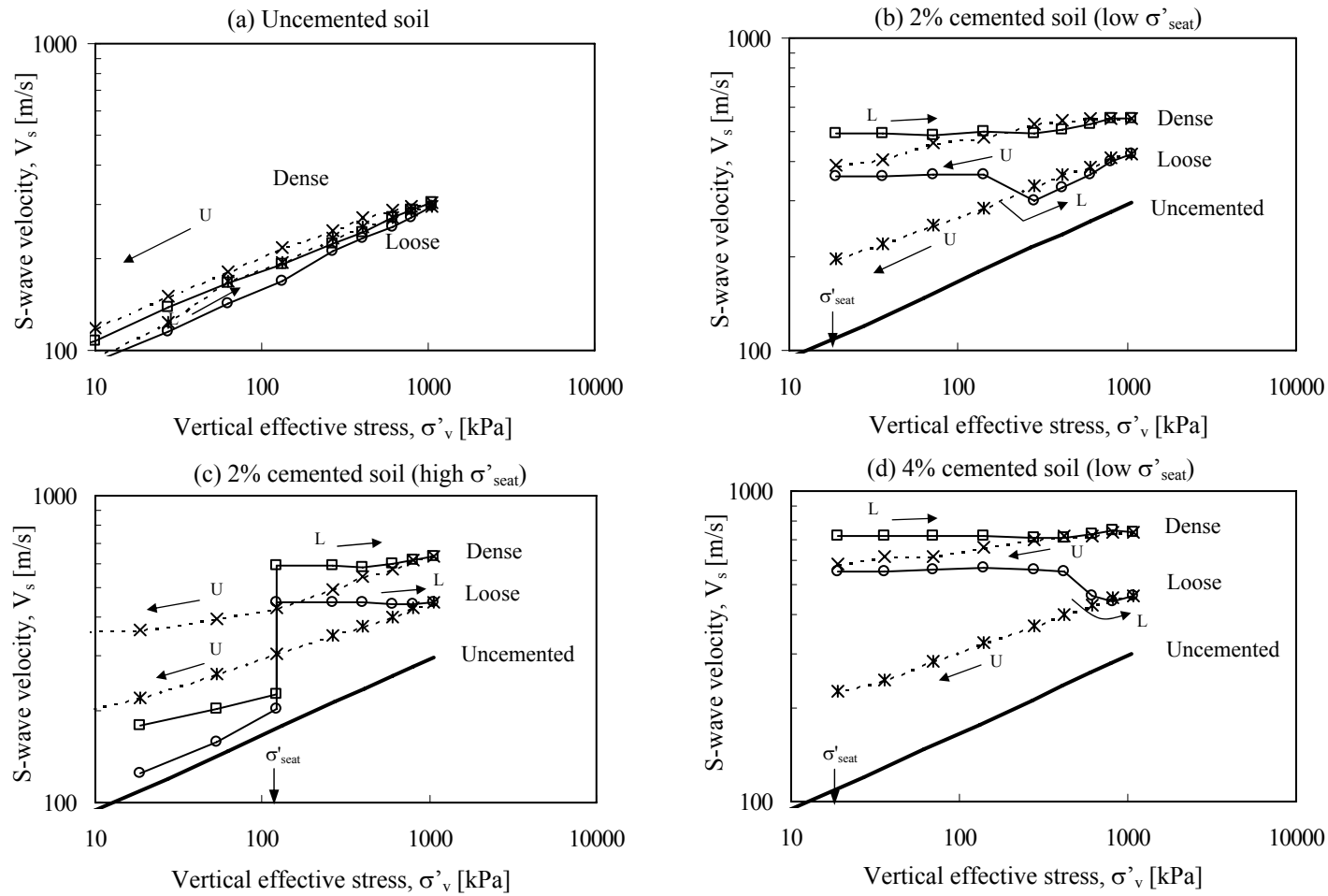


Figure 2.5 Shear wave velocity versus vertical effective stress - Summary. Note: The log-log plot highlights global trends but diminishes the effect of collapse on stiffness. (L: Solid line-loading. U: Dotted line-unloading. Initial vertical seating pressures during hardening $\sigma'_{seat} = 18.7$ kPa and $\sigma'_{seat} = 122.8$ kPa).

Loose Cemented Soils. The 2% cemented loose sand under an initial vertical seating pressure of $\sigma'_{seat} = 18.7\text{kPa}$ shows a distinctly different trend from the uncemented specimen (Figure 2.5-b). At the beginning of loading, until a vertical effective stress $\sigma'_v \cong 140\text{kPa}$, the shear wave velocity increases very slightly, and then additional load causes the collapse of the specimen and a significant decrease in stiffness. During further loading, the velocity never drops below that of the uncemented soil and increases with stress. The loading and unloading trends cross; this is not observed in uncemented soils.

The 2% cemented loose soil specimen formed under high initial vertical pressure, $\sigma'_{seat} = 122.8\text{kPa}$, permits assessing the importance of seating pressure relative to cementation (the seating pressure is six times higher than in the previous specimen). During early confinement prior to cementation, in Figure 2.5-c, the velocity increase with stress as in uncemented soils (albeit with higher values due to increased interparticle capillary forces). Cement hardening after 24 hrs renders a velocity higher than for the 2% cement specimen cured at low confinement (Figure 2.5-c). Loading after hardening does not cause a velocity drop. However, the unloading trend runs below the loading trend in the range $\sigma'_{seat} < \sigma'_v < \sigma'_{max}$ suggesting loss of cementation.

The increase in velocity during hardening for the 4% cemented loose specimen is much higher than for either of the 2% cemented loose specimens (low and high seating pressure - Figure 2.5-d). First, the velocity remains fairly constant during loading, and then falls during collapse-decementation and increases again upon further loading. The 4% cement specimen collapses at around 450-500kPa, which is three times higher than the collapse load for the 2% cement soil. The shear wave velocity during unloading reaches much lower values than those observed during loading at similar confinement.

Dense Cemented Soils. The specimens prepared with 2% and 4% cement and dense packing show similar trends as the loose cemented specimens during cementation. Decementation-collapse is either absent in dense specimens or less defined than in loose specimens. At any given stress, the velocity V_s is higher in dense specimens than in the corresponding loose specimens. During unloading, the shear wave velocity remains lower than during loading indicating that some decementation has taken place.

2.4.2 Volume Change – Threshold Vertical Strain

The $e-\sigma'_v$ response is a fingerprint of the evolution of decementation and collapse (Figure 2.6 - see also Fedá, 1982 and 1994). For reference, data for uncemented loose and dense specimens are presented in Figure 2.6-a. During early stages of loading when the interparticle cementation contributes to load-bearing, the cemented soil behaves elastically, albeit not necessarily linear. Once the vertical applied stress reaches the decementation-collapse load (or yield vertical stress σ'_y) of loose specimens, a significant reduction in void ratio is observed for both the 2% and 4% cemented loose soils (Figure 2.6-b,d). The collapse load increases with the amount of cement from $\sigma'_y = 140\text{kPa}$ for the specimen with 2% cement to $\sigma'_y = 450\text{-}500\text{kPa}$ for the one with 4% cement. The threshold vertical strain on the verge of collapse-decementation ε_{th} is estimated from the initial void ratio (e_o) and the change in void ratio to the moment when collapse starts $\varepsilon_{th} = (e_o - e)/(1 + e_o)$. Almost identical values are obtained from duplicate tests: $\varepsilon_{th} = 0.002$ for the 2% cement specimens, and $\varepsilon_{th} = 0.003\text{-}0.004$ for the 4% cement specimens. Therefore, these data suggest that the collapse stress and the associated threshold vertical

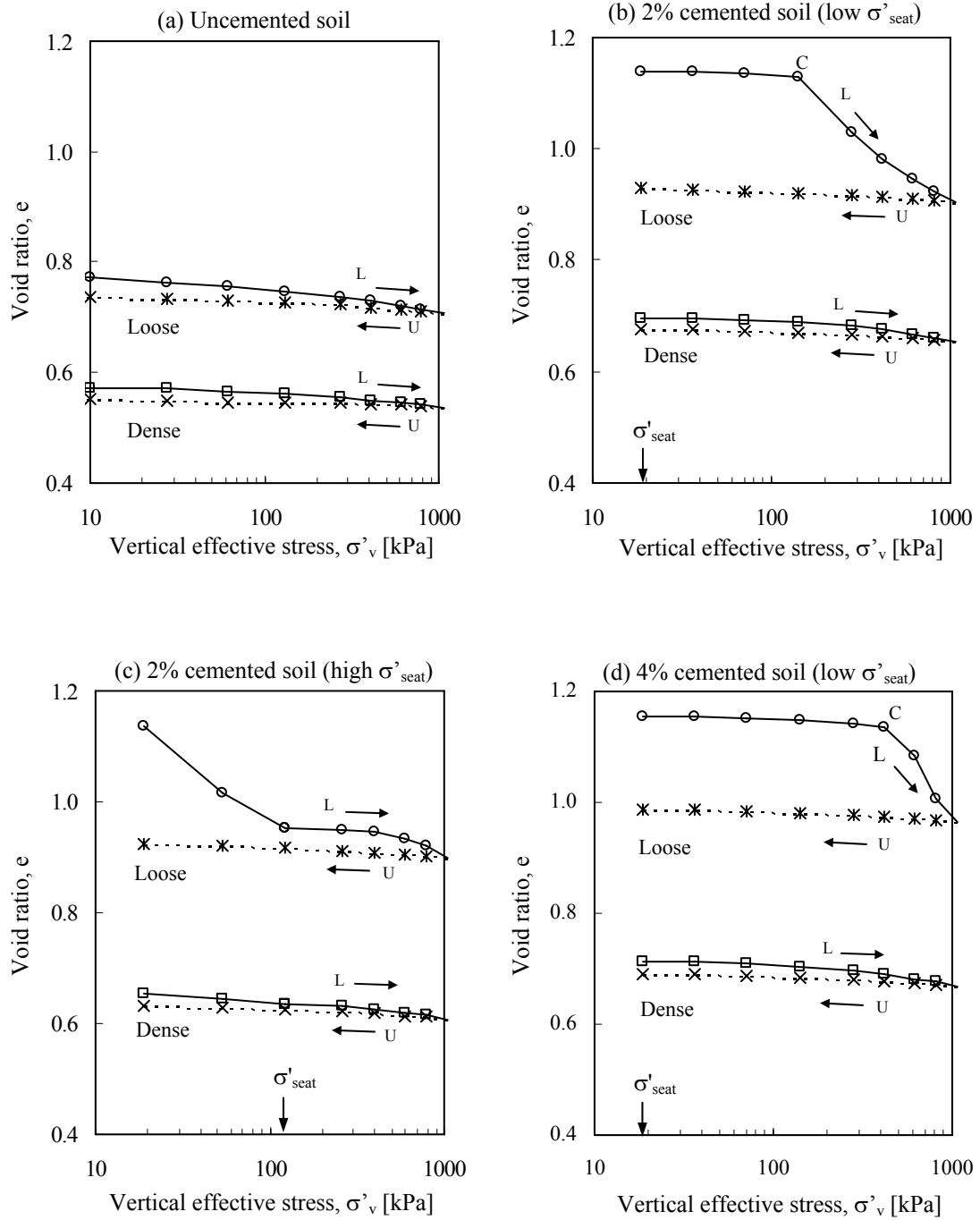


Figure 2.6 Changes in void ratio with vertical effective stress in oedometric cell (L: Solid line-loading. U: Dotted line-unloading. C: Collapse. Vertical seating pressures during hardening $\sigma'_{seat} = 18.7$ kPa, $\sigma'_{seat} = 122.8$ kPa).

strain for collapse-decementation increases with cement content (Note that this is not the strain at peak strength, see for example Clough et al., 1981; Lade and Overton, 1989).

Dense specimens do not exhibit collapse in e - $\log \sigma'_v$ (Figure 2.6-b,c,d). These specimens have higher interparticle coordination number, experience small strain upon loading, and can better preserve interparticle bonds to high stress levels.

2.4.3 *Optical Observations*

Specimens are removed from the oedometric cell after final unloading. The loose cemented soil specimens are broken with a blocky structure suggesting partial decementation. The dense cemented soil specimens remain as a monolith stack to the cell, and decementation is not visually apparent. Particle crushing is not observed.

2.5 ADDITIONAL OBSERVATIONS

Load-induced decementation and collapse are simultaneously explored in the V_s - e plots for all specimens shown in Figure 2.7. The trajectory is concave upwards; that is, decementation softening takes place prior to collapse.

The amount of cementation is the most important factor on shear wave velocity, while density and pressure exert a lesser influence. For example, the dense 2% cement specimen cured under 122.8kPa (high) vertical seating pressure reaches a lower shear wave velocity than the dense 4% cement specimen cured under 18.7kPa (low) vertical seating pressure (Figure 2.5-c,d). In fact, the cemented specimens exhibit higher shear wave velocity than the uncemented specimens at the same stress level, even after collapse

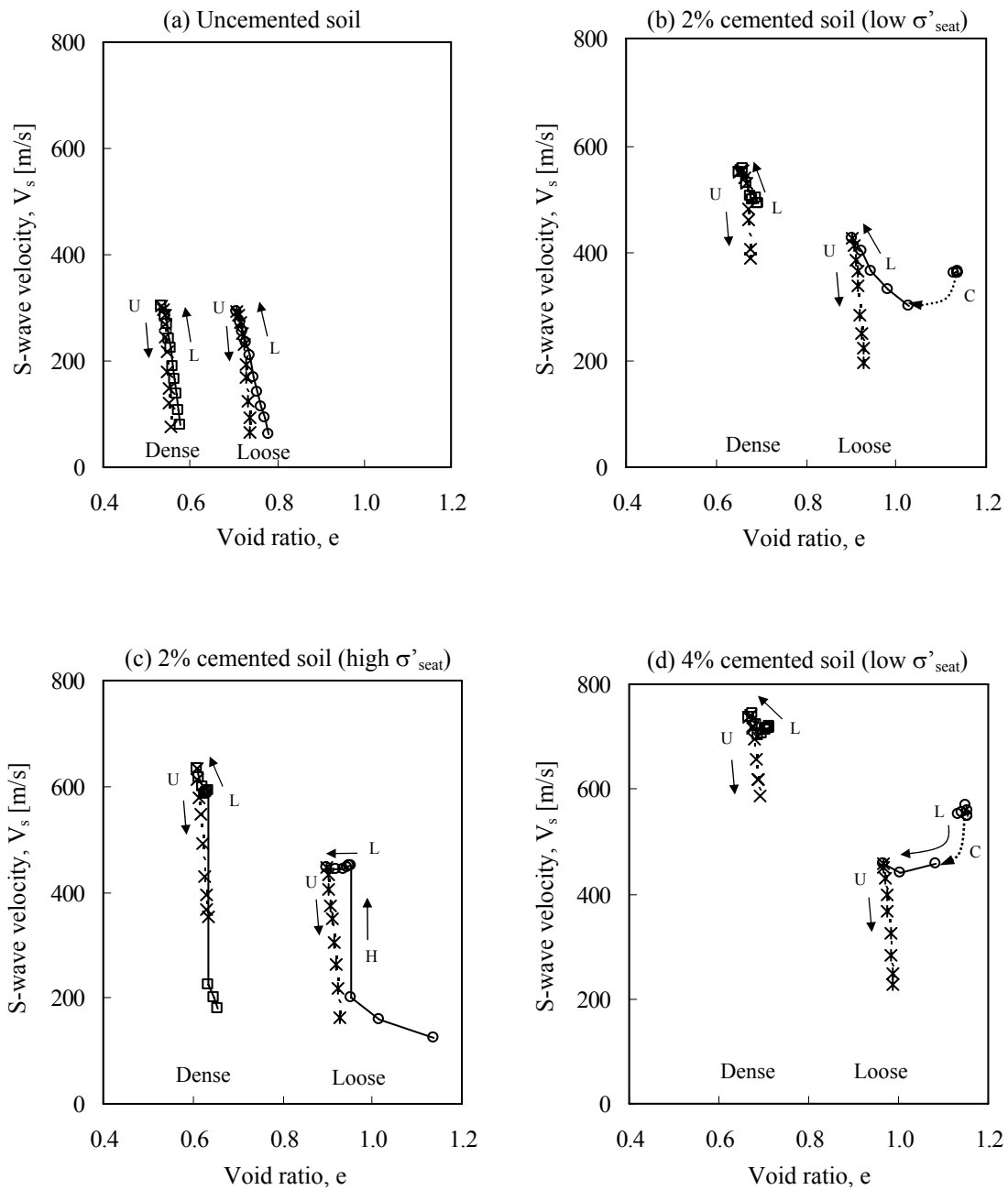


Figure 2.7 Decementation softening and collapse: void ratio vs. shear wave velocity (L: Solid line-loading. U: Dotted line-unloading. H: Hardening. C: Collapse. Vertical seating pressures during hardening $\sigma'_{seat} = 18.7$ kPa and $\sigma'_{seat} = 122.8$ kPa).

and decementation.

The stiffening effect of capillary interparticle forces is clearly seen in soil-cement mixtures prior to cement hardening: menisci that form at grain-to-grain contacts add a compressive interparticle force and the shear wave velocity increases. Experimental results confirm that the higher the cement content, the higher the specific surface of the sand-cement mixture, and the higher the suction for the same water content.

The velocity-stress sensitivity is lower in cemented specimens in the low-confinement regime than in uncemented soils. Velocity-stress trends appear to converge for both cemented and uncemented specimens at high confinement (see also Dvorkin et al., 1991).

Partial, rather than massive decementation explains the higher stiffness of cemented specimens after collapse, as compared to uncemented specimens. Analytical results indicate that the shear wave velocity decreases as the size of cemented blocks decreases (Fratta and Santamarina, 2002). In general, the higher the strain imposed during loading, the higher the stiffness loss that is observed upon unloading.

Figure 2.8 summarizes observed trends in the $\log V_s$ -vs- $\log \sigma'_v$ space. Velocity-stress trends during unloading are not sketched on Figure 2.8 for clarity. Results presented in Figure 2.5 suggest that K_o -unloading renders higher velocity in uncemented soils, but lower velocities in cemented soils. This observation can be used as a diagnostic tool for sampling effects.

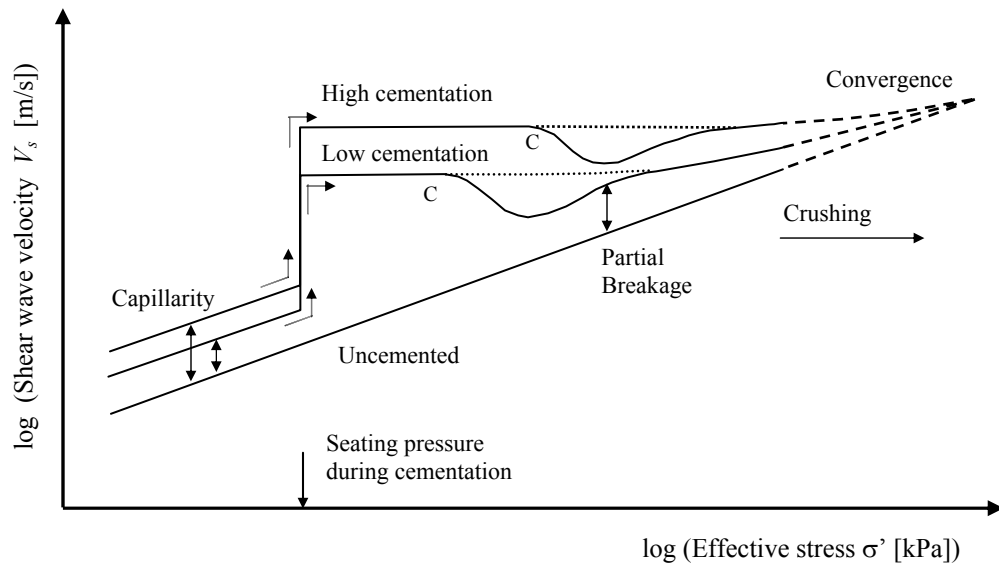


Figure 2.8 Schematic trends - Summary. Before cement hydration: fresh mixtures exhibit shear wave velocity higher than saturated uncemented soils due to capillarity. After cementation: the low-cementation loose soil collapses at lower stress than the high-cementation loose soil (solid lines correspond to loose specimens; "C" denotes collapse); the dense cemented soil specimens do not collapse (dotted lines correspond to dense specimens). At very high confinement: the shear wave velocity of cemented soils appears to asymptotically approach the shear wave velocity of uncemented soils (dashed lines).

While load-induced collapse is considered herein, it is expected that similar methodology and observations can be applied to decementation-collapse upon chemical changes, wetting and dissolution (Abduljawad and Al-Amoudi, 1995).

2.6 CONCLUSIONS

Published results show that the behavior of cemented soils depends on the amount and type of cement, the grain size distribution, the packing density of the soil, and the cementation-stress history. Cementation affects small-strain stiffness, dilative tendency during shear, liquefaction resistance and both drained and undrained strengths. At high stress, all soil parameters gradually revert to the stress-controlled behavior that characterizes uncemented soils.

The small-strain stiffness is determined by the size of contact areas, i.e., flatness. Hence, even light cementation can have a more pronounced effect than confinement on the small-strain stiffness of hard-grained soils. Then, shear wave velocity provides valuable information about the degree of cementation, and the evolution of cementation and decementation in soils, without perturbing ongoing processes.

There is increasing interest in engineering design using small strain stiffness inferred from in-situ shear wave velocity measurements. Such design approaches have resulted in much better agreement between predicted and measured settlements. However, results presented in this study show that loose, cemented materials may exhibit high initial stiffness but collapse upon loading leading to large deformations.

Furthermore, loose, lightly-cemented soils that experience load-induced collapse under K_0 -conditions can exhibit small-strain stiffness loss as a precursor to collapse. This observation may be used in the context of geophysics-based field monitoring.

The higher the density, the cement content and the effective confinement during cementation, then the lower is the possibility of decementation-collapse during

subsequent loading. Nevertheless, some breakage of interparticle bonds may take place even in the absence of collapse and a reduction of the small strain stiffness is detected when the soil is K_0 -unloaded to the same initial confinement.

The cemented soil behaves elastically albeit not necessarily linear during the early stages of loading. Stiffness, collapse load and the corresponding threshold strain increase with cement content. While the small-strain stiffness determines the deformation before the collapse load, it is inadequate for predicting collapse deformation.

While these results apply to all types of cemented soils, cementation induced by hydrates has the additional complication of pressure and temperature dependent phase transformation. Therefore, load-decementation effects in hydrate bearing sediments require further analysis.

CHAPTER III

MECHANICAL PROPERTIES OF TETRAHYDROFURAN HYDRATE BEARING SEDIMENTS

3.1 INTRODUCTION

Clathrate hydrates or gas hydrates consist of a hydrogen bonded water lattice and guest molecules (e.g., natural gases such as CH₄, C₂H₆, CO₂, and H₂S) held by van der Waals attraction forces (Tulk et al., 1998). Hydrates form under high pressure and above the freezing temperature of water.

The mechanical properties of hydrate bearing sediments are poorly known. Theoretical approaches, non-destructive methods and sampling-based attempts have been used to investigate the mechanical properties of hydrate bearing sediments (Theoretical approaches in Ecker et al., 2000; Lee and Collett, 2001; Lee, 2002; Chand et al., 2004. Seismic methods in Hyndman and Spence, 1992; Mi et al., 1999; Pecher and Holbrook, 2000). However, theoretical studies make untested assumptions to interpret the mechanical behavior of hydrate bearing sediments, the small strain response does not necessarily correlate with strength, and sampling causes disturbance and degradation of in situ properties.

Therefore, laboratory studies are necessary to explore the properties of gas hydrate bearing sediments in particular its large-strain response. The synthesis of methane hydrate in sediments is the greatest challenge in laboratory testing. Flushing methane

through sediments produces gas percolation paths and creates highly porous and heterogeneous methane hydrate bearing sediments. Surfactant used to reduce the gas-water interfacial tension fundamentally alters the process of hydrate crystallization. The low solubility and the long diffusion time of methane gas demand very long time for any reasonable size specimen.

This study focuses on the mechanical properties of hydrate bearing sediments at intermediate and large strains. Variables include: mean particle size, applied pressure, and hydrate concentration in pore space. This chapter begins with a literature review on the behavior of frozen soils and hydrates bearing sediments, followed by experimental studies and data analysis.

3.2 LITERATURE REVIEW

The phase transformation of the pore fluid affects the mechanical properties of sediments. Conversely, the presence of sediments alters the equilibrium boundary for phase transformation (Riestenberg et al., 2003). Hydrates enhance the strength and stiffness of sediments by increasing interparticle coordination, cementing particles and filling the pore space (Ladanyi and Benyamina, 1995; Kunerth et al., 2001; Da Re et al., 2003; Durham et al., 2003-a). The parallelism between hydrate and ice (Table 3.1) permits cautiously extending frozen soil knowledge to hydrate bearing sediments (Ashworth et al., 1985; Wittebolle and Segó, 1985; Parameswaran et al., 1989; Cameron et al., 1990). For example, it is known that even small amounts of ice in soils can improve stiffness and strength (Durham et al., 2003-a; see Andersen et al., 1995 for numerical modeling), and enhance the tendency to exhibit strain localization and dilation

Table 3.1 The physical properties of ice, methane and THF hydrates.

Property	Ice	CH ₄ hydrate	THF hydrate
Bulk compressibility [Pa]	12x10 ⁻¹¹	~14x10 ⁻¹¹	~14x10 ⁻¹¹
Density [kg m ⁻³]	917	910	~910
Strength hydrate +sand [MPa] at $\dot{\epsilon} = 10^{-6} \text{ s}^{-1}$	10.5		16.0
Vp [m s ⁻¹]	~3800	3369	3665
Heat capacity [J K ⁻¹ g ⁻¹]	2.097	2.07	2.07
Heat of dissociation [kJ kg ⁻¹] at 0°C	333.5	338.7	262.9
Thermal conductivity [W m ⁻¹ K ⁻¹]	2.23	0.5	0.53
Thermal diffusivity [m ² s ⁻¹]	15.4x10 ⁻⁷ at -17°C	3x10 ⁻⁷ at 3°C	
Thermal linear expansivity [K ⁻¹] at -67°C	56x10 ⁻⁶	77x10 ⁻⁶	52x10 ⁻⁶

source: pers.comm. from Santamarina (2002).

(Ladanyi and Benyamina, 1995).

At small-strains, the behavior is governed by the presence of hydrate or ice in sediments. Young's modulus is independent of relative density, confinement, and strain rate (Andersen et al., 1995; Da Re et al., 2003). Relative density and confinement have a minor effect on stiffness (Andersen et al., 1995; Da Re et al., 2003).

The strength of frozen soils combines friction between particle grains, the strength of ice, and the synergetic interaction between ice and particles (Sayles and Carbee, 1981; Ladanyi and Benyamina, 1995; Da Re et al., 2003). The relative roles of these mechanisms are determined by variables such as mean particle size (unfrozen water content / specific surface), volumetric fraction of ice and soil, porosity, dry unit weight, confining pressure and stress history, temperature and strain rate (loading condition). In general, the frictional resistance determines strength in densely packed soils (Andersen et

al., 1995). The overall stress-strain behavior of frozen soils (and hydrate bearing sediments) exhibits remarkable features: The peak strength increases when temperature and strain rate increase. (Stoll et al., 1971; Wijeweera and Joshi, Andersen et al., 1995; Li et al., 2001; Da Re et al., 2003). Hydrates bearing sediments are less sensitive to strain rate than ice (Parameswaran et al., 1989; Cameron et al., 1990). Compressive strength decreases with increasing fines content, which is closely related to the specific surface of soil particles. (Parameswaran et al., 1989; Wijeweera and Joshi, 1990; Ladanyi and Benyamina, 1995). The non-linear stress-strain response is initiated when the ice matrix begin to yield (Sayles and Carbee, 1981; Andersen et al., 1995; Da Re et al., 2003). Soil skeletal force affects the global behavior and strain localization and dilatancy are observed in post-peak range (Ladanyi and Benyamina, 1995).

Table 3.2 summarizes test methods, specimen preparation techniques and salient observations from previous studies.

3.3 EXPERIMENTAL STUDY

Sediments with synthesized tetrahydrofuran (hereafter THF) hydrates are tested with different THF·H₂O concentration and at selected confining pressures in a modified triaxial cell. Soils, hydrate contents and confining pressures are summarized in Table 3.3.

3.3.1 Tested Materials

Four soils are selected for this study, covering a mean particle size between $D_{50} = 1\mu\text{m}$ and $120\mu\text{m}$. Characteristics and SEM pictures of tested soils are presented in Figure 3.1. The specific surface S_a of precipitated silt and kaolinite are measured with the

Table 3.2 Features of frozen soil and hydrate bearing sediments.

Literature	Soil / Guest material	Test / Variables	Specimen preparation	Salient observations
Wittebolle and Segó (1985)	<ul style="list-style-type: none"> ▪ Sand (0.85-1.7mm) ▪ Freon 12 gas 	<ul style="list-style-type: none"> ▪ Triaxial compression ▪ Confinement (σ_c) ▪ Hydrate vs. Ice 	<ul style="list-style-type: none"> ▪ Introducing gas to soil with 0.3MPa under cooling 	<ul style="list-style-type: none"> ▪ $V_p \rightarrow 1.96, 2.46$ and 3.6 km/sec (7, 1.89 and 0°C) ▪ $\sigma_c \uparrow$, strength \uparrow
Li et al (2001)	<ul style="list-style-type: none"> ▪ Silty sand (5-50μm) ▪ H₂O 	<ul style="list-style-type: none"> ▪ Triaxial compression ▪ Temperature (T) ▪ Strain rate (ϵ) 	<ul style="list-style-type: none"> ▪ Soil+H₂O mixture ▪ Trim after freezing ▪ Curing 	<ul style="list-style-type: none"> ▪ T \uparrow, strength \downarrow ▪ Strain rate \uparrow, strength \uparrow ▪ Water content less important ▪ $\sigma_c = \sigma_o + 1.547 (\epsilon / \epsilon_o) T$
Da Re et al. (2003)	<ul style="list-style-type: none"> ▪ Manchester fine sand (150μm) ▪ H₂O 	<ul style="list-style-type: none"> ▪ Triaxial compression ▪ Relative density (D_r) ▪ Confinement (σ_c) ▪ Strain rate (ϵ) ▪ Temperature (T) 	<ul style="list-style-type: none"> ▪ Soil+H₂O mixture under vacuum ▪ Trim after freezing 	<ul style="list-style-type: none"> ▪ T \uparrow, strength \downarrow ▪ Strain rate \uparrow, strength \uparrow ▪ Strength at small strain region : insensitive to D_r, σ_c ▪ Young's modulus : insensitive to D_r, σ_c, ϵ
Andersen et al. (1995)	<ul style="list-style-type: none"> ▪ Manchester fine sand (180μm) ▪ H₂O 	<ul style="list-style-type: none"> ▪ Triaxial compression ▪ Relative density (D_r) ▪ Confinement (σ_c) ▪ Strain rate (ϵ) ▪ Temperature (T) 	<ul style="list-style-type: none"> ▪ Soil+H₂O mixture ▪ Trim after freezing ▪ Seating (0.3MPa) pressure 	<ul style="list-style-type: none"> ▪ Strength at small strain region : independent on density : dependent on strain rate and T ▪ $\sigma_c \uparrow$, strength \uparrow (stress sensitivity) ▪ Young's modulus : independent on $D_r, \sigma_c, T, \epsilon$
Sayles and Carbee (1981)	<ul style="list-style-type: none"> ▪ Silt (30mm) ▪ H₂O 	<ul style="list-style-type: none"> ▪ Uniaxial compression ▪ Water (ice) content ▪ Constant strain rate 	<ul style="list-style-type: none"> ▪ Consolidation /Saturation ▪ Trim after freezing 	<ul style="list-style-type: none"> ▪ Water (ice) content \uparrow, strength \uparrow ▪ Dry unit weight \uparrow, strength \downarrow

Table 3.2 Continued.

Literature	Soil / Guest material	Test / Variables	Specimen preparation	Salient observations
Wijeweera and Joshi (1990)	<ul style="list-style-type: none"> ▪ Benonite, clay, silt kaolin ▪ H₂O 	<ul style="list-style-type: none"> ▪ Uniaxial compression ▪ Fine content ▪ Particle size ▪ Water content ▪ Constant strain rate 	<ul style="list-style-type: none"> ▪ Freezing after consolidation (0.07-2.45MPa) 	<ul style="list-style-type: none"> ▪ Dry unit weight ↑, strength ↑ (high plastic clays) ▪ Specific surface ↑, strength ↓ ▪ Fine content ↑, strength ↑ ▪ High w/c, w/c ↑, strength ↑ ▪ Low w/c, w/c ↓, strength ↑
Cameron et al. (1990)	<ul style="list-style-type: none"> ▪ Sand (0.2-0.6mm) ▪ THF·16.7H₂O 	<ul style="list-style-type: none"> ▪ Uniaxial compression ▪ Temperature (T) ▪ Strain rate (ε) 	<ul style="list-style-type: none"> ▪ Soil+solution mixture ▪ Trim after freezing 	<ul style="list-style-type: none"> ▪ Similar strength between frozen soils and hydrate bearing sediments ▪ Hydrate bearing sediment insensitive to strain rate ▪ T ↓, strength ↑
Stoll et al. (1971)	<ul style="list-style-type: none"> ▪ Ottawa sand 20-30 ▪ Methane gas 	<ul style="list-style-type: none"> ▪ P-wave measurement ▪ Temperature (T) ▪ Hydrate phase 	<ul style="list-style-type: none"> ▪ Water+soil mixture under 3.3 °C/1100 psi ▪ Inject methane (700 psi) 	<ul style="list-style-type: none"> ▪ V_p (sand+fluid) → 1850 m/s ▪ V_p (sand+hydrate) → 2690 m/s
Kunerth et al. (2001)	<ul style="list-style-type: none"> ▪ Garnet sand ▪ THF·17H₂O 	<ul style="list-style-type: none"> ▪ P- and S-wave measurement ▪ Temperature (T) ▪ Hydrate phase 	<ul style="list-style-type: none"> ▪ Oversaturate soil with fluid 	<ul style="list-style-type: none"> ▪ V_p (sand+fluid) → 1635 m/s ▪ V_p (sand+hydrate) → 3400 m/s ▪ V_s (sand+hydrate) → 2400 m/s ▪ Bulk modulus increases prior to shear modulus increase by second event of phase transformation

Table 3.3 Test variables.

Soils	% hydrate-filled porosity [%] THF·H ₂ O ratio	Confining pressures, σ_c
Sand (F110)	0% H ₂ O (unfrozen)	0.03 MPa
Crushed silt (Sil Co Sil 106)	50% THF·2.95H ₂ O	0.5 MPa
Precipitated silt (Silica zeofree 5161)	100% THF·17H ₂ O	1.0 MPa
Kaolinite (SA1)		

Note: all possible combinations are tested except crushed silt which is not tested for 50% hydrate concentration only.

methylene blue method (wet method). Note that the specific surface of precipitated silt is larger than that of crushed silt even though their D_{50} is the same. This indicates the presence of internal porosity in precipitated silt.

THF is herein selected as a surrogate molecule for laboratory studies (Gough and Davidson, 1971; Rueff and Sloan, 1985; Pearson et al., 1986; Cameron et al., 1990; Devarakonda et al., 1999). THF is in liquid phase of room temperature and atmospheric pressure, is fully miscible in water, and presents a low freezing temperature (Table 3.4).

A comparative analysis of methane and THF hydrates is presented in Table 3.1. The stoichiometric mixture of THF and water (THF·17H₂O) forms clathrate hydrate structure II under atmospheric pressure and at ~-4.4°C (Sloan, 1990). THF properties are useful to control the hydrate fraction in the pore space when the fluid mixture goes through phase transformation.

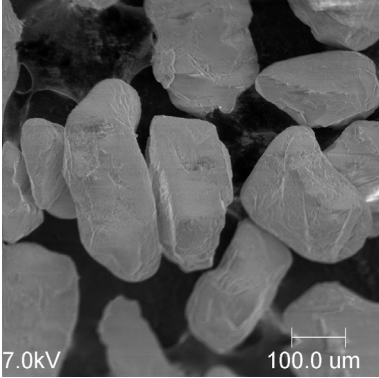
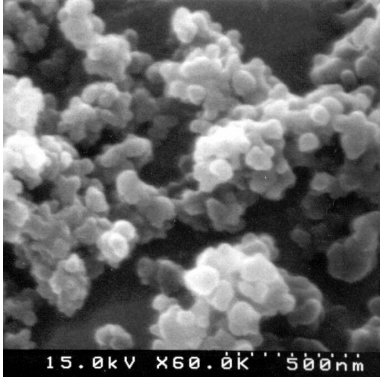
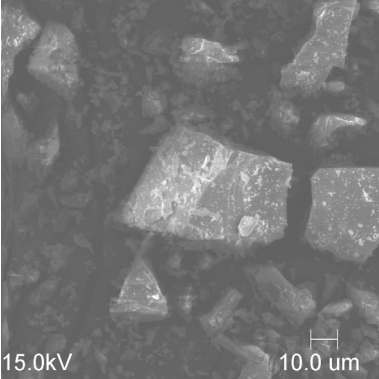
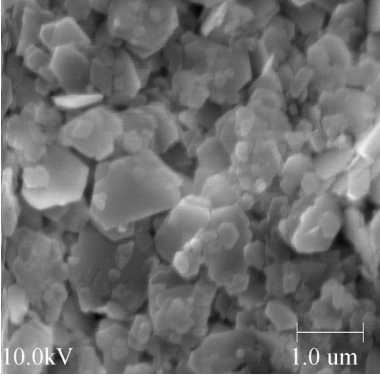
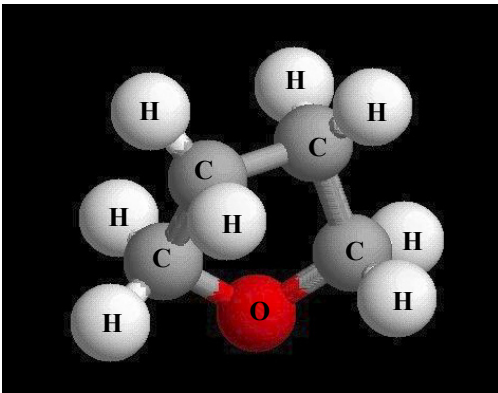
Sand (F110)		Precipitated silt (Silica zeofree 5161)	
			
$D_{50} = 120 \mu\text{m}$	$e_{max} / e_{min} = 0.85 / 0.54$	$D_{50} = 20 \mu\text{m}$	Sphericity = 0.9
$G_s = 2.65$	Sphericity = 0.7	$G_s = 2.2$	Roundness = 0.7
$S_a \cong 0.019 \text{ m}^2/\text{g}$	Roundness = 0.7	$S_a^* = 5\sim7 \text{ m}^2/\text{g}$	
Crushed silt (Sil Co Sil 106)		Kaolinite (SA1)	
			
$D_{50} = 20 \mu\text{m}$	$e_{max} / e_{min} = 1.51 / 0.67$	$D_{50} = 1.1 \mu\text{m}$	Sphericity = 0.7
$G_s = 2.65$	Sphericity = 0.9	$G_s = 2.6$	Roundness = 0.1
$S_a \cong 0.113 \text{ m}^2/\text{g}$	Roundness = 0.1	$S_a^* = 36\sim37 \text{ m}^2/\text{g}$	

Figure 3.1 Characteristics of tested soils and SEM pictures (SEM pictures: courtesy of Angelica Palomino, 2003. Data: Santamarina and Cho 2001, Klein 1999, Parks 1990 and Guimaraes 2001)

*: Specific surface is measured with the methylene blue method (wet method)

Table 3.4 Properties of tetrahydrofuran (THF).

Material	Tetrahydrofuran (THF)
Molecule in 3D	
	(http://people.ouc.bc.ca/woodcock/molecule/modelfiles/jb05thf.html)
Molecular formula	C ₄ H ₈ O
Molecular weight	72.05 g
Composition	Tetrahydrofuran (>99.0%) / Butylated Hydroxytoluene (0.025%)
Appearance	Colorless liquid
Odor	Ethereal odor
Vapor pressure	160 mmHg (23.7 mmHg for water) @ 25 °C
Boiling point	65.4 °C
Freezing/melting point	-65 °C
Solubility in water	100% miscible
Specific gravity / density	0.89

sources: Fisher Scientific (www.fisherscientific.com)

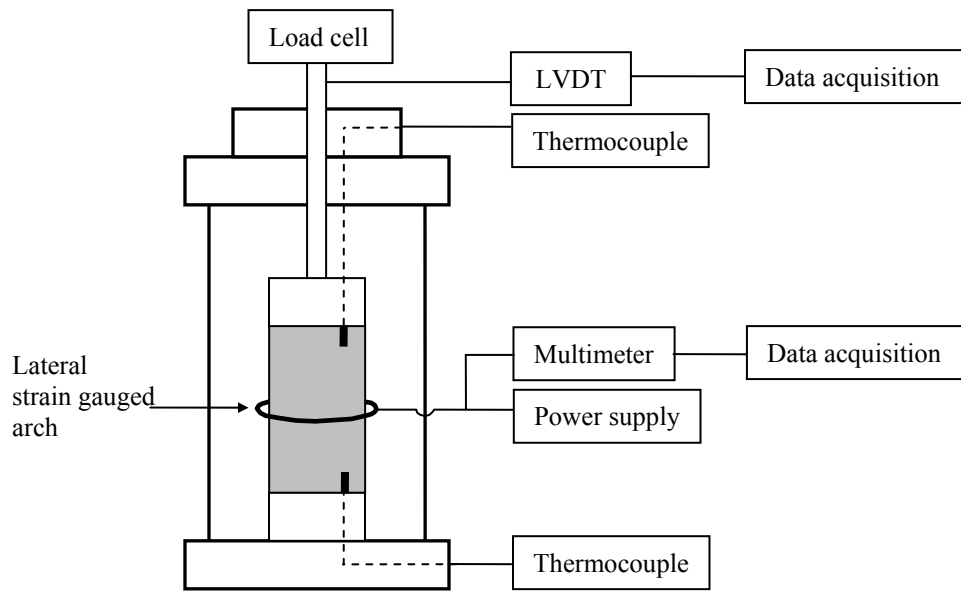


Figure 3.2 Triaxial cell and peripheral electronics. Two thermocouples are embedded on the top and bottom plates. A strain gauged arch is mounted at the middle height of the specimen.

3.3.2 Devices

A conventional triaxial cell is modified to house electronics for specimen monitoring and thermocouples (TP29, BK precision) to assess phase transformation. Cell details are shown in Figure 3.2.

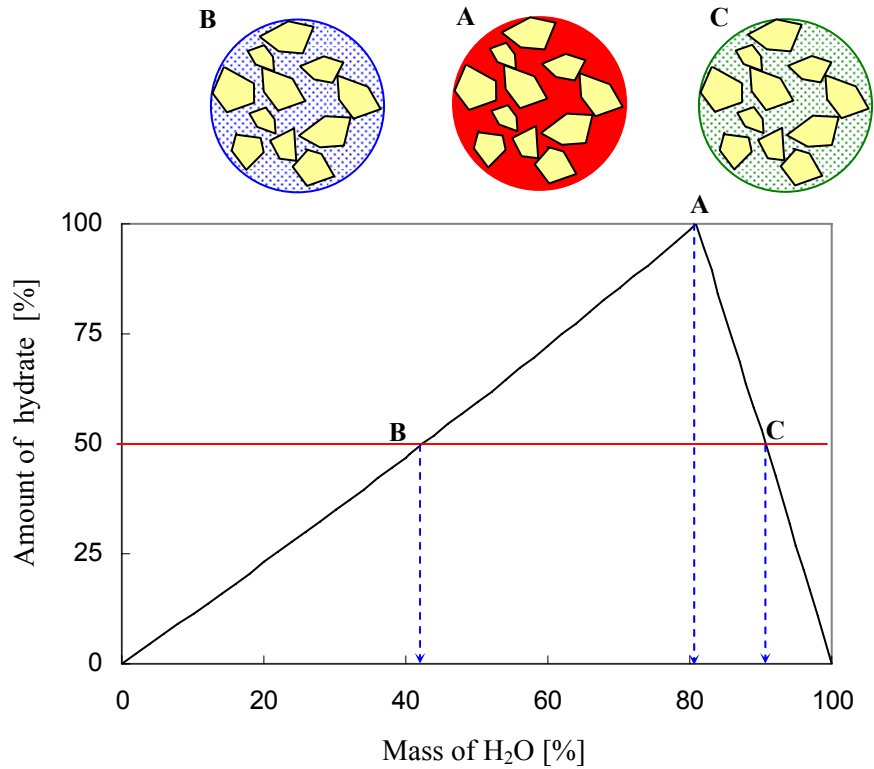
Lateral displacement is measured with a metal arch instrumented with half of a bridge. The two active gauges are installed on both sides of the thin metal arch (one in compression and the other in tension). The other half of the bridge is placed outside the cell (strain gauge: CEA-06-240UZ-120, Measurement Group INC.). This configuration cancels non-linear and temperature effects. The resolution of this full bridge displacement

transducer is 5-to-6 μ m. The direct measurement of lateral displacement with a digital caliper confirms the reliability of the strain gauged arch (Note that this lateral strain is not the same as one used for the calculation of Poisson's ratio).

3.3.3 *Specimen Preparation and Test Procedure*

The ratio between THF and H₂O controls the amount of hydrate concentration in the pore space (Table 3.3). THF hydrate forms with 81% of H₂O and 19% of THF by mass (point A in Figure 3.3). Specimens with 50% hydrate-filled porosity are obtained by choosing either point B or C in Figure 3.3. Point B corresponds to excess THF while THF hydrate formation at point C leaves excess water. The fraction at point B (42.4%/57.6% as H₂O/THF) is used to make 50% hydrate-filled porosity in this study due to the convenience of temperature control (freezing temperature of THF is $\sim -65^{\circ}\text{C}$). The maximum exposure time to prepare the solution does not exceed 2 minutes.

Dry soils are thoroughly mixed with the prepared solution under a ventilation hood. Then the soil-fluid mixture is poured into the membrane set in the triaxial cell. Detailed specimen preparation procedures are summarized in Table 3.5. Fluid saturated filter paper surrounds kaolinite and precipitated silt specimens to facilitate drainage. Once specimens are closed with the top cap, vacuum is applied to erect the specimens; the initial volume is determined at this point. The lateral strain gauge is mounted onto the middle height of the specimen. The chamber is filled with mineral oil; then, specimens are isotropically consolidated until the predetermined effective confining pressure is attained (For comparison, Table 3.1 summarizes specimen preparation procedures followed by previous researchers).



	Fraction of pore filling hydrate	H ₂ O [%]	THF [%]
A	100% hydrate / no liquid	80.9	19.1
B	50% hydrate / 50% excess THF	42.4	57.6
C	50% hydrate / 50% excess water	90.6	9.4

Figure 3.3 Hydrate fraction by volume filling the pore space.

The volume change in the specimen during consolidation is monitored using a graduated burette. After consolidation, specimens are frozen to -10°C while monitoring temperature changes. It takes 6-8 hours to freeze the specimen. The system is stabilized for an additional 12 hours. The specimen with 0% hydrate-filled porosity (100% H₂O) is not subjected to freezing.

The deviatoric stress is applied to impose 0.1%/min strain rate in specimens with

Table 3.5 Specimen preparation procedures.

Soils	Procedures
Sand	<ol style="list-style-type: none"> 1. Prepare solution mixture with defined ratio. 2. Mix the soil with the solution. 3. Fill the membrane / cell with the solution. 4. Pour the soil and solution mixture into the membrane / cell by scooping. 5. Tamp and tap the specimens with 6-8 layers. 6. Close the specimen with top cap.
Kaolinite / Precipitated silt	<ol style="list-style-type: none"> 1. Prepare solution mixture with defined ratio. 2. Mix the soil with the solution thoroughly. 3. Fill the auxiliary cell with the soil-fluid mixture. 4. Surround the inner wall of the membrane / cell with filter paper. 5. Extrude the mixture in the auxiliary cell into the membrane / cell. 6. Place the top cap.
Crushed silt	<ol style="list-style-type: none"> 1. Prepare solution mixture with defined ratio. 2. Mix the soil with the solution thoroughly. 3. Fill membrane / cell with the mixture. 4. Close membrane cell temporarily. 5. Iterate <i>step 4</i> 2-3 times to fill the membrane / cell. 6. Place the top cap.

0% hydrate-filled porosity and 1%/min strain rate in specimens with 50% and 100% hydrate-filled porosity specimens. The triaxial cell is kept below freezing temperature with dry ice during the test duration (less than 20 min for specimens with hydrates). The applied load, and ensuing vertical and lateral displacements are recorded during loading. All specimens are optically observed after the test to identify heterogeneities (ice lenses) and the failure mode.

3.3.4 Precautions Taking During the Experiments

THF evaporation. The vapor pressure of THF is 6~7 times higher than water (Table 3.4); this situation leads to experimental difficulties related to preferential evaporation of THF (Cameron et al., 1990).

An experimental study is performed to assess evaporation effects. Pure THF and the optimal THF+H₂O solution are exposed to the atmosphere to allow evaporation. The weight of the mixture is monitored with time and resultant *n*-values (THF·*n*H₂O) are calculated assuming the worst condition whereby all weight loss is due to THF evaporation only. Results are presented in Figure 3.4. The THF+H₂O solution shows lower evaporation rate than pure THF when both fluids are subjected to stirring during evaporation. The evaporation of pure THF under static conditions is lower. The time range between 10 and 20 minutes represents the approximate sample preparation time. The estimated *n*-value of the optimal THF+H₂O solution after evaporation is 17.5 ~ 18.2. It is believed that *n*-values for THF+H₂O mixtures in soils are closer to the pre-selected value because mixing is minimal (compared to this test) and because the porous network prevents evaporation.

Surface effects. Soil mixtures with THF·17H₂O solution would lead to incomplete hydrate formation with excess THF because water molecules are preferentially attracted to the mineral surface. This situation gains relevance in high specific surface sediments such as kaolinite, illite and montmorillonite. Let's assume that water molecules in the double layer do not react with THF. Then the effective number of water molecules per molecule of THF is

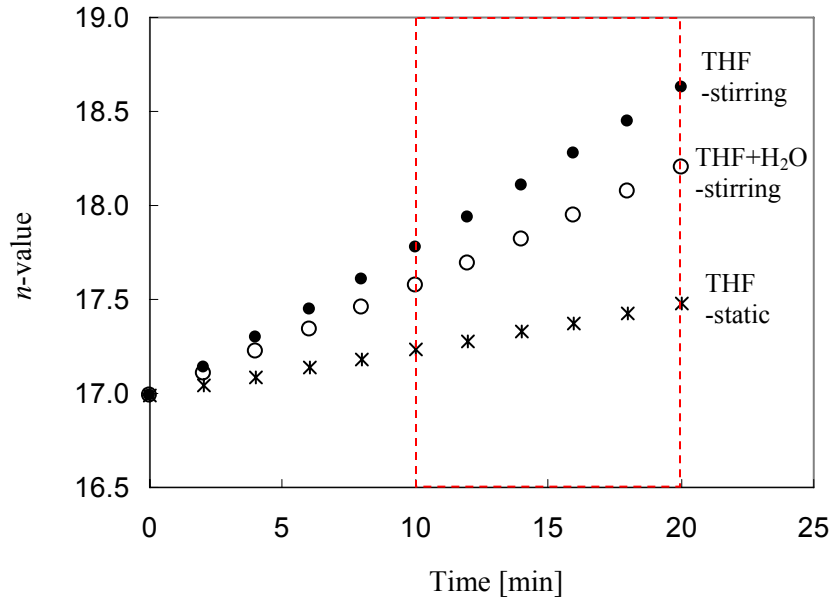


Figure 3.4 Evaporation: evolution of n -value in THF· n H₂O solution with time for fluids with and without stirring (Assumption: all mass loss is due to THF evaporation).

$$n = R \cdot \frac{(wc - S_a \cdot d \cdot \rho_w)}{wc} \quad (3.1)$$

where $R = 17$ is the optimal ratio between THF and H₂O, S_a specific surface of soils (m²/g), d diffuse double layer thickness (m), ρ_w unit weight of water (g/m³), and wc is the volumetric water content in the soil. Figure 3.5 shows the maximum estimated n -values with varying specific surface and water content assuming $d=5 \cdot 10^{-10}$ m. The value of n remains constant at 17 when the specific surface is small but it declines for high specific surface sediments at low wc . The estimated n -values to produce 100% hydrate filling voids are 17.00 for sand, 17.13 for precipitated silt and 17.76 for kaolinite.

Hydration memory: The temperature of a cell filled with THF·17H₂O solution is monitored during repeated freezing-thawing cycles. The phase transformation during the

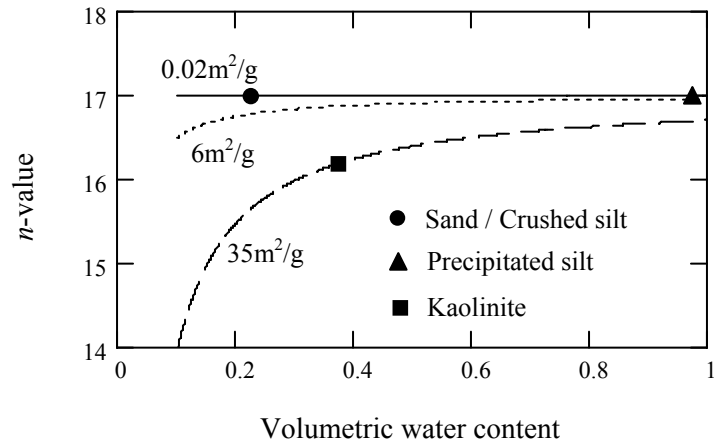


Figure 3.5 Effective number of available water molecules, starting from the stoichiometric mix ($n=17$) as a function of the water content and the specific surface of the soil. The assumed thickness of the double layer is $d = 5 \cdot 10^{-10}$ m.

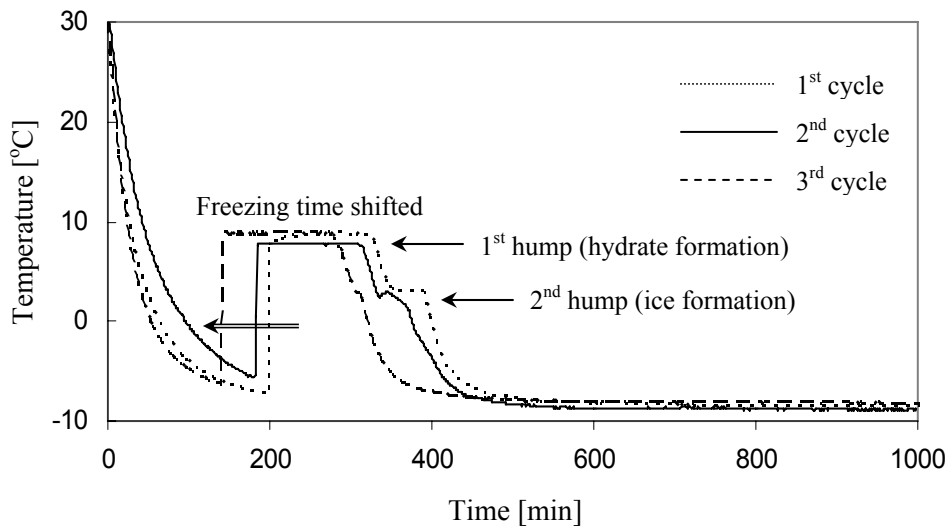


Figure 3.6 Phase transformation cycles. The freezing time decreases with increasing number of cycles.

first cycles is shown in Figure 3.6. The second hump indicates ice formation that results from THF evaporation. It is observed that formation occurs in shorter time during subsequent cycles. It is inferred that THF hydrate formation has a freezing history memory (Sloan, 1998; e.g., Iida et al., 2001). The internal mechanisms remain unclear.

3.4 EXPERIMENTAL RESULTS

The stress-strain response and post-failure specimen characteristics are documented in this section. It is assumed that specimens fail at the maximum deviatoric stress, $\sigma_{dev-max} = (\sigma_1 - \sigma_3)_{max}$.

3.4.1 *Stress-Strain Response*

Figure 3.7 shows the stress-strain curves during undrained deviatoric loading for all tested specimens and confining pressures (0.03 MPa to 1 MPa). The following salient observations can be made:

- Specimens with 0% hydrate-filled porosity primarily show strain hardening behavior.
- Hydrate bearing sediments exhibits high stiffness at low strains. The quasi-elastic behavior extends to higher axial strain as confining pressure increases.
- Sand and crushed silt with 100% hydrate exhibit a second region with lower tangential stiffness before failure (strain level 1~2%). This is observed at all confining pressures (see also Andersen et al., 1995; Ting et al., 1983).

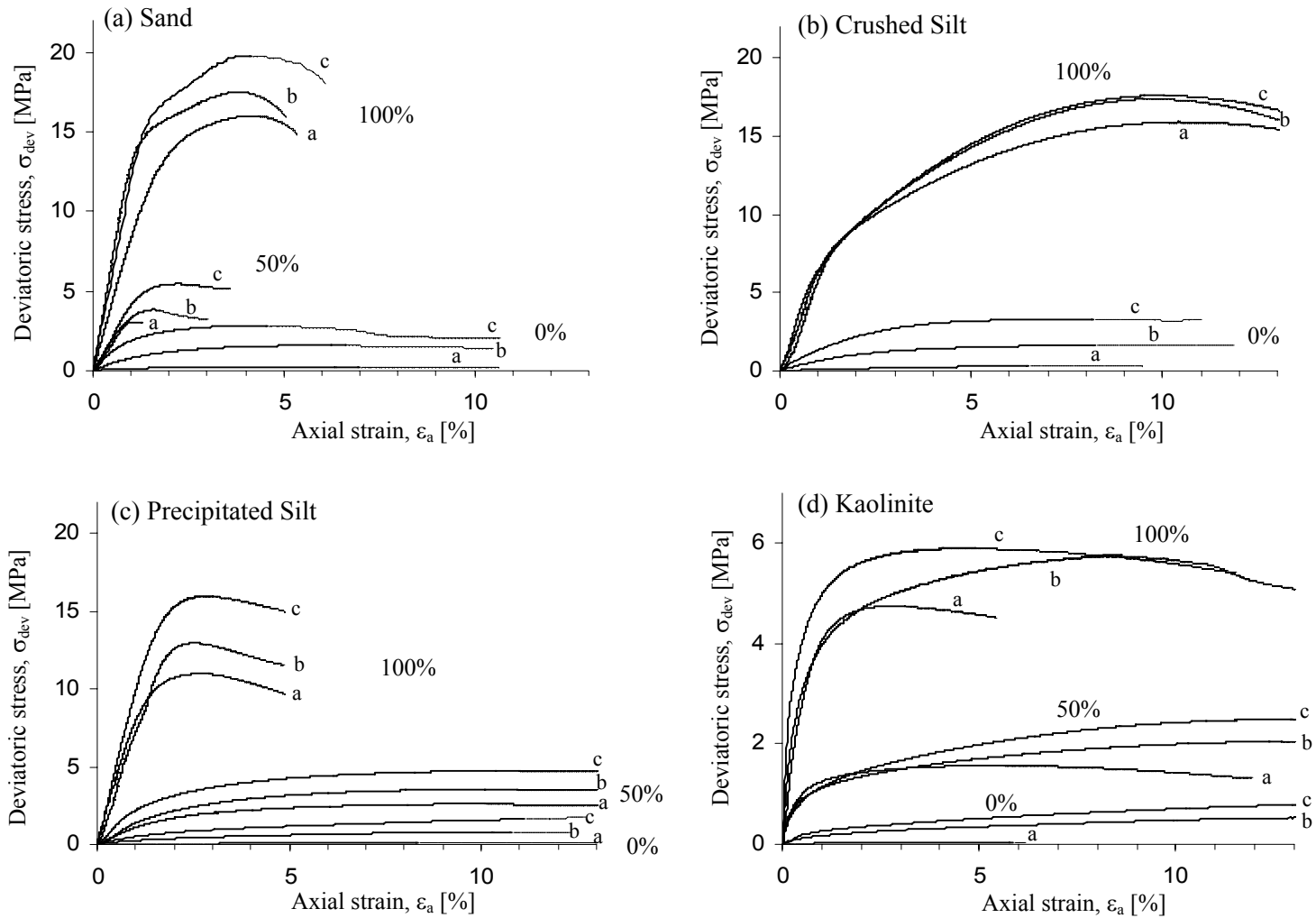


Figure 3.7 Stress versus axial strain. Thin lines are the post-peak response where localization is expected. Letters a, b and c denote 0.03, 0.5 and 1 MPa confining pressure. Note that kaolinite is plotted in a larger stress scale.

- Precipitated silt and kaolinite with 100% hydrate-filled porosity exhibit quasi-brittle behavior.
- The range of σ_{dev} values at failure under different confining pressures becomes narrower as hydrate concentration increases, and the stress-strain response becomes less sensitive to confining pressure.

3.4.2 *Post-Failure Visual Inspection*

No ice lens or noticeable heterogeneity is observed in all tested specimen. Fast freezing rates and confining pressure appear to promote self-homogenization. Figure 3.8 shows pictures obtained from sand specimens after failure. Specimens with 50 and 100% hydrate-filled porosity tested at 0.03MPa show vertical fractures similar to those commonly reported in rock tests at low confinement. The specimens at 0.5MPa show clear shear planes while sand with 100% hydrate-filled porosity develops a fracture network at 1MPa.

3.5 ANALYSIS

3.5.1 *Stiffness*

Intermediate-strain stiffness is obtained at $(\sigma_1 - \sigma_3)_f / 2$, for the corresponding axial strain. Figure 3.9 shows the variation in stiffness with confinement and hydrate concentration. The stiffness of sediments without hydrate is governed by the confining pressure: as confinement increases, the interparticle coordination and contact area increase and the skeletal stiffness increases. On the other hand, hydrate concentration

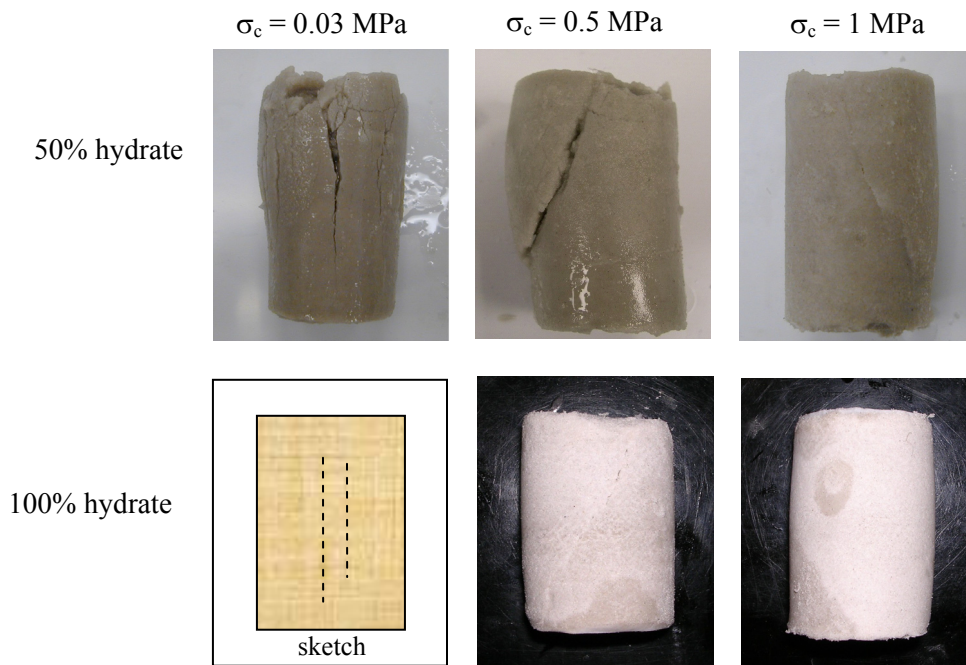


Figure 3.8 Sand specimens after failure.

controls the stiffness in hydrate bearing soils and confinement has a negligible effect (the same trend is observed at small strains, see Figure 2.5 in Chapter II).

The strength and stiffness dependency on the initial effective confinement and hydrate cementation suggest a correlation between τ_{peak} and E . The stiffness E is plotted versus the peak shear strength for all tested soils (with and without hydrate and all effective confinement) in Figure 3.10. Assuming a relation of the form:

$$E = A \cdot \left[\frac{\tau_{peak}}{kPa} \right]^B \quad (3.2)$$

The inverted parameters are $A = 96.1$ and $B = 1.13$.

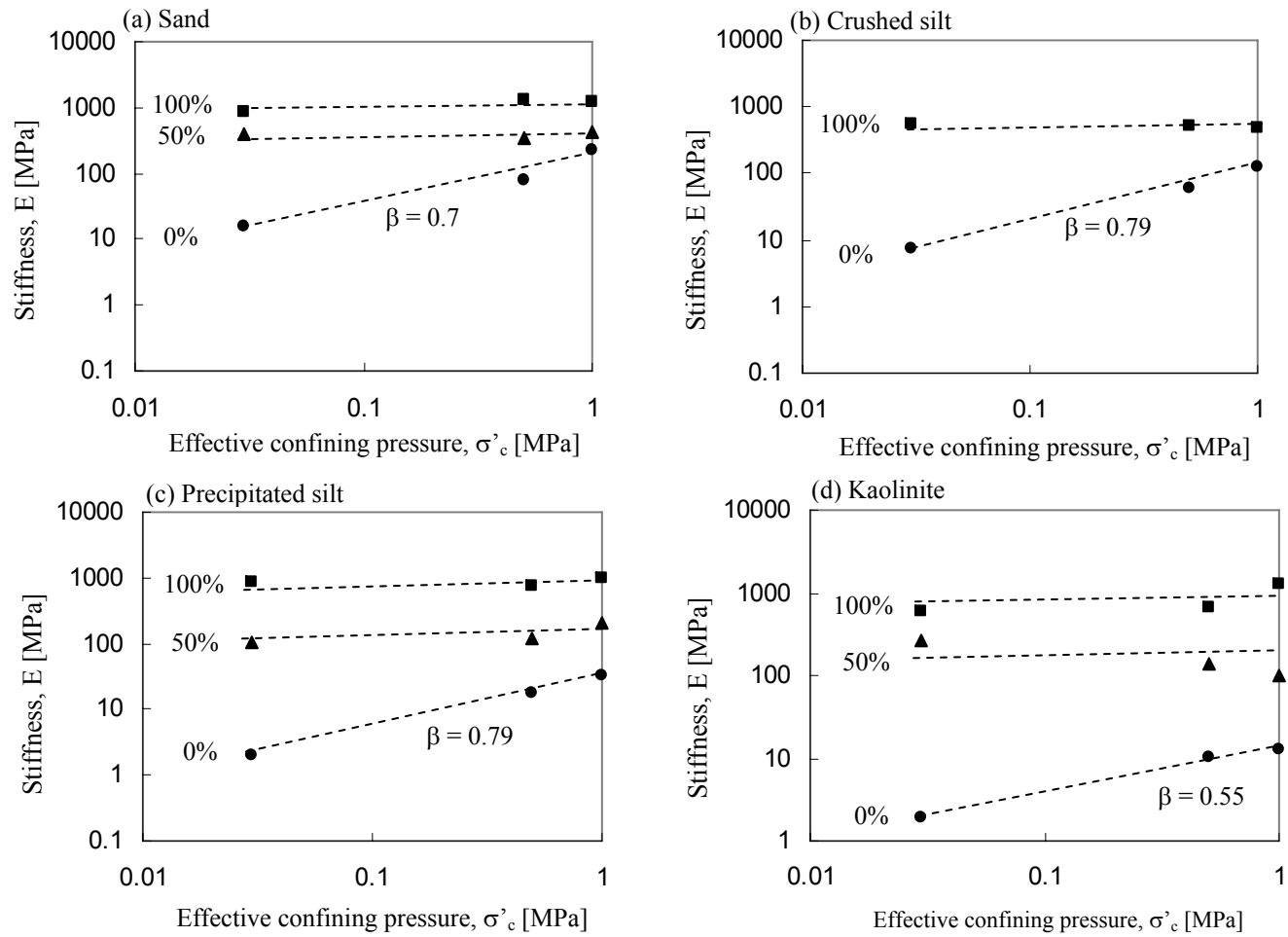


Figure 3.9 Longitudinal stiffness at $(\sigma_1 - \sigma_3)_f/2$ versus effective confining pressure. The parameter β is computed for 0% hydrate bearing sediments. The exponent of the power relation $E = \alpha \cdot \sigma'^{\beta}$.

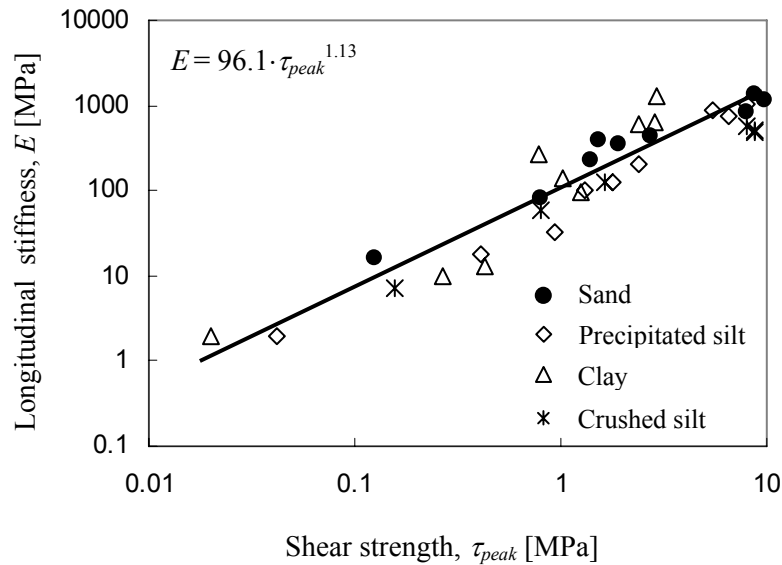


Figure 3.10 Longitudinal stiffness at $(\sigma_1 - \sigma_3)/2$ versus undrained shear strength for all tested soils, with and without hydrates, and at all confining pressures.

3.5.2 Undrained Strength

The undrained peak shear strength τ_{peak} is plotted for all tested soils in Figure 3.11. The undrained shear strength increases as hydrate concentration increases, it is confinement-dependent in 0% hydrate bearing sediments, and it is quasi confinement-independent in the 50% and 100% hydrate bearing soils (Recall that specimens subjected to higher effective confinement σ'_c reach a lower void ratio prior to the undrained deviatoric loading stage).

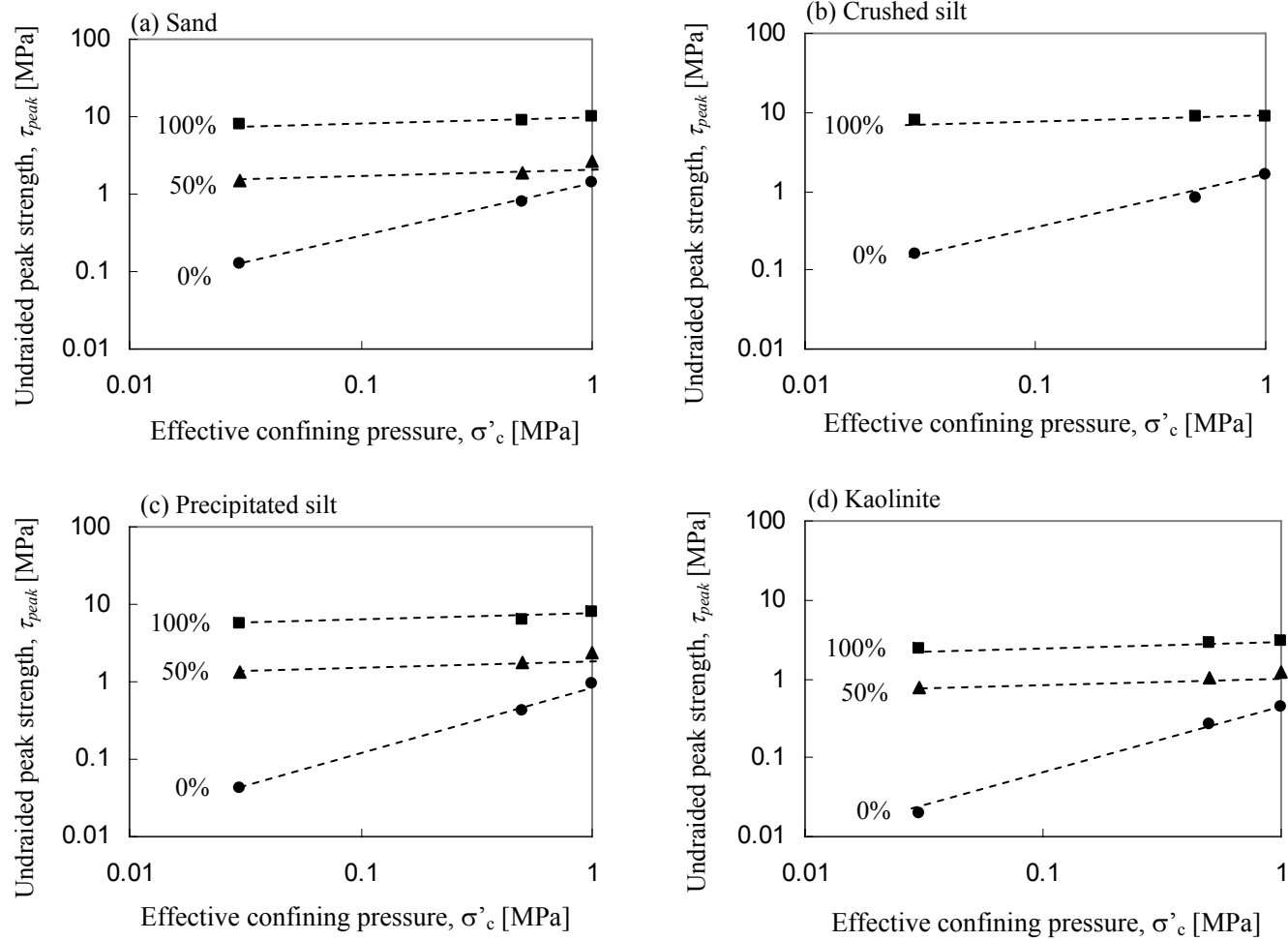


Figure 3.11 Undrained peak strength versus effective confining pressure and hydrate-filled porosity.

Table 3.6 Computed fitting parameters.

Soils	D_{50} [μm]	S_a [m^2/g]	α [MPa]	β	μ
Sand	120	0.019	7.97	3.69	1.82
Crushed silt	20	0.113	5.97	1.81	1.1
Precipitate silt	20	6	2.49	1.88	0.52
Kaolinite	1.1	36	7.75	2.51	1.43

3.5.3 Strength as a Function of Hydrate Concentration and Confinement

The Coulomb strength criterion is properly defined in terms of effective stress σ'_n

$$\tau = c + [\sigma'_n] \cdot \tan(\phi) \quad (3.3)$$

where c is the cementing strength, and ϕ is the friction angle. However, pore pressure generation during shear cannot be measured with certainty in hydrate bearing systems. Instead, the measured undrained shear strength S_u is related to the initial isotropic, effective confinement σ'_o and the hydrate concentration S_{hyd} ($0 \leq S_{hyd} \leq 1$) as follows:

$$S_u = \alpha \cdot S_{hyd}^\beta + \sigma'_o \cdot \mu \quad (3.4)$$

α , β and μ are model parameters. The first term $\alpha \cdot S_{hyd}^\beta$ captures the cementing contribution of the hydrate mass, while the second term $\sigma'_o \cdot \mu$ reflects the consequences of higher interparticle coordination due to a higher initial effective stress. Fitting parameters are listed in Table 3.6 and plotted versus specific surface in Figure 3.12. The cementation terms (α and β) and the stress dependent strength parameter (μ) decrease

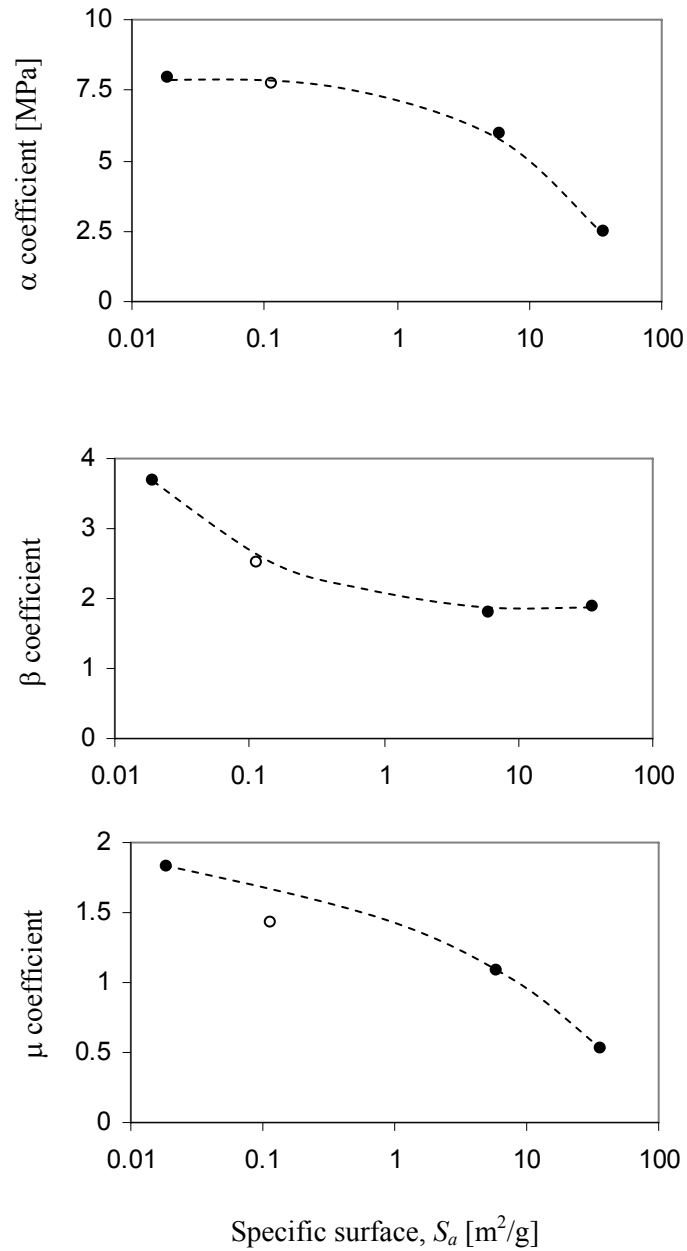


Figure 3.12 Model coefficients estimated by Equation 3.4 (o indicates the precipitated silt specimens).

with the specific surface S_a . Experimental results and predicted values are plotted in Figure 3.13.

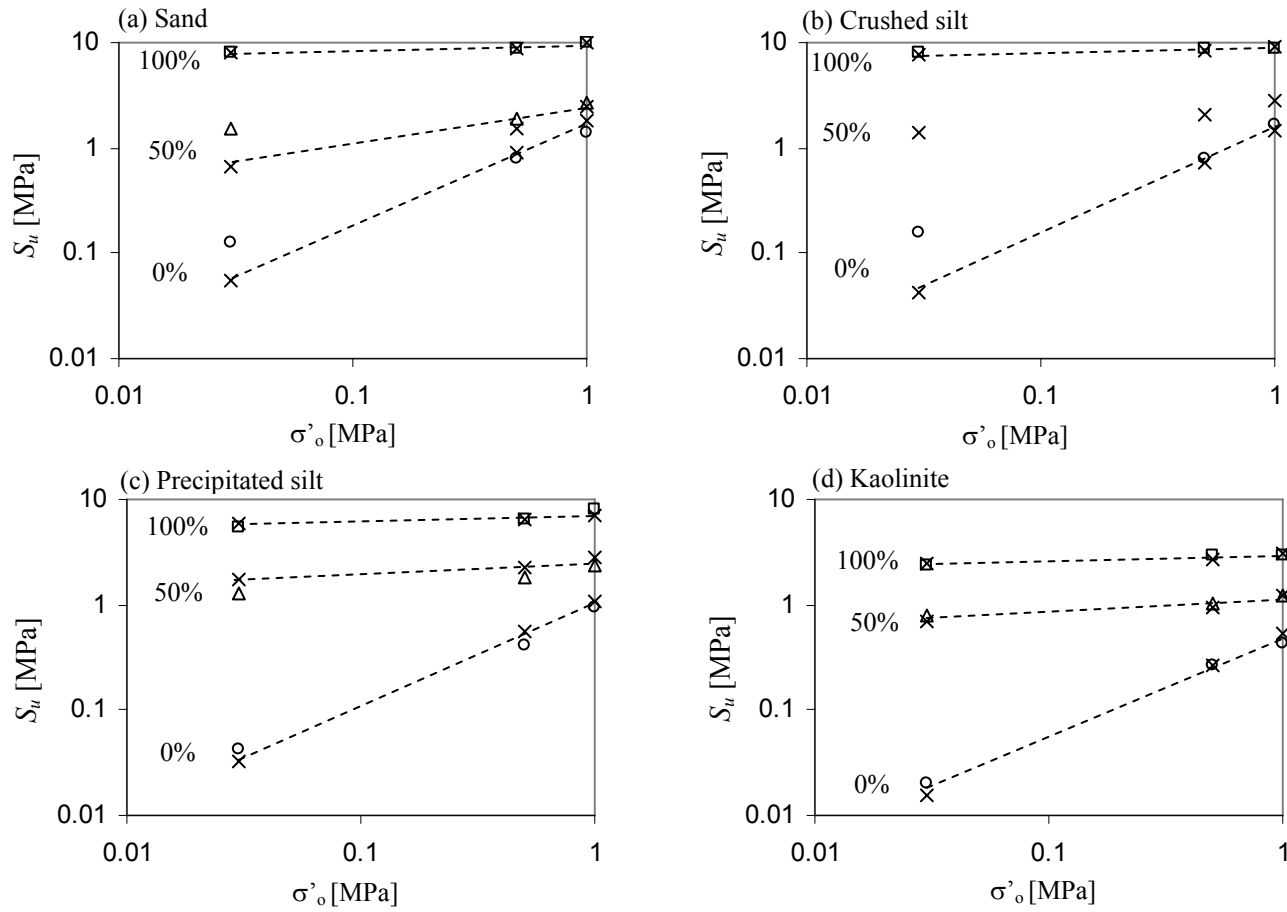


Figure 3.13 Measured (symbol: o) and predicted (symbol: x) undrained shear strength.

3.5.4 Poisson's Ratio

The zero-volume change condition for saturated near surface soils implies a Poisson's ratio of $\nu=0.5$. However, when measurements are corrected for geometric effects, the estimated Poisson's ratios vary between ~ 0.05 and ~ 0.35 . The exact cause for these values remains unclear. It is anticipated that $\nu < 0.5$ values may reflect material behavior, such as: (1) contractile tendency magnified at large stress, (2) cemented skeleton in the presence of hydrates, (3) unsaturation, and (4) the development of cavitation during shear. In addition, $\nu < 0.5$ values may also be the results of measurement difficulties associated with: (1) membrane penetration in coarser materials and its effects on measured lateral strains ε_r , (2) shear band formation and its effects on measured lateral strains ε_r at large strains as specimens approach peak strength, and (3) seating effects which would affect the measured axial strains ε_a at low strain levels.

Nevertheless, the evolution of lateral strain ε_r versus axial strain ε_a shows characteristic trends that reflect soil type, confinement and hydrate content. Summary plots for all tested soils are presented in Figure 3.14. The following observations can be made:

- The evolution of lateral strains is similar for soils with similar hydrate concentration, regardless of confining stress.
- The lateral strain evolution is similar in crushed silt and sand, it is independent of hydrate concentration in precipitated silt, and it is affected more by hydrate concentration than by confinement in kaolinite.

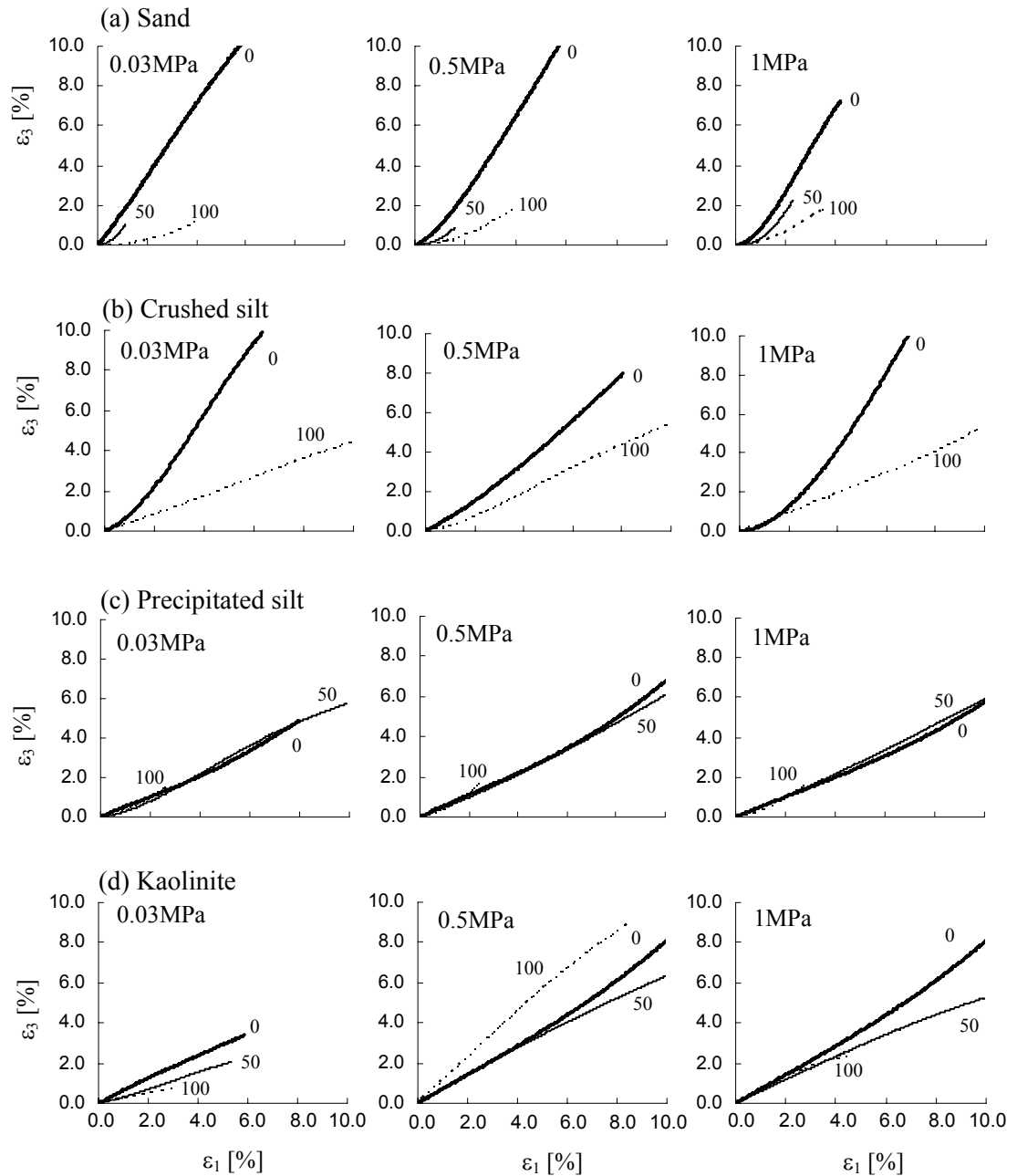


Figure 3.14 Lateral strain versus axial strain for tested specimens with different hydrate concentration, and subjected to various confining stresses. The thick solid line is 0% hydrate-bearing sediment, thin solid line denotes 50% hydrate-bearing sediments, and dotted line presents 100% hydrate-bearing sediments.

- Lateral strains manifest at higher axial strains with increasing hydrate concentration.
- Note that strain localization leads to either no lateral strain (if the sensing band is not across a shear band) or constant slope (when the sensing band is across a shear band).

These trends capture the competing effects between increased contractive behavior with increased confinement and increased dilative trend with increased hydrate content: (1) specimens without hydrates become less dilative as σ'_c increases; (2) sand specimens with hydrates (50% and 100%) exhibit low lateral strains and they are independent of the confining pressure at intermediate axial strains.

3.5.5 *Micro-Mechanism of Shear Strength and Failure*

$E_{tan} = \Delta\sigma_d / \Delta\varepsilon_a$ is computed along the load-deformation for each specimen. The computed value is normalized by the initial confinement (E/σ'_o) and plotted versus axial strain ε_a in Figure 3.15. Specimens with the same hydrate concentration show similar stiffness evolution for a given soil, and confining pressure has almost no effect. Hydrate bearing sediments tend to exhibit a sudden drop in E_{tan} (except kaolinite) while specimens without hydrate show a gradual decrease axial strain. The 100% hydrate bearing sand and crushed silt specimens show two yield points. The first yield point may correspond to the hydrate-particle debonding, while the second one is considered to indicate the global structural collapse of the soil-hydrate structure. Strain localization could begin at the first yield point (Ting, 1983; Lo et al., 2003). The 100% hydrate bearing precipitated silt specimens show only one yield point, and there is no clear yield

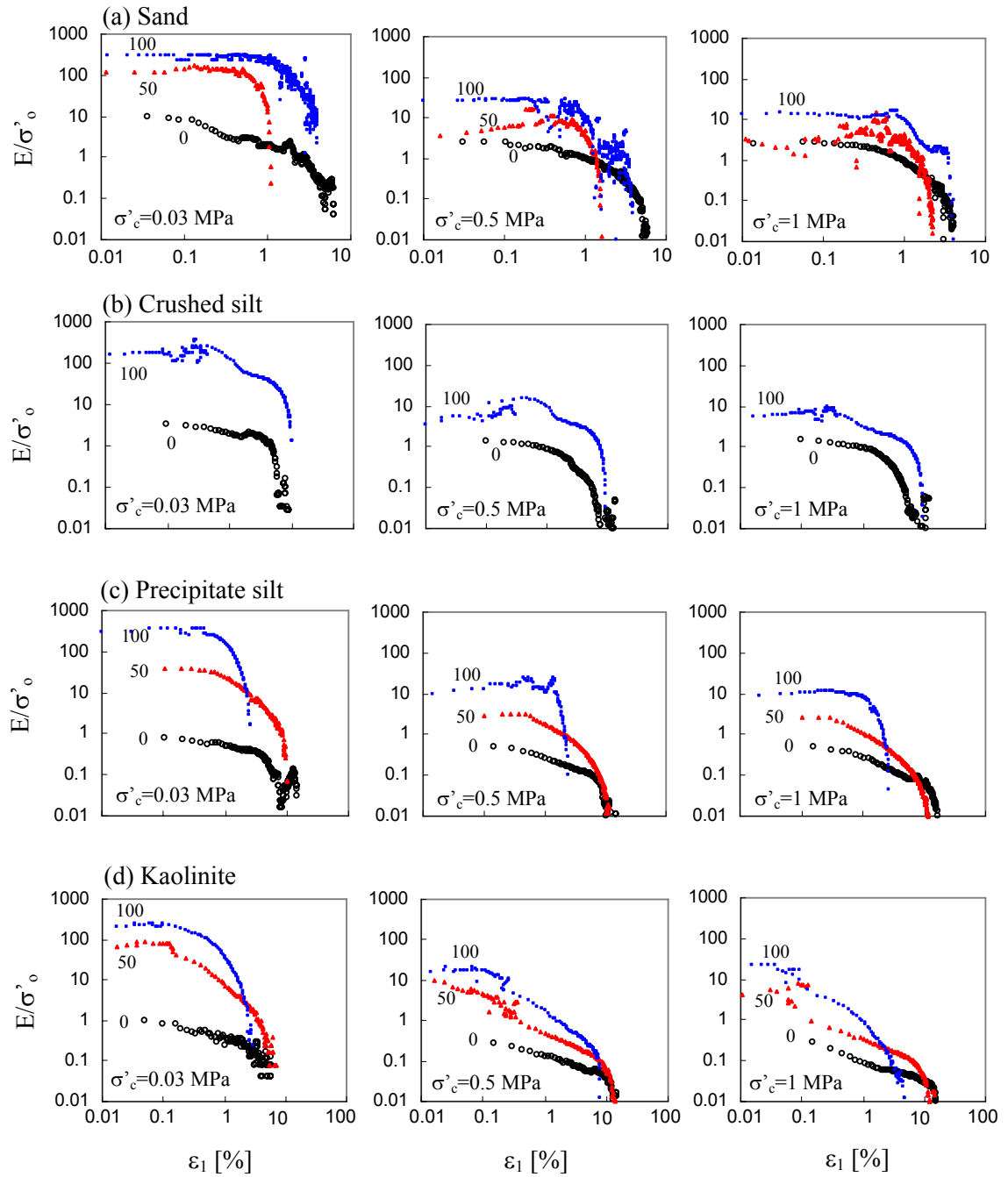


Figure 3.15 Tangential stiffness normalized by the confining pressure σ'_0 versus axial strain. The number 0, 50 and 100 represents the hydrate fraction in pore space. The arrow in each plot indicates the noticeable stiffness loss.

point in kaolinite specimens. Therefore, it appears that high specific surface soils do not present the yield point.

3.6 DISCUSSION

Shear wave velocity measurements indicate that hydrate tends to nucleate in the pore space (most likely on the grain surface) and to grow towards the pore space causing no significant change in V_s until hydrate concentration exceeds $S_{hyd} \sim 45\%$ (Yun et al., 2005). Strength exhibits a similar evolution with hydrate concentration (Figure 3.16): there is a decisive increase in strength when $S_{hyd} > \sim 45\%$.

Micro-mechanisms for shear strength at different hydrate concentration are hypothesized in this study. Figure 3.17 shows possible particle-level mechanisms that may explain the role of hydrates on sediment strength. In the absence of hydrates, $S_{hyd} \sim 0\%$, shear causes the rotation and rearrangement of particles; rotational frustration is overcome by dilation or slippage. At low hydrate concentration, $S_{hyd} < 45\%$, hydrate crystals may shear, detach or interfere with rotation, and cause minor increase in sediment strength; the extent of this effect depends on the hydrate-particle bonding strength, the hydrate strength and hydrate concentration. At high hydrate concentration, $S_{hyd} > 45\%$, the cementing strength provided by the hydrate mass and the bonding between particles and hydrates govern deformation and strength response. A shear plane develops through the hydrate mass when the hydrate strength (τ_{hyd}) is smaller than the hydrate-grain bonding strength (τ_{hbs}); in this case, τ_{hyd} dominates the overall strength evolution. On the other hand, failure occurs along the hydrate-particle interface when the

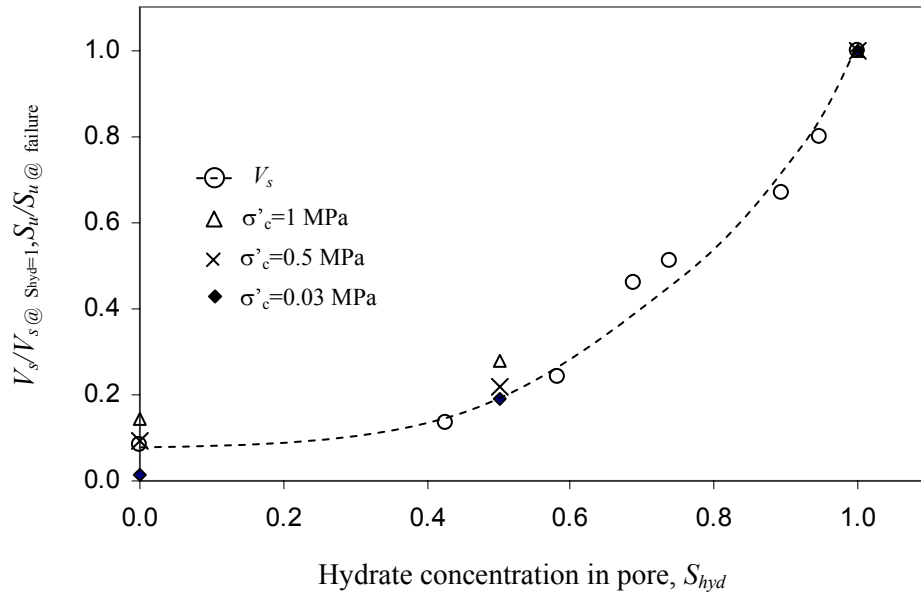


Figure 3.16 Hydrate concentration versus normalized shear wave velocity (trend from Yun et al., 2005) and shear strength.

hydrate strength (τ_{hyd}) is greater than than the hydrate-grain bonding strength (τ_{hbs}); this case is more likely when smooth particles or high specific surface soils are involved. In all cases, the presence of hydrate promotes enhanced dilation.

From this analysis, it is concluded that extending experimental results gathered with THF hydrate to methane hydrate depends on hydrate and bonding strengths. Only part of this information is currently available: the strength of THF hydrate varies between 3-to-44MPa and for methane hydrate varies between 16-to-102MPa depending on temperature, confining pressure and strain rate (Ohmura et al., 2002).

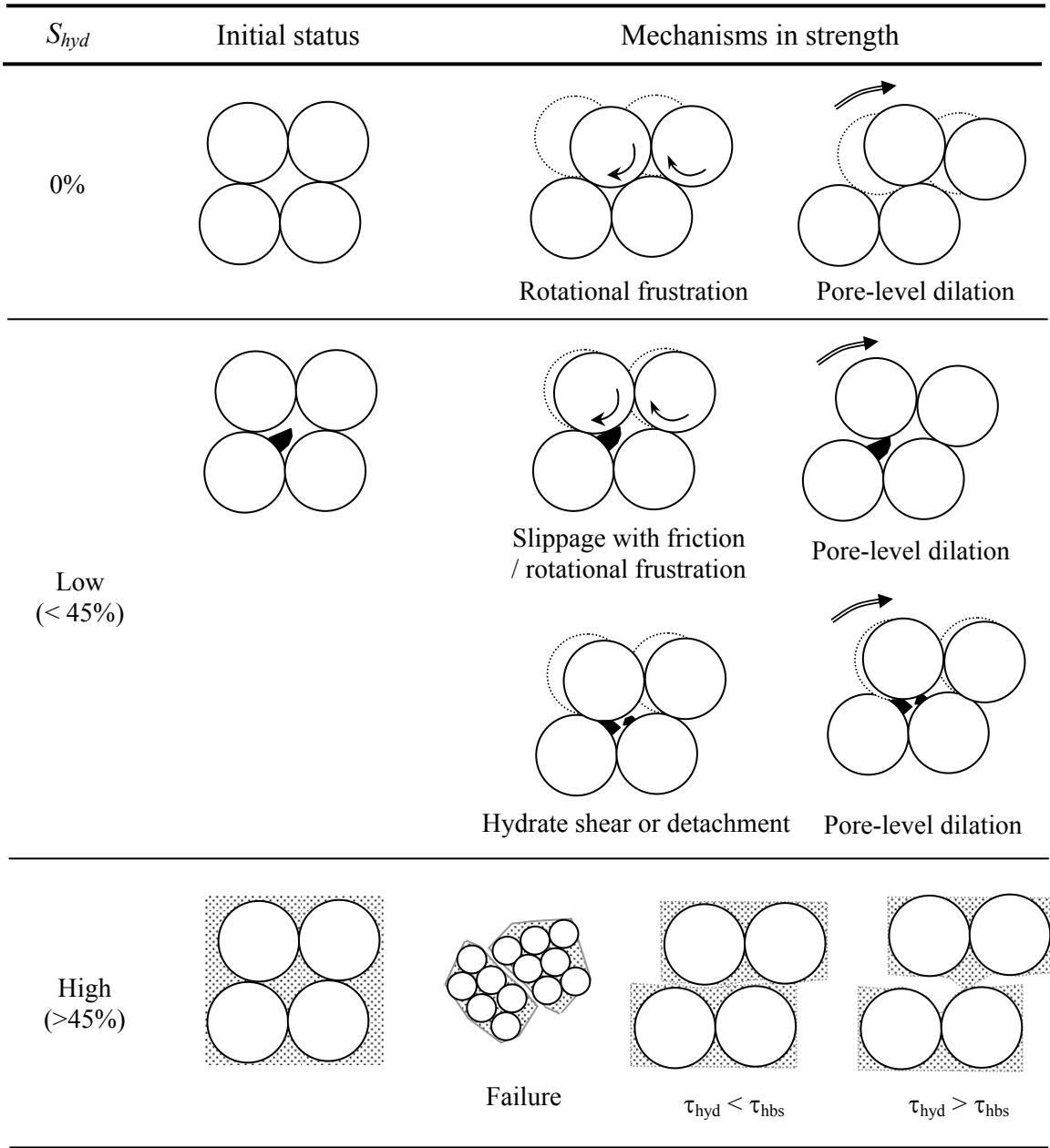


Figure 3.17 Possible particle-level mechanisms involved in the shear strength of hydrate bearing sediments.

3.7 CONCLUSIONS

- Soil type, confining pressure and hydrate concentration in the pore space determine the deformation, the failure behavior and the strength of THF hydrate bearing sediments.
- Hydrate bearing sediments have high intermediate strain stiffness and the quasi-elastic behavior extends to higher strain levels as the confining pressure increases. As the hydrate concentration increases above $S_{hyd} \sim 45\%$, the stress-strain response becomes less sensitive to the confining pressure.
- The undrained shear strength and elastic stiffness increase as hydrate concentration increases.
- Lateral strain evolution mainly depends on the hydrate concentration rather than confining pressure. Hydrate bearing specimens are less dilative at the global scale than specimens without hydrate.
- Two yield points are identified in coarse-grained soils (sand and crushed silts) and high hydrate-filled porosity. It is hypothesized that hydrate-grain debonding marks the first yield point, while the structural collapse of the soil-hydrate structure determines the second yield point.
- The shear strength of hydrate bearing sediments evolves depending on the hydrate concentration in pore space, the hydrate strength, the hydrate-particle bond strength and confining pressure. Possible particle-level mechanisms include interference in particle rotation, enhanced pore-level dilation, hydrate-particle debonding, and hydrate shear.

CHAPTER IV

MICRO-SCALE STUDY OF HEAT TRANSFER IN PARTICULATE MATERIALS

4.1 INTRODUCTION

The internal structure of the earth consists of a hot core (3000-5000°C); more than 95% of the earth's volume is at a temperature higher than 1000°C. This great geothermal dynamo has determined the geological history of the earth. Heat flux in oceans and climate change are macro-scale manifestations of geothermal phenomena. Geotechnical engineering examples include thermal stabilization, foundation effects in permafrost regions, geothermal energy resources, thermal storage, radioactive waste disposal, pavements in extreme climates and methane hydrates (Miller, D. L. 1985; Joshi et al., 1994; Singh and Devid, 2000).

Scientific studies on temperature, thermal properties and thermal phenomena date back to Galileo (1564-1642) who devised the thermoscope to measure temperature changes. Issac Newton (1642-1727) suggested the scaling of temperature from the freezing temperature of water to the temperature of the human body. Anders Celcius (1701-1744) established the celcius temperature scale and the absolute temperature was introduced by William Thompson (1824-1907). Issac Newton observed that the rate of heat loss relates to the temperature difference between the body and its surroundings, Joseph Fourier (1768-1830) postulated that the rate of heat transfer is proportional to the temperature gradient through the '*thermal conductivity*'. Joseph Stefan (1835-1893)

discovered radiation, which was later analyzed by Ludwig Boltzmann (1844-1906) resulting in the *Stefan-Boltzmann Law*.

The formation and stability of gas hydrate bearing soils are controlled by the sensitivity of gas hydrate to temperature. Drilling operation into the seafloor and pipelines in cold regions create a thermal gradient near gas hydrate bearing sediments, which could result in hydrate dissociation and sediment instability (Hovland and Gudmestad, 2001).

The thermal conductivity k of the different soil components varies across two order of magnitude: $k_{mineral} \gg 3 \text{ W}\cdot\text{m}^{-1}\cdot\text{K}^{-1}$, $k_{water} = 0.56 \text{ W}\cdot\text{m}^{-1}\cdot\text{K}^{-1}$ and $k_{air} = 0.026 \text{ W}\cdot\text{m}^{-1}\cdot\text{K}^{-1}$. While the thermal conductivity of minerals is high, the thermal conductivity of the dry soil skeleton is typically $k_{soil} < 0.5 \text{ W}\cdot\text{m}^{-1}\cdot\text{K}^{-1}$ depending on mineral composition and packing density. The ordered sequence of thermal conductivity for saturated soils is typically $k_{air} < k_{dry-soil} < k_{water} < k_{saturated soil} < k_{mineral}$. These observations suggest that the main heat transfer path in soils is through contacts and the pore fluid (Carslaw and Jaeger, 1959; Murashov and White, 2000).

The purpose of this study is to explore particle-level mechanisms that govern heat transfer in particulate materials. The manuscript begins with a literature review on heat transfer in soils, followed by particle-level and macro-scale experimental and numerical results.

4.2 LITERATURE REVIEW

Energy flow is driven by hydraulic, chemical, electrical and thermal gradients. The heat flux q in steady state is proportional to the thermal gradient by the coefficient of thermal conductivity k , according to Fourier's law: $q=k \cdot (dT/dx)$. The rate of heat transfer in transient conditions is equal to the heat stored within the medium and the rate of internal heat generation.

$$\frac{d}{dx}q = q_{generated} - q_{stored} \quad (4.1)$$

The heat stored in the material is

$$q_{stored} = \rho \cdot c \cdot \frac{\partial T}{\partial t} \quad (4.2)$$

where ρ is the material mass density and c is heat capacity. Combining the above equations,

$$\frac{\partial^2 T}{\partial x^2} = \frac{1}{k} q_{generated} - \frac{\rho \cdot c}{k} \cdot \frac{\partial T}{\partial t} \quad (4.3)$$

If there is no heat generation within the material, the first term on the right hand-side vanishes and

$$\frac{\partial^2 T}{\partial x^2} = -\frac{1}{D} \cdot \frac{\partial T}{\partial t} \quad (4.4)$$

where $D = k/(\rho \cdot c)$ is thermal diffusivity of the material (Note that the sign in Equation 4.4 depends upon the direction of heat flow).

Table 4.1 summarizes values for the thermal conductivity, diffusivity and heat capacity of soils and soil components. The governing particle-level and macroscale factors that determine the thermal behavior of soils are compiled in Table 4.2. The relevance of interparticle contacts and water content is highlighted.

There are three heat transfer mechanisms in a medium: conduction prevails in solids, convection in fluids, and radiation does not require a material medium. The solid contact is the most effective way to transfer heat in dry particulate materials, while conduction through the gas phase and radiation have minute effects (Carslaw and Jaeger, 1959; Murashov and White, 2000). On the other hand, heat transfer by convection becomes effective if the particle size D_{50} is larger than ~ 6 mm permitting fluid currents in pores and through the porous network (Thalmann, 1950).

There are several soil thermal conductivity data sets. These have supported the development of empirical correlation that is summarized in Table 4.3. In addition, mixture models have been developed to predict the thermal properties of soil-fluid mixtures (Tarnawski et al., 2002; Gori and Corasaniti, 2004); these are summarized in Table 4.4. The theoretical prediction of thermal conductivity requires detailed knowledge of the mixture geometry, the properties of each phase and the volumetric fractions. In general, theoretical mixture models predict higher conductivity values than measured values. This is attributed to restricted heat transfer through interparticle contacts; the concept of a “contact heat resistance” is often argued (Tarnawski et al., 2002; Kumlutas et al., 2003; Song and Chen, 2004). Heat transfer between particles is addressed in the following section.

Table 4.1 Thermal properties of materials.

Material	Density [kg·m ⁻³]	Heat capacity [kJ·kg ⁻¹ ·K ⁻¹]	Thermal conductivity [W·m ⁻¹ ·K ⁻¹]	Thermal diffusivity [m ² ·s ⁻¹] × 10 ⁻⁷		
Air – 10°C	1.25	1.00	0.026	0.21		
Water	999.87	4.2	0.56	1.4		
THF (25°C)	890	1.72	0.6	3.92		
Ice (-10°C)	900	2.09	2.25	11.2		
CH ₄ hydrate	910	2.07	0.5	2.654		
THF hydrate	~910	2.07	0.53	2.814		
Soil	Clay	Dry	1700	0.92	0.9	5.754
		Saturated			0.6~2.5	
	Sand	Dry	2000	0.80	1.1	6.875
		saturated			2~4	
Mineral	quartz	2660	0.733	8.4	43.08	
	Mica	2883	0.88	0.75	2.956	
Aluminum bronze (630)	7584	0.38	39.1	136.8		
Wood	780	1.75	0.04 ~ 0.15	0.293 ~ 1.1		
Metal Patch			2.3012			

source: <http://www.jukseflux.com>; Becker et al., 1992; Andersland and Ladanyi, 2004.

Table 4.2 Governing factors controlling thermal conductivity of soils.

Factors	Features
Mineralogy	<ul style="list-style-type: none"> ▪ Thermal conductivity of quartz > feldspar and mica (Gangadhara Rao and Singh, 1999; Tarnawski et al., 2002)
Particle size	<ul style="list-style-type: none"> ▪ Heat flux between particles is proportional to the radius of particle and reciprocal to the contact distance (numerical solution in Batchelor and O'Brien, 1977). ▪ Larger particles and fewer contacts in a given volume result in higher thermal conductivity (Aduba, 1996; Gangadhara Rao and Singh, 1999).
Packing geometry	<ul style="list-style-type: none"> ▪ Higher interparticle coordination increases the thermal conductivity for a given particle size (Tarnawski et al., 2002). ▪ The contact conductance is more important than the radiational conductance (Lambert and Fletcher, 1997-a, b). ▪ The thermal conduction at contacts results in percolation-type conduction process (Sahimi and Tsotsis, 1997).
Applied pressure	<ul style="list-style-type: none"> ▪ Heat flux increases with contact radius; therefore k increases with load. (Batchelor and O'Brien, 1977; Sridhar and Yovanovich, 1996; Lambert and Fletcher, 1997-b; Vargas and McCarthy, 2001). Contact orientation affects thermal conductance. ▪ Granular chains in particulate materials determine heat transfer (Vargas and McCarthy, 2001): $H = a \cdot k_{solid} \cdot \left[\frac{F_n}{E^*} \right]^{1/3}$ <p>where H is heat flux, k_{solid} is thermal conductivity of solid material (mineral), F_n is the normal force on contacts and E^* is the effective stiffness of two particles.</p>

Table 4.2 Continued.

Factors	Features
Water content	<ul style="list-style-type: none"> ▪ Adding small amount of water dramatically improves the thermal conduction (Singh and Devid, 2000). ▪ On the other hand, the thermal conductivity in partially saturated soils increases with water content suggesting the important role of pore fluid conduction (Farouki, 1985; Andersland and Layandi, 2004; Singh and Devid, 2000).
Density / Gradation	<ul style="list-style-type: none"> ▪ The lower the void ratio the higher the thermal conductivity. ▪ Well-graded soils exhibit higher heat transfer since smaller particles fill the interstitial pore and increasing interparticle coordination (Esch, 2004)
Particle size	<ul style="list-style-type: none"> ▪ Thermal conductivity is proportional to the particle size (Gangadhara Rao and Singh, 1999). ▪ Soils with flat surface present high thermal conduction by large interparticle contact area (Becker et al., 1992).
Cementation	<ul style="list-style-type: none"> ▪ Cement and colloids precipitated at particle contacts increase the thermal conductivity (Tarnawski et al., 2002).

Table 4.3 Empirical methods to estimate the thermal conductivity of soils.

Empirical correlations	
	<ul style="list-style-type: none"> Correlation with particle size, saturation, and particle conductivity. $k = (k_{sat} - k_{dry})K_e + k_{dry}$
Johansen's correlation (1975)*	<p>K_e = Kersten number. Each parameter has its own empirical relations (see Andersland and Ladanyi, 2004 for details)</p> <ul style="list-style-type: none"> $k_{dry} (W / m \cdot K) = \frac{0.137\rho_d + 64.7}{2700 - 0.947 \cdot \rho_d} \pm 20\%$ $k_{dry} (W / m \cdot K) = 0.039n^{-2.2} \pm 25\%$ for crushed rock materials
Becker et al., (1992)	<ul style="list-style-type: none"> Correlation with saturation. $S = \lambda_1 [\sinh(\lambda_2 k + \lambda_3) - \sinh(\lambda_4)]$ <p>S = saturation. k = thermal conductivity (Btu·in/ft²·hr·°F)</p> <p>$\lambda_1 \sim \lambda_4$ = coefficients fitted. <ul style="list-style-type: none"> k linearly increases with dry density. </p>
Esch (2004)	$k_{dry} = 0.025 + 0.238\gamma_d - 0.193\gamma_d^2 + 0.114\gamma_d^3$ for mineral / organic soil <p>γ_d = dry density (< 2g/cm³)</p>

*: summarized in Andersland and Ladanyi (2004)

Table 4.4 Theoretical thermal conductivity mixture models.

Effective thermal conductivity	Model
$\frac{1}{k_{eff}} = \frac{\phi}{k_a} + \frac{1-\phi}{k_m}$	Series type – Ruess (1929)
$k_{eff} = \phi \cdot k_a + (1-\phi) \cdot k_m$	Parallel – Voigt (1910)
$k_{eff} = k_a^\phi \cdot k_m^{1-\phi}$	Geometric Mean Method Kumlutas (2003)
$k_{eff} = k_{sc} \left[1 - \frac{3 \cdot \phi(1-A)}{2 + A + \phi(1-A)} \right] \quad A = \frac{k_{fc}}{k_{sc}}$	Nimick and Leith (1992)
k_{fc} and k_{sc} are Hashin and Shtrikman's upper and lower bound.	
$k_{eff} = \frac{1}{3} \left[\frac{1-\phi}{2k_{eff} + k_m} + \frac{\phi}{2k_{eff} + k_a} \right]^{-1}$	Self Consistent Method Tarnawski and Leong (2000)
$k_{eff} = k_m \cdot \frac{1 + a \cdot B \cdot \phi}{1 - B \cdot \phi \cdot \psi}$	Kumlutas (2003)
$B = \frac{k_a / k_m - 1}{k_a / k_m + a}, \quad \psi = 1 + \left(\frac{1 - \phi_m}{\phi_m^2} \right) \cdot \phi$	
a and ϕ_m are particle shape and packing parameters.	
$\frac{1}{k_{eff}} = \frac{\beta - 1}{k_a \cdot \beta} + \frac{\beta}{k_a \cdot (\beta^2 - 1) + k_m}, \quad \beta = \frac{1}{1-\phi}^{1/3} \text{ for dry soil}$	Cubic Cell Model Gori and Corasaniti (2004)
$k_{eff} = k_m + \frac{\phi}{\frac{1}{k_a - k_m} + \frac{1-\phi}{3k_m}} : \text{Upper bound}$	Hashin and Shtrikman bounds (1962)
$k_{eff} = k_a + \frac{1-\phi}{\frac{1}{k_m - k_a} + \frac{1-\phi}{3k_a}} : \text{Lower bound}$	

ϕ : porosity, k_a : thermal conductivity of air, k_m : mineral thermal conductivity.

4.3 HEAT TRANSFER BETWEEN TWO PARTICLES - CONTACT LEVEL

A numerical simulation and complementary experimental study of heat transfer through contacts are documented in this section.

4.3.1 Numerical Simulation

The two-dimensional numerical simulation of contacts between “cylinders” is implemented using the following form of the thermal diffusion equation

$$\frac{\partial T}{\partial t} = D \left(\frac{\partial^2 T}{\partial x^2} + \frac{\partial^2 T}{\partial y^2} \right) \quad (4.5)$$

In finite differences, and assuming that $\Delta x = \Delta y$, Equation 4.5 becomes

$$T_{i,j}^{t+1} = M \cdot T_{i+1,j}^t + M \cdot T_{i-1,j}^t + (1 - 4M) \cdot T_{i,j}^t + M \cdot T_{i,j+1}^t + M \cdot T_{i,j-1}^t \quad (4.6)$$

where $M = D \cdot \Delta t / (\Delta x)^2$. Three cases are simulated: 1) particles surrounded by air, 2) particles with a water meniscus at the contact and 3) particles surrounded by water. The particle geometry and boundaries are pre-defined for the three cases (Figure 4.1). The value of M at boundaries is taken as a local average, i.e., the adopted diffusion coefficient D is the average of D for the two media in the explicit scheme for nonlinear diffusion problem (see Press et al., 1992). A constant high temperature boundary is assumed at the equatorial plane of the lower particle.

The evolution of the heat front is shown in Figure 4.2. As heat flows from the lower boundary, it reaches the particle contact in a similar fashion in all three cases (~4 sec for a 12.7mm radius metal particle), and the isothermal front closely delineates the particle

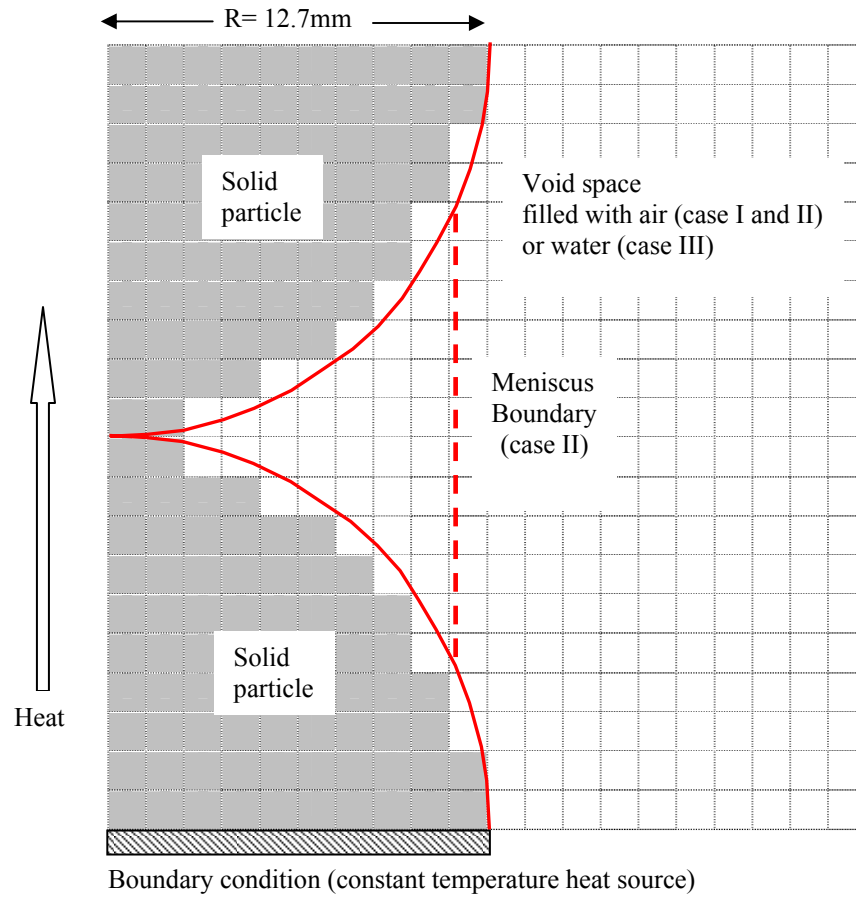


Figure 4.1 FDM modeling condition. The shadowed and white region stand for the solid particle and pore space.

geometry. Thereafter, heat transfer is much more effective when water is present (case II and III) than in the dry system (case I). In the three cases, the particle contact is the primary path for heat transfer. The presence of water at the contact plays a critical role bridging the gap between the two particles and reducing the contact resistance.

The temperature field along the particle axis is plotted in Figure 4.3 at different times (solid lines). In addition, the temperature evolution in an infinite solid block is

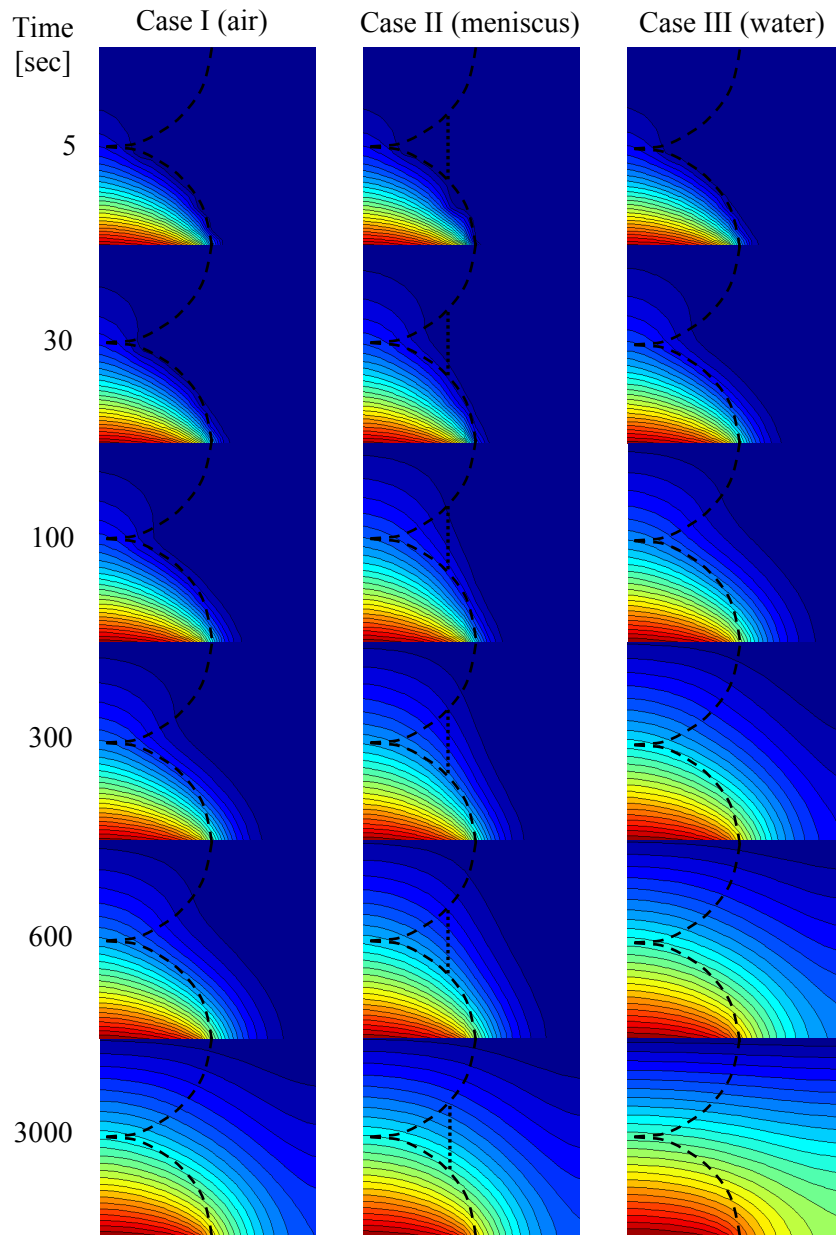


Figure 4.2 Numerical study: heat evolution for different particle contact conditions. Case I: air in void space. Case II: air in void space and water meniscus at contact. Case III: water in void space.

shown for comparison. The retardation effect of particle contacts is highlighted at early times. Eventually all cases evolve toward the same temperature field.

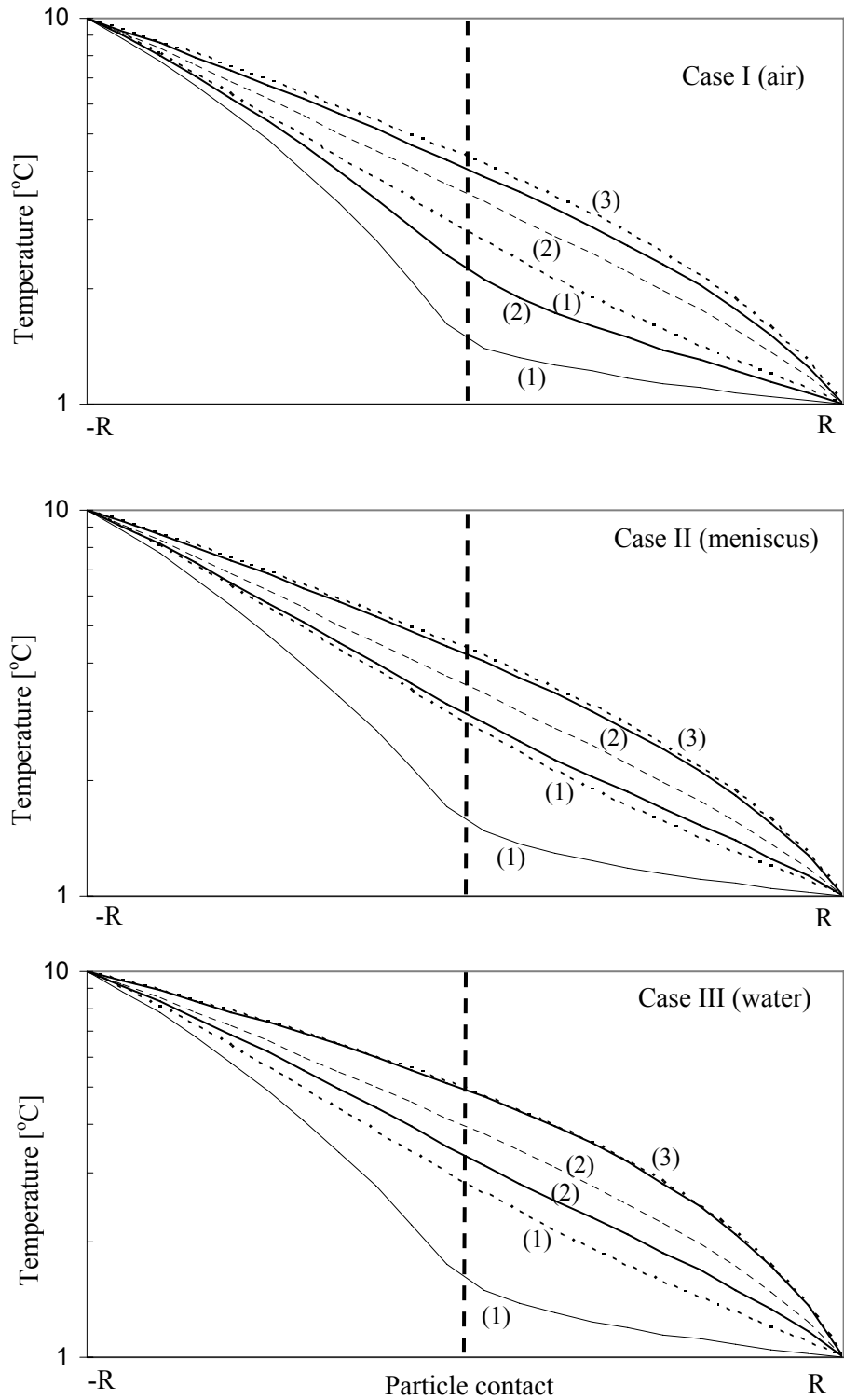


Figure 4.3 Temperature evolution with particle geometry. The continuous lines correspond to the granular case simulated in Figure 4.2. The dotted line is for an infinite solid medium (1: $t=6\text{sec}$, 2: $t=150\text{sec}$, 3: $t=3000\text{sec}$).

4.3.2 *Experimental Study: Infrared Imaging*

A series of three spherical particles (aluminum bronze alloy – 25.4 mm diameter) are coated with black paint to monitor the surface temperature evolution by black body radiation using an infrared camera (Delta therm 1400, Stress Photonics Inc.). The temperature at the center of each particle is monitored with thermocouples. The test begins when a constant temperature $T_o \cong 100$ °C heat source is brought into contact with the bottom sphere. Infrared images are sequentially taken with time.

Figure 4.4 shows the evolution of internal temperature with time for the three particles. The bottom particle that contacts the heat source exhibits the earliest temperature increase while the middle and top particles experience a lower rate. The higher the particle is, the lower the final temperature is due to radiation loss.

4.3.3 *Observations*

Numerical simulation results and infrared images show that heat transfer in particulate materials involves:

- transport through interparticle contacts; in fact, isothermal lines inside the particle are “centered” at the contact.
- transport through liquids near contacts.
- heat loss observed in the IR study (lower steady state temperature away from lower particle) indicates that there is surface radiation driven by the temperature gradient between the particle and the medium.

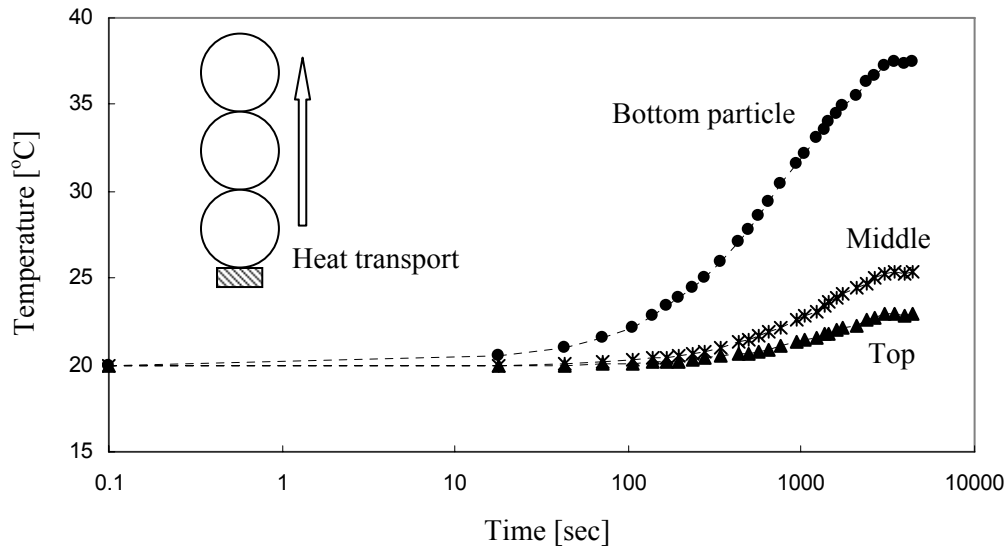


Figure 4.4 Internal temperature evolution at the center of the three particles measured with thermocouples. The series of particles are heated at the bottom.

Therefore, the increase in contact area by loading or moisture will cause higher thermal conductivity in the medium.

4.4 THERMAL CONDUCTION IN A 1-D GRANULAR CHAIN - CHAIN LEVEL

An experimental study is designed to extend prior observations to a long column of spherical metal particles to simulate an “equivalent 1-D” column. The experimental study is complemented with an equivalent 1D continuum analysis.

4.4.1 *Experimental Design*

The test configuration is shown in Figure 4.5. The 15 aluminum-bronze spheres (Alloy 630- 25.4 mm diameter, $k=39.1 \text{ W}\cdot\text{m}^{-1}\cdot\text{K}^{-1}$, $D=136.8\cdot 10^{-7} \text{ m}^2/\text{sec}$) are vertically

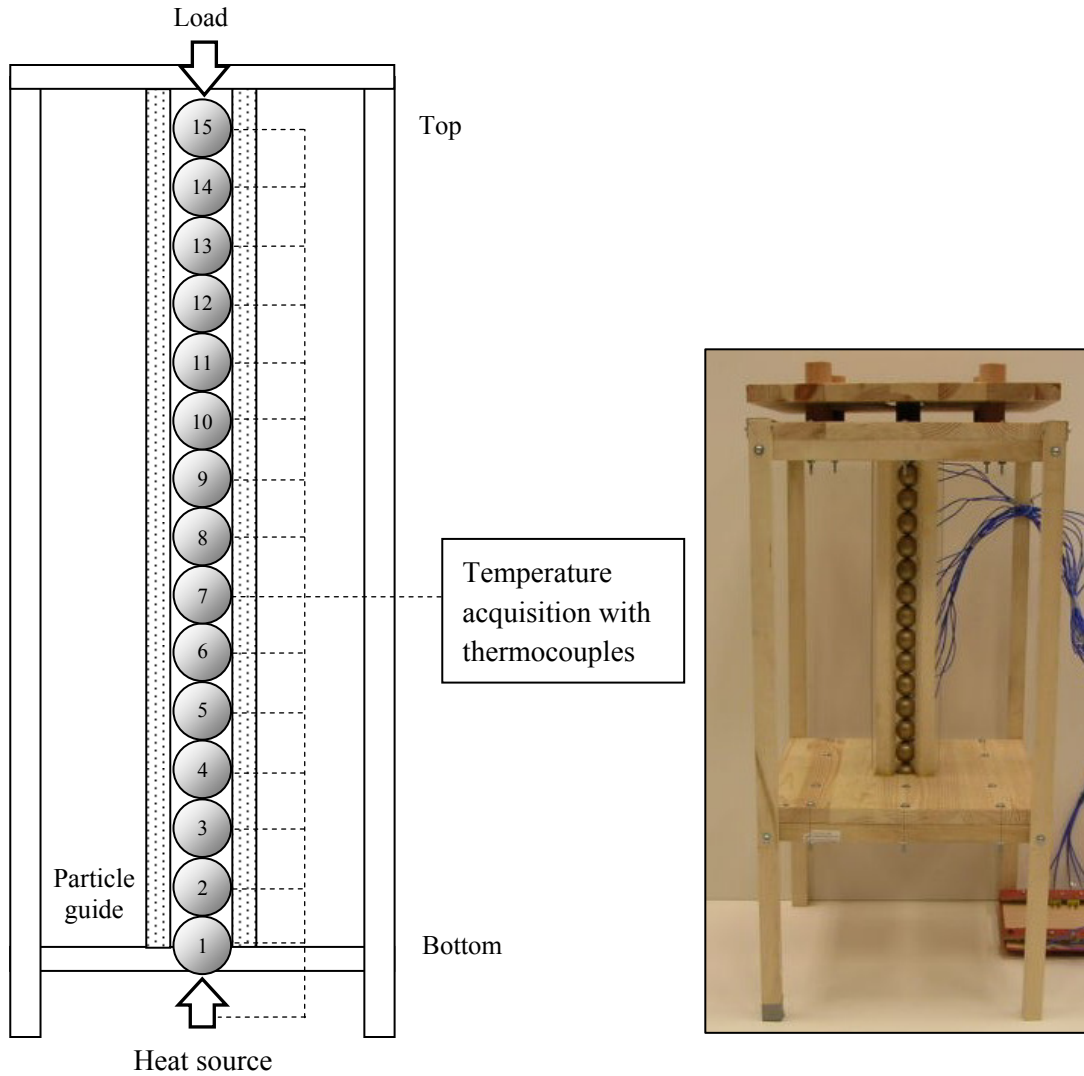


Figure 4.5 Heat transfer in a granular chain - Test design. The core temperature in each particle is monitored while the heat is applied from the bottom.

aligned within a wooden guide ($k=0.1 \text{ W}\cdot\text{m}^{-1}\cdot\text{K}^{-1}$, $D=0.5\cdot 10^{-7} \text{ m}^2/\text{sec}$). A heat source applies a constant temperature at the bottom. The source temperature ranges between 103°C and 107°C for all tests (room temperature $\sim 20^\circ\text{C}$). Each particle has a small perforation (1.8mm diameter) that permits mounting a thermocouple (TP-29, B&K Precision) to monitor the core temperature. Temperature values in the 15 particles and at

the source are logged every 10 seconds until the temperature reaches equilibrium. Figure 4.6 shows sketches of contact and boundary conditions for the 6 different tests performed as part of this study:

- *Reference column (O)*: Particles are vertically aligned without any contact modification or special boundary condition.
- *Contact Retardation (RO)*: A single sheet of filter paper (medium porosity) is placed between particles to hinder heat transfer at contacts.
- *Load (LO)*: A force of 160 N is applied at the top to improve interparticle contact coupling the equivalent effective stress is $\sim 30\text{kPa}$.
- *Load - Meniscus (LMO)*: The interparticle contact areas are purposely enlarged with metal patch (S-50, Devcon Inc., $k=2.3 \text{ W}\cdot\text{m}^{-1}\cdot\text{K}^{-1}$). A vertical force 160 N is applied as well.
- *Boundary Insulation (IO or LIO)*: The entire column is insulated with a foam sealant to reduce radiation and convection heat loss. Tests are repeated with and without load (160 N).

The temperature-time histories at selected particles (#2~9) are presented in Figure 4.7 for the 6 test configurations. The temperature of the bottom particle that is in direct contact with the heat source increases first followed by the upper particles. There is a time lag for each successive particle. The steady-state temperature reached by each particle does not converge to the same plateau and the equilibrium temperature decreases from the bottom to the top particle; this implies heat loss along the 1-D column.

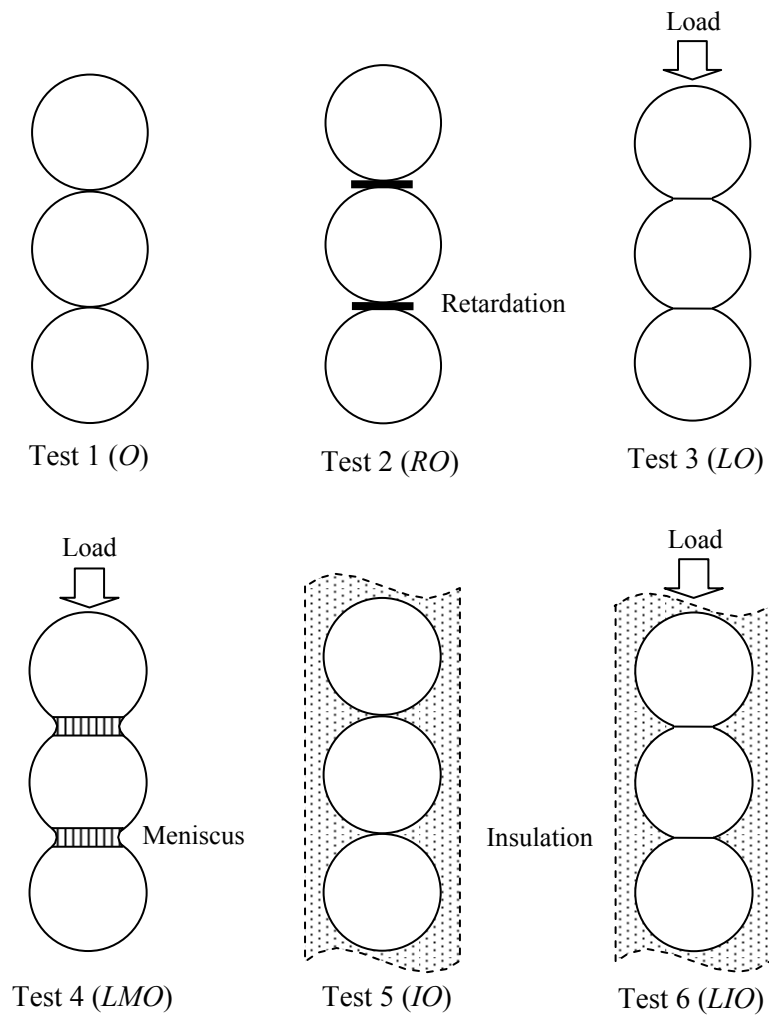


Figure 4.6 Particle column - Test conditions. The test name indicates: O-reference, R: retardation, L: load, M: meniscus, I: insulation.

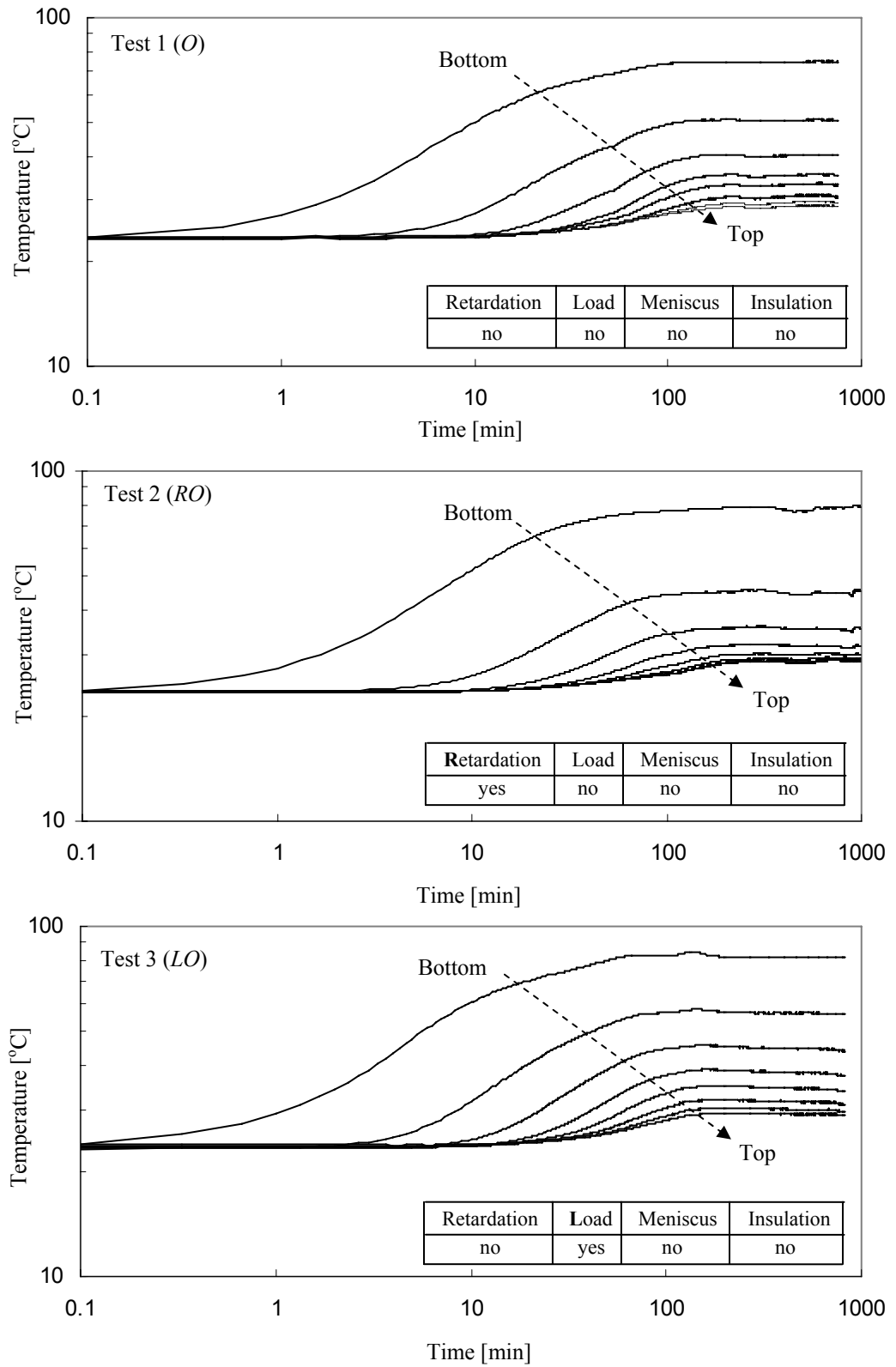


Figure 4.7 Temperature evolution with for particles #2~9.

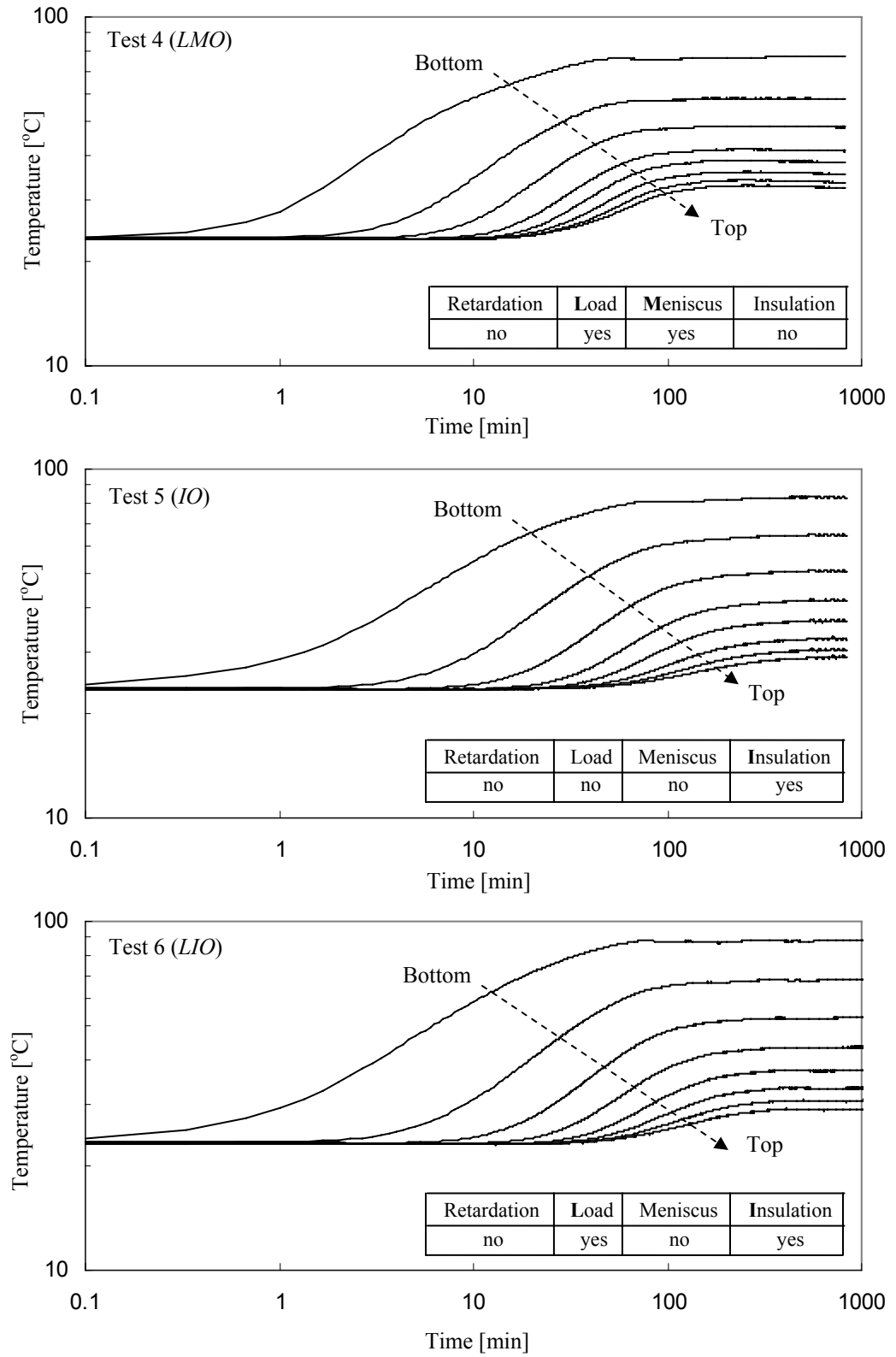


Figure 4.7 Continued.

Figure 4.8 compares temperature time histories for particles #2 and #4 under different test conditions arranged into two groups. Taking the results of test 1 as reference (*O: thick solid line*), the following observations can be made:

- *Group 1* (Figure 4.8-a): The paper at contacts hinders heat conduction. Thus, the initial temperature evolution of test 2 (*RO: dotted line*) is shifted to later time. Furthermore, radiation loss increases and the steady-state temperature is lower than in test 1. On the other hand, loading in test 3 (*LO: dashed line*) enhances thermal conduction due to increased contact area and contact improvement related to flattening of surface roughness; the equilibrium temperature is higher than in tests 1 and 2. Test 4 (*LMO: solid line*) shows faster and steeper thermal evolution, and higher equilibrium temperature as a result of the added metal meniscus. Therefore, particle contact conditions determine both the rate of heat transfer and the relevance of heat loss at equilibrium.
- *Group 2* (Figure 4.8-b): Convective air circulation and radiation heat losses are reduced in tests 5 and 6 by foam shielding. Heat loss reduction leads to increased conduction and higher equilibrium temperature. In addition, the normal load further promotes heat conduction in test 6 (*LIO: solid line*).

Heat loss and contact resistance have different affects on the measured time histories. Heat loss is solely responsible for lower equilibrium temperatures in test 6 (*LIO*) and test 3 (*LI*) in Figure 4.9. The particle contact condition determines the rate of transfer and is best detected in early stages of heating. For example, the temperature rise in test 4 (*LMO*) precedes that of test 6 (*LIO*) during transient conditions, while test 6 still has higher equilibrium temperature (Figure 4.9-b). Note that there is heat loss even in

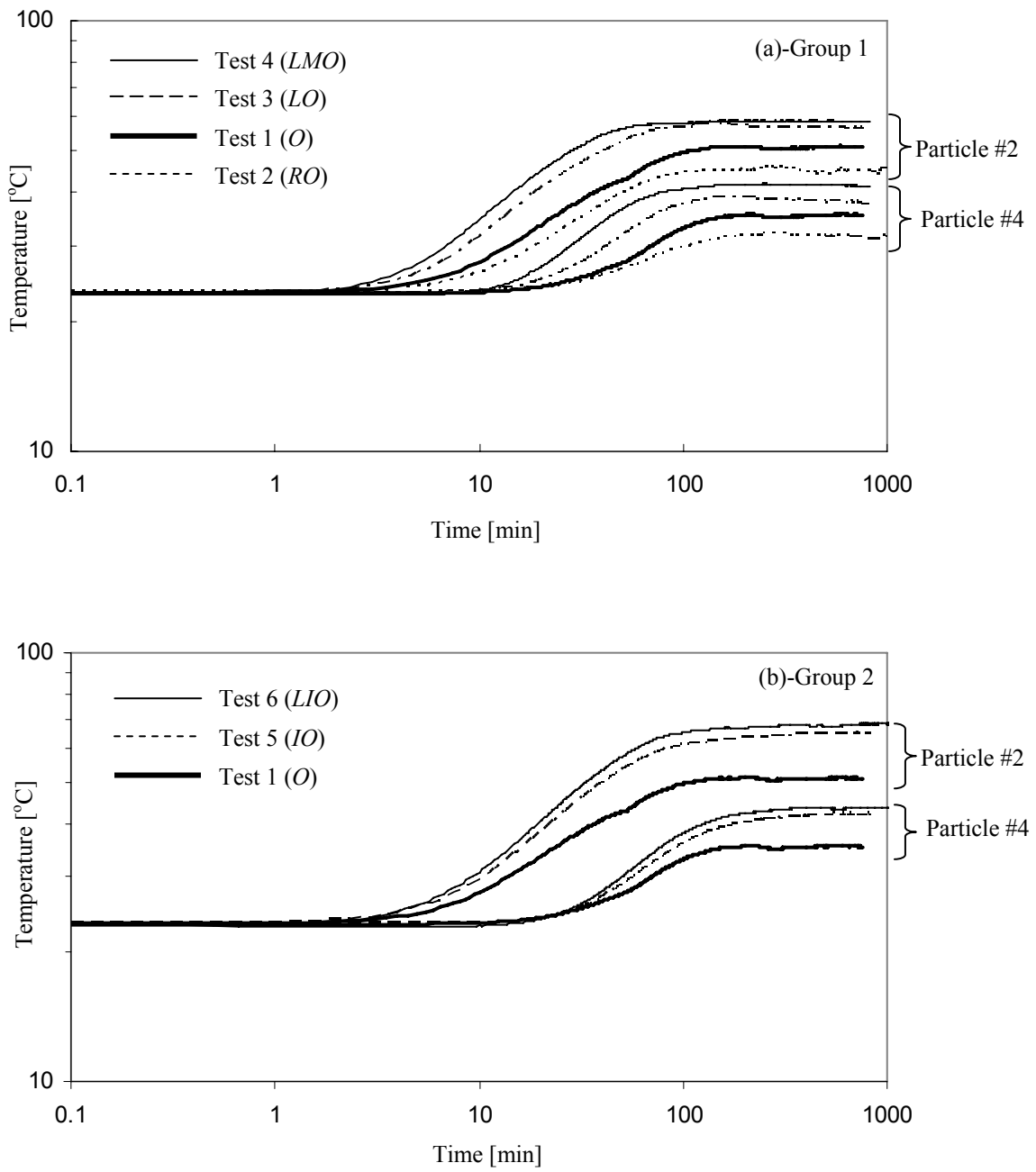


Figure 4.8 Time history comparison – Heat transfer under different contact and boundary conditions.

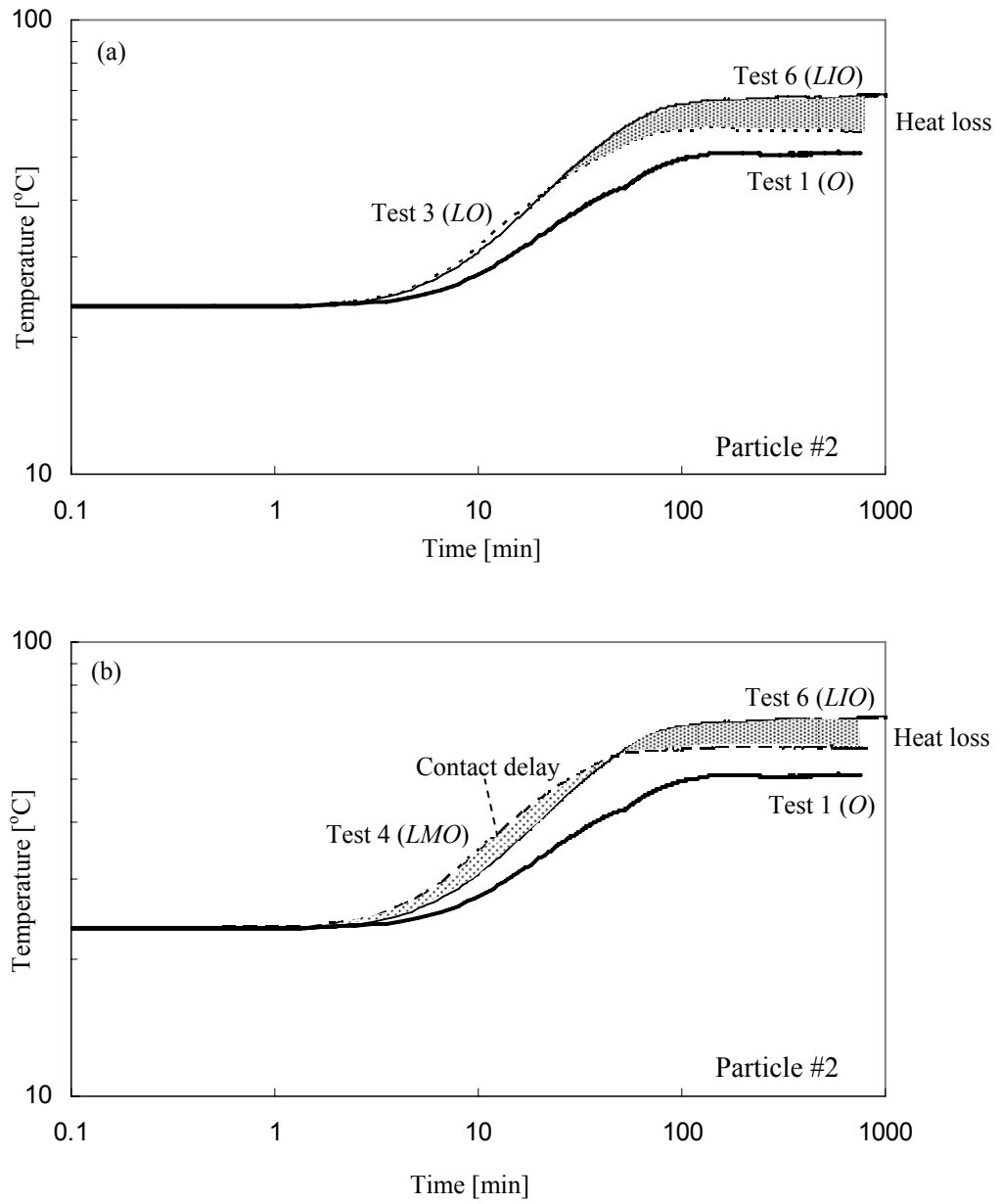


Figure 4.9 The effects of heat loss and contact resistance on measured time histories.

insulated cases.

4.4.2 Equivalent 1-D Continuum Numerical Analysis

The numerical analysis in this section is based on equivalent heat conduction theory, and takes heat loss into consideration as follows:

$$Q_{out} = Q_{in} - c_v \cdot \rho \cdot dz \cdot A \cdot \frac{dT}{dt} - L \cdot T^* \quad (4.7)$$

units: $\left[\frac{cal}{sec} \right]$ $\left[\frac{cal}{sec} \right]$ $\left[\frac{cal}{kg \cdot ^\circ C} \right] \cdot \left[\frac{kg}{m^3} \right] \cdot [m] \cdot [m^2] \cdot \left[\frac{^\circ C}{sec} \right]$ $\left[\frac{cal}{sec \cdot ^\circ C} \right] \cdot [^\circ C]$

This equation indicates that the outflow heat is the sum of the inflow heat, the heat used for heating the material, and the heat loss, where c_v is heat capacity, ρ mass density, z distance, A area, T temperature, and L the loss factor that relates the heat loss to the instantaneous thermal difference between the particles and the medium. Rearranging Equation 4.6,

$$\frac{dQ}{dz} = c_v \cdot \rho \cdot A \cdot \frac{dT}{dt} + \frac{L}{dz} \cdot T^* \quad (4.8)$$

The rate of heat transfer by conduction is

$$Q = k \cdot A \cdot \frac{dT}{dz} \quad (4.9)$$

where k is the thermal conductivity. Combining Equations 4.8 and 4.9 results in

$$\frac{d^2T}{dz^2} = \frac{c_v \cdot \rho}{k} \cdot \frac{dT}{dt} + \frac{L}{dz \cdot k \cdot A} \cdot T^* \quad (4.10)$$

Rearranging

$$\frac{dT}{dt} = D \cdot \frac{d^2T}{dz^2} - \lambda \cdot T^* \quad (4.11)$$

where $D = k / (c_v \cdot \rho)$ and $\lambda = L / (dz \cdot A \cdot c_v \cdot \rho)$. In finite difference form, Equation 4.11 becomes:

$$T_{i+1} = M \cdot T_{i+1} + (1 - 2M - \lambda \cdot \Delta t) \cdot T_i + M \cdot T_{i-1} + \lambda \cdot \Delta t \cdot T_{sur} \quad (4.12)$$

where T_{sur} is the surrounding room temperature and $M = D \cdot \Delta t / \Delta z^2$. The value of M should be less than 0.5 to prevent numerical divergence. Equation 4.11 captures the interplay between thermal diffusion D and loss λ . In particular, higher thermal conduction and smaller loss λ have a similar effect while modeling the early time history for a single particle. Therefore, the thermal diffusivity D and the loss coefficient λ must be simultaneously fitted to a complete set of thermal time histories in order to extract correct value of the equivalent continuum diffusion coefficient D . A least square inversion is implemented. The error in temperature is computed in log-scale to emphasize early low values. The corresponding error for the i -th measurement and the total L_2 error norm are:

$$e_i = \log \left[\frac{T_i^{measured}}{^{\circ}C} \right] - \log \left[\frac{T_i^{measured}}{^{\circ}C} \right] = \log \left[\frac{T_i^{measured}}{T_i^{predicted}} \right]$$

$$L_2 = \left[\sum_i e_i^2 \right]^{0.5} \quad (4.13)$$

The iterative algorithm continues until the inverted variables D and λ are stable for a minimum error L_2 . Figure 4.10 shows measured and predicted time series. The equivalent 1-D column adequately captures experimental results; the major derivations are deserved for Test 4 (*LMO*). Figure 4.11 shows the contours of error surface for the joint inversion of D and λ . The dots represent the selected optimal values for the minimum errors. In all cases, λ increases with D . The loss coefficient λ is more sensitive in test 2 (*RO*) rather than in test 5 (*IO*) and 6 (*LIO*) showing the higher contour slope. There is a trade off between the two values.

The evaluated thermal diffusivity and loss coefficient values are summarized in Table 4.5. The following observations can be made:

- Diffusion decreases when poor contact conditions prevail (improving radiation heat loss) for example in test 2.
- Diffusion increases when heat can be more easily transported across larger contact areas attained by loading (examples: test 3 and test 6) or cementation (test 4). A larger interparticle contact area facilitates heat conduction yet it also causes an increase in the loss term λ because more heat supply induces a higher temperature gradient with the surrounding temperature (Figure 4.10 shows that both D and λ increases to fit experimental results) (Sridhar and Yovanovich, 1996; Lambert and Fletcher, 1997-a).
- Peripheral insulation prevents heat loss and leads to higher heat conduction and smaller λ (test 5 and 6).
- Retardation causes a decrease in D and a slight increase of λ in all cases.

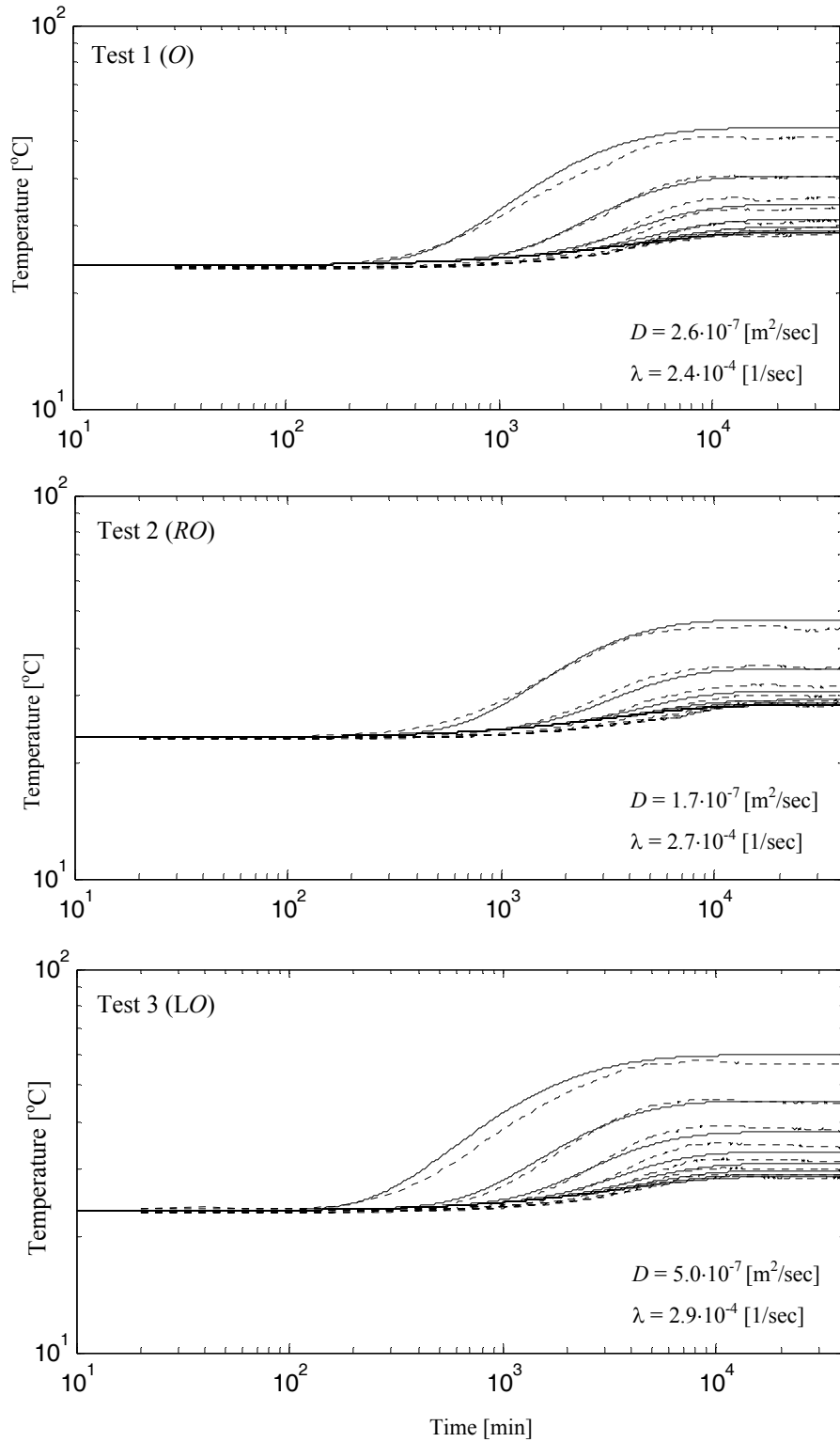


Figure 4.10 Measured and fitted thermal histories - Shown for selected particles (dotted line: experiment; solid line: numerical analysis).

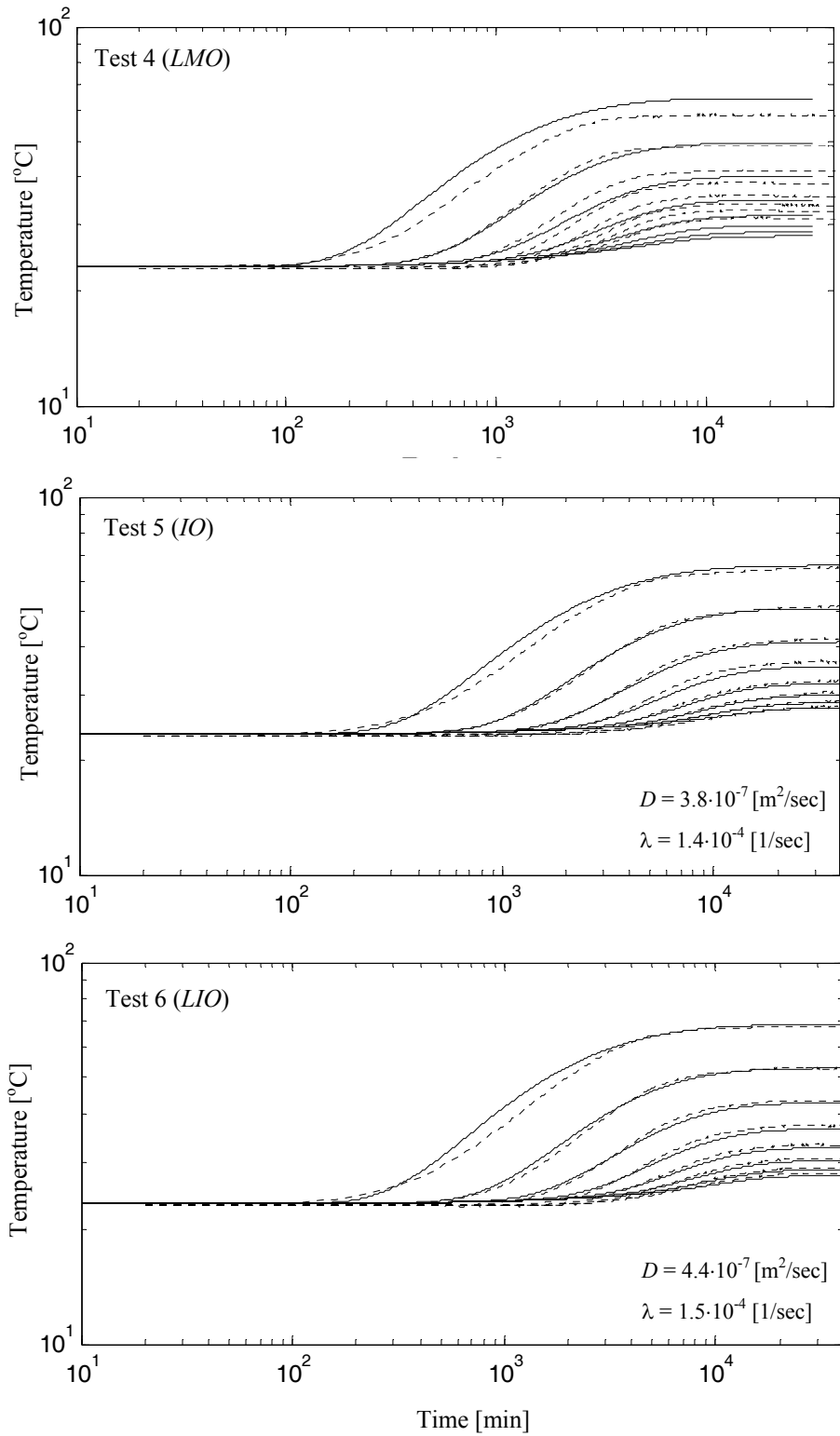


Figure 4.10 Continued.

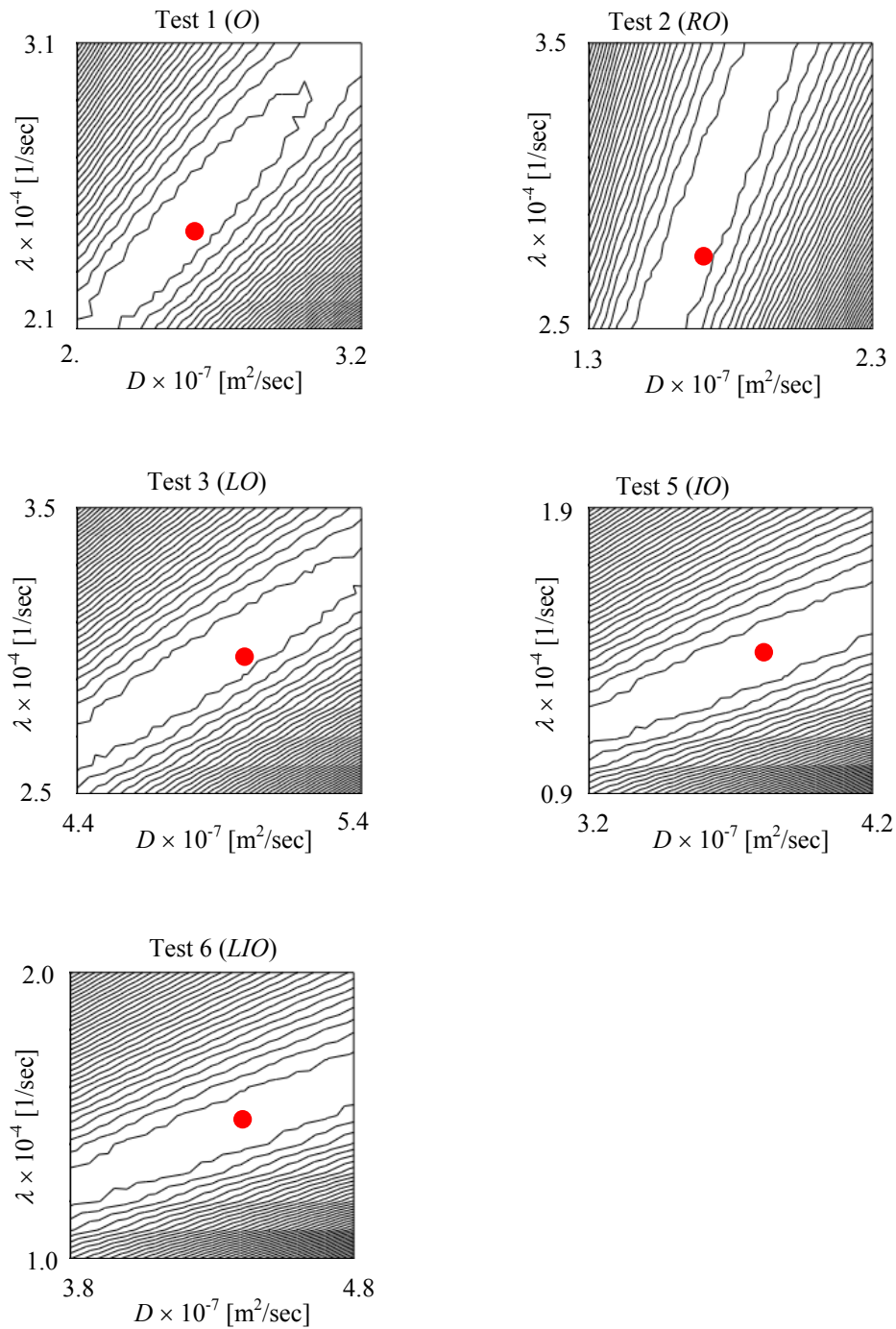


Figure 4.11 Contours of L_2 error surfaces for the joint inversion of D and λ . The value of λ increases linearly with D . Note that this trade off hinders inversion uniqueness.

Table 4.5 Thermal diffusivity D and loss coefficient λ .

Test #	Error		Thermal diffusivity [m ² /sec] × 10 ⁻⁷		Loss coefficient [1/sec] × 10 ⁻⁴	
	Normalized	Log scaled	Normalized	Log scaled	Normalized	Log scaled
1 (<i>O</i>)	11.192	4.494	2.5	2.6	2.5	2.4
2 (<i>RO</i>)	4.549	2.253	1.8	1.7	3.0	2.7
3 (<i>LO</i>)	8.709	2.663	4.9	5.0	3.0	2.9
4 (<i>LMO</i>)	44.494	13.329	6.5	6.5	3.3	2.8
5 (<i>IO</i>)	3.134	0.862	3.7	3.8	1.4	1.4
6 (<i>LIO</i>)	2.875	0.887	4.3	4.4	1.5	1.5

- Above all, the diffusion coefficient in the particle column is only 4% of the diffusion coefficient in the metal that makes the particles.

Note that the thermal time history gathered at any given particle can be very closely fitted with Equation 4.12 (rather than simultaneously fitting all time series). This provides a new set of D and λ parameters which are summarized in Table 4.6 and compared in Figure 4.12. While results are similar, fitting single time histories is less robust than extracting D and λ by simultaneously satisfying all time histories.

4.5 THERMAL CONDUCTION IN SOILS – MACRO-SCALE

The effect of contact quality, area size and coordination number on the thermal conductivity of natural soils is studied by varying the void ratio, gradation and particle shape of dry sands. The thermal needle probe method is used for these measurements.

Table 4.6 Thermal diffusivity D and loss coefficient λ for individual particles with log scaled temperature calculation.

Test #	D [m ² /sec] $\times 10^{-7}$						λ [1/sec] $\times 10^{-4}$					
	3 rd	4 th	5 th	6 th	7 th	8 th	3 rd	4 th	5 th	6 th	7 th	8 th
1	2.8	3.2	3.5	3.6	3.3	3.2	2.6	2.5	2.3	2.4	2.4	2.6
2	2.2	2.3	2.4	2.3	1.9	2.0	3.3	3.0	2.8	2.6	1.9	1.9
3	5.1	5.7	6.3	6.1	5.9	5.6	3.1	3.1	3.1	3.2	3.2	3.3
4	6.5	6.5	6.5	6.5	6.5	6.5	3.3	2.9	2.7	2.1	1.9	1.7
5	4.0	4.1	4.2	4.1	4.1	3.9	1.5	1.5	1.5	1.5	1.5	1.5
6	4.8	4.7	4.9	4.9	4.8	4.8	1.6	1.6	1.6	1.6	1.6	1.6

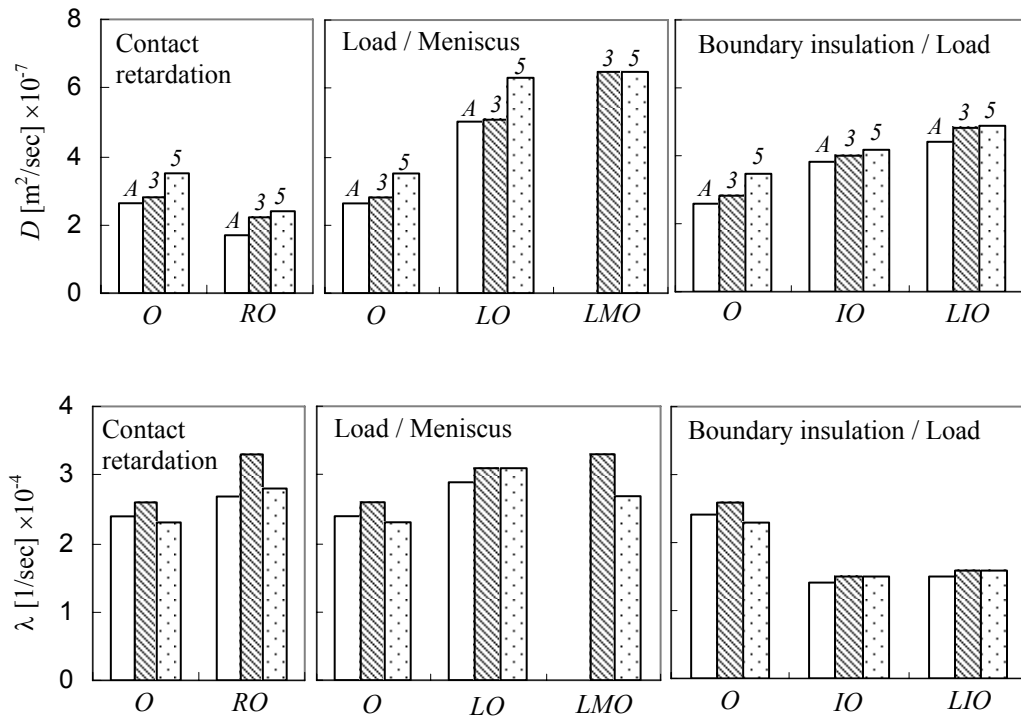


Figure 4.12 Profile of evaluated thermal diffusivity and loss coefficient. ‘A’ stands for the overall estimated value obtained by simultaneously taking into consideration all time series. Numbers 3 and 5 denote values computed for individual time series, in this case for the 3rd and 5th particles. In all cases, the logarithmic error definition and the L_2 norm are used to guide the inversion.

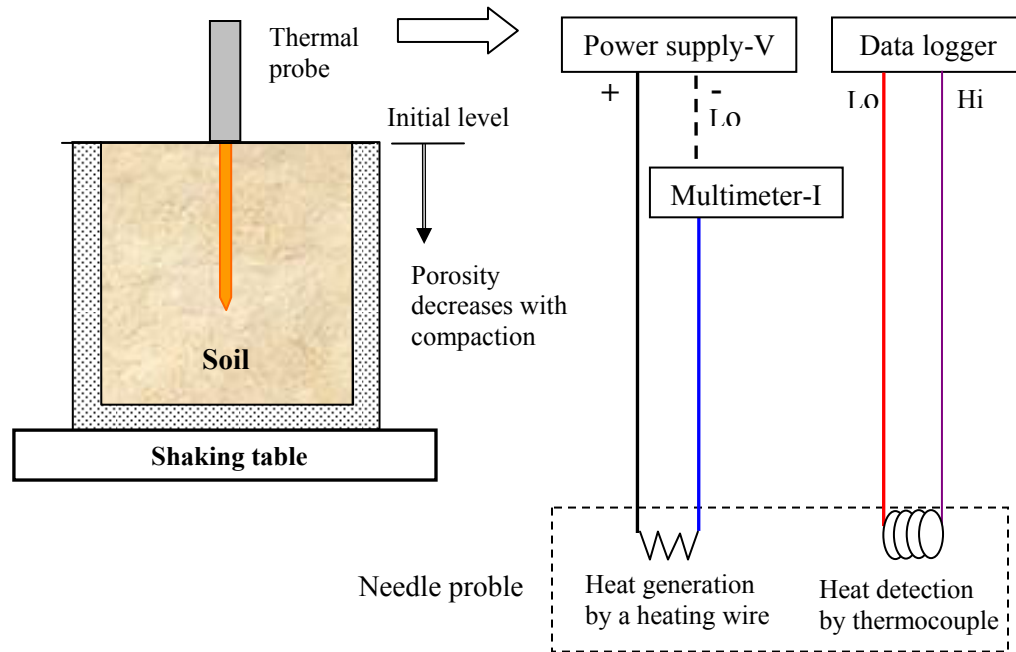


Figure 4.13 Thermal conductivity measurement circuit - Thermal needle probe method.

4.5.1 Test Method

The thermal needle probe consists of a heating wire and a thermocouple installed within a 1 mm diameter metal needle (Thermal Logic). Heat is generated by imposing a DC current through the heating wire and the temperature evolution within the needle is monitored with the thermocouple (Figure 4.13): the higher the thermal conductivity of the medium, the higher the rate of heat dissipation and the lower the rate of temperature increase detected with the thermocouple. The electric current I is related to the voltage drop V_{ref} across a reference resistor R_{ref} placed in series with the heating wire,

$$I = V_{ref} / R_{ref} \quad (4.14)$$

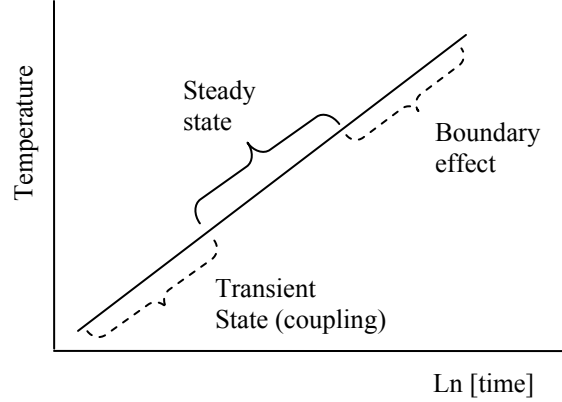


Figure 4.14 Temperature-time series. Identification of the steady state region.

The input heat energy Q is

$$Q = I^2 \cdot R_m = \left(\frac{V_{ref}}{R_{ref}} \right)^2 \cdot R_m \quad (4.15)$$

where R_m is the resistance of the heating wire. The early portion of the temperature time series is affected by the needle-soil coupling while long-time data are affected by specimen boundaries. Therefore, the thermal conductivity is obtained from the linear, central portion of temperature versus log of time plot (Figure 4.14). The thermal conductivity is computed as (derivation in Carslaw and Jaeger, 1959):

$$k = \frac{Q}{4\pi} \cdot \frac{\ln(t_2/t_1)}{(T_2 - T_1)} = \left(\frac{V_{ref}}{R_{ref}} \right)^2 \cdot \frac{R_m}{4\pi} \cdot \frac{\ln(t_2/t_1)}{(T_2 - T_1)} \quad (4.16)$$

This test method is valid in homogeneous, isotropic materials (for details on this procedure, see Monohar et al., 2000; ASTM D5334-00).

4.5.2 *Experimental Study*

Index properties and microscopic images of the tested soils are presented in Table 4.7 and Figure 4.15. Ottawa 20/30 and F110 are round sands while blasting and crushed sand have low roundness and sphericity. Crushed sand-I and sand-III have significant fines content. In all cases, sand is air-pluviated into a zero lateral strain cell to attain the loosest possible state (cell diameter = 15.25 cm, height = 15.50 cm - Figure 4.13). The thermal needle probe is then vertically inserted into the soils. The temperature is logged every 0.5 second for 2 minutes (Agilent multimeter 34401A). The voltage drop V_{ref} remains relatively constant throughout the test and it is recorded to calculate the input energy. Measurements are repeated after 10 minutes. Once three measurements are completed, the specimen is tamped and /or densified on a shaking table to attain gradual reductions in porosity (5~6 steps).

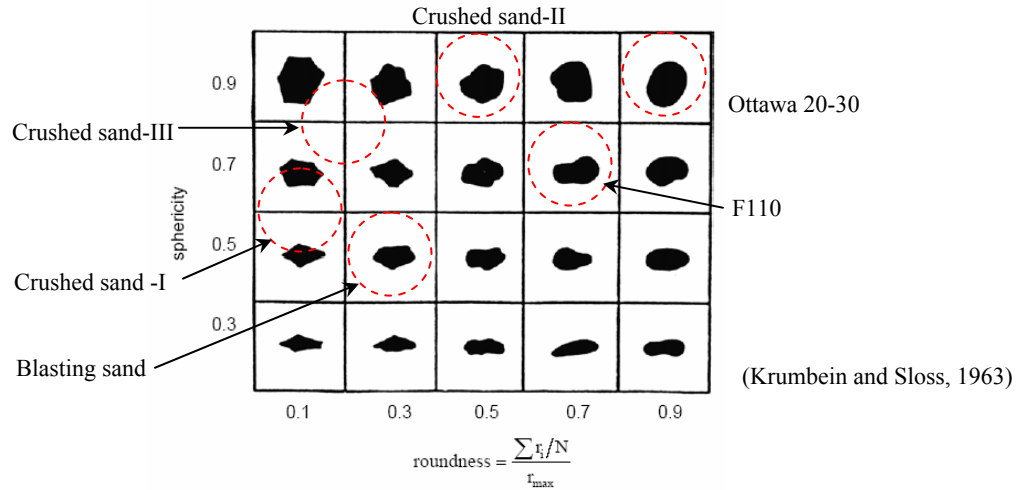
4.5.3 *Test Results*

Results are shown in Figure 4.16. Following prior particle-level studies, it is inferred that the increase in thermal conductivity with decreasing porosity reflects the increase in interparticle coordination and possible improvements in “contact quality”. There is a weak correlation between particle shape and the slope of the k vs. n line ($\Delta k/\Delta n$). Results for crushed sand-I and sand-III suggest that well graded sands attain lower porosities and higher k values as smaller particles fill voids left between larger particles; the result is improved heat transfer and higher thermal conductivity.

Table 4.7 Tested soil properties.

Soil	Mineralogy	Void ratio		Gradation				G_s	Shape	
		e_{max}	e_{min}	D_{50} (mm)	D_{10} (mm)	C_u	C_c		Roundness	Sphericity
Ottawa 20/30 sand ⁽¹⁾	quartz	0.742	0.502	0.72	0.65	1.15	1.02	2.65	0.9	0.9
Ottawa F110 sand ⁽¹⁾	quartz	0.848	0.535	0.12	0.081	1.62	0.99	2.65	0.7	0.7
Blasting sand ⁽¹⁾	quartz	1.025	0.698	0.71	0.42	1.94	0.94	2.65	0.3	0.55
Crushed sand-I ⁽²⁾	granite, gneiss	0.93	n/a	0.33	N/A	5.5	n/a	n/a	0.1	0.6
Crushed sand-II ⁽²⁾	n/a	0.91	n/a	0.52	N/A	2.3	n/a	n/a	0.5	0.9
Crushed sand-III ⁽²⁾	granite	0.79	n/a	0.3	N/A	3.2	n/a	n/a	0.2	0.8

Note: ⁽¹⁾ Cho (2002). ⁽²⁾: Dodds (2003)



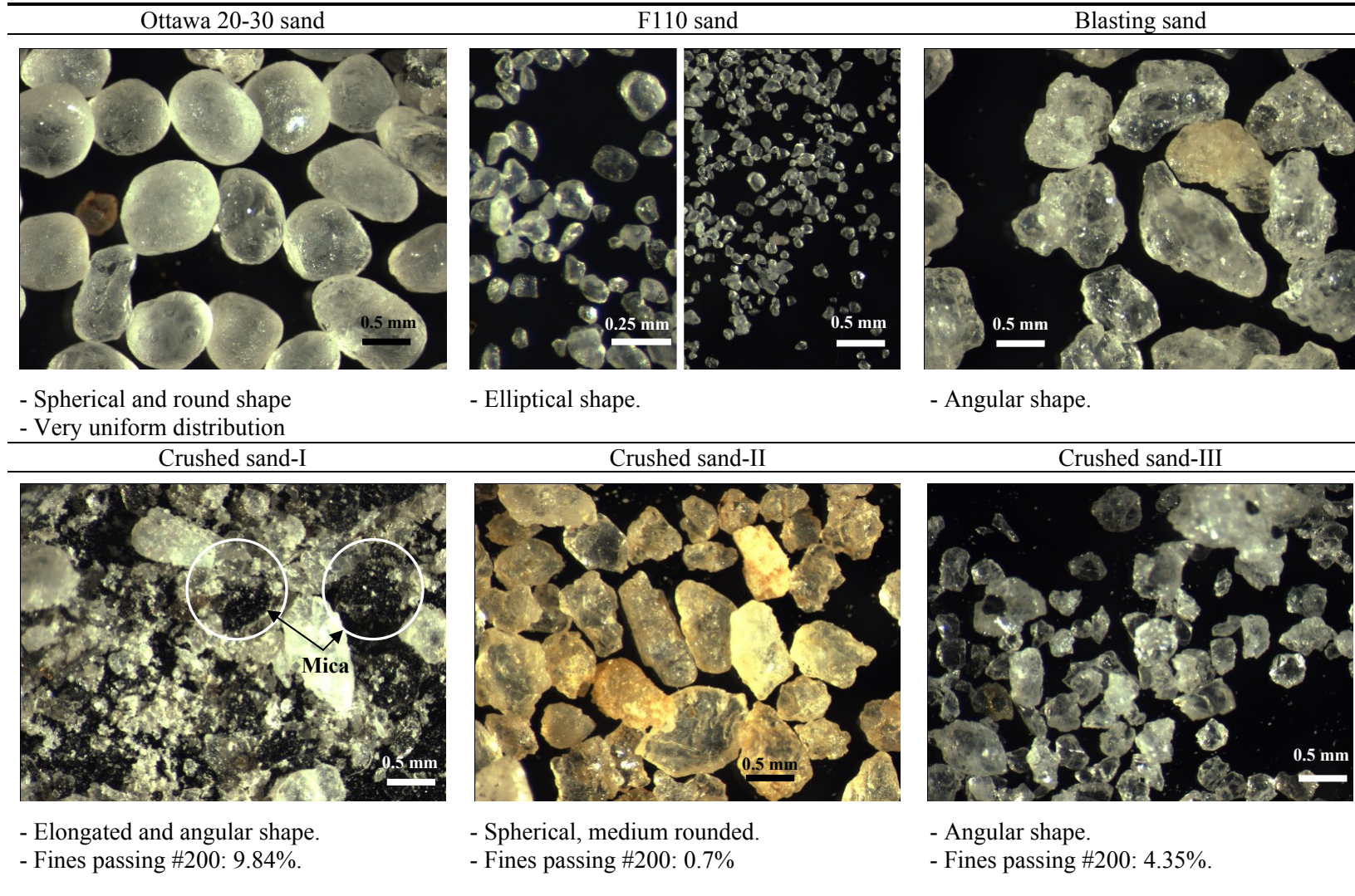


Figure 4.15 Microscopic images of tested sands.

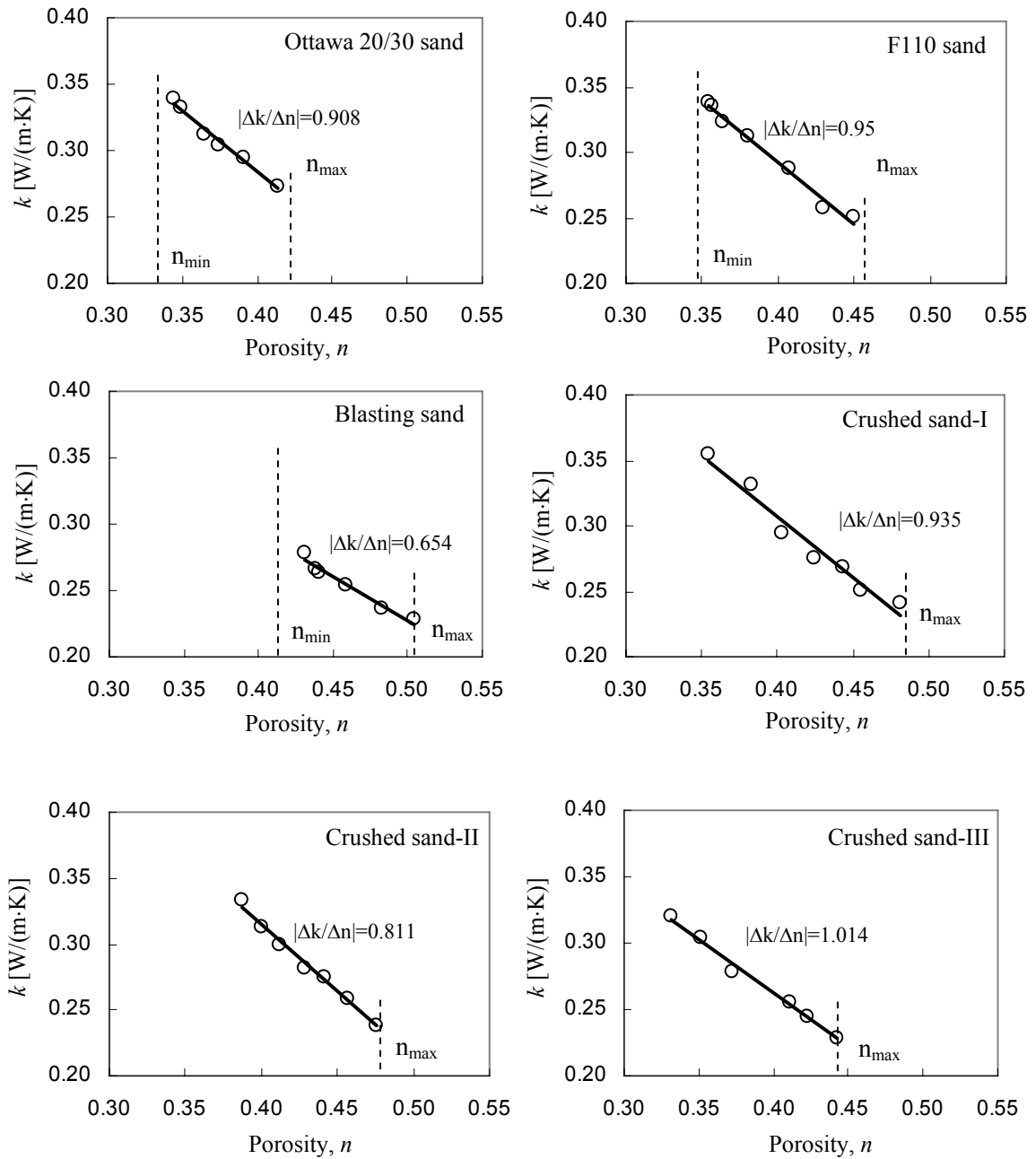


Figure 4.16 Changes in thermal conductivity with porosity. Maximum and minimum porosities are calculated from maximum and minimum void ratios $n=e/(1+e)$. Refer to Table 4.7.

Figure 4.17 shows thermal conductivity versus porosity trends predicted with thermal conductivity models summarized in Table 4.4. These trends are computed assuming that the thermal conductivity of quartz and air are $k_m = 8.4 \text{ W}\cdot\text{m}^{-1}\cdot\text{K}^{-1}$ and $k_a = 0.026 \text{ W}\cdot\text{m}^{-1}\cdot\text{K}^{-1}$. Experimental data are superimposed on the same plot.

The thermal conductivity of the tested sands drops sharply from the thermal conductivity of quartz mineral (Note that the y-axis is in log scale in Figure 4.17). Series and Hashin-Shtrikman lower bound (HS-L) models plot below experimental results, while other predictive models overestimate the thermal conductivity of these dry sands. The volume fraction model (same as the Complex Refractive Index Method CRIM) and the log-model are fitted as:

$$k_{eff} = [n \cdot k_a^c + (1-n) \cdot k_m^c]^{1/c} \quad \text{with a value } c = -0.25 \quad (4.17)$$

$$k_{eff} = -a \cdot \ln(n) + p$$

with values $a = 0.291 \text{ W}/(\text{m}\cdot\text{k})$ and $p = 0.026 \text{ W}/(\text{m}\cdot\text{k}) \quad (4.18)$

On the other hand, the semi-empirical models (in Table 4.3) fit the experimental result in Figure 4.17-b. These results suggest that effective thermal conductivity models for particulate materials must not only consider volumetric fractions and the bulk conductivity of each phase but also the inherent presence of contacts in particulate materials (Tarnawski et al., 2002; Kumlutas et al., 2003; Song and Chen, 2004).

4.6 DISCUSSION

Previously published results, particle-level and macro-scale measurements and simulations in this study permit identifying several heat transfer paths in granular

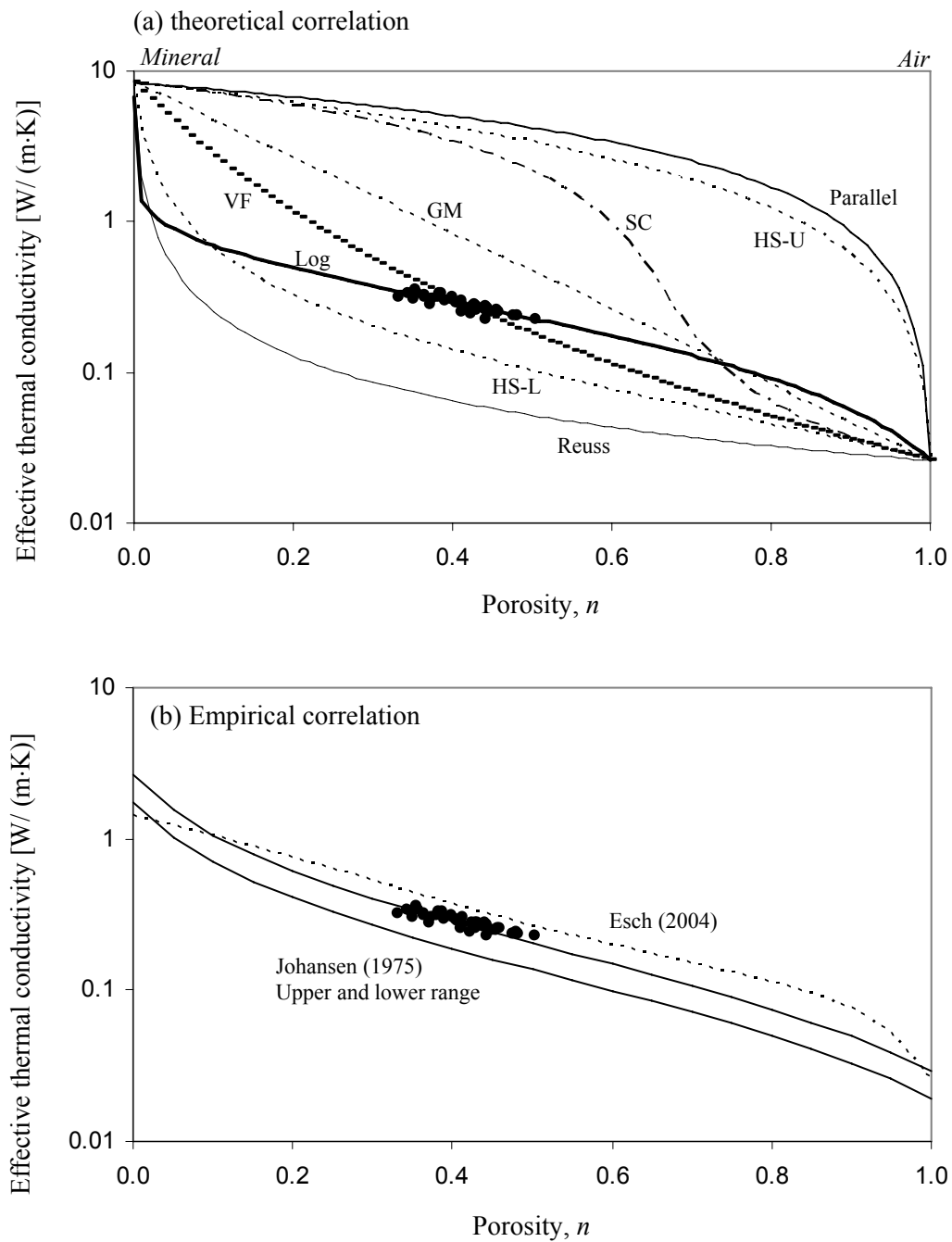


Figure 4.17 Effective thermal conductivity versus porosity. Experimental results shown as black dots (total of 39 measurements-6 sands). Model predictions are shown with lines.

Series: Reuss (1929), Parallel: Voigt (1910), HS: Hashin-Shtrikman (U: upper bound and L: lower bound), GM: Geometric mean (Kumlutas, 2003), SC: Self consistent (Tarnawski and Leong, 2000), VF: Volume fraction (Roth et al., 1990)

materials refer to (Figure 4.18):

- Conduction in solid: Heat propagates within the material that makes the particle. Solid-to-solid conduction: This is the main path at particle contacts. Its effectiveness is controlled by the contact area.
- Conduction in fluid: Heat is conducted from the particle into the fluid and back into neighboring particles. Heat is also conducted through the fluid within the porous network.
- Convection: Heated particles warm the surrounding fluid and convective heat circulation develops.
- Radiation conduction at interparticle contacts: The geometry of spherical particles allows radiation heat propagation across particles.
- Radiation from the particle surface into the surrounding medium (Aduda, 1996).

4.7 CONCLUSIONS

Heat transfer in soils affects geotechnical design in permafrost regions, and potential methane formation and recovery from gas hydrate bearing sediments. The thermal condition in soils depends on particle size and grain size distribution, packing geometry, pressure, water content and density. The thermal conductivity in soils and among soil components is related as $k_{\text{mineral}} > k_{\text{saturated soil}} > k_{\text{water}} > k_{\text{dry-soil}} > k_{\text{air}}$.

Interparticle contacts govern thermal conduction. The presence of high thermal conductive fluids or cementing agents at contacts promotes heat transfer. Larger contact

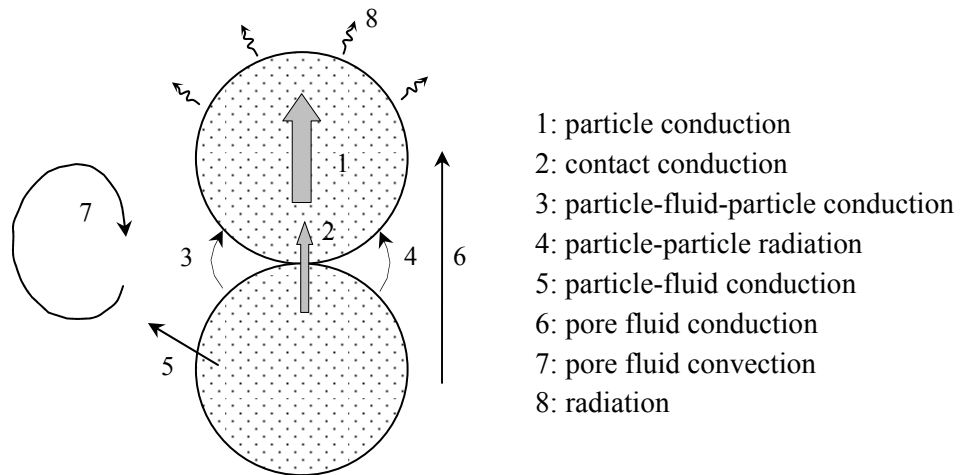


Figure 4.18 Summary: possible heat transfer paths through particulate materials.

areas (for example by loading, creep, or diagenesis) enhance thermal diffusion.

There are competing effects between heat transfer within the granular skeleton and heat loss to the surroundings. Improvement in interparticle contacts results in higher thermal gradient with the surrounding medium eventually leading to higher heat loss.

Effective thermal conductivity models must be carefully applied in particulate materials because interparticle contacts play a decisive role in thermal conduction and diffusion.

CHAPTER V

MECHANISTIC STUDY OF LENSING RELATED TO GAS HYDRATE FORMATION

5.1 INTRODUCTION

Natural gas hydrate is found in various morphological patterns: disseminated, nodular, layered and massive forms (Sloan, 1990). The evidence of segregation and lensing in gas hydrate includes:

- Nodular and vein hydrate in marine sediments at ODP Leg 164 (Paull, 1997).
- Pervasive gas hydrate lenses, vein or nodules at ODP Leg 204 in the Cascadia continental margin (Leg 204 preliminary report, 2002).
- Lens shape hydrate in marine sediments at the Gulf of Mexico (2002).
- Nodule, vein and dyke hydrate from Mallik 2L-38 in permafrost region in Alaska (Uchida et al., 2001).
- Gas hydrate in layered bands within a mud matrix offshore from northern California (Brooks et al., 1991).

Examples of hydrate lenses are shown in Figure 5.1.

It is herein hypothesized that knowledge of ice lens formation in soils may help the interpretation and prediction of gas hydrate lens formation. However, any analogy must take into consideration differences in boundary conditions, formation history, and both thermal and mechanical properties.

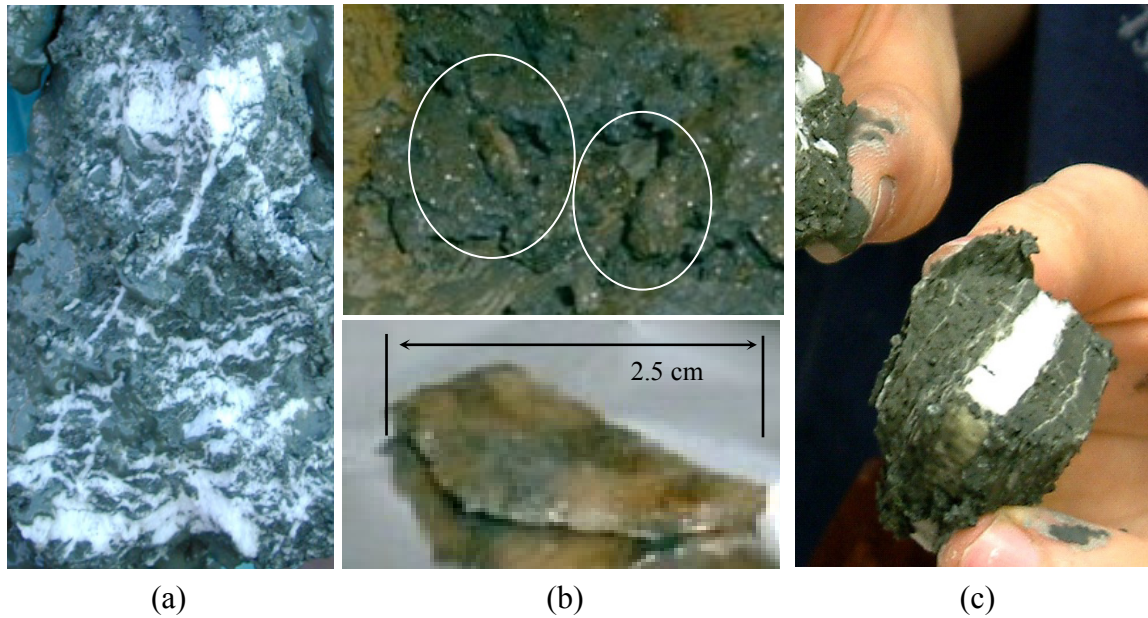


Figure 5.1 Evidence of hydrate segregation in natural systems. (a) Hydrate lenses parallel to the strata. Hydrate vein normal to bedding from ODP Leg 204, (b) lens shape gas hydrate in the marine sediments at Gulf of Mexico (2002), (c) Hydrate vein (GeoTek, Inc.)

Ice lensing in soils is a common phenomenon in cold and permafrost regions. Engineering consequences include highway and pavement damage, buried pipe breakage and slope instability (Everett, 1961; Tsytoich, 1973; Konrad, 1989). Previous studies using experimental and numerical techniques have attempted to correlate soil properties, thermal boundary conditions and state of stress with the formation of ice lenses in soils. Ice lensing in typical near-surface conditions is mainly observed in “frost-susceptible” fine-grained soils and they form parallel to the bedding plane that is typically parallel to the thermal boundary (Taber, 1929; Penner, 1963; Miller, 1980).

The purpose of this study is to discern the mechanisms of ice lens formation and to extend this enhanced understanding to gas hydrate formation. The study begins with a literature review of physical process involved in ice lens formation. Then, an exploratory

experimental study is conducted to identify mechanisms in ice lensing. Finally, the discussion addresses the case of gas hydrate lensing.

5.2 LITERATURE REVIEW

5.2.1 Ice Lens Formation in Soils

Nine percent volume expansion by phase transformation of water is not enough to explain the frost heave phenomenon (Miller, 1980). The systematic research effort by Taber (1929) identifies that frost heave is induced by ice segregation called “ice lens” depending on soil particle size, available water, freezing rate and overburden pressure.

Ice lenses form either parallel to the freezing front or in multiple directions depending on the thermal boundary. And the segregated ice lenses form the blocky soil aggregates and increase the water content of layered ice, and the surrounding soils are compressed by the growth of ice lens (Hutchinson, 1974; McRoberts, 1975).

Water in soils can be found freely in the pore space and in diffuse double layers around particles (Gold, 1957; Penner, 1958, 1963; Everett, 1961; Anderson et al., 1973). Diffused double layers are connected through the soil skeleton in fine particles (silty clay and clay). Therefore, the adsorbed water film is an effective migration path in fine grained soils (Taber, 1930; Jumikis, 1966; Jinsheng and Rong, 1983). The water migration rate in double layers is proportional to the specific surface of soil particles (Jumikis, 1958). As water within this layer migrates to the ice front, the film thickness becomes thinner; then, soil particles tend to retain the constant thickness by taking water molecule from the warmer side (Taber, 1930; Penner, 1963; O’Neill and Miller, 1985).

The adsorbed moisture has little mobility perpendicular to the soil particles, but it can easily move parallel to particles (Jumikis, 1966). In a closed system, lens formation decreases the water content near the ice lens (redistributed water content along the ice lens profile in Mageau and Morgenstern, 1980).

The inter-connected ice lenses act as pre-existing fractures within the soil structure during melting and provide high hydraulic diminishing excess pore pressure generation. In-situ studies show that segregated ice decreases the shear strength in the basal ice layer and may finally cause slope instability (Harris and Lewkowicz, 2000, Analytical solution for shear resistance and critical slope angle in Vallejo, 1980).

5.2.2 Thermodynamics

This section introduces basic concepts in thermodynamics considering free energy in freezing phenomena. First of all, the energy U is defined as heat Q and work W

$$dU = dQ + dW = dQ - P \cdot \Delta V \quad (5.1)$$

Defining the entropy S is dQ/T , the heat is expressed

$$dU = T \cdot dS - P \cdot dV \quad (5.2)$$

Also, enthalpy H is

$$dQ = dU + d(PV) = dQ = d(Q+PV) = d(H) \quad (5.3)$$

The differential form of enthalpy defines the free energy

$$dH = dU + P \cdot dV + V \cdot dP$$

$$dH = T \cdot dS - P \cdot dV + P \cdot dV + V \cdot dP = T \cdot dS + V \cdot dP \quad (5.4)$$

Adding the entropy term,

$$d(H - TS) = T \cdot dS + V \cdot dP - S \cdot dT - T \cdot dS \quad (5.5)$$

where $H - TS =$ Gibbs free energy G . The Gibbs free energy is

$$dG = V \cdot dP - S \cdot dT \quad \text{Gibbs-Durham equation} \quad (5.6)$$

The chemical potentials of water and ice for phase equilibrium are

$$\mu_w = V_w \cdot dP_w - S_w \cdot dT \quad \text{for water} \quad (5.7)$$

$$\mu_i = V_i \cdot dP_i - S_i \cdot dT \quad \text{for ice} \quad (5.8)$$

The above two phases reach equilibrium if the chemical potential is zero. Therefore,

$$V_w \cdot dP_w - S_w \cdot dT = \mu_i = V_i \cdot dP_i - S_i \cdot dT = 0$$

$$V_w \cdot dP_w - V_i \cdot dP_i = (S_w - S_i) \cdot dT = (dQ/T_o) \cdot dT = \Delta H_{wi} \cdot dT \quad (5.9)$$

Dividing Equation 5.9 by V_w and expressing it in terms of the chemical potential

$$d\mu_w - d\mu_i \frac{V_i}{V_w} = \frac{L}{T_o} dT \quad (5.10)$$

where L is latent heat and T_o is the temperature when ice forms. This is the generalized Clapeyron equation and it presents the inter-dependence between pressure and temperature gradient. Thus, the two phases at equilibrium produce a pressure difference and cause water migration.

5.2.3 Governing Factors

The effective parameters that govern ice lens formation in soils delineate the lower and upper limits of favorable conditions for lens formation. Figures 5.2-to-Figure 5.4

summarize the observed lens formation conditions observed by previous researches in terms of consideration particle size, overburden pressure and hydraulic conductivity effects. The following observations facilitate the interpretation of these figures:

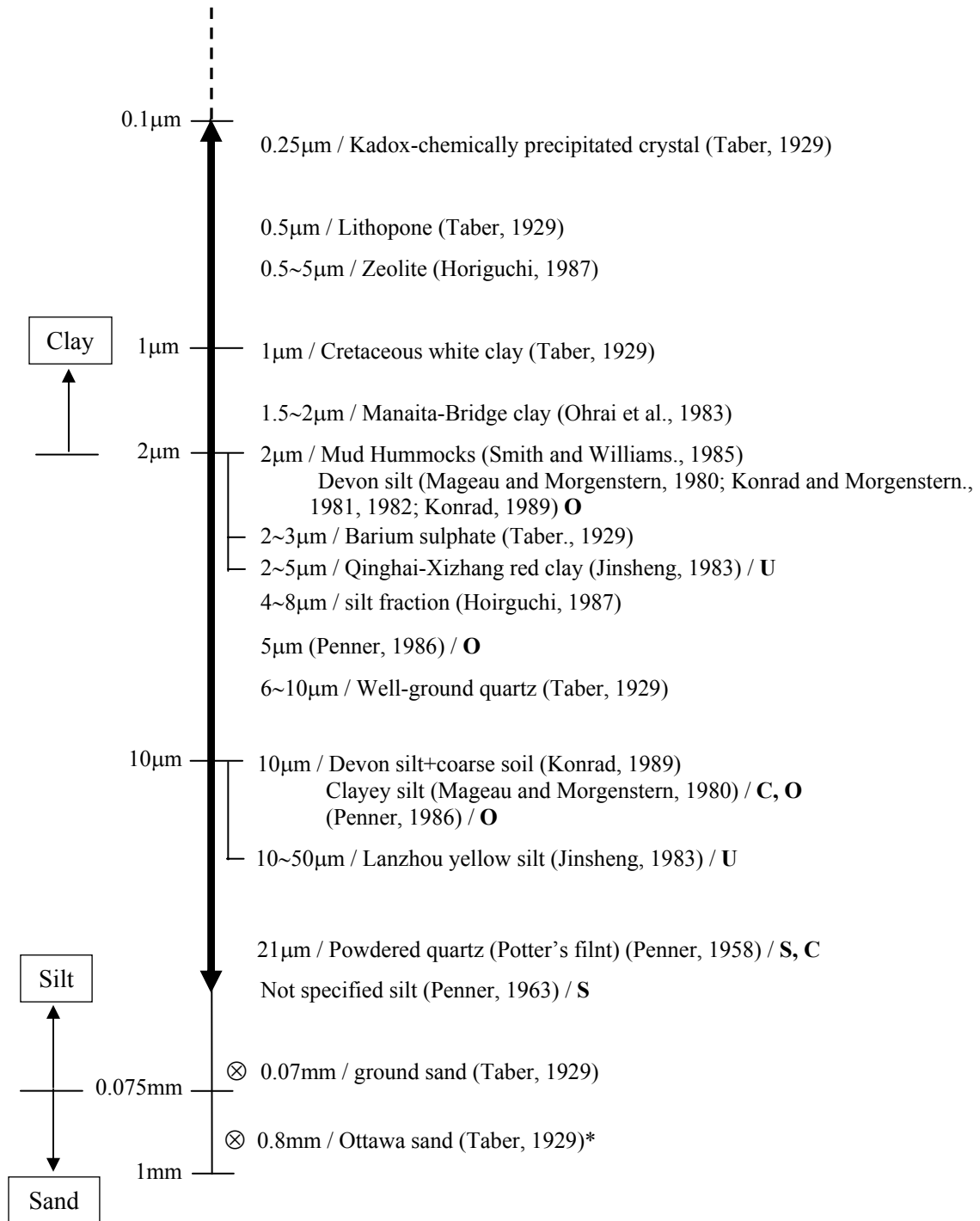
- Smaller particles have a larger specific surface area, therefore, a higher relative volume of unfrozen water in double layers. On the other hand, larger particles have higher thermal conductivity and may support a faster freezing rate.
- As the overburden pressure increases, the ice pressure required to form ice lenses increases and the freezing temperature for ice lens initiation decreases (Jumikis, 1957; Gilpin, 1980; Nixon, 1991). The hydraulic conductivity decreases (Konrad and Morgenstern, 1982; Benson and Othman, 1993) and the length of frozen fringes increases with overburden pressure (Anderson, 1967; Penner and Walton, 1978; Gilpin, 1980).
- Lower hydraulic conductivity prevents water movement toward the ice lens.

Besides these factors, Carlson and Nixon (1988) report that layered soils facilitate ice lens formation. In addition, surface irregularities enhance ice crystallization (Golubev, 1997).

The freezing temperature decreases with the increase in ionic concentration in the pore fluid:

$$\Delta T = -i \cdot K_f \cdot m \quad (5.11)$$

where $i=1.81$ for NaCl, K_f =freezing temperature depression constant ($=-1.86^\circ\text{C/mol}$) and m molar concentration. Ice formation causes salt exclusion and the concentration in surrounding pore fluid increases. Hence, the ice lens formation temperature decreases



*: The mixture of Ottawa sand and clay: Ice observed with more 50% clay.
 S: saturated, U: unsaturated, O: open, C: closed system.

Figure 5.2 Particle size effect. The bold line constrains the range where ice lens is experimentally observed.

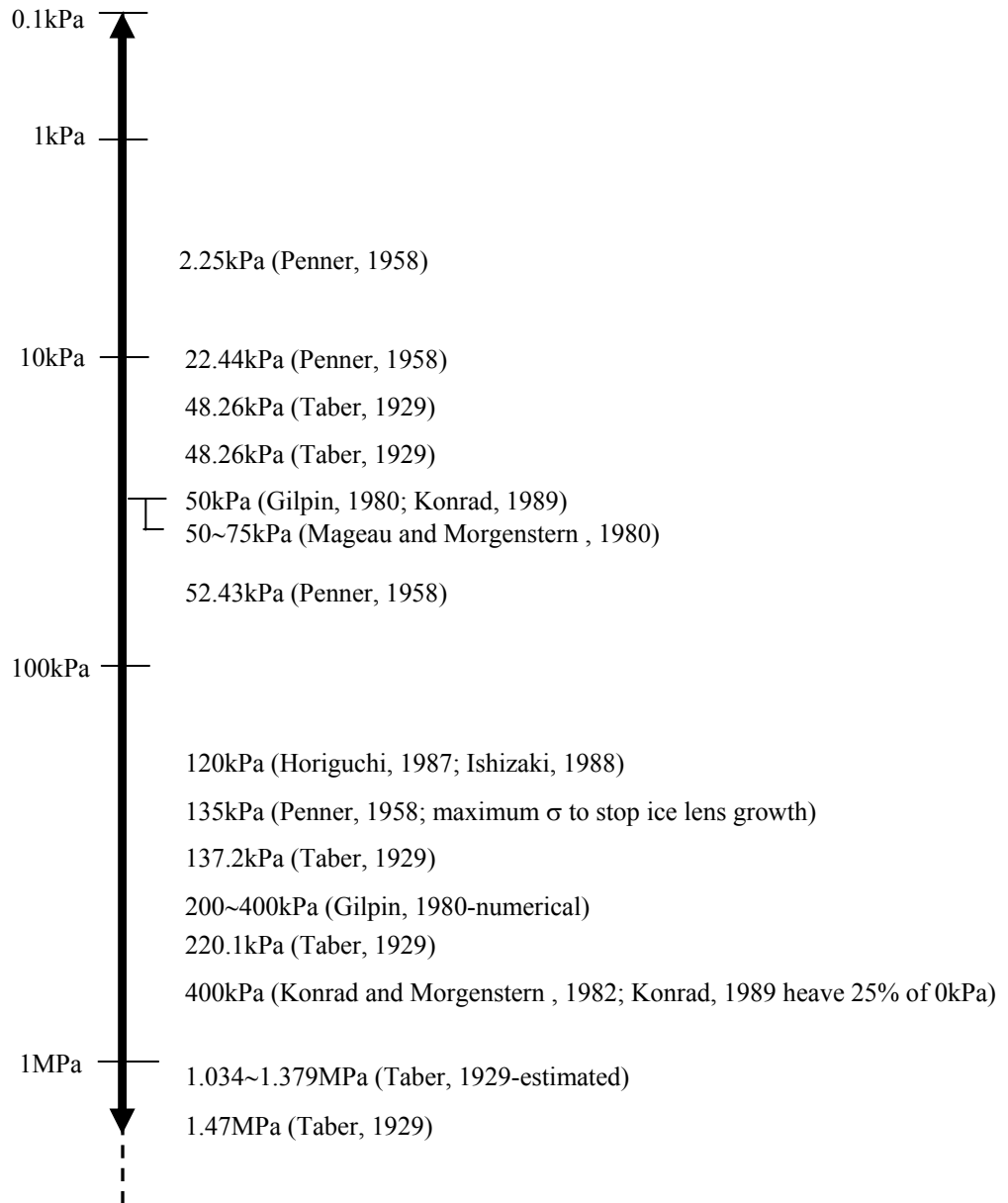


Figure 5.3 Overburden pressure effect. The bold line constrains the range where ice lens is experimentally observed.

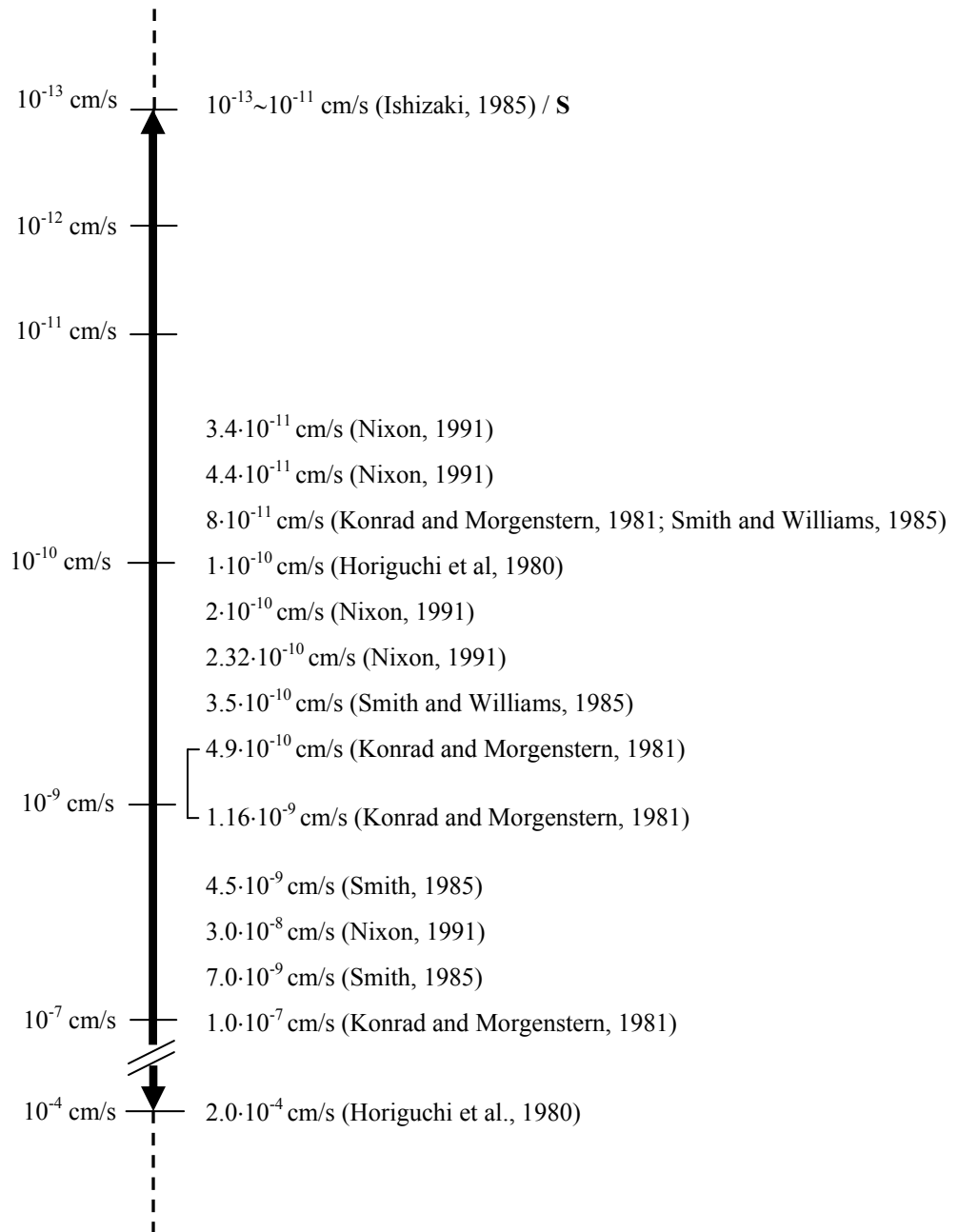


Figure 5.4 Hydraulic conductivity effect. The bold line constrains the range where ice lens is experimentally observed.

and further growth hindered and new ice nucleation occurs away from the initial lens. This sequence of events leads to many micro- ice lenses in salty pore fluid. The excluded salt and micro-lenses reduce the hydraulic conductivity as well. There is more than 50% reduction in frost heave in saline soils (Chamberlain, 1983).

5.2.4 Ice Lensing Models

Capillary theory. This model explains ice lens formation at the freezing front. The pressure difference between ice and water induced by surface tension is predicted by Laplace's equation

$$\Delta P_{iw} = P_i - P_w = \frac{2 \cdot \gamma_{iw}}{r} \quad (5.12)$$

where γ_{iw} is the surface tension between ice and water and r is the pore radius. If ΔP_{iw} is larger than $2 \cdot \gamma_{iw}/r$, ice can form penetrating the pore space. Ice lenses form in pore space and push particles away (Everett, 1961). This model known as *primary heaving theory* only includes pore size and surface tension without heat and mass conservation. It also underestimates frost heave pressure and fails to explain periodic ice lenses (Miller, 1980; Loch, 1981).

Secondary frost heave theory. Miller (1972) assumed that there is a transition zone between the unfrozen region in soils and the freezing front (called frozen fringe). Pore ice and unfrozen water in the water film between ice and particles coexist in pore spaces. Regulation by exothermic heat of phase transformation causes a partially molten ice to move toward the ice lens (an example of a particle migration away from the lens face is shown in Romkens and Miller, 1973). This model predicts that ice lenses form when the

ice pressure exceeds the overburden pressure (the Terzaghi's effective stress = 0), soil particles do not sustain the force, and grain separation takes place (Gilpin, 1980). This model has been widely accepted by previous researchers to model frost heave and it can explain periodic ice lens (Holden, 1983; O'Neill and Miller, 1985; Black, 1995). However, the model is complex and requires many physical parameters.

Osmotic model. It is hypothesized that connected with diffused double layers in frost-susceptible soils such as silts and clays have enough ions to produce osmotic pressure in addition to secondary frost heave pressure (Horiguchi, 1987). Furthermore, phase transformation causes ion exclusion, lowers the freezing temperature, ice does not tend to segregate, and nucleation occurs elsewhere (Martin, 1959; Chamberlain, 1983).

Segregation potential model. This model focuses on water migration to the ice lens as a function of the temperature gradient in the frozen fringe (Konrad and Morgenstern, 1981). The driving force for water migration is suction by phase transformation and the segregation potential decreases as overburden pressure increases (Konrad and Morgenstern, 1982).

5.3 EXPERIMENTAL STUDY AND ANALYSIS

Ice lenses form in different soils and under various stress boundary conditions. These conditions are explored next.

5.3.1 Ice Lens Formation

Specimens made of sand, precipitated silt or kaolinite are prepared at different water content. Each mixture is placed into a foam container, and inside a styrofoam box

so that heat is removed from the top while the other sides are thermally insulated. Test conditions are shown in Figure 5.5. Phase transformation is monitored with thermocouples buried in the specimen. After phase transformation, specimens are dissected and the spatial distribution of ice lenses is documented. Table 5.1 and Figure 5.6 summarize typical results. The following observations are made:

- Kaolinite and precipitated silt are susceptible to lens formation. Lenses are not observed in sand.
- Periodic ice lenses form normal to the heat flux direction in the mixture of kaolinite and water (this is also the σ_3 direction).
- Soils between ice lenses are not frozen (Figure 5.6-a, b - see also Penner 1963 for a similar observation of unfrozen soils).
- Omnipresent needle shape ice lenses form in kaolinite saturated with a 0.6molar NaCl solution, and in precipitated silt saturated with deionized water (Figure 5.6-c, d).

There is water content redistribution after lens formation, therefore water in neighboring pores feeds ice lens growth (Figure 5.6-a, see also Miller, 1980).

5.3.2 *Lens Growth - Micro-Scale Study*

Ice lens growth on the surface of a shallow specimen is continuously monitored using a digital microscope. The soil mixture consists of kaolinite (Wilkey SA1- liquid limit: 43%) saturated with deionized water ($w_c \sim 40\%$). The cylindrical cell is 1cm height and 4cm in diameter. The black granules passing through sieve #270 (53 μ m) are spread

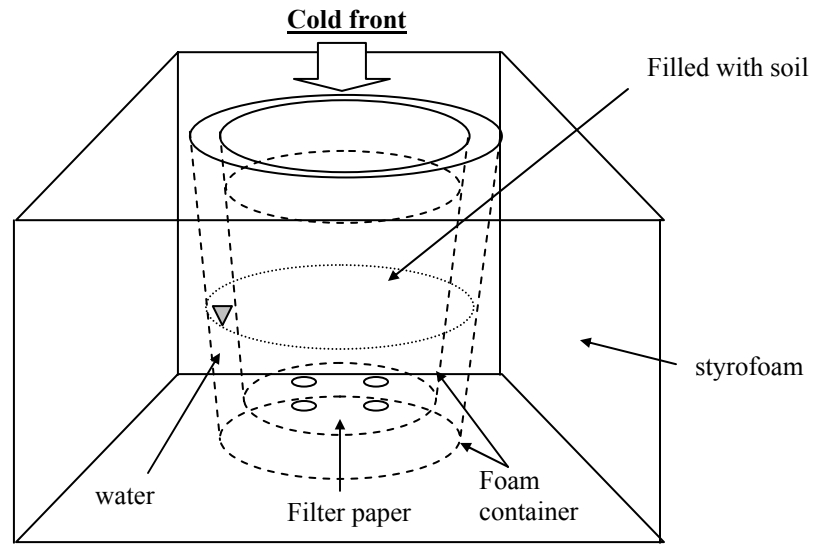


Figure 5.5 Experimental device designed to study ice lens formation – 1D heat front.

Table 5.1 Test conditions and observed features.

Soil	w/c	Ice lens	Features
Nevada Sand	~ 25 %	No	
Kaolinite	~ 2LL	No	Without heat insulator
Kaolinite	~ 2LL	Yes	Bottom part w/c=57.2%
Precipitated silt	~ 350 %	Yes	Needle shape lenses
Sand / Kaolin	~ 30 %	Yes	Striation distribution with very fine needle shape lens
Kaolinite	53.3 %	Yes	Undulated lensing
Kaolinite	33.2 %	Yes	Overburden pressure during freezing
Kaolinite*	54.6 %	Yes	Thin plate shape lenses locally grouped

*: Mixed with salt water (0.6 mol)

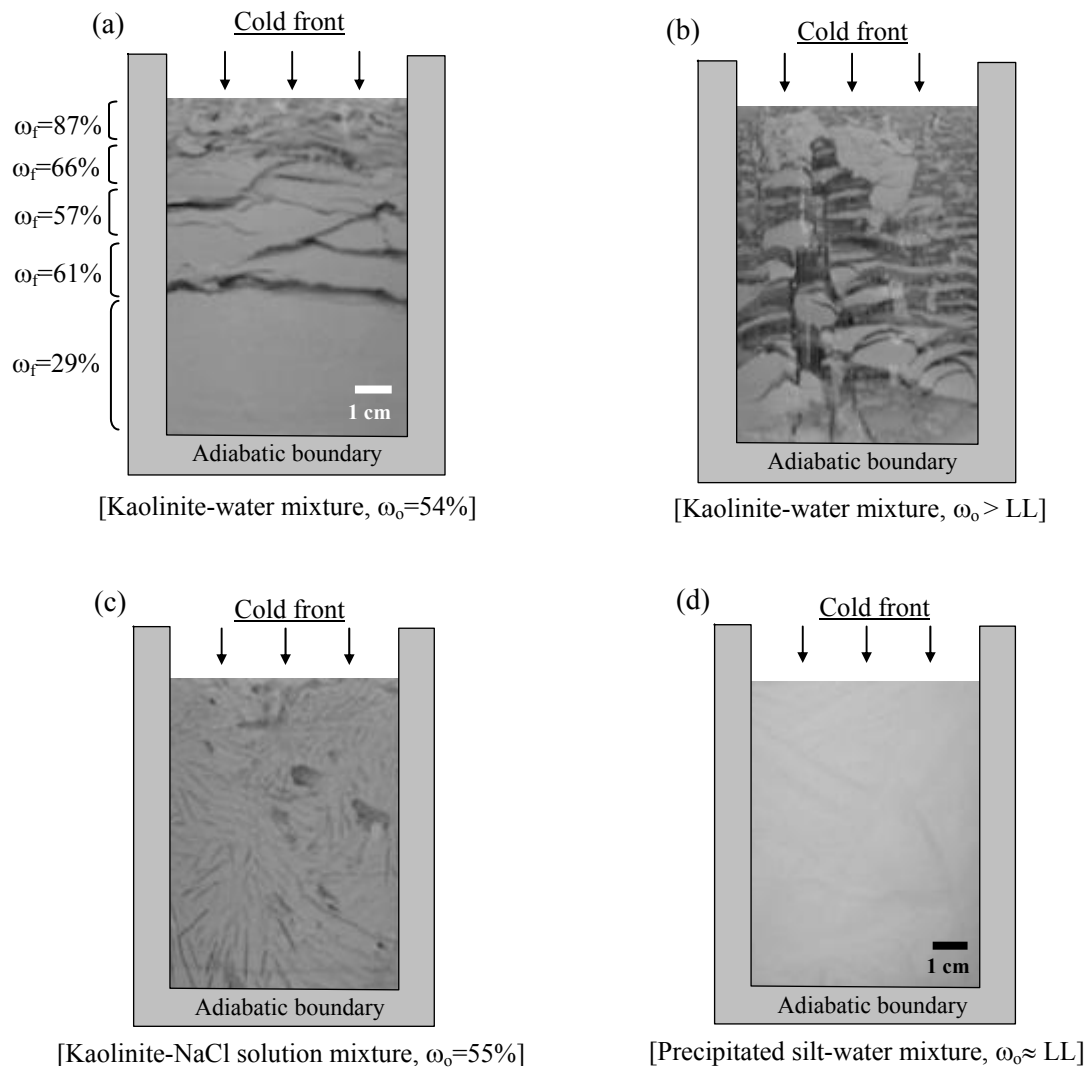


Figure 5.6 Ice lens formation within different soils at various water content and salt concentration. Heat is removed from the top; the other specimen walls are thermally insulated.

on the surface of the specimens to monitor surface displacements. The specimen and the microscope are placed inside a cooling chamber (at -15°C). As the ice lens grows, the displacement of granules is sequentially traced in digital microphotographs.

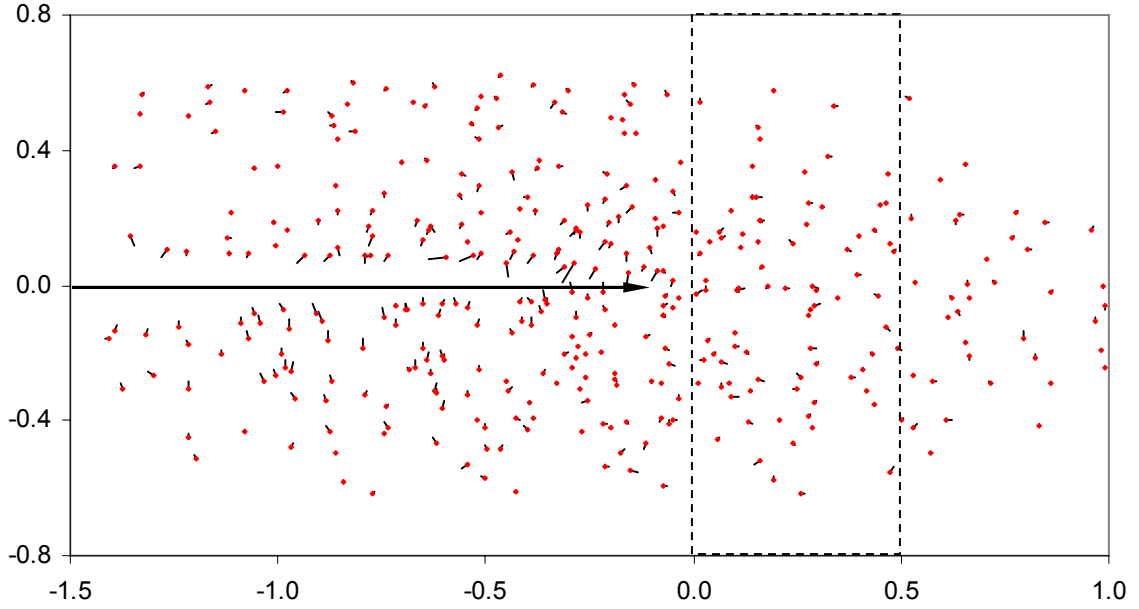
Figure 5.7 shows the growth of an ice lens with time. Displacement vectors are plotted in Figure 5.8. It is observed that displacements are normal-to and away-from the lens face. Therefore, the surrounding soil is compressed by the increasing volume of the lens body. On the other hand, granules move toward the lens tip ahead of the lens. This suggests water intake to the lens tip (Figure 5.8-b). A thin opening at the lens tip is observed prior to lens propagation. Apparently, pore water migration associated to lens growth and the corresponding stress field induced by the lens support its continuous growth.

5.3.3 *Lens Formation Controlled by Stress Boundary Condition*

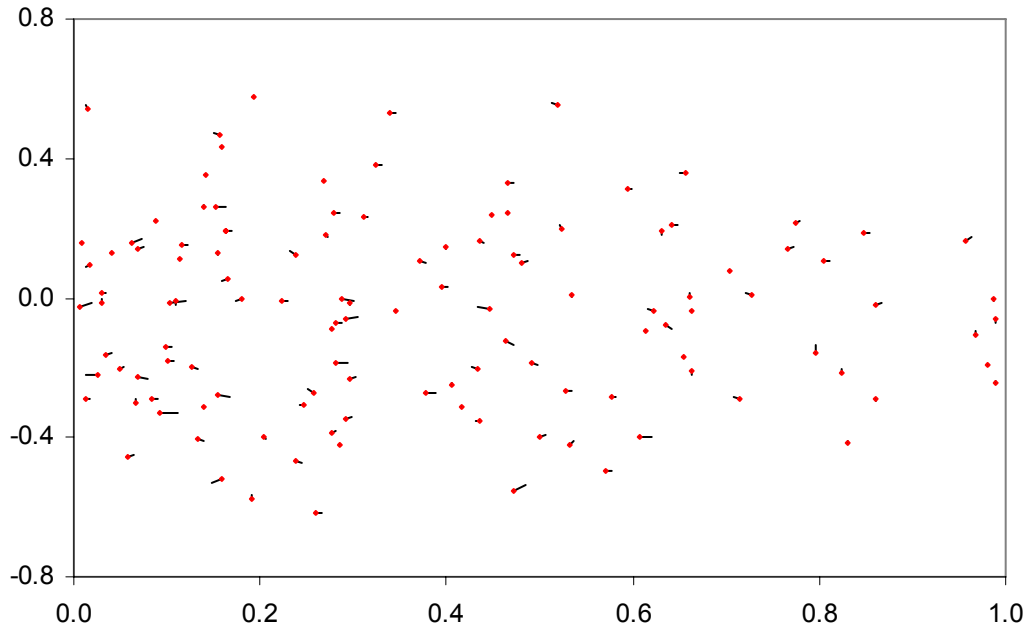
The effect of the stress field on lens formation is explored herein. Kaolinite specimens (Wilkey SA-1, LL=43%; mixed at $w_c \sim 36\%$ -to-40% near liquid limit) are consolidated to $\sigma_v' = 30\text{kPa}$ under k_0 conditions. After consolidation, the cylindrical specimen (10cm diameter and 7cm height) is extruded from the k_0 cell and a V-shape groove (1cm width x 4cm depth) is made along its height; then, a thin slot is cut at the tip using a sharp blade. Tension at the groove tip is exerted by loading the groove faces with 200g weights on each side. Alternatively, compression is applied by sitting the specimen on lateral points so to cause the groove to close. Figure 5.9 shows the experimental conditions in both cases. An example of the evolution of ice lenses from the tip in tension is shown in Figure 5.10.



Figure 5.7 Ice lens growth with time. A thin opening at the lens tip is observed prior to lens growth.



(a) Ice lens propagation (arrow indicates the lens growth direction).



(b) The movement of granules ahead of lens tip.

Figure 5.8 Displacement vectors in the sediment near the ice lens tip denoted. The red dots show the final point of each displacement. The bottom figure is an enlarged display of the region ahead of lens tip (unit: mm).

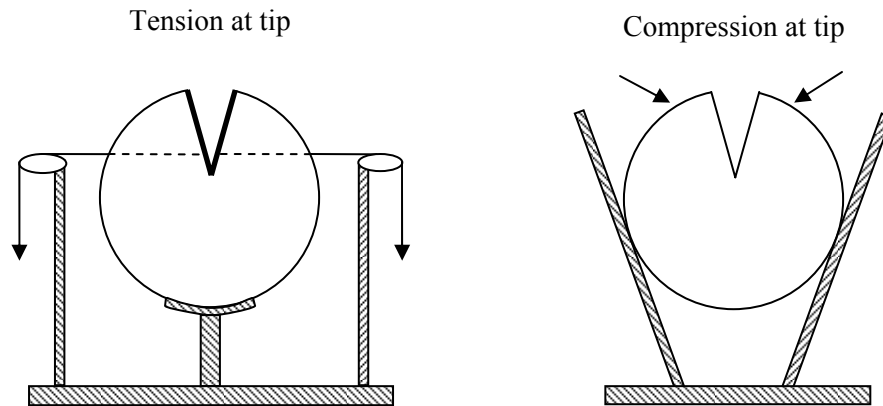


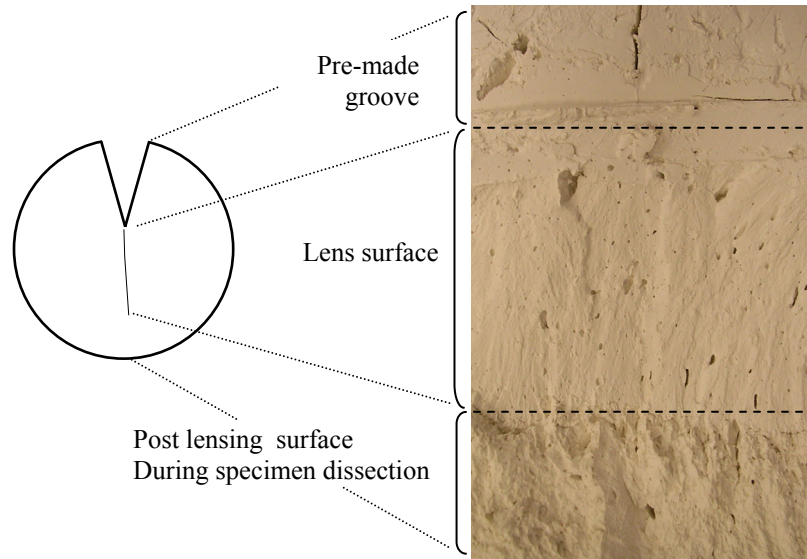
Figure 5.9 Experimental configuration to study the effect of stress on lens formation.

Experiments are repeated 6 times in tension and 3 times in compression. In all tension cases, an ice lens propagates vertically from the groove tip, following the tensile field (Figure 5.10-a, minor ice lenses form around the specimen). It appears that the tensile stress field promotes water migration towards the slot tip driven by the pressure gradient. Lenses do not form in the specimens where the stress field at the slot tip is in compression.

Tensile specimens are dissected upon completion of each test. The ice lens face has a unique texture. Ripple marks parallel to the lens growth direction are readily identified and exhibit very distinct surface texture compared to the rest of the surface created during dissection (Figure 5.10-b). Sketches of ice lens development in all 8 specimens are summarized in Table 5.2. Additional comments follow. A uniaxial cold front is applied and water fills the groove in test 1. A well defined ice lens forms from the groove tip, gradually deviating from the



(a) Ice lens evolution when subjected to tension



(b) Dissected lens surface

Figure 5.10 Lens formed in tension.

Table 5.2 Ice lenses formation under different stress boundary conditions.

Test	Stress	Ice lens evolution		
1	Tension			
2	Tension			
3	Tension			
4	Tension $wc=37.4\%$			
5	Tension $wc=36.3\%$			
				Tension stops
6	Tension + compression			
7	Compression $wc=37.1\%$			
8	Compression $wc=37.3\%$			

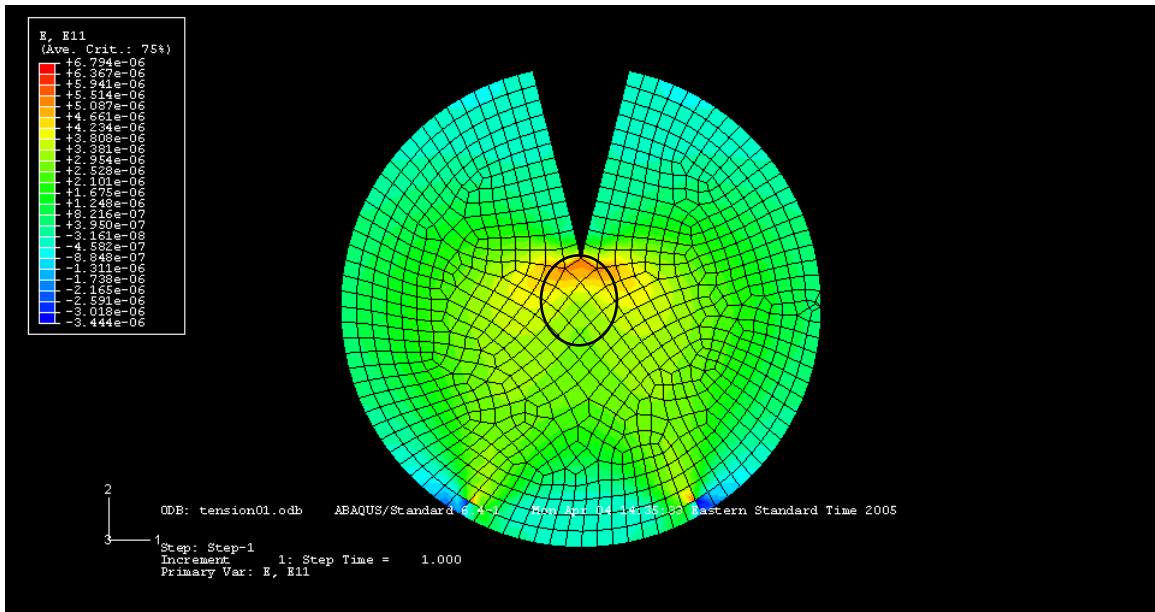
Stress: / cold front:

vertical direction. In all other tests, equal cold conditions are applied in all directions and no water is added at the groove. Applying tension at the groove tip promotes lens growth in all cases (test 1~4). The effect of tension is again verified in test 5, where tension is removed after a certain lens length, and the lens stops growing (other lenses develop throughout the specimen). Both compression and tension are applied in test 6 and a lens grows vertically upwards from the bottom groove that is on the tension side. Lenses initiate at the periphery of the specimen rather than at the tip in compression tests 7 and 8. In all cases where lenses grow, the lens tip curves away from regions under compression.

5.3.4 *Finite Element Model*

Specimens subjected to tension are modeled using the finite element method to confirm the stress and strain fields (homogeneous, elastic and isotropic model in plain strain-ABAQUS 6.4). A fixed displacement boundary condition is modeled at the bottom of the specimen (see Figure 5.9 for test condition). The specimen self weight and the pressure exerted on the groove faces are imposed. Figure 5.11 shows the evolution of strains in the specimen. Dilation develops near the groove tip (volumetric strain $2.93\text{E-}06 \sim 6\text{E-}08$ in the lens tip indicated by a circle in Figure 5.11-a). While self weight causes contraction at the center of the specimen the additional load on the groove faces causes a stress distribution at the groove tip that promotes the ice lens initiation and growth. It is herein hypothesized that growth is dominated by water migration to the tip caused by the lens propagation itself, rather than by the applied stress. Note that the strain field becomes contractive towards that lower part of the specimen and lenses curve away from the vertical plane.

(a) ϵ_1



(b) ϵ_2

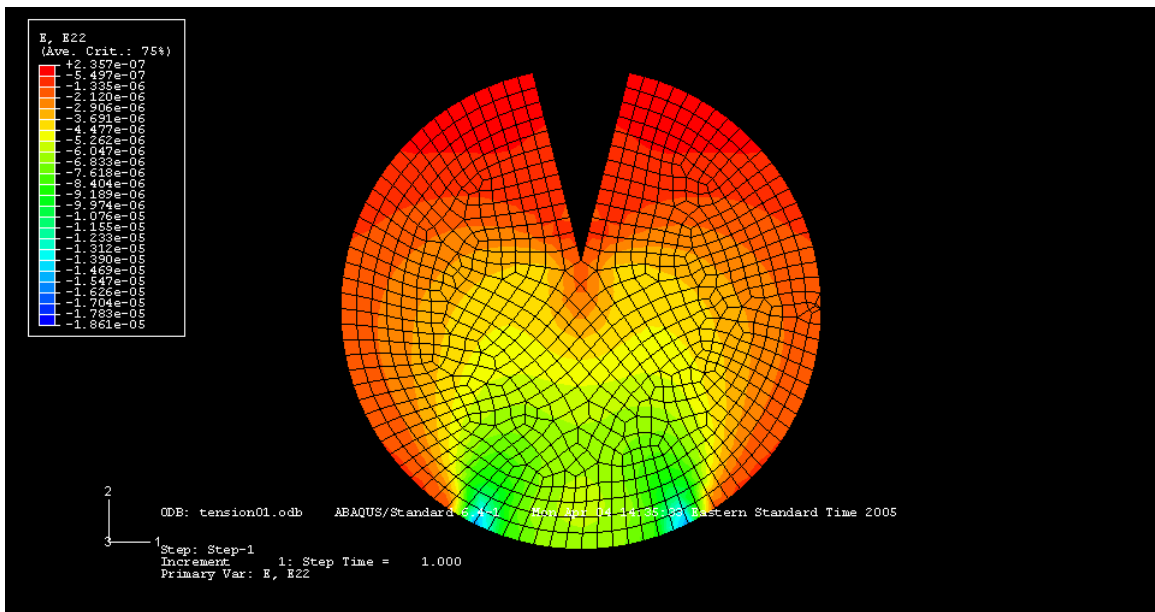


Figure 5.11 Strain evolution within the cylindrical specimen subjected to loading on the groove faces (plain strain – elastic FEM).

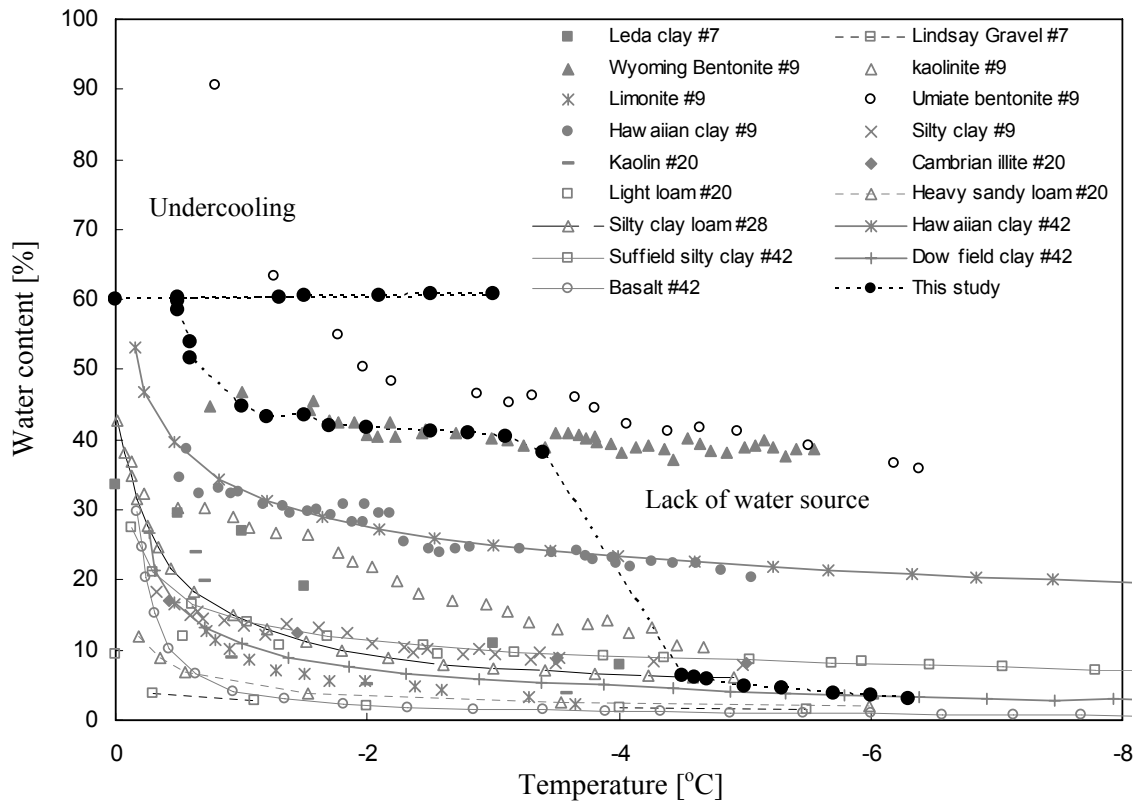


Figure 5.12 Unfrozen water content below 0°C temperature.
 Source: #7-Penner (1963), #9-Anderson and Morgenstern (1973), #20-Akimov et al.(1983), #28-Smith (1985), #42-Konrad and Duquenoii (1993)

5.3.5 Unfrozen Water Content

Unfrozen water can exist below the freezing temperature in small pores. Unfrozen water plays an important role in ice lensing. The existence of unfrozen water changes the soil-ice mixture properties such as hydraulic and thermal conductivities. The amount of unfrozen water is governed by the specific surface of soils, the electrolyte concentration, fabric type, packing geometry and P-T condition. The unfrozen water between particle and ice favorably reduces the interfacial free energy (Watanabe, 1999).

The unfrozen water content of a clayey soil (kaolinite SA-1, $S_a \approx 36\text{m}^2/\text{g}$) below freezing temperature is evaluated using permittivity measurements ($f = 300\text{kHz}\sim 1.3\text{GHz}$; device-HP 8752A; probe-HP 85070A). Permittivity is first related to water content through calibration tests. Then, the unfrozen water content is determined at different temperatures. Data are shown in Figure 5.12 where additional data found in the literature are also plotted. The water content does not decrease $\sim 40\%$ at -2 to -4 °C for high specific surface soils like kaolinite and bentonite; thereafter, it drops sharply as temperature decreases further.

The unfrozen water network in the pore space serves as water feeding paths to ice lenses. Indeed, ice lenses can not grow if pore ice blocks the void space in soils and lowers the hydraulic conductivity. These observations are compatible with observations of unfrozen layers after lens formation mentioned earlier in this chapter.

5.3.6 Particle Size and Freezing Rate

Ice lenses do not develop if the cooling front advances fast enough to trap solid particles. The attractive force causing the viscous drag between a particle and the cooling front and the repulsive force are

$$F_a = 6\pi\eta V_g \frac{R^2}{d - a_o} \quad (5.13)$$

$$F_r = 8\pi a_o^2 \Delta\gamma \frac{R^3}{d^2 (d + 2R)^2} \quad (5.14)$$

where η is fluid viscosity [poise], V_g ice lens growth rate [m/s], R particle radius [m], d distance between cooling front and a particle [m], a_o average molecular distance in water

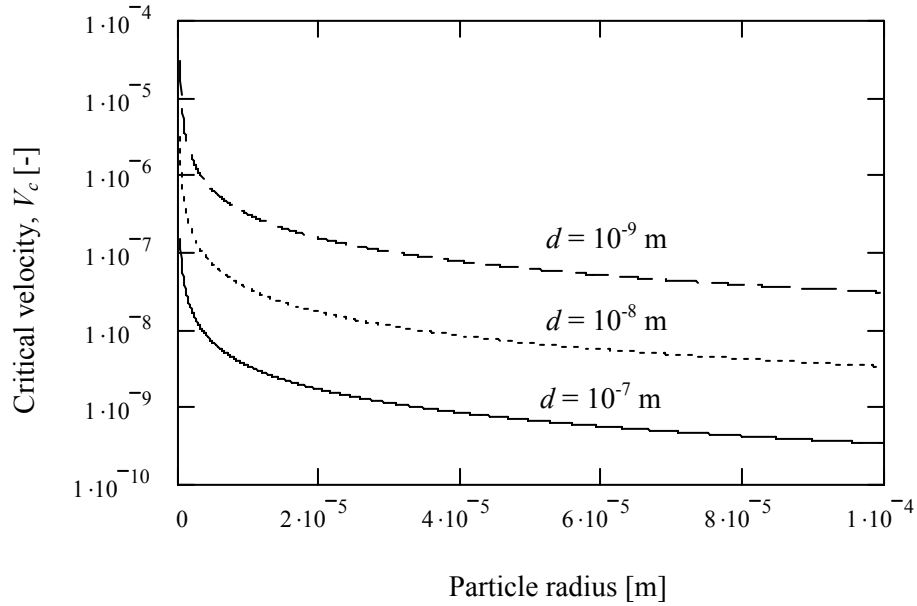


Figure 5.13 Critical velocity (V_c) versus particle radius (R). As the particle radius increases, a low critical velocity is needed to form ice lens.

$[1 \cdot 10^{-10} \text{ m}]$, and $\Delta\gamma$ surface tension difference between particle-water and ice-water $[0.342 \text{ N/m}]$. Ice lens can form in case that $F_r > F_a$. The critical ice lens growth velocity is determined from the force equilibrium between two forces (Watanabe, 1999). The dimensionless form of the critical velocity V_c is

$$V_c \cdot \frac{\eta}{\Delta\gamma} = \frac{4}{3} \cdot a_o^2 \cdot R \cdot \frac{(d - a_o)}{d^2 \cdot (2R + d)^2} \quad (5.15)$$

Figure 5.13 shows a plot of the critical velocity as a function of particle radius R and distance d . Sand-size sediments require a very low critical velocity to form ice lens (see also Rempel and Worster, 1999). However, phase transformation begins just after the temperature drops below the freezing temperature, and then the high thermal conductivity of sediments controls the evolution of freezing. Therefore, ice lenses rarely form in coarse grained soils because the freezing rate is faster than in fine grained soils. As the

freezing rate increases, the spacing between ice lenses decreases and lens formation is inhibited. The freezing rate is more effective than temperature gradient to control ice lens formation (Konrad, 1989).

5.4 DISCUSSION - GAS HYDRATE FORMATION

The formation of gas hydrate lenses in nature is analyzed herein on the bases of the insight gained with ice lensing.

The gas hydrate stability boundary depends on temperature and fluid pressure conditions. Formation in the seafloor typically takes place under several hundred meters of water and sediment. Then the question arises whether gas hydrate formation can develop in this natural setting.

Ice lenses form preferably under low overburden pressure. The discrete ice lens theory (Nixon, 1991) is invoked to address this problem. It has a much simpler form than the rigid ice model theory (O'Neill and Miller, 1985) and it encompasses the segregation potential theory (Konrad and Morgenstern, 1980). The criterion for lens initiation is that the ice pressure P_i overcomes the sum of the overburden pressure P_o acting on incompressible particles and the particle separation pressure P_{sep} in a frozen fringe (for a the detailed discussion of this model, see Gilpin 1980 and Nixon 1991). The ice pressure is

$$P_i = \frac{1}{1.09} \cdot \left[\left[(1.09 \cdot (P_o + P_{sep}) + \beta \cdot T - P_u) \cdot \left(1 - \frac{x}{a}\right)^{1+\alpha} + P_u \right] - \beta \cdot T \right] \quad (5.16)$$

where $\beta = 1.222$ [MPa/K], T freezing temperature, P_u hydrostatic pressure, “ a ” frozen fringe length, and α experimentally determined coefficient between hydraulic conductivity and temperature (typically $\alpha = 1.5$). The particle separation pressure P_{sep} is

$$P_{sep} = \frac{2\sigma_{sL}}{R} Pr \quad (5.17)$$

where σ_{sL} is 0.028 [N/m], $R=1 \cdot 10^{-6}$ [m] and $Pr=1$ (see Nixon, 1991 for the calculation of parameter Pr). The calculated value is $P_{sep}=56.6$ kPa.

In permafrost region. It is assumed that the hydrostatic pressure is 0 Pa since the region above the lens initiation location is completely frozen. The calculated ice pressure (P_i solid line) and total pressure (P_o+P_{sep} dotted line) in a frozen fringe are plotted versus depth in Figure 5.14. As depth increases, the total pressure exceeds the ice pressure and the possible region of lens initiation in a frozen fringe decreases as well. The total pressure exceeds the ice pressure at 492m depth so that no lens can form below this depth.

The overlapped area between the phase boundary for gas hydrate and the geothermal gradient indicates that the gas hydrate stability zone extends from 180m-to-1060m (Figure 5.15). However, the depth of potential hydrate lens formation is limited from 180m to 492m.

Seafloor. The ice pressure is calculated taking into consideration the hydrostatic pressure, the overburden pressure and the given ocean depth (assumed to be 1200m for this analysis). Furthermore, it is assumed that sediments are fully saturated. The total pressure is higher than the ice pressure at a depth of 804m from the seafloor (Figure 5.16). The hydrate stability zone in the ocean is narrower than that in permafrost regions, and it is 300m deep from the seafloor. Then hydrate lenses can occur everywhere in the stability

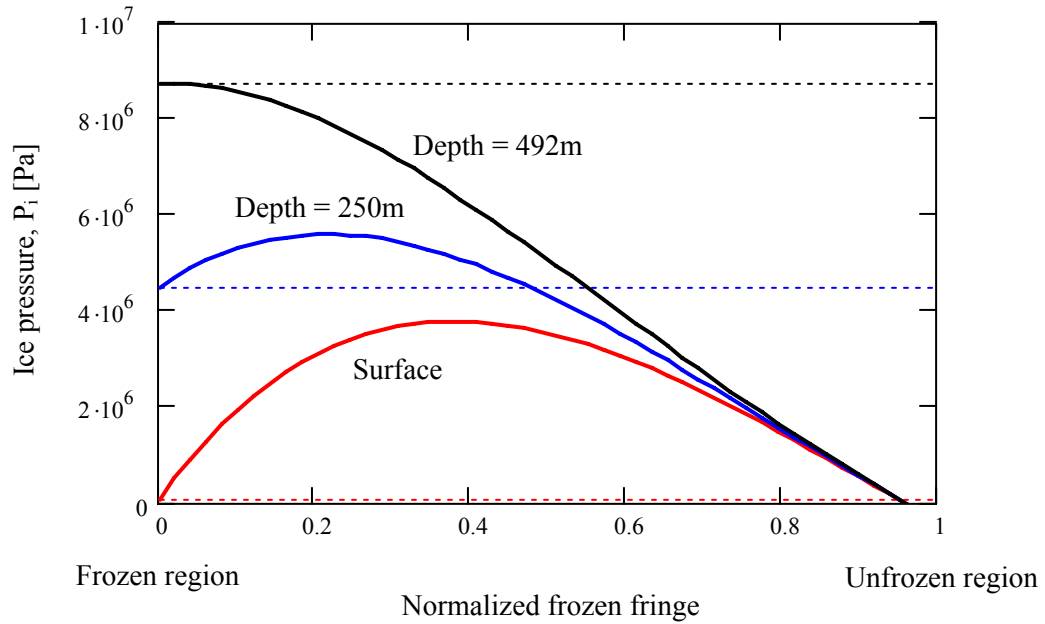


Figure 5.14 Calculated ice pressure in a frozen fringe in permafrost region. Dotted lines indicate the critical pressures (overburden pressure P_o + separation pressure P_{sep}). Ice lenses initiate when $P_i \geq P_o + P_{sep}$. The maximum depth where lenses can form is 492m.

zone (Figure 5.17). Note that hydrate lens formation in natural systems is also affected by other parameters such as sediment type, methane source, pore fluid concentration and geological structure. It is important to highlight that this analysis was conducted using pressure and associated volumetric strain for gas hydrate equal to ice.

5.5 CONCLUSIONS

Natural gas hydrates form in different ways such as disseminated, nodular, layered and massive forms. The understanding of ice lensing in shallow soils can help explain hydrate lens formation in nature. Many governing factors determine ice lens

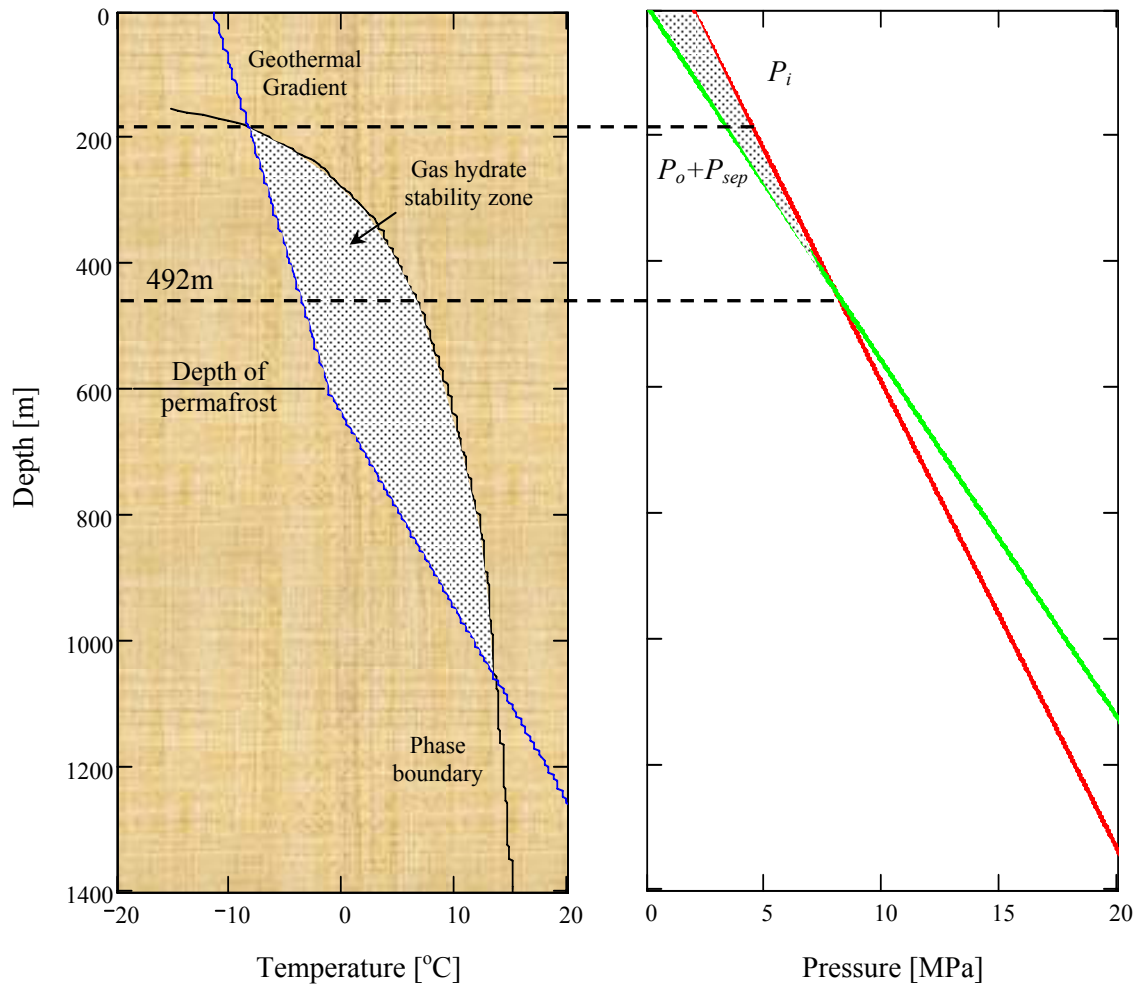


Figure 5.15 Gas hydrate stability zone and the possible lensing region in permafrost.

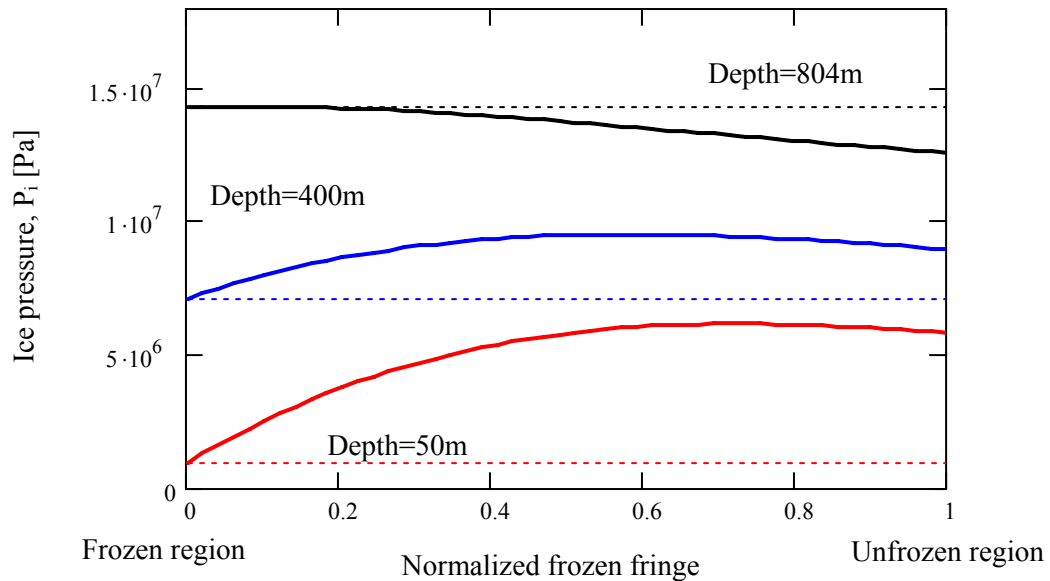


Figure 5.16 Calculated ice pressure in a frozen fringe in seafloor condition. Dotted lines indicate the critical pressure (overburden pressure P_o + separation pressure P_{sep}). Ice lenses initiate when $P_i \geq P_o + P_{sep}$. The maximum depth where lenses can form is 804m from the seafloor.

formation, including soil type, stress boundary and freezing condition. New experimental results show that:

- Ice lenses form normal to the heat flux direction in high specific surface soils – kaolinite and precipitate silt.
- Unfrozen water in the pore space migrates to the lens tip during phase transformation, lens propagation compresses the surrounding soils and the water content in soils is redistributed after phase transformation.

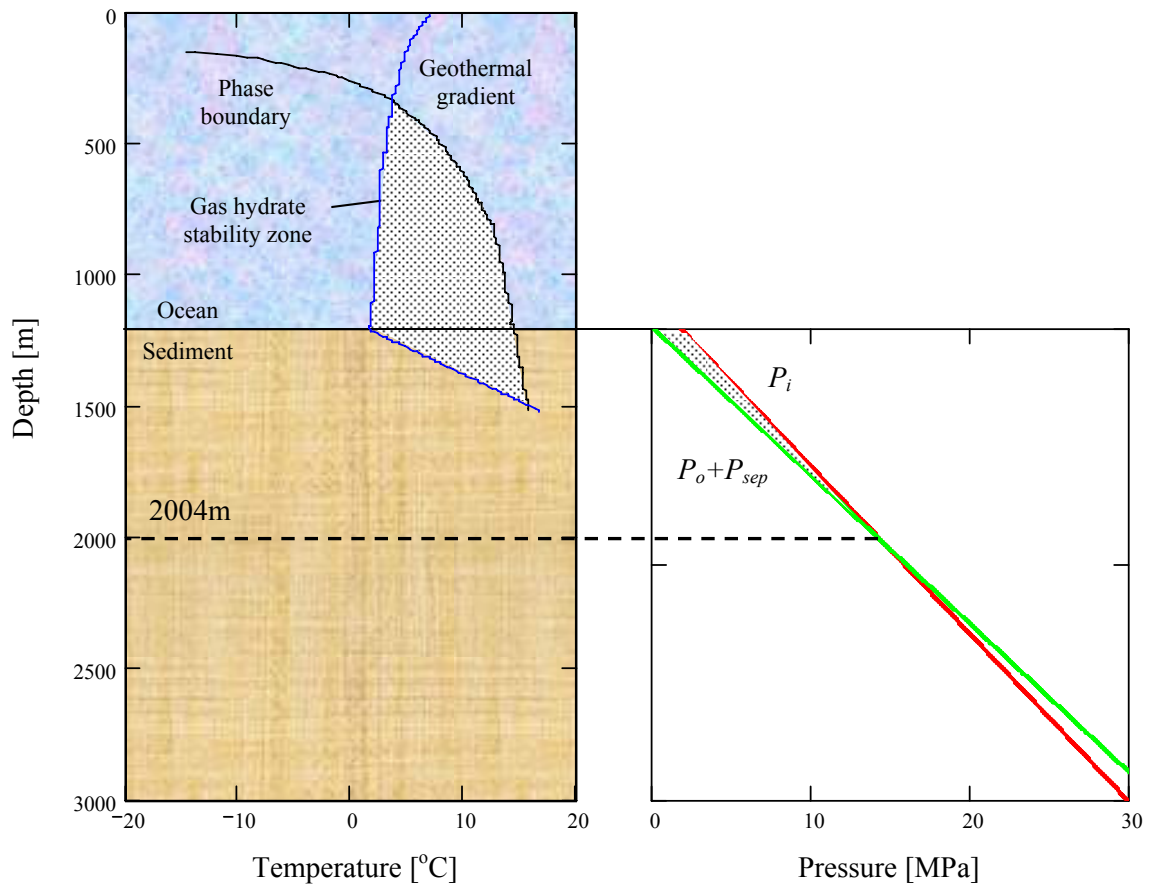


Figure 5.17 Gas hydrate stability zone and the possible lensing region in seafloor.

- The initial stress field in soils plays an important role in lens formation and growth. Tension (low compression) facilitates lens initiation, and lens formation is hindered under high compression.
- As particle size increases, a lower freezing rate is required to form ice lenses.
- Hydrate lenses can form everywhere of the stability zone in the seafloor while they have a limited formation range (~490 m depth) in permafrost regions.

CHAPTER VI

INSTRUMENTED HIGH-PRESSURE CHAMBER

6.1 INTRODUCTION

The study of gas hydrates is important to engineers and scientists who study energy resources, oil recovery, seafloor stability and global climate change. The local and global characterization of gas hydrates beneath the seafloor is necessary to understand the fundamental behavior of hydrate bearing sediments in the context of these scientific and engineering challenges. However, the unique pressure and temperature stability conditions of gas hydrate challenges the research efforts. In particular, hydrate is not stable in boreholes under atmospheric pressure and it dissociates during standard core recovery operations. Indeed proper sampling requires maintaining the in-situ pore pressure, effective stress and temperature during the recovery of hydrate-bearing sediments.

Various Ocean Drilling Programs (ODP) coring, sampling and downhole measurement methods have been developed and they are briefly described in Table 6.1. Conventional coring technology causes sediment destruction and hydrate destabilization due to pressure release during recovery. After ODP leg 164 in 1995, researchers launched the development of advanced tools designed to maintain the in-situ fluid pressure during and after core recovery. The resulting HYACE system (HYdrate Autoclave Coring Equipment) by the European MAST programme (from 1998 to 2001) included a

Table 6.1 Features of ODP (Ocean Drilling Program) coring techniques.

Coring Method	Features
APC (Advanced Piston Corer)	<ul style="list-style-type: none"> - Hydraulically actuated piston corer. - Relatively undisturbed and continuous (9.5m) samples. - Proper for very soft to firm sediment. - 200-250m below the mud-line. - Not good for stiff sediments.
XCB (Extend Core Barrel)	<ul style="list-style-type: none"> - Deployed when sediments are too stiff for APC. - 9.5m long and 500-600m below the mud-line.
PCB (Pressure Core Barrel)	<ul style="list-style-type: none"> - 1m core sample keeping 10,000 psi pressure. - Mainly used for recovery of gas hydrate sample.
MDCB (Motor Driven Core Barrel)	<ul style="list-style-type: none"> - For fractured crystalline rock, interbedded formation. - 4.75m core length.
RCB (Rotary Core Barrel)	<ul style="list-style-type: none"> - Rotary coring system. - Proper for firm to hard sediments and igneous basement. - 9.5m core length
ADCB (Advance Diamond Core Barrel)	<ul style="list-style-type: none"> - 4.75m core length - Proper for firm to well-lithified sediment or igneous formation.
APCT (Advanced Piston Corer Temperature)	<ul style="list-style-type: none"> - Instrumented version of APC. - Proper for soft sediments. - Temperature measurement to determine the heat flow gradient taking 8 min.
DVT(P)P (Davis-Villinger Temperature (pressure) Probe)	<ul style="list-style-type: none"> - Temperature gradient measurement instead of APCT (stiff). - 10 min for temperature / 40 min for pressure measurement. - 10,000 psi operation (DVTTP).
WSTP (Water Sampling Temperature Probe)	<ul style="list-style-type: none"> - Temperature measurement between cores. - 1-3 hours for each measurement.
APC Methane Tool	<ul style="list-style-type: none"> - Conductivity, temperature, pressure of core measured. - To determine the existence of hydrate by conductivity change.
JNOC PTCS (JNOC Pressure Temperature Core Sampler)	<ul style="list-style-type: none"> - Top-drive rotary / push (pressure-temperature)
HYACINTH (Pressure coring and logging)	<ul style="list-style-type: none"> - Consists of FPC (Fugro Pressure Corer) and HRC (HYACE Rotary Corer) coring tool. - Implemented with the associated pressure logging, transfer and storage data chamber.

Source: www.jamstec.go.jp

Table 6.2 HYACE and HYACINTH systems.

HYACE (HYdrate Autoclave Coring Equipment)		HYACINTH (Development of HYACE tools In New Tests on Hydrates)
FPC (Fugro Pressure Corer)	HRC (HYACE Rotary Corer)	
- Water hammer to drive the core barrel into the sediment	- Inverse Moineau Motor to rotate the cutting shoe.	HYACE operation and pressure core transfer system development for the further investigation.
- 1m ahead of drill bit	- 1m (max 1.5m) ahead of drill bit.	
- Unlithified sediment covering stiffclay to sandy material	- Lithified sediment or rock	
- Diameter: 57mm	- Diameter: 50mm	

Source: www.geotek.co.uk

percussion corer (called Fugro Pressure Corer) and the HYACE rotary corer. The features of these pressure corers are summarized in Table 6.2. The main advantages of the HYACE system are:

- The corer is much more stable in the borehole since the coring tool is driven from the bottom not from the drilling string on the ship. This results in good quality cores.
- The wireline coring tool in the HYACE system permits the transfer of recovered cores to the laboratory transfer chamber while maintaining the fluid pressure.

The next generation system, named HYACINTH (development of HYACE tools In New Tests on Hydrates) came on line in 2001. In this system, pressure equilibrium and longitudinal transfer into a shear transfer chamber enable the obtained pressure core to be transferred to the storage chamber of the laboratory transfer chamber without losing the in-situ pressure. This is beneficial for geophysical logging (in particular, P-wave velocity

and gamma density measurements), microbiological and petrophysical studies. Nevertheless, the identification of gas hydrate bearing sediments by non-destructive tests remains limited and more direct and sophisticated measurement techniques are necessary for gas hydrate research.

The design of a new instrumented high-pressure chamber is presented herein. This development is part of the joint industry drilling project in the Gulf of Mexico, led by ChevronTexaco as part of the U. S. department of Energy's National Methane Hydrate Research and Development program. The goals in the design of the instrumented high-pressure chamber are to collect mechanical and electrical properties (P- and S-wave velocity, strength and electrical resistance) of gas hydrate bearing sediments by means of direct measurements on stable, pressured cored specimens. This chapter documents the development of the high-pressure chamber, the instrumentation, and corresponding data reduction techniques.

6.2 DESIGN AND CONSTRUCTION

The design of the instrumented high-pressure chamber (hereafter IHPC) has gradually evolved to take into consideration unique design criteria – compatibility with peripheral instrumentation, workability (fast and robust), and safety. The IHPC consists of three parts: 1) pressure chamber, 2) instrumented rods, 3) rod guide and position control system. The design criteria satisfy ESH manual Doc. 18.2 (pressure vessel and system design). Stainless steel (316 SS) is selected for all components to resist corrosion by seawater.

6.2.1 *Design Evolution*

The different design alternatives, their advantages and disadvantages are summarized in Table 6.3. Alternative I consists of a 1m-long core chamber with equally spaced measurement ports; the specimen is fixed inside the chamber. Alternative II has a single measurement test station and the end manipulators control longitudinal displacement and rotation. Alternative III has a short section of aligned measurement ports and manipulators that control the longitudinal position of the specimen. Alternative III is selected as an optimal combination of versatility and robustness. Detailed design considerations and solutions are summarized in Table 6.4.

The core transfer mechanism is shown in Figure 6.1. The IHPC is connected to the storage chamber where the pressure core is kept after drilling (within its plastic liner), and to the extension chamber. Quick clamps fix components together. The ball valve in the storage chamber is opened after the inside pressure of the IHPC reaches the same fluid pressure as the storage chamber. The manipulators grab the pressure core and slide it into the IHPC without allowing rotation. Then, the properties of gas hydrate bearing sediments are sequentially measured through instrumentation ports. This operation starts by drilling two diametrically opposite holes through the plastic liner.

6.2.2 *Pressure Chamber*

The pressure chamber is designed to accommodate the instrumented rods. The overall length is 690.5mm. The wall thickness is 12.5mm to sustain a fluid pressure of ~36MPa with a safety factor ~5 (Mathgram 6.1). Flanges at both ends match similar flanges in the storage and extension chambers (by GeoTek, Inc.). The IHPC has two

Table 6.3 Design evolution of instrumentation.

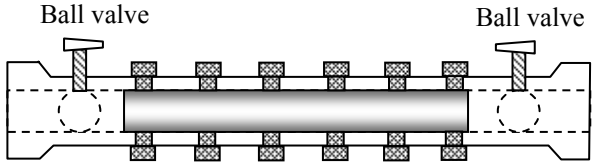
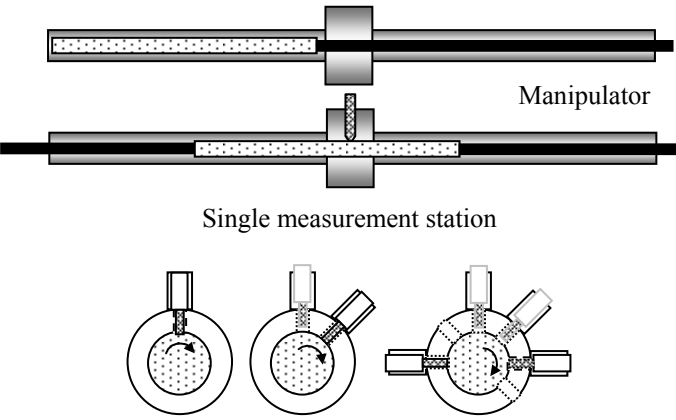
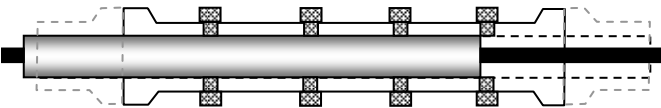
Alternative	Schematic Design	Features	
		Advantages	Disadvantages
I	 <p>Multiple ports along the chamber per side</p>	<ul style="list-style-type: none"> - No depressurization - No gas expansion 	<ul style="list-style-type: none"> - Measuring at each section iteratively requires connecting / disconnecting each tool. - Test would be slow. - Possible safety concern in terms of many steps.
II	 <p>Single measurement station</p>	<ul style="list-style-type: none"> - All of above - Tools remains under pressure. - Mounting / dismounting operations are avoided. - Safer and faster. - Similar measurement station could be added in series 	<ul style="list-style-type: none"> - Manipulator does not allow the rotation.
III		<ul style="list-style-type: none"> - All of the above - Rotation is not needed. 	<ul style="list-style-type: none"> - Relatively long string is involved.

Table 6.4 Design considerations and solutions.

Considerations	Solutions
Couple the pressure chamber with the storage chamber housing pressure core	Identical flange design with storage chamber
Pressure chamber factor of safety	FS=5 @ 36 MPa
Advancing / rotational motion of drill bit and force against high pressure	Advancing motion by screw force / rotation by drilling with ball bearing / high pressure O-ring (30MPa) for helical motion
Advancing motion and force against high pressure / pressure and fluid leakage / shielding electronics	Advancing motion by screw force and ball bearing / 8mm diameter rods / same O-ring as drilling / Strong epoxy with low viscosity
Maintain pressure / spare parts	Ball valve controls pressure / spare sensors
Simple / robust / reliable / minimal machining	Design with readily available off-shelf parts

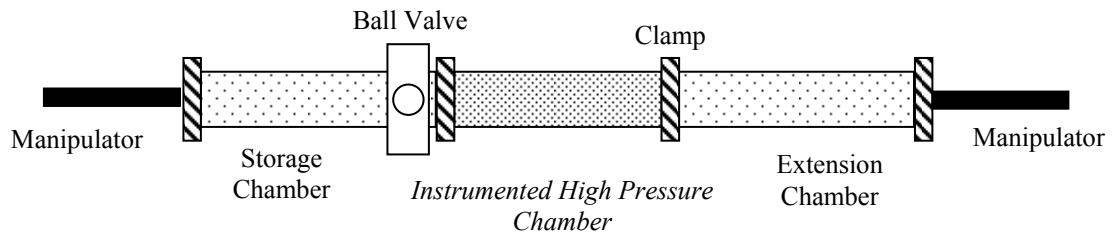
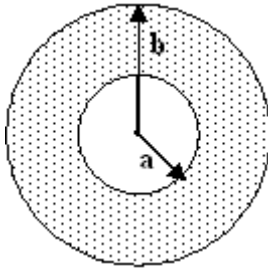


Figure 6.1 Pressure core transfer mechanism. The manipulator slides the pressure core from the storage chamber into the instrumented high-pressure chamber.

Mathgram 6.1 Pressure chamber mechanical design.

Depth	$z := 3600 \text{ m}$	
Water unit weight	$\gamma_w := 10 \cdot 10^3 \cdot \frac{\text{N}}{\text{m}^3}$	
Pressure	$P := z \cdot \gamma_w$	$P = 3.6 \times 10^7 \text{ Pa}$
Yield Strength	$S_y := 40 \cdot 6.895 \cdot 10^6 \cdot \frac{\text{N}}{\text{m}^2}$	$S_y = 2.758 \times 10^8 \text{ Pa}$
Tensile Strength	$S_t := 84 \cdot 6.895 \cdot 10^6 \cdot \frac{\text{N}}{\text{m}^2}$	$S_t = 5.792 \times 10^8 \text{ Pa}$
Young's modulus	$E := 15.5 \cdot 10^6 \cdot \text{psi}$	$E = 1.069 \times 10^{11} \text{ Pa}$
Poisson ratio	$\nu := 0.26$	
Internal radius	$r_i := \frac{2.559}{2} \text{ in}$	$r_o := \frac{3.543}{2} \text{ in}$ $th := r_o - r_i$

Transverse assessment



$$\sigma_r = \frac{a^2 \cdot \pi}{b^2 - a^2} \left(1 - \frac{b^2}{r^2} \right)$$

$$\sigma_\theta = \frac{a^2 \cdot \pi}{b^2 - a^2} \left(1 + \frac{b^2}{r^2} \right)$$

when outer pressure is equal to zero.

And, the radial stress (σ_r) is compressive and tangential stress (σ_θ) is tensile. The tangential stress is the greatest at the inner surface $r=a$.

$$a := r_i \quad b := r_o$$

$$\sigma_{\theta \max} := \frac{P}{b^2 - a^2} \cdot (a^2 + b^2)$$

$$\sigma_{\theta \max} = 1.145 \times 10^8 \text{ Pa}$$

$$\frac{S_t}{\sigma_{\theta \max}} = 5.057$$

parallel rows of 4 identical sequential ports. The chamber design and the manufactured chamber are shown in Figure 6.2. An auxiliary tube is designed to house and align smaller diameter cores (HRC) (Figure 6.3).

6.2.3 Instrumented Rods

The drill bit and transducers are installed at the end of 8mm diameter and 30cm long stainless steel rods. The force on a rod tip is ~1 kN under 20 MPa fluid pressure. The buckling load is computed in Mathgram 6.2. For elastic wave velocity and strength measurements, rod endings are trimmed (6mm) to facilitate introducing transducers into drilled holes.

Drill rods. Various commercially available drill bits are tested. Shapes include pilot tip, flute bit, no wing bit and tip with a cone shape and large angle (Table 6.5). All these drill bits are tested to identify the characteristics that lead to best performance. The selected drill bit design (built by Withers. Co.) is also shown in Table 6.5.

P-wave measurement & Rods (Figure 6.4-a). The miniature pinducer barrel (Valey Fisher, VP1093) and connecting coaxial cable (Belden, 8216) slide inside the rod that are fixed with a high strength, low viscosity epoxy (EPO-TEK, 301).

S-wave measurement & Rods (Figure 6.4-b). Bender elements (PIEZO, Y-poles for parallel operation) are used for S-wave measurements. The 4mm bender element sticks out of the rod to attain optimal signal generation and detection. The connecting co-axial cable and pinducers are fixed to the rod with epoxy.

Electrical resistance measurement & Rod (Figure 6.4-c). The electrical needle probe described in Cho et al. 2004 is used to measure the electrical resistance of the specimen.

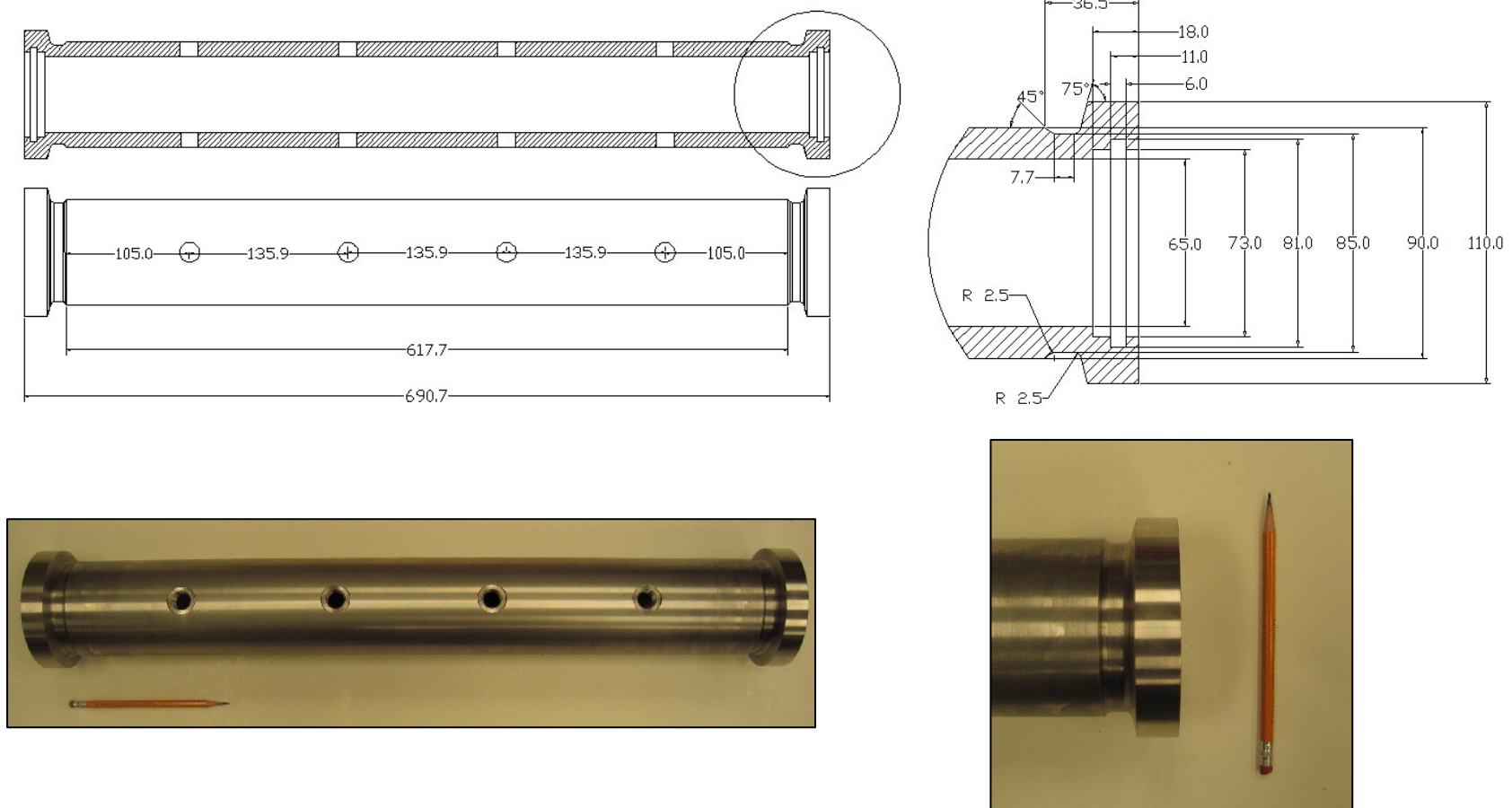


Figure 6.2 The high pressure chamber (without instrumentation ports). End flanges are designed to attach to storage and extension chambers with quick clamps (all dimensions in mm).

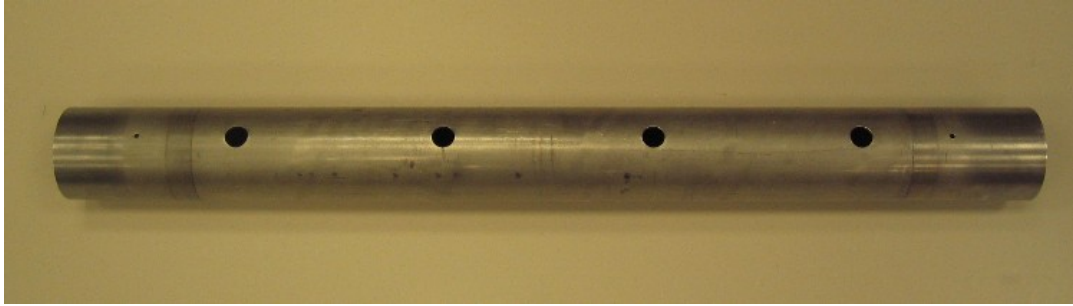










Figure 6.3 Auxiliary tube to align smaller diameter core (HRC). 4 bolts tighten the tube.

Mathgram 6.2 Buckling load for instrumented rods.

Critical buckling load:	$P_{cr} = \frac{\pi^2 \cdot E \cdot I}{L^2}$	
Tube length:	$L := 1\text{ft}$	
Diameter	$R_o := \frac{5}{32}\text{in}$ (outside)	$R_i := \frac{0.147}{2}\text{in}$ (inside)
Elastic modulus:	$E := 1.069 \cdot 10^{11}\text{Pa}$	
Wall thickness:	$t := R_o - R_i$	$t = 2.102\text{mm}$
Radius:	$R := R_i + \frac{t}{2}$	$R = 2.918\text{mm}$
Moment of Inertia:	$I := \pi \cdot R^3 \cdot t$	$I = 1.64 \times 10^{-10}\text{m}^4$
Calculated CBL:	$P_{cr} := \frac{\pi^2 \cdot E \cdot I}{L^2}$	$P_{cr} = 1.863 \times 10^3\text{N}$

Table 6.5 Drill bit - Tested and selected bit.

Bits		Features
Forstner Bit		<ul style="list-style-type: none"> - Pilot point at bit tip - Remnant shape: thin disc (into a liner) - Small pieces / twisted long remnant
Spade Bit		<ul style="list-style-type: none"> - Pilot point at bit tip - Remnant shape: thin disc (into a liner) - Aggregated remnant remains at tip - Small pieces before the wing bits touch
Glass Bit		<ul style="list-style-type: none"> - No thin disc into a liner / small pieces - Need more sharpen tip
Flute bit		<ul style="list-style-type: none"> - Positioning is difficult - Remnant shape: aggregated at bit tip
Twist bit		<ul style="list-style-type: none"> - Remnant shape: small thin disc (into a liner) - Twisted long remnant
Cone bit		<ul style="list-style-type: none"> - No pilot point at bit tip - Smaller remnant than others - No thin disc into a liner
Brad Point Bit		<ul style="list-style-type: none"> - Pilot point at bit tip - Remnant shape: thin disc (into a liner) - Twisted long remnant
		<ul style="list-style-type: none"> - Tip angle: 150° - Long flutes - Produce the small chips

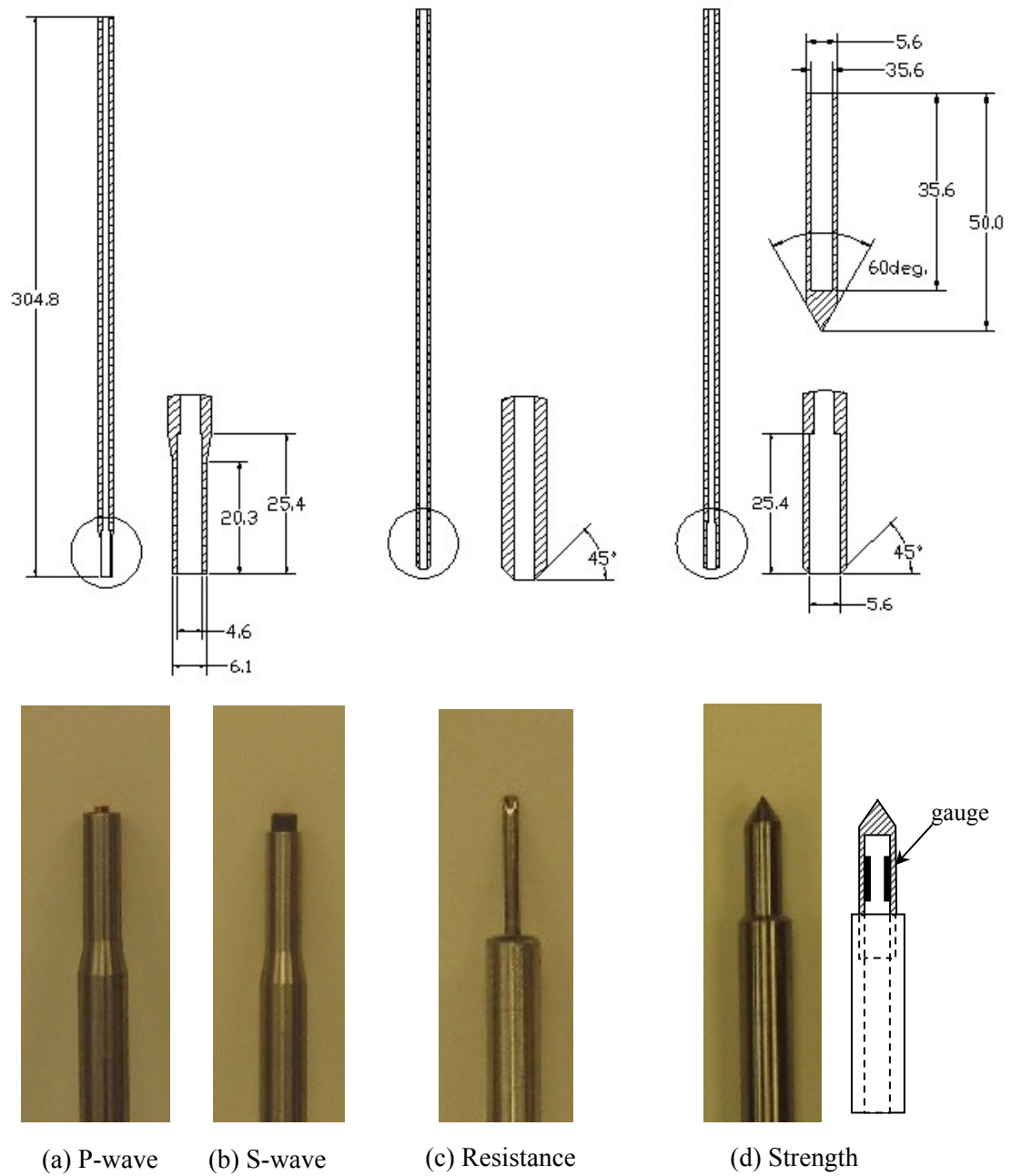


Figure 6.4 Instrumented rods - Details (all dimensions in mm).

The needle tip sticks 2.5cm ahead of the rod to profile the specimen.

Strength measurement & Rod (Figure 6.4-d). Strength is measured using a specially designed cone-shaped stud. The full-bridge strain gauge circuit is mounted on the inner wall of the cone tube (StrainSert, Inc.) which is fixed to the rod with epoxy.

In all rods, the electrical wire is protected as it exits the rod with shrink tube to prevent shearing it. The maximum penetration depth of each instrumented rod into the specimen is 15.2mm for elastic wave measurements, 35.5mm for strength measurements and 33.0mm for resistance measurements.

6.2.4 *Rod Guide and Position Control System*

Instrumented rods penetrate into the pressurized chamber through 2.54 cm diameter rod guides (Figure 6.5-a). The inside hole houses a high-pressure O-ring which can accommodate rotation, oscillation, and helicoidal motion of instrumented rods while withstanding ~30 MPa (Busakshamban, Turcon Roto Glyd Ring-TGX000313-Z80NA, PTFE, polytetrafluoroethylene sea-water resistant).

The driver consists of a cylinder welded to a drive nut that advances along the externally threaded rod guide, and in so doing pushes the instrumented rods (Figure 6.5-b). The torque required to rotate the nut is 7.6 Nm for a 20 MPa chamber pressure (Mathgram 6.3). Flat ball bearings between instrumented rods and drivers minimize friction, facilitate drilling and prevent rotation of direction-dependent bender elements (Figure 6.5-c).

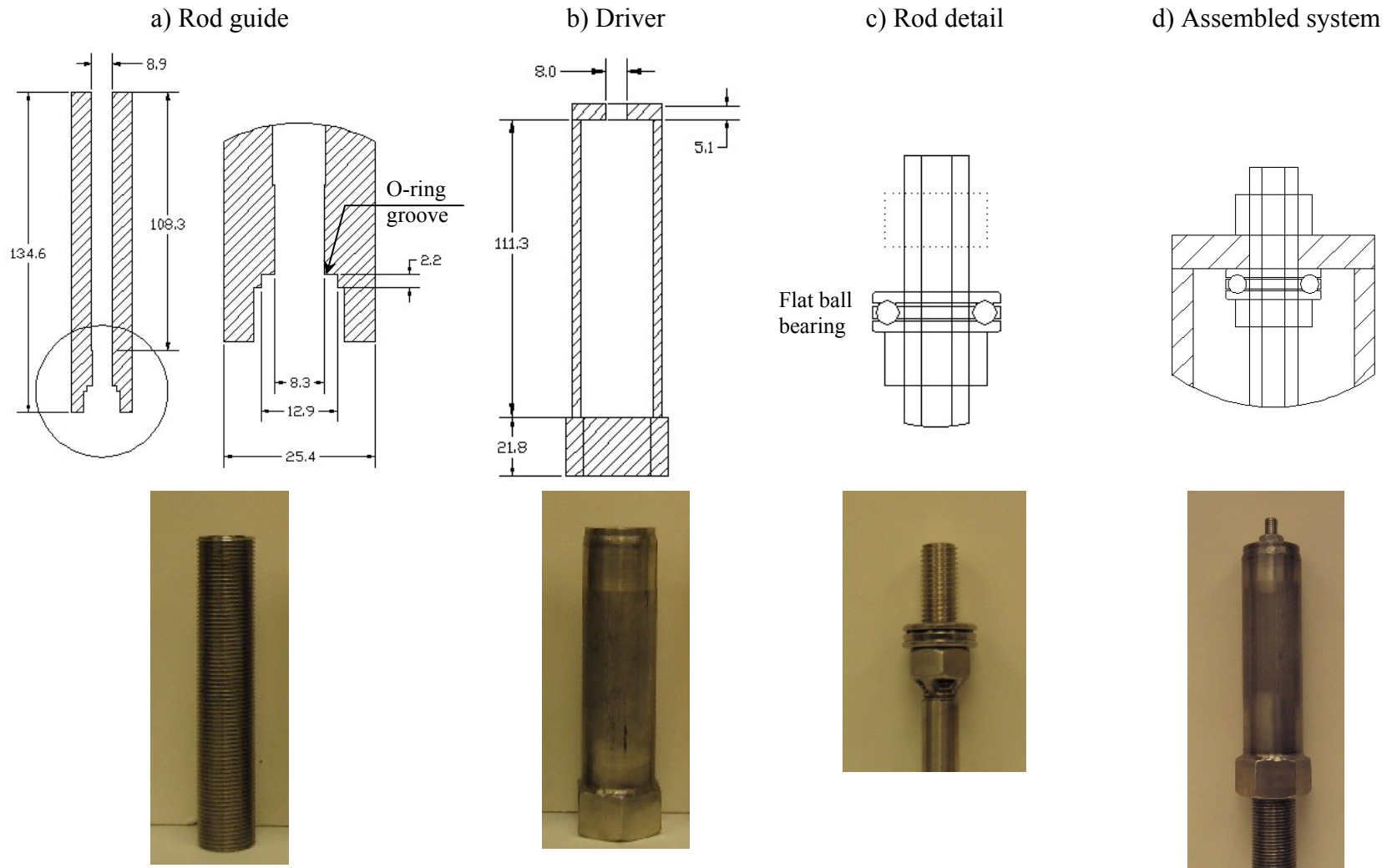
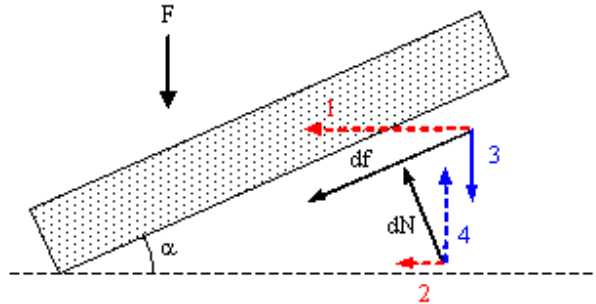


Figure 6.5 Rod guide and position control system.

Mathgram 6.3 Screw equation: required torque.



$$1 = \cos(\alpha) \cdot df$$

$$2 = \sin(\alpha) \cdot dN$$

$$3 = \sin(\alpha) \cdot df$$

$$4 = \cos(\alpha) \cdot dN$$

Thread number: 1-14" $\text{atan}\left(\frac{1}{14}\right) \cdot \frac{180}{\pi} = 4.086$

Vertical force = F F = 1005N Thread width = w w = 2mm

Screw radius = r r = $\frac{1}{2}$ in Thread angle = α $\alpha = 4.086 \frac{\pi}{180}$ rad

Friction coefficient = μ $\mu = 0.5$

If we assume that the external pressure P and frictional stress S are constant, the normal force and friction force on the element of the screw are the followings.

Normal force: $dN = P \cdot dA$

Frictional force: $df = S \cdot dA$

The frictional force is also expressed $df = \mu \cdot dN$

The differential area A is $dA = w \cdot \left(\frac{r \cdot d\theta}{\cos(\alpha)}\right)$

Vertical component (3+4) $-F + \int \cos(\alpha) dN - \int \sin(\alpha) df = 0$

$$F = \int (\cos(\alpha) - \mu \cdot \sin(\alpha)) dN$$

$$F = \int (\cos(\alpha) - \mu \cdot \sin(\alpha)) \cdot \left(\frac{P \cdot r \cdot w}{\cos(\alpha)}\right) d\theta$$

$$F = r \cdot w \cdot (1 - \mu \cdot \tan(\alpha)) \cdot \int P d\theta \quad (\theta \text{ is the total angle of thread})$$

Horizontal component (1+2)

$$M - \int r \cdot \sin(\alpha) dN - \int r \cdot \cos(\alpha) df = 0$$

$$M = \int r \cdot \sin(\alpha) \cdot \left(\frac{P \cdot r \cdot w}{\cos(\alpha)} \right) d\theta + \int r \cdot \cos(\alpha) \cdot \left(\frac{\mu \cdot P \cdot r \cdot w}{\cos(\alpha)} \right) d\theta$$

$$M = r^2 \cdot w \cdot (\tan(\alpha) + \mu) \cdot \int P d\theta$$

$$M = r^2 \cdot w \cdot (\tan(\alpha) + \mu) \cdot \frac{F}{r \cdot w \cdot (1 - \mu \cdot \tan(\alpha))}$$

$$M := \frac{F \cdot r \cdot (\mu + \tan(\alpha))}{1 - \mu \cdot \tan(\alpha)} \quad \boxed{M = 7.564 \text{ N}\cdot\text{m}}$$

If the larger radius handle is used, $H_r := 10\text{cm}$ $F_f := \frac{M}{H_r}$ $\boxed{F_f = 75.637\text{N}}$

A ball valve (Jamesbury, 3/8 5H-36HBRT) is placed between the rod-guides and the chamber to permit replacing instrumented rods during high pressure operation. Figure 6.6 shows the assembled parts.

6.3 MEASUREMENT PROCEDURE – DATA REDUCTION

Instruments are calibrated first, followed by high-pressure testing of the IHPC coupled with the manipulators provided by GeoTek, Inc.

The design and instrumented rods are prototyped and tested in a one-segment pressure chamber before building the entire IHPC system (Figure 6.7). Figure 6.8 presents measured elastic wave signals in compacted Georgia silts saturated, subjected to

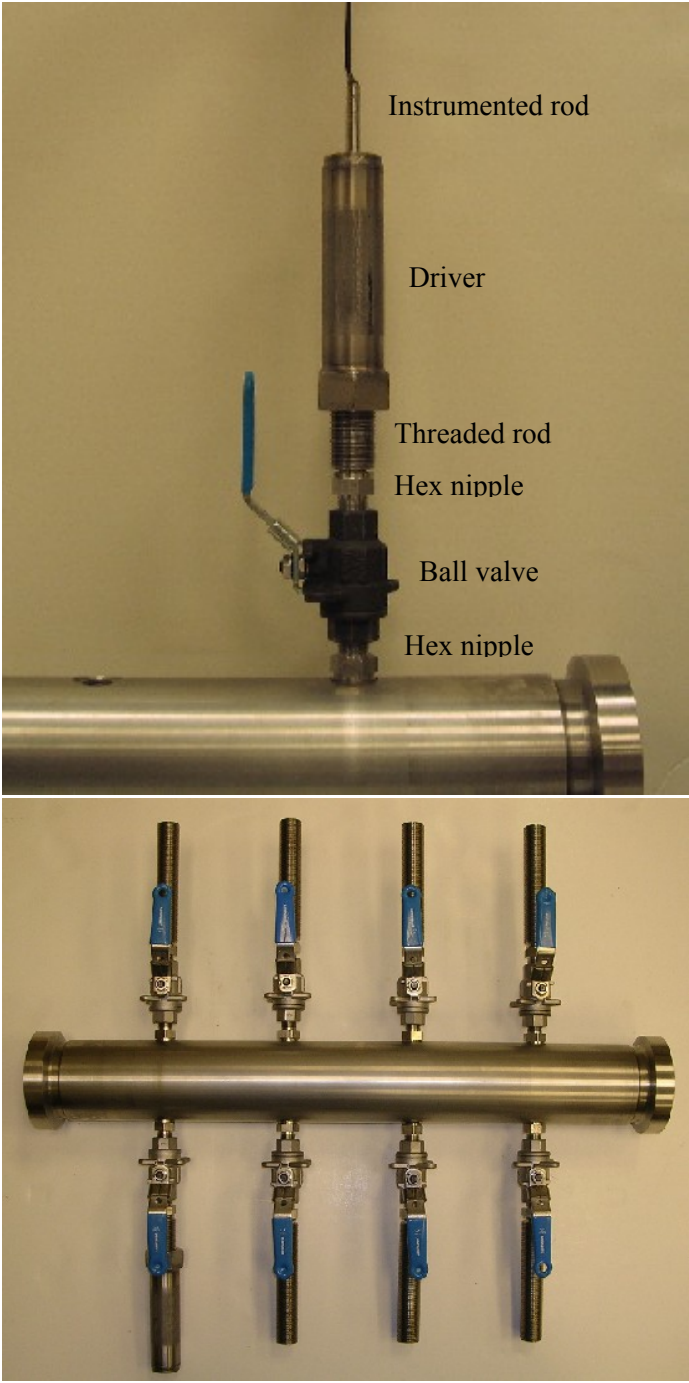


Figure 6.6 Rod guide and position control system assembled in pressure chamber.

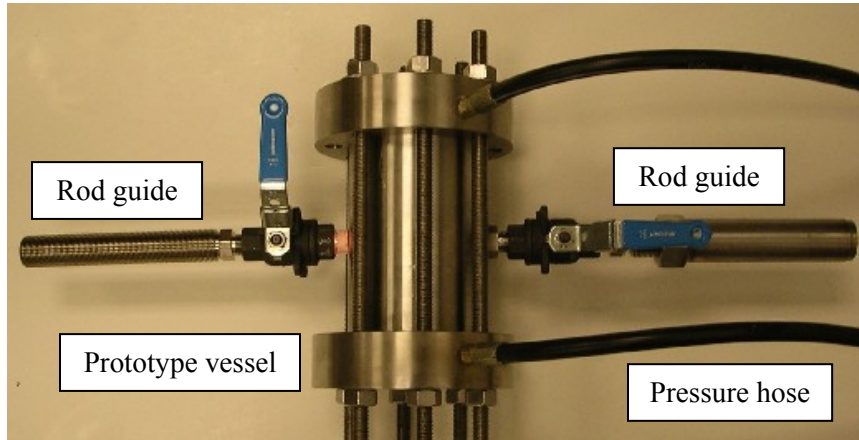


Figure 6.7 Prototype of the IHPC. Instrumentation and parts are tested before building the entire IPHC system.

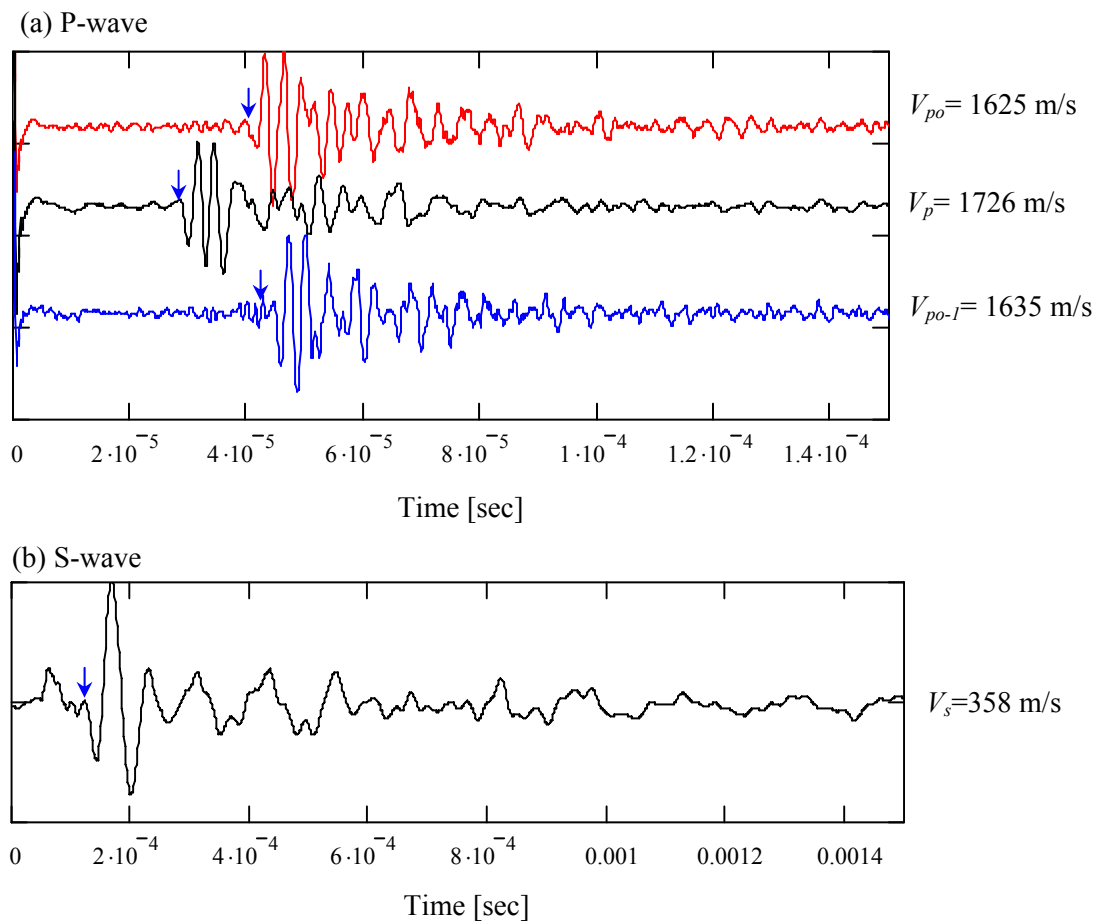


Figure 6.8 Elastic wave signals measured in IHPC ($\sigma_c = 17 \text{ MPa}$).

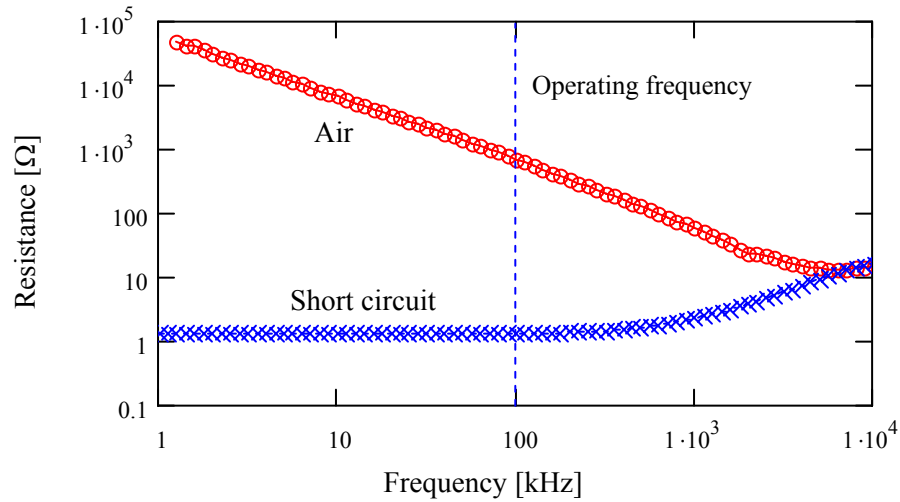


Figure 6.9 Needle probe – Spectral response.

a fluid pressure of $\sigma_c=17$ MPa. P-wave signals are obtained while the transducer is introduced into the specimen (V_{po}) as well as through water coupling (V_{po-l}).

The operating frequency for the needle probe is explored with measuring the spectral response with a LF impedance analyzer (HP 4192A - Figure 6.9). A $f = 100\text{kHz}$ is selected. The simplified measurement procedure is implemented for off-shore measurements; it consists of connecting the needle in series to a known resistor (R_{known}); the voltage drop at the needle and at the resistor permit computing the resistance at the needle tip R_{needle}

$$R_{needle} = \frac{\Delta V_{needle}}{\Delta V_{known}} \cdot R_{known} \quad (6.1)$$

where $R_{known} = 100 \Omega (\pm 5\%)$. The measured R_{needle} reflects the material conductivity. Figure 6.10 shows calibration data in terms of electrolyte conductivity versus measured conductance.

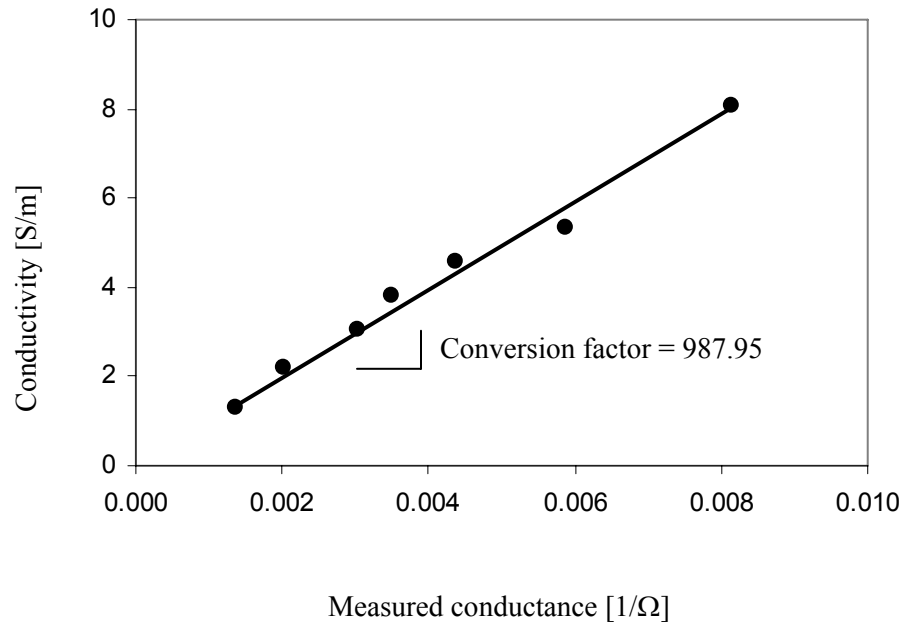


Figure 6.10 Needle probe calibration.

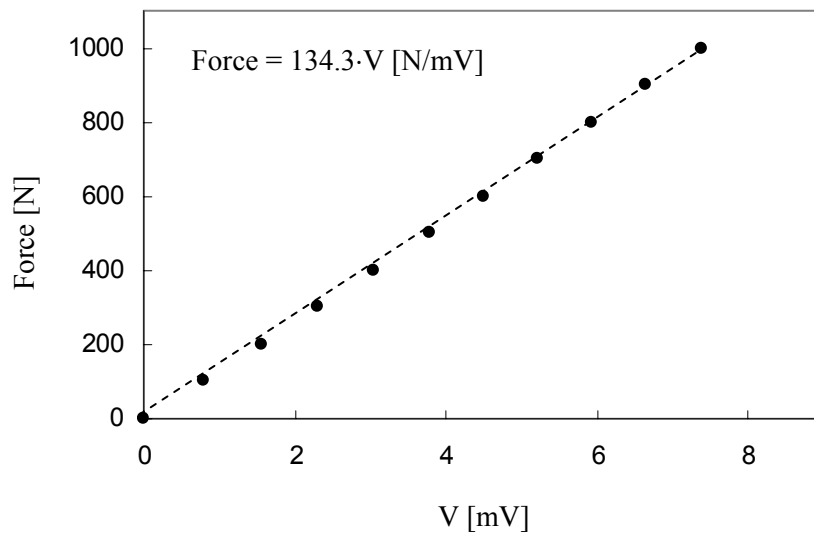
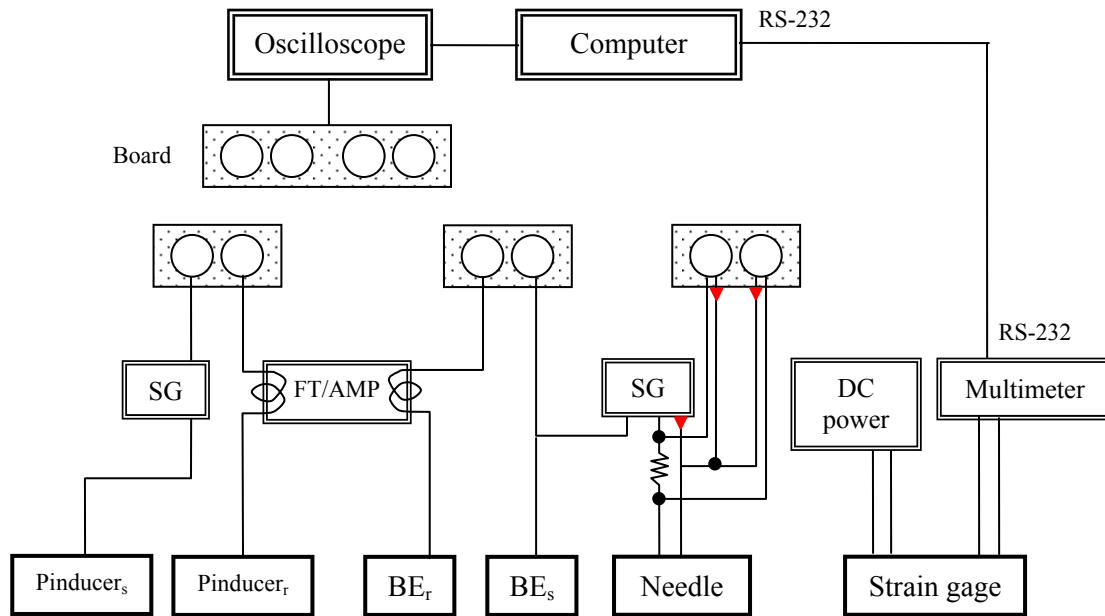


Figure 6.11 Load cell calibration



SG: Signal generator
 FT/AMP: 4-CH Filter / amplifier

Figure 6.12 Peripheral electronics (Notation: that s is source, r is receiver)

The load cell tip for strength measurement is calibrated up to 1000 N. Data in Figure 6.11 shows the measured voltage V versus normal force F at the cone stud

$$F = 134.3 \cdot V [N/mV] \quad (6.2)$$

The connection to peripheral electronics is designed to minimize duplicating electronics and to simplify the measurement procedure (Figure 6.12). The signal generator (Krohn-Hite 1400A) produces sine and square waves for the electrical resistance and S-wave velocity measurements. The impulse generator provides the source signal for P-wave velocity measurements. Received signals (P- and S- time series) are

filtered and amplified (Krohn-Hite 3364), and are digitized and stored in a 4-channel oscilloscope (DSO Agilent 54624A). A multiple BNC adapter board facilitates switching connections for the different measurements. Strength is independently measured using a multimeter (HP 34401A) and it is automatically logged into the computer via a RS-232 data port.

6.4 FIELD TEST

Two sites in the Gulf of Mexico are chosen for the JIP 2005 research cruise; Atwater Valley *AT* and Keathley Canyon *KC* (Figure 6.13). Both sites have similar water depth $\sim 1300\text{m}$. Difficulties encountered with the IHPC in the field and possible solutions are summarized in Table 6.6.

Four pressure cores are recovered. The properties of 2 pressure cores (FPC and HRC) are measured with the IHPC. Ice bags are placed on the chambers to prevent hydrate instability during the test. Figure 6.14 shows the measured elastic wave velocities from the FPC specimens (KC151-#3-11P, 227mbsf) recovered at Keathley Canyon under 14MPa fluid pressure. First, non-invasive P-wave scanning is performed every 3cm along the specimen (dotted line) to monitor the overall sample condition. Then, the P-wave velocity is measured before introducing the transducer once the holes are made (empty circle) and invasively by pressing the transducer onto the specimens (solid circle). The shear wave velocity measured at three locations is $V_s \sim 230\text{m/s}$. The penetration resistance into the specimen is monitored as the transducer is penetrated to different depths. Figure 6.15 presents the penetration force versus time. The peak value is followed by a minor relaxation. The penetration force increases with penetration depth.

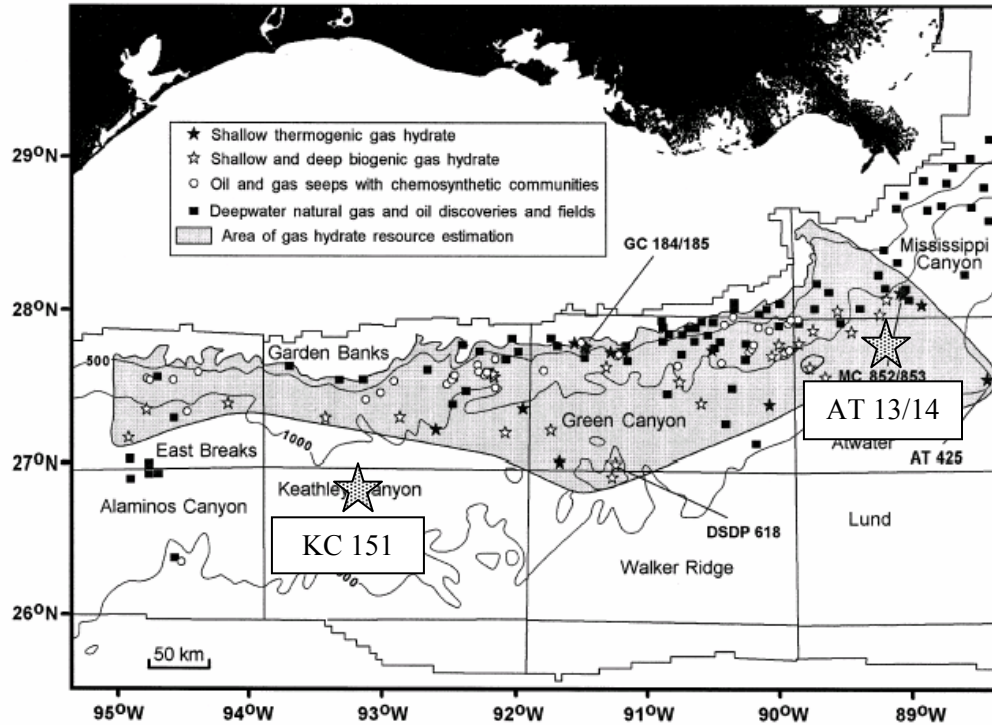


Figure 6.13 Test sites during the April – May 2005 research cruise (map from Milkov and Sassen, 2001).

6.5 CONCLUSIONS

A new, instrumented, high-pressure chamber is designed and manufactured to measure the mechanical and electrical properties of methane hydrate bearing sediments recovered by pressure coring. The chamber and sensors are calibrated and tested in the lab and field test. Results show the unique potential of this unprecedented device to characterize the physical properties of pressure core samples.

Table 6.6 Experienced difficulties and possible improvements for the IHPC system.

Difficulties	Observation and Potential Solutions
Sensor positioning	<ul style="list-style-type: none"> ▪ The current design requires less than 1mm resolution for sensor positioning. ▪ Either small size sensor diameter or bigger holes can better accommodate the introduction of sensors and prevent the sensor damage.
Core reducer	<ul style="list-style-type: none"> ▪ The core reducer for HRC measurement is not enough to guide the sample. ▪ A second chamber is needed for smaller specimens.
S-wave measurement	<ul style="list-style-type: none"> ▪ It is not easy to get a signal for very stiff sediments with bender elements. ▪ More robust S-wave transducers are needed.
Non-invasive P-wave measurement	<ul style="list-style-type: none"> ▪ A proper model of the fluid-liner-core-chamber system is needed to interpret non-invasive P-wave measurement results.

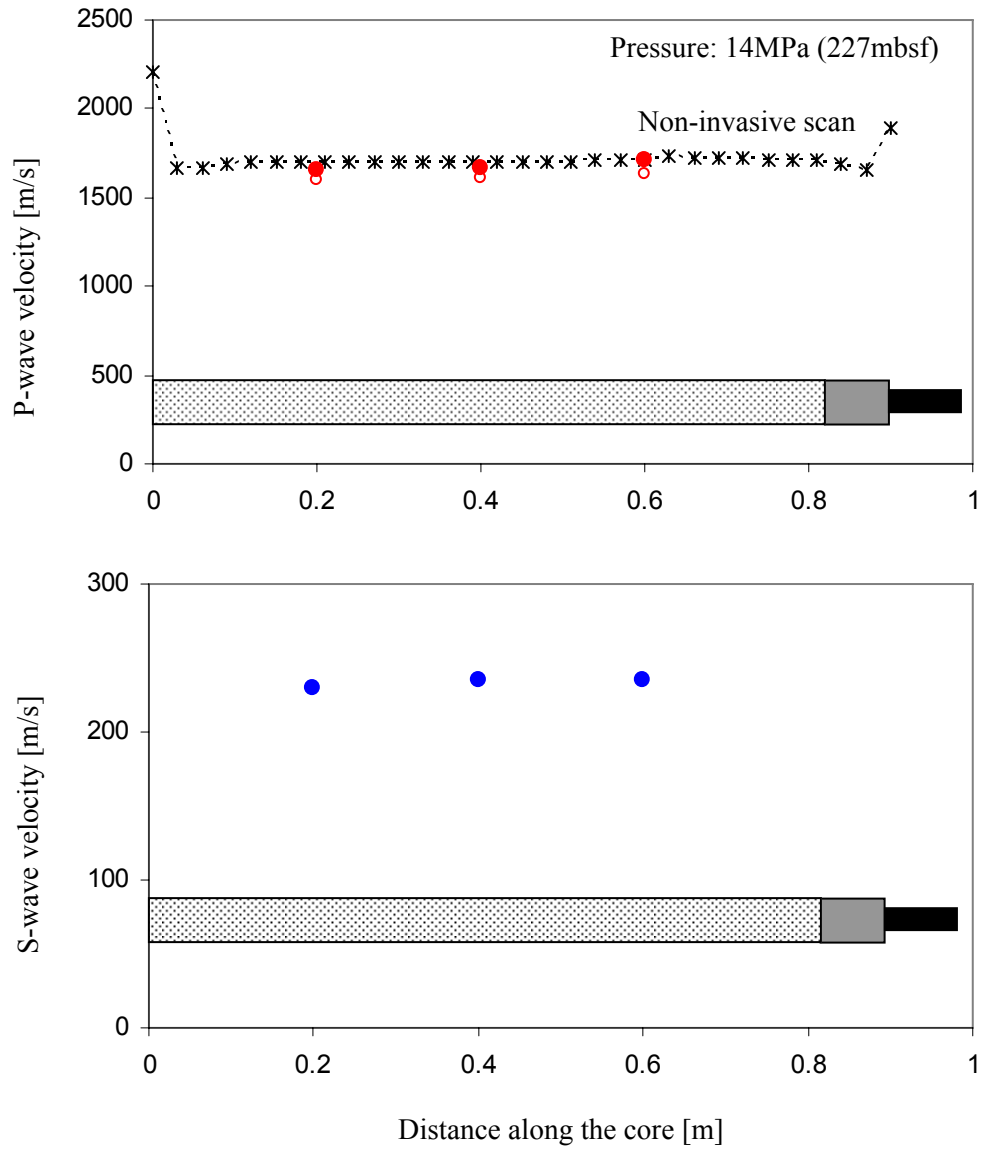


Figure 6.14 Elastic wave velocities for recovered pressure core.

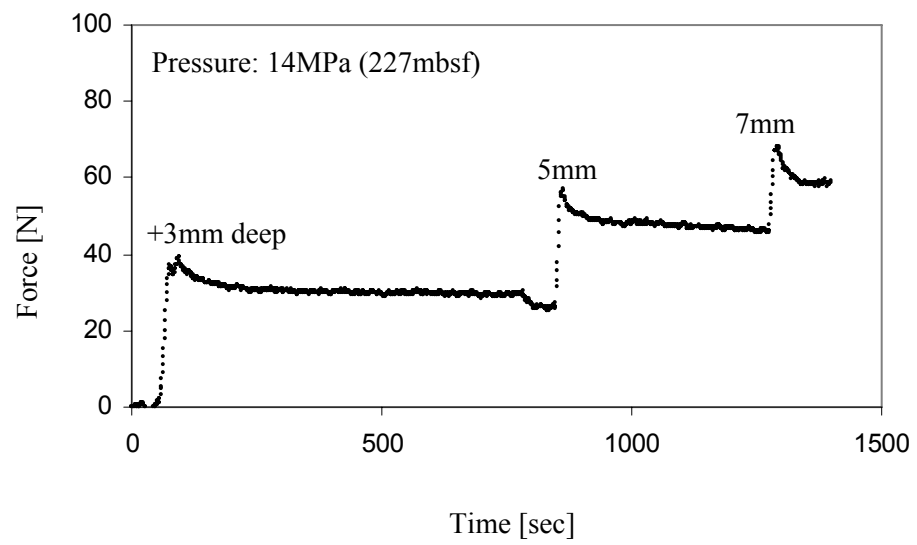


Figure 6.15 Penetration force versus time at different penetration depths (hole #1).

CHAPTER VII

CONCLUSIONS AND RECOMMENDATIONS

7.1 CONCLUSIONS

This research has attempted to provide fundamental mechanistic understanding of hydrate bearing sediments, including the effects of cementation and decementation on small-strain stiffness, medium and large-strain deformation and strength, thermal properties, and the development of lenses. Unique experimental studies and numerical analyses have been implemented, including a newly designed and built instrumented high-pressure chamber that allows the measurement of the mechanical and electrical properties of natural methane hydrate bearing sediments while under 20 MPa pressure inside pressure cores. The most important conclusions from this study follow.

Decementation. The small-strain shear stiffness inferred from shear wave velocity measurements is affected by the state of stress and the presence of cementing phases. The evolution of cementation and load-induced collapse under K_0 -conditions are uniquely denoted in the evolution of G_{max} .

- The velocity-stress sensitivity is lower for cemented soils in low effective confinement than for uncemented soils. Velocity-stress trends converge for cemented and uncemented soils at high confinement.

- Cemented loose soils may have high initial stiffness but decement and collapse upon further loading; decementation precedes skeletal collapse. Debonding may also occur upon loading without collapse; in this case, stiffness loss manifests during unloading.
- The possibility for decementation and collapse decrease with increasing density, cement content and effective confinement during cementation. All these observations point to the role of contact stability and coordination number on the behavior of granular materials.

Strength and stiffness. The mechanical properties of hydrate bearing sediments are governed by soil type, confining pressure and hydrate concentration in the pore space.

- Hydrate bearing sediments have high value of low- and intermediate-strain stiffness. As confining pressure increases, the quasi-elastic behavior extends to higher strain levels.
- The increased hydrate concentration stiffens the granular skeleton and strengthens the sediments causing larger undrained shear strength.
- The decisive increase in strength takes place when $S_{hyd} > 45\%$. This hydrate concentration corresponds to the amount needed to increase interparticle coordination for hydrate nuclei growing in the pore space.
- The breakage of hydrate-to-particle bonding precedes the deformation of hydrate-soil structures towards failure. Possible particle-level mechanisms include interference in particle rotation, enhanced pore-level dilation, hydrate-particle debonding, and hydrate shear.

Heat transfer in particulate materials. Micro- and macro-scale test results, parallel analyses and simulations show that

- Interparticle contacts dominate the thermal properties of dry particulate materials. Two related conclusions follow. First, thermal diffusion increases when interparticle contact areas increase due to creep, loading, or the presence of a cementing agent. Second, thermal diffusion increases with increasing interparticle coordination (i.e., with increasing density and decreasing porosity).
- The presence of water in the pore space enhances heat transfer at contacts and within the porous network. Mechanisms include mineral-water-mineral conduction and conduction within the pore fluid.
- There are competing effects between heat transfer through the granular skeleton and heat transfer from the mineral to the pore fluid. Better interparticle contact causes higher thermal conduction in the skeleton and more heat transfer to the pore fluid due to higher gradient.

Lensing. The study of ice lens formation leads to an enhanced understanding of hydrate lens formation in natural sediments.

- Ice lenses form normal to the heat flux direction in high specific surface soils. The self-stabilizing effect of the phase transformation isothermal makes the isothermal direction more relevant than the state of stress in typical, near-surface frozen ground conditions.
- Tension (i.e., low effective confining stress) facilitates lens formation while compression hinders lens initiation.

- Unfrozen water in neighboring pore space sustains ice lens growth; double layers act as conduction paths.
- Salt exclusion leads to high local salt concentrations, lower freezing temperature, halted lens growth, and nucleation at new locations.
- Lens formation requires lower freezing rate when coarser soils are involved.

Instrumented high-pressure chamber. The instrumented high-pressure chamber is a new device -first in its kind- designed to measure the mechanical and electrical properties of methane hydrate bearing sediments recovered from pressure cores. The direct measurement of material properties takes place under high pressure (~20MPa) and requires the perforation of the plastic liner. This unique device permits extending the understanding of hydrate bearing sediments formed in situ. The data will have a crucial effect to the analysis of methane production and related stability problems.

7.2 RECOMMENDATIONS AND FUTURE RESEARCH

- Development of realistic synthetic methane hydrate formation in soils to conduct systematic laboratory studies with adequate pressure and temperature control.
- Thermal properties of heterogeneous and anisotropic mixtures in view of hydrate formation and dissociation problems.
- Further development of instrumented chamber to re-generate the effective stress experienced by methane hydrate bearing sediments in situ.

REFERENCES

- Abduljawwad, S. N., and Al-Amoudi, O. S. B. (1995). "Geotechnical Behavior of Saline Sabkha Soils." *Geotechnique*, 45(3), 425-445.
- Acar, Y. B., and El-Tahir, A. (1986). "Low Strain Dynamic Properties of Artificially Cemented Sand." *Journal of Geotechnical Engineering*, ASCE, 112(11), 1001-1015.
- Aduda, B. O. (1996). "Effective Thermal Conductivity of Loose Particulate System." *Journal of Material Science*, 31, 6441-6448.
- Airey, D. W., and Fahey, M. (1991). "Cyclic Response of Calcareous Soil from the North-West Shelf of Australia." *Geotechnique*, 41(1), 101-121.
- Andersen, G. R., Swan, C. W., Ladd, C. C., and Germaine, J. T. (1995). "Small-Strain Behavior of Frozen Sand in Triaxial Compression." *Canadian Geotechnical Journal*, 32, 428-451.
- Andersland, O. B. and Ladanyi, B. (2004). *Frozen Ground Engineering*, 2nd edition, John Wiley & Sons, Inc., 384.
- Anderson, D.M., (1967), "The Interface between Ice and Silicate Surfaces", *Journal of Colloid and Interface Science*, 25, 174-191
- Ashworth, T., Johnson, L. R., and Lai, L-P. (1985), "Thermal Conductivity of Pure Ice and Tetrahydrofuran Clathrate Hydrates." *High Temperature-High Pressures*, 17, 413-419.
- ASTM D 5334-00, Standard Test Method for Determination of Thermal Conductivity of Soil and Soft Rock by Thermal Needle Probe Procedure.
- Baig, S., Picornell, M., and Nazarian, S. (1997). "Low Strain Shear Modulus of Cemented Sands." *Journal of Geotechnical and Geoenvironmental Engineering*, ASCE, 123(6), 540-545.
- Batchelor, G. K., and O'Brien, R. W. (1977). "Thermal or Electrical Conduction Through a Granular Material." Proceedings of the Royal Society of London. Series A, *Mathematical and Physical Sciences*, 355(1682), 313-333.
- Becker, B. R., Misra, A., and Fricke, B. A. (1992). "Development of correlations for soil thermal conductivity." *International Communications in Heat and Mass Transfer*, 19, 59-68.

- Benson, C. H., and Othman, M. A. (1993). "Hydraulic Conductivity of Compacted Clay Frozen and Thawed in situ." *Journal of Geotechnical Engineering*, 119(2), 276-294.
- Bernabe, Y., Fryer, D. T., and Hayes, J. A. (1992). "The Effect of Cement on The Strength of Granular Rocks." *Geophysical Research Letters*, 19(14), 1511-1514.
- Black, P. B. (1995). "Applications of Clapeyron Equation to Water and Ice in Porous Media." *CRREL report* (U.S. Army Cold Regions Research and Engineering Laboratory) 95-6.
- Brooks, J. M., Field, M. E., and Kennicutt, M. C. (1991). "Observations of Gas Hydrates in Marine Sediments, Offshore Northern California." *Marine Geology*, 96(1-2), 103.
- Cameron, I., Handa, Y. P., and Baker, T. H. W. (1990). "Compressive Strength and Creep Behavior of Hydrate-consolidated sand." *Canadian Geotechnical Journal*, 27, 255-258.
- Carlson, L. E. and Nixon, J. F. D. (1988). "Subsoil Investigation of Ice Lensing at the Calgary, Canada, Frost Heave Test Facility." *Canadian Geotechnical Journal*, 25(2), 307-319.
- Carslaw, H. S. and Jaeger, J. C. (1959). *Conduction of Heat in Solids*. Oxford, Clarendon Press, 510.
- Chamberlain, E. J. (1983). "Frost Heave of Saline Soils." *Proceedings of the Fourth International Conference on Permafrost*, Fairbanks, Alaska, July 17-22, 121-126.
- Chand, S., Minshull, T. A., Gei, D. and Carcione, J. M. (2004). "Elastic Velocity Models for Gas-Hydrate Bearing Sediments – a Comparison." *Geophysical Journal International*, 159, 573-590.
- Cho, G. C. (2002). *Unsaturated Soil Stiffness and Post Liquefaction Shear Strength*. Ph.D. Thesis, School of Civil and Environmental Engineering, Georgia Institute of Technology, Atlanta, GA.
- Cho, G. C., Lee, J.-S., and Santamarina, J. C. (2004). "Spatial Variability in Soils: High Resolution Assessment with Electrical Needle Probe." *Journal of Geotechnical and Geoenvironmental Engineering*, 130(8), 843-850.
- Clough, G. W. and Sitar, N. (1981). "Cemented Sand under Static Loading." *Journal of Geotechnical Engineering*, ASCE, 107(GT6), 799-817.
- Clough, G. W., Sitar, N., and Bachus, R. C. (1981). "Cemented Sands under Static Loading." *Journal of Geotechnical Engineering Division, ASCE*, 107(6), 799-817.
- Cochonat, P., Cadet, J. -P., Lallemand, S. J., Mazzotii, S., Nouze, H., Fouchet, C., and Foucher, J. P. (2002). "Slope Instability and Gravity Processes in Fluid Migration

- and Tectonically Active Environment in the Eastern Nankai Accretionary Wedge (KAIKO-Tokai'96 cruise)." *Marine Geology*, 187, 1-2, 193-202.
- Collett, T. S. (2002). "Energy Resource Potential of Natural Gas Hydrates." *American Association of Petroleum Geologists Bulletin*, 86(11), 1971-1992.
- Collett, T. S. and Kuuskraa, V. A. (1998). "Emerging U.S. Gas resources - 4. Hydrates Contain Vast Store of World Gas Resources." *Oil and Gas Journal*, 96(19), 90-95.
- Coquard, P., and Boistelle, R. (1994). "Water and Solvent Effects on the Strength of Set Plaster." *Int. J. Rock Mech. Min. Sci. & Geomech. Abstr.*, 31(5), 517-524.
- Da Re, G., Germaine, J. T., and Ladd, C. C. (2003). "Triaxial Testing of Frozen Sands: Equipment and Example Results." *Journal of Cold Regions Engineering*, Sept. 90-118.
- Dass, R. N., Yen, S. S., Das, B. M., Puri, V. K., and Wright, M. A. (1994). "Tensile Stress-Strain Characteristics of Lightly Cemented Sand." *Geotechnical Testing Journal*, 17(3), 305-314.
- Devarakonda, S., Groysman, A., and Myerson, A. S. (1999). "THF-Water Hydrate Crystallization: an Experimental Investigation." *Journal of Crystal Growth*, 204, 525-538.
- Dickens, G. R. (2001) "The Potential Volume of Oceanic Methane Hydrates with Variable External Conditions." *Organic geochemistry*, 32, 1179-1193.
- Dickens, G. R. (2003). "Rethinking the Global Carbon Cycle with a Large Dynamic and Microbially Mediated Gas Hydrate Capacitor." *Earth and Planetary Science Letters*, 213, 169-183.
- Dodds, J. (2003). *Particle Shape and Stiffness – Effect on Soil Behavior*. Master Thesis, School of Civil and Environmental Engineering, Georgia Institute of Technology, Atlanta, GA.
- Dupas, J. M., and Pecker, A. (1979). "Static and Dynamic Properties of Sand-Cement." *Journal of Geotechnical Engineering*, ASCE, 105(GT3), 419-435.
- Durham, W. B., Kirby, S. H., Stern, L. A., and Zhang, W. (2003-a). "The Strength and Rheology of Methane Clathrate Hydrate." *Journal of Geophysical Research*, 108(B4), 2182.
- Durham, W. B., Stern, L. A., and Kirby, S. H. (2003-b). "Ductile Flow of Methane Hydrate." *Canadian Journal of Physics*, 81, 373-380.
- Dvorkin, J., and Yin, H. (1995). "Contact Laws for Cemented Grains: Implications for Grain and Cement Failure." *Int. J. Solids. Structures*, 32(17), 2497-2510.

- Dvorkin, J., Mavko, G., and Nur, A. (1991). "The Effect of Cementation on the Elastic Properties of Granular Material." *Mechanics of Materials*, 12(3-4), 207-217.
- Dyvik, R., and Madshus, C. (1985). "Lab Measurements of G_{max} using Bender Elements." *Advances in the art of testing soils under cyclic conditions, ASCE*, 186-196.
- Ecker, C. Dvorkin, J. and Nur, A. M. (2000). "Estimating the Amount of Gas Hydrate and Free Gas from Marine Seismic Data." *Geophysics*, 65(2), 565-573.
- Eigenbrod, K. D. and Kennepohl, G. J. A. (1996). "Moisture Accumulation and Pore Water Pressures at Base of Pavements." *Transportation Research Record*, 1546, 151-161.
- Esch, D. C. (2004). *Thermal Analysis, Construction and Monitoring Methods for Frozen Ground*. Reston, VA., American Society of Civil Engineers. 492.
- Everett, D. H. (1961). "The Thermodynamics of Frost Damage to Porous Solids." *Transactions of the Faraday Society*, 57, 1541-1551.
- Fam, M. and Santamarina, J. C. (1995). "Study of Geoprocesses with Complementary Wave Measurements in an Oedometer." *Geotechnical Testing Journal, ASTM*, 18(3), 307-314.
- Farouki, O. T. (1985). *Thermal design considerations in Frozen Ground Engineering - Ground Thermal Properties*, Krzewinski, T. G. and Tart, R. G., Eds., New York, American Society of Civil Engineer, 186-203.
- Feda, J. (1982). *Mechanics of Particulate Materials*, Amsterdam, New York, Elsevier Scientific Pub. Co., 446.
- Feda, J. (1994). "Collapse of Soil Structure." *Proc .Int. Symp. Engineering Characteristics of Arid Soils*, P.G. Fookes & R.H.G. Parry (eds.), London U.K., Balkema, 237-240.
- Feda, J. (1995). "Behavior of Cemented Clay." *Canadian Geotechnical Journal*, 32(5), 899-904.
- Fernandez, A., and Santamarina, J. C. (2001). "Effect of Cementation on the Small Strain Parameters of Sands." *Canadian Geotechnical Journal*, 38(1), 191-199.
- Fratta, D., and Santamarina, J. C. (2002). "Shear Wave Propagation in Jointed Rock – State of Stress." *Geotechnique*, 52(7), 495-505.
- Gangadhara Rao, M. V. B. B., and Singh D. N. (1999). "A Generalized Relationship to Estimate Thermal Resistivity of Soils." *Canadian Geotechnical Journal*, 36, 767-773.

- Gilpin, R. R. (1980). "Model for Prediction of Ice Lensing and Frost Heave in Soils." *Water Resources Research*, 16(5), 918-930.
- Gold, L. W. (1957). "A Possible Force Mechanism Associated with the Freezing of Water and Porous Materials." *Highway Research Bulletin*, 168, NAS-NRC, Washington, 65-72.
- Golubev, V. N. (1997). "Ice Formation in Freezing Grounds." *Proceedings of the 1997 International Symposium on Ground Freezing and Frost Action in Soils*, April, 15-17, Lulea, Sweden, 87-91.
- Gori, F., and Corasaniti, S. (2004). "Theoretical Prediction of the Thermal Conductivity and Temperature Variation inside Mars Soil Analogues." *Planetary and Space Science*, 52, 91-99.
- Gough, S. R., and Davidson, D. W. (1971). "Composition of Tetrahydrofuran Hydrate and the Effect of Pressure on the Decomposition." *Canadian Journal of Chemistry*, 49, 2691-2699.
- Guerin, G., Goldberg, D., and Meltser, A. (1999). "Characterization of In Situ Properties of Gas Hydrate-bearing Sediments on the Blake Ridge." *Journal of Geophysical Research*, 104(B8), 17, 781-17, 795.
- Guimaraes, M. (2001). Crushed Stone Fines and Ion Removal from Clay Slurries. Ph.D. Thesis. School of Civil and Environmental Engineering, Georgia Institute of Technology, Atlanta, GA.
- Hardin, B. O., and Richart, F. E. (1963), "Elastic Wave Velocities in Granular Soils." *Journal of Soil Mechanics and Foundations*, ASCE, 89, SM1, 33-65.
- Harris, C. and Lewkowicz, A. G. (2000). "Analysis of the Stability of Thawing Slopes, Ellesmere Island, Nunavut, Canada." *Canadian Geotechnical Journal*, 37(2), 449-462.
- Hashin, Z., and Shtrikman, S. (1962). "A Variational Approach to the Theory of the Effective Magnetic Permeability of Multi-Phase Materials." *Journal of Applied Physics*, 33(10), 3125-3131.
- Holden, J. T. (1983). "Approximate Solutions for Miller's Theory of Secondary Heave", *Proceeding of Fourth International Conference on Permafrost*, Fairbanks, Alaska, July 17-22, National Academy Press, 498-503.
- Horiguchi, K. (1987). "An Osmotic Model for Soil Freezing." *Cold Regions Science and Technology*, 14, 13-22.
- Hornbach, M. J., Saffer, D. M. and Holbrook, W. S. (2004). "Critically Pressure Free-Gas Reservoirs Below Gas-Hydrate Provinces." *Nature*, 427(6970). 142-144.

- Hovland, M. and Gudmestad, O. T. (2001) "Potential Influence of Gas Hydrates on Seabed Installation." Natural gas hydrates - Occurrence, Distribution and detection, editor; Paull, C. K. and Dillon, W. P. American Geophysical Union. 307-315.
- Hutchison, J. N. (1974). "Periglacial Solifluxion: an Approximate Mechanism for Clayey Soils." *Geotechnique*, 24(3), 438-443.
- Hyndmann, R. D. and Spence, G. D. (1992). "A Seismic Study of Methane Hydrate Marine Bottom Simulating Reflectors by Vertical Fluid Expulsion." *Journal of Geophysical research*, 97, 6683-6698.
- Iida, T., Mori, H., Mochizuki, T., and Mori, Y. H. (2001). "Formation and Dissociation of Clathrate Hydrate in Stoichiometric Tetrahydrofuran-Water Mixture Subjected to One-dimensional Cooling and Heating." *Chemical Engineering Science*, 56, 4747-4758.
- Indraratan, B., Balasubramanian, A. S., and Khan, M. J. (1995). "Effect of Fly Ash with Lime and Cement on the Behavior of a Soft Clay." *Quarterly Journal of Engineering Geology*, 28, 131-142.
- Ishizaki, T., Yoneyama, K. and Nishio, N. (1985). "X-ray Technique for Observation of Ice Lens Growth in Partially Frozen, Saturated Soil." *Cold Region Science and Technology*, 11, 213-221.
- Jarrad, R. D., Niessen, F., Brink, J. D., and Bucker, C. (2000). "Effects of Cementation on Velocities of Siliciclastic Sediments." *Geophysical Research Letters*, 27(5), 593-596.
- Jinsheng, Z. and Rong, Fu. (1983). "Preliminary Experimental Study of Water Migration at the Ice/Soil Interface." *Proceedings of the Fourth International Conference on Permafrost*, 1469-1472. Fairbanks, Alaska, July 17-22, National Academy Press, 498-503.
- Joshi, R. C., Achari, G., Horsfield, D., and Nagaraj, T. S. (1994). "Effect of Heat Transfer on Strength of Clay." *Journal of Geotechnical Engineering*, 120(6), 1080-1088.
- Penner, E. (1957). "Soil Moisture Tension and Ice Segregation." *Highway Research Bulletin* 168, 50-64.
- Jumikis, A. R. (1958), "Some Concepts Pertaining to the Freezing Soil Systems", Highway, Res. Board Spec. Rep. (40), 178-190.
- Jumikis, A. R. (1966). *Thermal Soil Mechanics*. New Brunswick, N.J., Rutgers University Press, 267.
- Kayen, R. E. and Lee, H. J. (1991). "Pleistocene Slope Instability of Gas Hydrate-Laden Sediment on the Beaufort Sea Margin." *Marine Geotechnology*, 10, 125-141.

- Klein, K. (1999). Electromagnetic Properties of High Specific Surface Minerals. Ph.D. Thesis. School of Civil and Environmental Engineering, Georgia Institute of Technology, Atlanta, GA.
- Konrad, J. M. (1989). "Influence of Cooling Rate on the Temperature of Ice Lens Formation in Clayey Silts." *Cold Regions Science and Technology*, 16, 25-36.
- Konrad, J. M. (1989). "Pore Water Pressure at an Ice Lens: Its Measurement and Interpretation." *Cold Regions Science and Technology*, 16, 63-74.
- Konrad, J. M. and Morgenstern, N.R. (1980). "A Mechanistic Theory of Ice Lens Formation in Fine-Grained Soils." *Canadian Geotechnical Journal*, 17, 473-486.
- Konrad, J. M. and Morgenstern, N.R. (1981). "The Segregation Potential of a Freezing Soil." *Canadian Geotechnical Journal*, 18, 482-491.
- Konrad, J. M. and Morgenstern, N. R. (1982). "Effects of Applied Pressure on Freezing Soils." *Canadian Geotechnical Journal*, 19, 494-505.
- Kumlutas, D., Tavman, I. H., Coban, M. T. (2003). "Thermal Conductivity of Particle Filled Polyethylene Composite Materials." *Composite Science and Technology*, 63, 113-117.
- Kunerth, D. C., Weinberg, D. M., Rector, J. W., Scott, C. L., and Johnson, J. T. (2001). "Acoustic Laboratory Measurements During the Formation of a THF-Hydrate in Unconsolidated Porous Media." *Journal of Seismic Exploration*, 9, 337-354.
- Kuwano, R. and Jardine, R. J. (2002). "On the Applicability of Cross-Anisotropic Elasticity to Granular Materials at Very Small Strains." *Geotechnique*, 52(10), 727-749.
- Kvenvolden, K. A. (1999) "Potential Effects of Gas Hydrate on Human Welfare." *Proceedings of National Academy of Sciences*, 96 (7), Irvine, CA, November 8-9, 3420-3426.
- Kvenvolden, K. A. and Lorenson, T. D. (2001). "Global Occurrences of Gas Hydrate" *Proceedings of the International Offshore and Polar Engineering Conference*, 1, 462-467.
- Ladanyi, B., and Benyamina, M. B. (1995). "Triaxial Relaxation Testing of a Frozen Sand." *Canadian Geotechnical Journal*, 32, 496-511.
- Lade, P. V., and Overton, D. D. (1989). "Cementation Effects in Frictional Materials." *Journal of Geotechnical Engineering, ASCE*, 115(10), 1373-1387.
- Lajtai, E. Z., Schmidtke, R. H., and Bielus, L. P. (1987). "The Effect of Water on the Time-Dependent Deformation and Fracture of a Granite." *Int. J. Rock Mech. Min. Sci. & Geomech. Abstr.*, 24(4), 247-255.

- Lambert, M. A., and Fletcher, L. S. (1997-a). "Review of Models for Thermal Contact Conductance of Metals." *Journal of Thermophysics and Heat Transfer*, 11(2), 129-140.
- Lambert, M. A., and Fletcher, L. S. (1997-b). "Thermal Contact Conductance of Spherical Rough Metals." *Journal of Heat Transfer*, 119(4), 684-690.
- Landis, E. N., and Shah, S. P. (1995). "The Influence of Microcracking on the Mechanical Behavior of Cement Based Materials." *Advanced Cement Based Materials*, 2, 105-118.
- Lee, M. W. (2002). "Biot-Gassmann Theory for Velocities of Gas Hydrate-Bearing Sediments." *Geophysics*, 67(6), 1711-1719.
- Lee, M. W. and Collett, T. S. (2001). "Elastic Properties of Gas Hydrate-Bearing Sediments." *Geophysics*, 66(3), 763-771.
- Leg 204 Preliminary Report, Drilling Gas Hydrates on Hydrate Ridge, Cascadia Continental Margin (2002).
- Lerche, I. and Bagirov, E. (1998). "Guide to Gas Hydrate Stability in Various Geological Settings." *Marine and Petroleum Geology*, 15, 427-437.
- Leroueil, S. and Hight, D.W. (2003). "Behaviour and Properties of Natural Soils and Soft Rocks, in Characterization and Engineering Properties of Natural Soils." Eds. T.S. Tan, K.K. Phoon, D.W. Hight, and S. Leroueil, Balkema, Exton, Pennsylvania, Vol. 1, 29-254.
- Li, H., Yang, H., Chang, C., and Sun, X. (2001). "Experimental Investigation on Compressive Strength of Frozen Soil versus Strain Rate." *Journal of Cold Regions Engineering*, June, 125-133.
- Lo, S.-C. R., Lade, P. V., and Wardani, S. P. R. (2003). "An Experimental Study of the Mechanics of Two Weakly Cemented Soils." *Geotechnical Testing Journal*, 26(3), 328-341.
- Loch, J. P. G. (1981). "State-of-The-Art Report-Frost Action in Soils." *Engineering Geology*, 18, 213-224.
- Mageau, D. W. and Morgenstern, N. R. (1980). "Observation on Moisture Migration in Frozen Soils." *Canadian Geotechnical Journal*, 17, 54-60.
- Manohar, K., Yarbrough, D. W., and Booth, J. R. (2000). "Measurement of Apparent Thermal Conductivity by the Thermal Probe Method." *Journal of Testing and Evaluation*, 28(5), 345-351.
- Martin, R. T. (1959). "Rhythmic Ice Banding in Soil." *Highway Research Bulletin*, 218, 11-23.

- Maslin, M., Owen, M., Day, S. and Long, D. (2004). "Linking Continental-Slope Failures and Climate Change: Testing the Clathrate Gun Hypothesis." *Geology*, 32(1), 53-56.
- Max, M. D. and Lowrie, A. (1996). "Ocean Methane Hydrates: a 'Frontier' Gas Resource." *Journal of Petroleum Geology*, 19(1), 41-56.
- McRoberts, E. C. (1978). "Slope Stability in Cold Regions. In Geotechnical Engineering for Cold Regions Andersland, O. B. and Anderson, D. W., Eds., McGraw-Hill Book Company, New York, 363-403.
- McRoberts, E. C. (1975). "Pore Water Expulsion during Freezing." *Canadian Geotechnical Journal*, 12, 130-141.
- Mi, Y., Sakai, A., Walia, R., Hyndman, R. D. and Dallimore, S. R. (1999). "Vertical Seismic Profiling and Seismic Properties of Gas Hydrate in an Arctic Well." CREWES (Consortium for Research in Elastic Wave Exploration Seismology) research report, Vol. 11., 705-726.
- Milkov, A. V. and Sassen, R. (2001). "Estimate of Gas Hydrate Resource, Northwestern Gulf of Mexico Continental Slope." *Marine Geology*, 179, 71-83.
- Miller, D. L. (1985). *Thermal Design Considerations in Frozen Ground Engineering: a State of the Practice Report - Temperature Monitoring / Ground Thermometry*, Prepared by the Technical Council on Cold Region Engineering of the American Society of Civil Engineers, Krzewinski, T. G. and Tart, R. G., Eds., New York, ASCE, 53-71.
- Miller, R. D. (1972). "Freezing and Heaving of Saturated and Unsaturated Soils." *Highway Research Record*, 393, 1-11.
- Miller, R. D. (1980). Applications of Soil Physics – 11. Freezing Phenomena in soils. Hillel, D., Eds., New York, Academic Press. 385.
- Murashov, V. V. and White, M. A. (2000). "Thermal Conductivity of Crystalline Particulate Materials." *Journal of Materials Science*, 35, 649-653.
- Nimick, F. B., and Leith, J. R. (1992). "A Model for Thermal Conductivity of Granular Porous Media." *Journal of Heat Transfer*, 114, 505-508.
- Nixon, J. F. (1991). "Discrete Ice Lens Theory for Frost Heave in Soils." *Canadian Geotechnical Journal*, 28, 843-859.
- O'Neill, K. and Miller, R. D. (1985). "Exploration of a Rigid Ice Model of Frost Heave." *Water Resources Research*, 21(3), 281-296.
- Ohrai, T., Takahi, T., Yamamoto, H., and Okamoto, J. (1983), "Uniaxial Compressive Strength of Ice Segregated from Soil", National Academy Press, 945-950

- Ohmura, R., Shigetomim T., and Mori, Y. H. (2002). "Bending Tests on Clathrate Hydrate Single Crystals." *Philosophical Magazine A*, 82(9), 1725-1740.
- Parameswaran, V. R., Paradis, M., and Handa, Y. P. (1989). "Strength of Frozen Sand containing Tetrahydrofuran Hydrate." *Canadian Geotechnical Journal*, 26, 479-483.
- Parker, H. W. (2001). "After Petroleum is Gone, What Then?" *World Oil*, September.
- Parks, G. A. (1990). "Surface Energy and Adsorption at Mineral-Water Interfaces: An Introduction." *Reviews in Mineralogy*, 23, Chapter 4, Mineralogical Society of America. Hochella, M. F. Jr. and White, A. F., Eds., Published by the Mineralogical Society of America.
- Paull, C. K. (1997). "Drilling for gas hydrate: Ocean drilling program leg 164." *Proceedings of the 1997 29th Annual Offshore Technology Conference*, Part 1(of 4), May 5-8, Houston, TX, 8294
- Pearson, C., Murphy, J., and Hermes, R. (1986). "Acoustic and Resistivity Measurements on Rock Samples Containing Tetrahydrofuran Hydrates: Laboratory Analogues to Natural Gas Hydrate Deposits." *Journal of Geophysical Research*, 91(B14), 14,132-14,138.
- Pecher, I. A. and Holbrook, W. W. (2000). "Seismic Methods for Detecting and Quantifying Marine Methane Hydrate / Free Gas Reservoirs." *Natural Gas Hydrate in Ocean and Permafrost Environments*, Max, M .D., Eds., Chapter 22. Kluwer Academic publishers. 275-292.
- Penner, E. (1957). "Soil Moisture Tension and Ice Segregation." *Highway Research Bulletin*, 168, pp.
- Penner, E. (1958). "Pressures Developed in a Porous Granular System as a Result of Ice Segregation." *Highway Research Board*, 40, 191-199.
- Penner, E. (1963). "Frost-Heaving in Soils", *Proceedings of the First International Conference on Permafrost*, Lafayette, Ind. National Academy Sciences, November 11-15, 197-202.
- Penner, E. (1986). "Aspects of ice lens growth in soils." *Cold Regions Science and Technology*, 13, 91-100.
- Penner, E. and Walton, T. (1978). "Effects of temperature and pressure on frost heaving." *Engineering Geology*, 13(1-4), 29-39.
- Press, W. H. (1986). *Numerical recipes: the art of scientific computing*. Cambridge. New York, Cambridge University Press. 818.
- Rao, S. M., Sridharan, A., and Ramanath, K. P. (1995). "Collapse Behavior of an Artificially Cemented Clayey Silt." *Geotechnical Testing Journal*, 18(3), 334-341.

- Read, M. D., Ayling, M. R., Meredith, P. G., and Murrell, S. A. F. (1995). "Microcracking during Triaxial deformation of Porous Rocks Monitored by Changes in Rock Physical Properties, II. Pore Volumetry and Acoustic Emission Measurements on Water-Saturated Rocks." *Tectonophysics*, 245, 223-235.
- Reddy, K. R. and Saxena, S. K. (1993). "Effects of Cementation on Stress-Strain and Strength Characteristics of Sands." *Soils and Foundations*, 33(4), 121-134.
- Rempel, A. W. and Worster, M. G. (1999). "Interaction between a particle and an advancing solidification front." *Journal of Crystal Growth*, 205(3), 427-440.
- Richart, F. E., Hall, J. R., and Woods, R. D. (1970). *Vibrations of Soils and Foundations*, Englewood Cliffs, N.J., Prentice Hall, 414.
- Riestenberg, D., West, O., Lee, S., MaCallum, S., and Phelps, T. J. (2003). "Sediment Surface Effects on Methane Hydrate Formation and Dissociation." *Marine Geology*, 198, 181-190.
- Romkens, M. J. M. and Miller, R. D. (1973). "Migration of mineral particles in ice with a temperature gradient." *Journal of Colloid and Interface Science*, 42, 103-111.
- Roth, K., Schulin, R., Fluhler, H., and Attinger, W. (1990) "Calibration of time domain reflectometry for water content measurement using a composite dielectric approach." *Water Resource Research*. 26, 2267-2273.
- Rueff, R. M., and Sloan, E. D. (1985). "Effect of Granular Sediment on Some Thermal Properties of Tetrahydrofuran Hydrate." *Ind. Eng. Chem. Process Des. Dev.* 24, 882-885.
- Sahimi, M., and Tsotsis, T. T. (1997). "Transient Diffusion and Conduction in Heterogeneous Media: Beyond the Classical Effective-Medium Approximation." *Ind. Eng. Chem. Res.* 36, 3043-3052.
- Sánchez-Salineró, I., Roesset, J. M. and Stokoe, K. H. (1986). "Analytical Studies of Body Wave Propagation and Attenuation." *Geotechnical Engineering Report GR86-15*, University of Texas at Austin, Austin, 272.
- Santamarina, J. C., and Cho, G. C. (2001). "Determination of Critical State Parameters in Sandy Soils-Simple Procedure." *Geotechnical Testing Journal*, 24(2), 185-192.
- Santamarina, J. C., Klein K. A., and Fam, M. (2001). *Soils and Waves - Particulate Materials Behavior, Characterization and Process Monitoring*, New York: J. Wiley & Sons, 488.
- Saxena, S. K. and Lastrico, R. M. (1978). "Static Properties of Lightly Cemented Sands." *Journal of Geotechnical Engineering, ASCE*, 104(12), 1449-1464.

- Saxena, S. K., Reddy, K. R., and Avramidis, A. S. (1988). "Static Behavior of Artificially Cemented Sand." *Indian Geotechnical Journal*, 18(2), 111-141.
- Sayles, F. H., and Carbee, D. L. (1981). "Strength of Frozen Silt as a Function of Ice Content and Dry Unit Weight." *Engineering Geology*, 18, 55-66.
- Schanz, T. (1998). "A Constitutive Model for Cemented Sands." Proceedings of 4th International Workshop on Localization and Bifurcation Theory for Soils and Rocks. T. Adachi et al., Eds. Gifu, Balkema, 165-172.
- Shibuya, S., Mitachi, T., Temma, M., and Kawaguchi, T. (2001). "Interrelationship Between the Metastability Index and the Undrained Shear Strength of Six Clays." *Advanced Laboratory Stress-Strain Testing of Geomaterials*, Tatsuoka, R., Shibuya, S. and Kuwano, R. Eds., 111-186.
- Shirley, D. J. and Hampton, L. D. (1978). "Shear Wave Measurements in Laboratory Sediments." *Journal of the Acoustical Society of America*, 63(2), 607-613.
- Sienkiewicz, F., Shukla, A., Sadd, M., Zhang, Z., and Dvorkin, J. (1996). "A Combined Experimental and Numerical Scheme for the Determination of Contact Loads between Cemented Particles." *Mechanics of Materials*, 22, 43-50.
- Singh, D. N., and Devid, K. (2000). "Generalized Relationships for Estimating Soil Thermal Resistivity." *Experimental Thermal and Fluid Science*, 22, 133-143.
- Sloan, E. D. (1998). *Clathrate Hydrates of Natural Gases*. New York, Marcel Dekker.
- Sloan, E. D. (2003). "Fundamental Principles and Applications of Natural Gas Hydrates." *Nature*, 426(6964), 353-359.
- Smith, S. L. and Williams, P. J. (1995). "Ice Lens Formation at a Silt-Sand Interface." *Canadian Geotechnical Journal*, 32, 488-495.
- Song, D., and Chen, G. (2004). "Thermal Conductivity of Periodic Microporous Silicon Films." *Applied Physics Letters*, 84(5), 687-689.
- Sridhar, M. R., and Yovanovich, M. M. (1996). "Elastoplastic Contact Conductance Model for Isotropic Conforming Rough Surfaces and Comparison with Experiments." *Journal of Heat Transfer*, 118(1), 3-9.
- Stoll, R. D., Ewing, J., and Bryan, G. M. (1971). "Anomalous Wave Velocities in Sediments Containing Gas hydrates." *Journal of Geophysical Research*, AGU, 76(8), 2090-2094.
- Sultan, N., Cochonat, P., Cayocca, F., Bourillet, J.-F., and Colliat, J.-L. (2004-a). "Analysis of submarine slumping in the Gabon continental slope." *American Association of Petroleum Geologists Bulletin*, 88(6), 781-799.

- Sultan, N., Foucher, J. P., Cochonat, P., Tonnerre, T., Bourillet, J. F., Ondreas, H., Cauquil, E., and Grauls, D. (2004)^b. “Dynamics of gas hydrates: case of the Congo continental slope.” *Marine Geology*, 206, 1-18.
- Taber, S. (1929). “Frost Heaving.” *Journal of Geology*, 37, 428-461.
- Taber, S. (1930). “The Nucleation of Frost Heaving.” *Journal of Geology*, 38, 303-317.
- Tarnawski, V. R., Leong, W. H., Gori, F., Buchan, G. D., and Sundberg, J. (2002). “Inter-particle contact Heat Transfer in Soil Systems at Moderate Temperatures.” *International Journal of Energy Research*, 26, 1345-1358.
- Tarnawski, V. R., and Leong, W. H. (2000). “Thermal Conductivity of Soils at Very Low Moisture Content and Moderate Temperatures.” *Transport in Porous Media*, 41, 137-147.
- Tatsuoka, F., and Shibuya, S. (1991). “Deformation Characteristics of Soils and Rocks from Field and Laboratory Tests.” *Proc. Ninth Asian Regional Conf. Soil Mechanics and Foundation Engineering*, Bangkok, Thailand, December 9-13, Vol 2, 101-177.
- Thalmann, R. E. (1950). *Thermal Conductivity of Dry Soils*. M.S. Thesis dissertation, University of Kansas. Lawrence, KS.
- Thomann, T. G. and Hryciw R. D. (1990). “Laboratory Measurement of Small Strain Shear Modulus under K_0 Conditions.” *Geotechnical Testing Journal*, 13(2), 97-105.
- Ting, J. M., Martin, R. T. and Ladd, C. C. (1983). “Mechanisms of Strength for Frozen Sand.” *Journal of Geotechnical Engineering*, 109(10), 1286-1302.
- Tsyrovich, N. A. (1973). *The Mechanics of Frozen Ground*. New York, McGraw-Hill, 426.
- Tulk, C. A., Klug, D. D., and Ripmeester, J. A. (1998). “Raman Spectroscopic Studies of THF Clathrate Hydrate.” *Journal of Physical Chemistry*, 102, 8734-8739.
- Uchida, T., Dallimore, S. R., Lu, H., and Collett, T. S. (2001). “Comparison of Natural Gas Hydrate Occurrence Observed in the JAPEx/JNOC/GSC Mallik 2L-38 Well, Mackenzie Delta, N.W.T. with recently obtained natural gas hydrate.” *Rock the Foundation convention*, June 18-22, Canadian Society of Petroleum Geologists.
- Vallejo, L. E. (1980) “A New Approach to the Stability Analysis of Thawing Slopes.” *Canadian Geotechnical Journal*, 17, 607-612.
- Vargas, W. L. and McCarthy, J. J. (2001). “Heat Conduction in Granular Materials.” *AIChE Journal*, 47(5), 1052-1059.

- Watanabe, K. (1999). *Ice lensing mechanism during soil freezing*. Ph.D. Thesis. Graduate School of Bioresources, Mie University. Japan.
- Wijeweera, H., and Joshi, R. C. (1990). "Compressive Strength Behavior of Fine-Grained Frozen Soils." *Canadian Geotechnical Journal*, 27, 472-483.
- Winkler, K. W. (1983). "Contact Stiffness in Granular Porous Materials: Comparison between Theory and Experiment." *Geophysics Research Letter*, 10(11), 1073-1076.
- Wissa, A. E. Z., and Ladd, C. C. (1965). "Shear Strength Generation in Stabilized Soils." Report R65-17, Soils Publication No. 173. M.I.T., Cambridge, Massachusetts.
- Wittebolle, R. J., and Segoo, D. C. (1985). "A Laboratory Facility for Testing Sediments Containing Gas Hydrates." *Proceedings of the International Offshore Mechanics and Arctic Engineering Symposium*, 2, 52-58.
- Yin, H., and Dvorkin, J. (1994). "Strength of Cemented Grains." *Geophysics Research Letter*, 21(10), 903-906.
- Yun, T. S., Francisca, F. M., Santamarina, J. C. and Ruppel, C. (2005). "Compressional and Sshear Wave Velocities in Uncemented Sediment Containing Gas Hydrate." *Geophysical Research Letters*. 32 (10), L10609
- Zang, A., and Wong, T.-F. (1995). "Elastic Stiffness and Stress Concentration in Cemented Granular Material." *Int. J. Rock Mech. Min. Sci. & Geomech. Abstr.* 32(6), 563-574.

VITA

Tae Sup Yun was born on October 30, 1974 in Seoul, KOREA. He received his Bachelor's of Science degree in Geology from Yonsei University (Seoul, KOREA) in February 1997. In August 2001, he started research towards this doctoral dissertation at the Georgia Institute of Technology, and will receive his Ph.D. degree in Civil Engineering (Geosystems Group) in August 2005.